The University Of Sheffield.

COMPUTATIONAL FLUID DYNAMICS MODELLING OF CORONARY ARTERY DISEASE

Dr Paul David Morris BMedSci (Hons) MBChB (Hons) MRCP (Lond)

British Heart Foundation Clinical Research Training Fellow

Medical Physics Group

Department of Cardiovascular Science

Insigneo Institute for In Silico Medicine

University of Sheffield

Submitted for the degree of Doctor of Philosophy

September 2015

ABSTRACT

Background

Coronary artery disease (CAD) is the leading cause of death in the world. Physiological lesion assessment with indices such as fractional flow reserve (FFR) is now accepted as the invasive gold-standard for diagnosing the significance of CAD and for guiding treatment. Patients undergoing percutaneous coronary intervention (PCI) guided by FFR have better clinical outcomes than those undergoing standard assessment. Furthermore, FFR-guided PCI is associated with decreased stent implantation and reduced long-term cost. Only a minority of patients undergoing invasive coronary angiography are currently afforded these benefits due to a number of procedure, operator, and economic related factors. There may be additional benefits from combined pressure and flow measurement. There is therefore a need for a technology that delivers the benefits of physiological lesion assessment without the factors which limit use of the invasive technique.

Hypothesis

Computational fluid dynamics (CFD) modelling based upon invasive coronary angiographic images (ICA) can characterise and predict intracoronary physiology.

Aims

(i) To develop a CFD-based model capable of simulating and predicting clinically relevant intracoronary physiology and (ii) validate model performance using clinical data from patients with CAD.

Methods

A workflow, based upon 3-D CFD modelling, capable of predicting intracoronary pressure and 'virtual' FFR from ICA, was developed. The model was validated against in vivo clinical measurements in 35 unique arterial datasets. The model predicted physiological lesion significance with 97% overall accuracy. Computation was prolonged (>24hrs). Two novel methods for solving the 3-D CFD were therefore developed. These methods enabled accurate computation of results in clinically tractable timescales (<5mins), at least equivalent to invasive measurement. The critical influence of system boundary conditions was explored, characterised, and quantified. A novel approach to patient-specific tuning of the outlet boundary conditions was developed and evaluated. The workflow was adapted to compute the pressure-flow relationship from measured pressure boundary conditions within a fully patient-specific in silico model. Results were validated within a novel experimental flow circuit incorporating patient-specific 3-D printed coronary arterial phantom models.

Conclusions

It is possible to compute clinically relevant intracoronary physiology (pressure or flow) from ICA. Results can be generated in clinically tractable timescales. The CFD model can be tuned to individual patient characteristics. The developed tools may be commercially desirable. Prior to full clinical translation, the model must be evaluated in a clinical trial

ACKNOWLEDGMENTS

Paul Morris
August, 2015

PUBLICATIONS

MANUSCRIPTS

Morris PD, Ryan D, Morton AC, Lycett R, Lawford PV, Hose DR, Gunn JP. Virtual fractional flow reserve from coronary angiography: modeling the significance of coronary lesions: results from the VIRTU-1 (VIRTUal Fractional Flow Reserve From Coronary Angiography) study. *JACC Cardiovasc Interv.* 2013 6(2):149-57.

Çimen S, Hoogendoorn C, Morris PD, Gunn J, Frangi AF. Reconstruction of coronary trees from 3DRA using a 3D+t statistical cardiac prior. *Med Image Comput Comput Assist Interv.* 2014;17(Pt 2):619-26.

Morris PD, Taylor J, Boutong S, Brett S, Louis A, Heppenstall J, Morton AC, Gunn JP.
When is rotational angiography superior to conventional single-plane angiography for planning coronary angioplasty? *Catheter Cardiovasc Interv*. 2015. doi: 10.1002/ccd.26032. [Epub ahead of print]

Morris PD, van de Vosse FN. Lawford PV, Hose DR, Gunn JP. JACC Cardiovascular Interventions. 'Virtual' (Computed) Fractional Flow Reserve: current challenges and limitations. *J Am Coll Cardiol Intv.* 2013;6(2):149-57.

Morris PD, Narracott A, von Tengg-Kobligk H, Silva Soto A, Hsiao S, Lungu A, Evans P, Bressloff NW, Lawford PV, D. Hose R, Gunn JP. Computational Fluid Dynamics Modelling in Cardiovascular Medicine. *Heart*. 2015 (In press)

Morris PD, Feher JFA, Silva Soto D, Rafiroiu D, Lungu A, Varma S, Lawford PV, Hose DR, Gunn JP. Fast Virtual Fractional Flow Reserve Based upon Steady-State Computational Fluid Dynamics (CFD) Analysis: Results from the 'VIRTU-fast' study. 2015. *Journal of Biomechanics* (in review, 2015)

BOOKS /CHAPTERS

Morris PD. Vascular Haemodynamics (Chapter 1). Eureka: Cardiovascular Medicine. JP Medical Ltd; 1 edition (31 Mar. 2015). ISBN-13: 978-1907816826

KEY ABSTRACTS

Morris PD, Zwierzak I, Lawford P, Hose DR, Gunn JP. 209: The Development and Validation of an in silico Model of Coronary Arterial Physiology for Diagnostic Use. *Heart* 101 (Suppl 4), A115-A115

Morris PD, Ryan DM, Lycett R, Morton AC, Lawford PV, Hose DR, Gunn JP. Computer Modelled Coronary Physiology and Virtual Fractional flow reserve from Rotational Angiography. *Heart* 2012;98:A14

Morris PD, Ryan DM, Lycett R, Morton AC, Lawford PV, Hose DR, Gunn J. Virtual Coronary Physiology and Anatomy Derived From Rotational Angiography: The First Step. *J Am Col Cardiol*. 2011; 58: B189

AWARDS

First prize: British Cardiovascular Interventional Society; Young Investigator Award
London, 2013

****

Science, Engineering and Technology (SET) for Britain 2013 finalist
House of Commons, Westminster, London

****

First prize, Public Engagement and Enterprise (My Research in Your Eyes)
University of Sheffield, 2013

****

First prize, Young Life Scientists Symposium 2013; William Harvey Research
Institute, Queen Mary University of London, Charterhouse Square, London

****

Sheffield Medical School Research Day – Research Poster Prize 2014

****

Early Career Research Prize for *outstanding contributions to excellence in research
and impact*. University of Sheffield, May 2015.

****

School Research Day, First prize for oral presentations – Medical School Research
Day, 2015

TABLE OF CONTENTS

LIST OF TABLES

LIST OF FIGURES

ABBREVIATION LIST

0-, 1-, 2-, 3-, 4-D	Zero-, one-, two-, three-, and four-dimensions
ACC	American College of Cardiology
ACS	Acute coronary syndrome
AHA	American Heart Association
APV	Average peak velocity
AUC	Area under (ROC) curve
BCS	Batch compiler specification (file extension)
BE	Belgium
BSR	Baseline stenosis resistance
CABG	Coronary artery bypass graft
CAC	Coronary arterial calcium
CAD	Coronary artery disease
CFVR	Coronary flow velocity reserve
CI	Confidence interval
CMRI	Cardiac magnetic resonance imaging
CMV	Coronary microvasculature
CMVD	Coronary microvascular dysfunction
CMVR	Coronary microvascular resistance
CT	Computed tomography
CTCA	Coronary computed tomographic angiography
$_{CT}$FFR	Computed tomography derived fractional flow reserve
CTP	Computed tomographic perfusion
CTP	CT perfusion
DES	Drug eluting stent
EACTS	European Association for Cardio-Thoracic Surgery
ECG	Electrocardiography
ESC	European Society of Cardiology
ETT	Exercise tolerance testing
EU	European Union
FDA	Food and Drug Administration (USA)
FFR	Fractional flow reserve
FSI	Fluid solid interaction
GIMIAS	Graphical interface for medical imaging analysis and simulation
GMES	Global mesh element size
GTN	Glycerile trinitrate

HICF	Health Innovation Challenge Fund
HMR	Hyperaemic microvascular resistance
HR	Hazard ratio
HSR	Hyperaemic stenosis resistance
ICA	Invasive coronary angiography
iFR	Instantaneous wave free ratio
IHD	Ischaemic heart disease
IMR	Index of myocardial resistance
IVUS (-VH)	Intravascular ultrasound imaging (-virtual histology)
LAD	Left anterior descending coronary artery
LCX	Circumflex coronary artery originating from the left coronary artery
LMCA	Left main coronary artery
LVEF	Left ventricular ejection fraction
MACE	Major adverse cardiovascular events
mFFR	Measured FFR
MI	Myocardial infarction
MPS	Myocardial perfusion scintigraphy
MRI	Magnetic resonance imaging
NARMAX	Nonlinear autoregressive moving average model with exogenous inputs
NHLBI	National Heart, Lung and Blood Institute
NICE	National Institute for Clinical Excellence
NL	Netherlands
NPV	Negative predictive value
NSTEMI	Non ST segment elevation myocardial infarction
OCT	Optical coherence tomography imaging
OMT	Optimal medical therapy
PA	Per annum
Pa	Proximal pressure
PA	Per annum
PC	Personal computer
PCI	Percutaneous coronary intervention
Pd	Distal pressure
PET	Positron emission tomography
PPV	Positive predictive value
Q_{3-D}	Coronary flow derived from 3-D computational fluid dynamics analysis
Q_{optim}	Coronary flow derived from the optimisation algorithm
RCA	Right coronary artery
RCX	Circumflex coronary artery originating from the right coronary artery
Re	Reynold's number
ROC	Receiver operating characteristic

RoCA	Rotational coronary angiography
R_{total}	Total myocardial resistance
SD	Standard deviation
SP	Spain
SPECT	Single photon emission computed tomography
ssh	Secure Shell (file transfer)
STEMI	ST segment elevation myocardial infarction
STH	Sheffield Teaching Hospitals NHS Foundation Trust
SVES	Surface volume element size
UoS	University of Sheffield
vFFR	Virtual fractional flow reserve
$vFFR_{CT}$	Virtual fractional flow reserve derived from computed tomographic angiography
$vFFR_{ICA}$	Virtual fractional flow reserve derived from invasive coronary angiography
$vFFR_{ps\text{-}trns}$	Pseudo-transient virtual fractional flow reserve derived from steady-state analysis
$vFFR_{steady}$	Virtual fractional flow reserve derived from steady-state analysis
vMR	Virtual myocardial resistance
VRML	Virtual reality modelling language
vSR	Virtual stenosis resistance
VTK	Visualisation toolkit (file extension)
WHO	World Health Organisation

Chapter One:
Clinical Background

1.1 Ischaemic heart disease

Ischaemic heart disease (IHD) occurs when blood flow to the myocardium becomes impaired, resulting in downstream cellular hypoxia (ischaemia). IHD is caused almost exclusively by coronary artery disease (CAD). In turn, CAD is caused by atherosclerosis, a chronic, inflammatory, fibro-proliferative disease which affects medium to large arteries.

1.1.1 Epidemiology

In the UK, CAD affects 2.3 million people with a prevalence 3.5% (Townsend, 2012). Prevalence of CAD increases with age such that; over the age of 65 years, it affects 20.8% of men and 10% of

women. IHD is the leading cause of death in the UK accounting for ~80,000 deaths per annum (Townsend, 2012). In the USA, 16.3 million people are known to have CAD and >750,000 of these die of IHD or suffer a myocardial infarction (MI) each year (Roger et al., 2012, Go et al., 2013) with an associated cost of $195 billion per annum. IHD is now also the world's leading cause of death. Globally, IHD is responsible for 7 million deaths per annum which represents 11.2% of all deaths worldwide (World Health Organization, 2013) (**Figure 1.1**) IHD is the leading cause of disease burden as measured by the sum of years of potential life lost due to premature mortality and the years of productive life lost due to disability (disability adjusted life years; DALYs) (Murray et al., 2012). Irrespective of regional variations in prevalence, there is a male preponderance of IHD with a consistent case ratio of approximately 2:1 (Wingard et al., 1983).
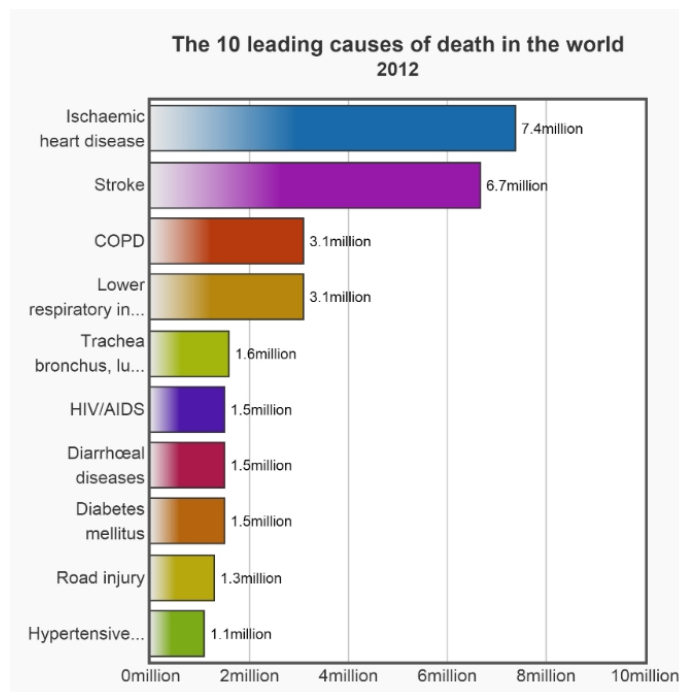
Figure 1.1. The top 10 leading causes of death
Reproduced with permission from the World Health Organisation
(World Heath Organization, 2014)

1.1.2 Pathology

Atherosclerotic streaks develop in most people from an early age. However, development into occlusive plaques is highly variable and is influenced by a number of risk factors which can be divided into non-modifiable risk factors such as increased age, male gender, family or personal history of CAD; and modifiable risk factors such as, diabetes mellitus, hypertension, metabolic syndrome, dyslipidaemia and smoking, the evaluation of which, plays a key role in the assessment

of patients with suspected CAD. The pathological development of coronary atherosclerosis is outlined in **Figure 1.2**.
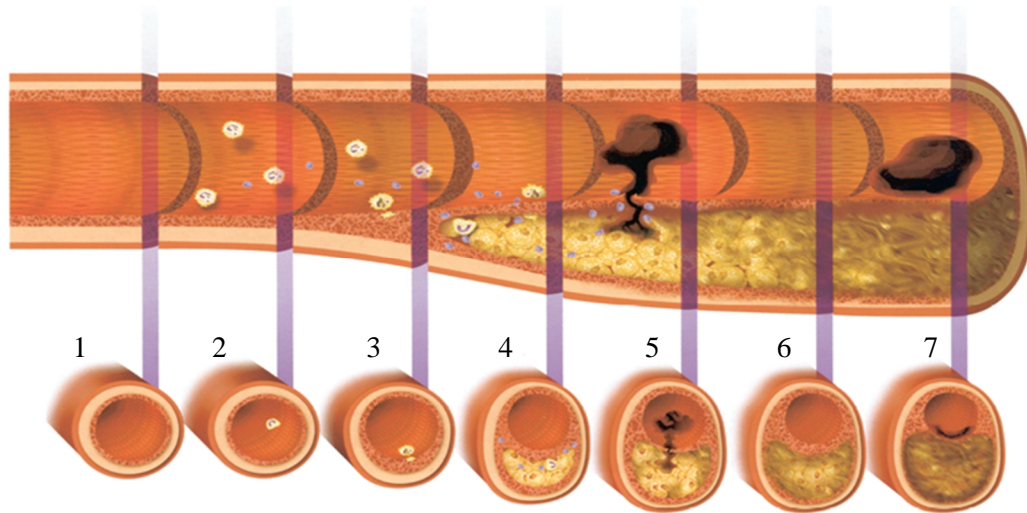
Figure 1.2. The pathological evolution of coronary atherosclerosis.
(1) Normal artery with well-developed intima containing smooth muscle (SM) cells. (2) Endothelial cell activation results in inflammatory cell (monocytes, T lymphocytes) recruitment and intimal lipid accumulation. (3) Fibrofatty stage: monocytes become macrophages and engulf modified lipoproteins becoming lipid-laden foam cells. Inflammatory cytokines and growth factors are secreted which amplify leukocyte recruitment and SM cell proliferation. (4) Lesion progression. Inflammatory mediators, tissue factors and proteinases weaken the fibrous cap of plaque. (5) Plaque rupture causes thrombus formation. Occlusive thrombus (acute coronary syndrome) or clot resorption depending on the balance of thrombotic and fibrinolytic mechanisms. (6) Thrombus resorption and healing leads to collagen accumulation and SM cell growth. The fibrofatty lesion evolves into fibrous, calcified plaque that may be flow limiting – associated with stable angina pectoris. (7) Plaque rupture or superficial endothelial erosion causing mural thrombus. Myocardial infarction results from occlusive thrombus blocking blood flow to the distal myocardium. Adapted from Libby et al with permission (Libby, 2001).

1.1.3   Clinical presentation and management

Stable coronary disease results from flow limiting but stable occlusive coronary plaque. Patients with stable CAD experience angina pectoris when blood flow (supply of oxygen) cannot match myocardial demand. Typically, this occurs during exertion and is relieved by rest. Stable disease is treated with combination of medical therapies designed to: augment plaque stability (3-hydroxy-3-methyl-glutaryl-CoA reductase inhibitors – 'statins'); reduce platelet activation (salicylate, thienopyridines and cyclo-pentyltriazolo-pyrimidine); and reduce cardiac sympathetic activation (beta adrenergic receptor inhibition). Percutaneous coronary intervention (PCI) or coronary artery bypass grafting (CABG) is effective in restoring flow to the distal myocardium in the presence of occlusive IHD. Unstable coronary disease results from plaque rupture and thrombus formation.

This results in acute coronary syndromes (ACS); unstable angina and MI. The focus of the current thesis is stable CAD and unless otherwise indicated CAD indicates stable disease.

1.1.4 Clinical assessment of stable coronary artery disease

Most adults develop coronary atherosclerosis from an early age (Joseph et al., 1993, Elveback and Lie, 1984). Loria *et al*, in a cohort of 33-45 year olds, reported that 15% of men and 5.1% of women had detectable CAD (Loria et al., 2007). However, in the context of stable CAD, it is not the presence atherosclerosis *per se* that causes morbidity and mortality, it is the haemodynamic consequence – ischaemia - which conveys risk of adverse clinical outcomes (Marie et al., 1995, Beller and Zaret, 2000, Shaw and Iskandrian, 2004, Shaw et al., 2008). This is reflected in clinical trials data. In the COURAGE (Clinical Outcomes Utilizing Revascularization and Aggressive Drug Evaluation) trial, the empirical use of PCI in those with stable CAD, as an initial management strategy, did not reduce the risk of mortality, MI, or other major adverse cardiovascular events (MACE) compared with optimal medical therapy (OMT) alone (Boden et al., 2007). Similar results were reported in a more recent meta-analysis of five major studies incorporating 4064 patients (Stergiopoulos et al., 2014). However, targeted alleviation of ischemia with PCI does improve symptoms and reduces MACE, with the greatest benefit observed in those with the highest ischaemic burden (Davies et al., 1997, Beller and Zaret, 2000, Smith et al., 2006, Erne et al., 2007, Shaw et al., 2008, Wijns et al., 2010). This is reflected in the guidelines of the European and American cardiac associations and societies. The 2012 joint ACCF/AHA Guidelines assign a class IIa (level of evidence: B) recommendation for revascularisation (CABG or PCI) of functionally significant CAD on the basis of prognosis (depending upon anatomical classification), class I (level of evidence: A) on the basis of symptom alleviation, and a class III (level of evidence: B) recommendation (indicating harm) in the context of non-significant disease (Fihn et al., 2012). Disease significance can be assessed by fractional flow reserve (FFR), with a value of ≤ 0.8 indicating significance (discussed in section 1.4.1).

Therefore, in addition to medical therapy (which promotes plaque stability) the primary motivation should be to identify the presence or absence of ischaemia because this defines patients at the highest risk of adverse outcomes. The detection of functionally non-significant coronary atherosclerosis should trigger lifestyle changes and, depending upon risk level, medical therapy, but this is a low risk group. The assessment of patients with suspected CAD should therefore reflect this.

Initial clinical assessment should elicit the nature, duration, character and pattern of symptoms, the presence or absence of risk factors, personal and family history and the patient's demographics

(age and gender). All of these factors are important in calculating risk. Physical examination is often normal in patients with significant or even extensive CAD, but may reveal evidence of contributory conditions such as hypertension, hyperlipidaemia, diabetes, or of complications such as heart failure or arrhythmia. The initial assessment defines the pre-test probability of CAD (see **Figure 1.3** below).

Age (years)	Non-anginal chest pain				Atypical angina				Typical angina			
	Men		Women		Men		Women		Men		Women	
	Lo	Hi	Lo	Hi	Lo	Hi	Lo	Hi	Lo	Hi	Lo	Hi
35	3	35	1	19	8	59	2	39	30	88	10	78
45	9	47	2	22	21	70	5	43	51	92	20	79
55	23	59	4	25	45	79	10	47	80	95	38	82
65	49	69	9	29	71	86	20	51	93	97	56	84

For men older than 70 with atypical or typical symptoms, assume an estimate > 90%.
For women older than 70, assume an estimate of 61–90% EXCEPT women at high risk AND with typical symptoms where a risk of > 90% should be assumed.

Values are per cent of people at each mid-decade age with significant coronary artery disease (CAD).
Hi = High risk = diabetes, smoking and hyperlipidaemia (total cholesterol > 6.47 mmol/litre).
Lo = Low risk = none of these three.
The shaded area represents people with symptoms of non-anginal chest pain, who would not be investigated for stable angina routinely.
Note: These results are likely to overestimate CAD in primary care populations.
If there are resting ECG ST-T changes or Q waves, the likelihood of CAD is higher in each cell of the table.

Figure 1.3. Estimating the pre-test probability of coronary disease
Reproduced with permission from the 2010 NICE guidelines for Chest Pain of Recent Onset (Cooper et al., 2010), and adapted from Pryor et al (Pryor et al., 1993)

Clinical assessment is completed with clinical investigations. These can be divided into:
- *anatomical tests*; which image the coronary lumen (see section 1.2 below).
- *functional tests*; which either directly or indirectly detect markers of myocardial ischaemia (see section 1.3 below). Also referred to as physiological investigations.

1.2 Anatomical coronary artery disease investigation

Anatomical tests comprise a variety of imaging based assessments including invasive coronary angiography (ICA) and CT coronary angiography (CTCA). Intravascular ultrasound (IVUS) and optical coherence tomography (OCT) are performed during ICA and provide additional anatomical detail.

1.2.1   Invasive coronary angiography

Since its inception in 1958, invasive coronary angiography (ICA) has remained the gold standard investigation for diagnosing and assessing coronary luminal anatomy. Moreover, it remains the only imaging modality capable of selecting patients for, and guiding revascularisation with either PCI or CABG surgery. ICA involves the passage of a catheter into the aortic root via a peripheral artery (typically radial or femoral). The distal end of the catheter is manoeuvred, under X-ray screening, so that it intubates one of the coronary ostia. Radio-opaque dye is injected into the coronary artery via the catheter and a series of X-ray images are acquired which are viewed as a movie. Because coronary atherosclerosis is usually eccentrically distributed, images are acquired from multiple projection angles in order to appreciate this.

In 2013, there were 402,979 diagnostic coronary angiograms and 94,033 PCI procedures performed in the UK, which represents a 67.5% increase over the last ten years (Ludman. P, 2014). In the USA, 1,029,000 diagnostic ICAs, 492,000 PCIs and 397,000 CABGs were performed in 2010 (Go et al., 2013, Mozaffarian et al., 2015).

ICA allows the lumen of the artery to be appreciated in two-dimensions (2-D). By acquiring images from multiple directions, the operator can reconstruct the 3-D structure of the artery in their mind. Work by Gould et al in the 1970s demonstrated with the use of a canine model that under hyperaemic conditions, coronary flow became limited only when a stenosis exceeded 50% of the lumen diameter in orthogonal views and that resting flow became limited only when the stenosis exceeded 85% of the diameter due to the compensatory, autoregulatory effects of the coronary microvasculature (CMV) (Gould et al., 1974, Gould et al., 1975). These historic visual criteria have governed revascularisation decisions ever since. It is now recognised that visual ICA assessment frequently over-estimates the severity of coronary stenoses whilst under-estimating lesion length, regardless of how skilled or experienced the operator may be (Fleming et al., 1991, Bertrand et al., 1993, Topol and Nissen, 1995, Mintz et al., 1996, Green et al., 2004, Nallamothu et al., 2013). Furthermore, despite providing unsurpassed anatomical detail, ICA does not reliably discern ischaemia-provoking lesions from haemodynamically non-significant lesions (Legrand et al., 1986, Miller et al., 1994, White et al., 1984, Yong et al., 2011, Nallamothu et al., 2013, Gould, 2009, Tonino et al., 2010). An approach involving visual assessment alone is subjective and may result in an inconsistent approach to PCI decisions since the prognostic benefit of revascularisation is limited to those with demonstrable ischaemia (Shaw et al., 2008).

1.2.2   Coronary computed tomographic angiography (CTCA)

Over the last decade, CTCA has emerged as a useful, non-invasive, imaging modality for evaluating coronary arterial luminal anatomy (Min et al., 2010). The emergence of 64-slice detector CTCA scanners in 2005 provided improved temporal and spatial resolution and allowed whole heart acquisitions on a single breath hold (8-12 seconds). This technology is now widely available (Min et al., 2010). Concerns regarding high radiation doses associated with CTCA (Hausleiter et al., 2009) have been alleviated since the development of dual source, prospectively ECG gated imaging techniques (Sun and Ng, 2012, Kim et al., 2012). Compared with ICA, 64-slice CTCA detects anatomically significant coronary stenoses (defined as >50% diameter loss in two views) with high sensitivity (c 95%) and with high negative predictive values (c 99%) (Meijboom et al., 2008a, Janne d'Othee et al., 2008). However, this is at the expense of specificity (77%) and positive predictive value (36%) (Budoff et al., 2008, Miller et al., 2008). Other studies similarly demonstrate that the majority of functionally significant stenoses detected by CTCA do not cause ischemia (Budoff et al., 2008, Miller et al., 2008, Meijboom et al., 2008a, Meijboom et al., 2008b). More recently, 256-slice CTCA has been assessed. Although this provides enhanced image quality, blooming artefact continues to pose challenges when assessing calcified disease (Hou et al., 2013).

For these reasons, CTCA has been widely adopted as a useful 'rule-out' tool for patients with a low-moderate pre-test probability of CAD (Sun et al., 2008) and, in many centres, is used effectively as a gatekeeper to ICA (Shaw et al., 2012). This is important because ICA is, in comparison, at increased risk, expensive and, by definition, invasive. The need for an effective gate-keeper was highlighted by Patel et al who demonstrated, in their study of 398,978 patients undergoing ICA, that 60% had non obstructive CAD and 39.2% had stenosis <20%, despite 83.9% having undergone prior non-invasive testing (Patel et al., 2010). More recently, results from the CONFIRM (COronary CT Angiography EvaluatioN For Clinical Outcomes: An InteRnational Multicenter) registry have suggested, for the first time, that CTCA may also have a role in selecting high risk CAD patients who gain prognostic benefit from revascularisation (Min et al., 2012, Shaw et al., 2012). However, these studies are based on purely anatomical criteria.

The principal limitation of CTCA is that it overestimates the presence and extent of CAD which increases the false positive rate (Mowatt et al., 2008, Meijboom et al., 2008a). The principal reason for this is the presence of calcium in the arterial wall which results in 'blooming' artefact and overestimation of lesion severity. The ACCURACY (Assessment by Coronary Computed Tomographic Angiography of Individuals Undergoing Invasive Coronary Angiography) trial

demonstrated that sensitivity and particularly specificity were reduced in those with coronary arterial calcium (CAC) scores > 400 Agatston units (a derivative of Hounsfield units of radiodensity) (95.8% vs 93.6% and 86.3% vs 52.6% respectively). Unhelpfully, this effect was greatest in lesions in the moderate range i.e. those which cause the greatest diagnostic challenge (Budoff et al., 2008). The method and protocol of CTCA means that it is also limited in those with dyspnoea, cardiac arrhythmia, tachycardia and obesity (Mowatt et al., 2008).

1.2.3 MRI angiography

The quality of MRI angiography is limited by the small size, tortuosity and movement of the coronary vessels. It does add value when combined with functional MRI perfusion (Greenwood et al., 2012) but, as a stand-alone investigation, is inferior to CTCA in detecting significant CAD (Schuijf et al., 2006a, Pennell et al., 2004). In a large meta-analysis of 993 patients (4,620 lesions), sensitivity and specificity for detection of significant CAD (compared with ICA) were 73% and 86%, respectively. Currently, none of the major guideline documents make any recommendations about the use of MRI angiography and this remains within the domain of academic research.

1.2.4 Intravascular ultrasound imaging

Intravascular ultrasound imaging (IVUS) involves passing an ultrasound probe along a diseased section of coronary artery in order to generate real-time cross sectional images of the coronary lumen area and plaque composition, size, and distribution within the vessel wall. Manual or automatic pull-back of the wire (at 0.5 - 2.0 mm/s) adds an additional dimension (length) to the tomographic representation. The generated images are of high spatial resolution that can detect otherwise 'silent' atherosclerotic plaque undetectable on standard ICA (Nissen and Yock, 2001, Mintz et al., 2001). IVUS can generate a number of clinically useful anatomical measures including: luminal area, total vessel area (area within the external elastic membrane), plaque plus media area (difference between luminal and total vessel area), percentage plaque area, and a plaque eccentricity index (Windecker et al., 2014). In vessels treated with PCI, immediate IVUS is used to assess stent deployment, whereas delayed interrogation quantifies in-stent re-stenosis. Radiofrequency analysis of the echo back-scatter allows enhanced patient-specific characterisation of the components within atherosclerotic plaque. This is known as IVUS 'virtual histology' (IVUS-VH) and can discriminate between stable and unstable plaque (Nair et al., 2002). IVUS provides superior spatial resolution at length scales which are not possible with ICA. IVUS is particularly useful in assessing plaque burden, coronary dissection (Peters et al., 1997, Stone et al., 1997) and for adequacy of stent deployment. IVUS is therefore a useful adjunct to ICA which is capable of reducing PCI related complications and mortality (Roy et al., 2008, Zhang et al., 2012) even with drug eluting stents (DES) (Witzenbichler et al., 2014). However, it is not a stand-alone

technique. According to the European guidelines, IVUS is indicated for optimising stent implantation in selected patients (IIa, B), for assessing and optimising PCI in left main coronary artery (LMCA) disease (IIa, B), and for assessing mechanism of stent failure (IIa, C) (Windecker et al., 2014).

1.2.5 Optical coherence tomography

Optical coherence tomography (OCT) is similar to IVUS but is light-based. The reduced wavelength allows higher spatial resolution (15 vs 150 μm), at the cost of reduced wall penetration. OCT is therefore apposite for the detection of structures within, or just beyond the intimal surface (including plaque composition) but cannot assess total plaque burden. OCT can detect thickness and even minor disruption of the atherosclerotic fibrous cap (Cassar et al., 2013). OCT is superior to IVUS for assessing: the subtleties of neointimal thickness and disruption, markers reflecting the effectiveness of stent deployment (class IIa C) and the underlying mechanisms behind stent failure (class IIb, C) (Windecker et al., 2014).

1.3 Functional coronary assessment methods

Functional (or physiological) tests directly, or indirectly, detect markers of ischaemia. A large number of functional investigations exist. Many combine a rest and a stress phase to identify inducible ischaemia. Stress can be initiated with exercise or pharmacologically (inotropic or distal vasodilating agents). Functional tests focus on stages of the ischaemic cascade. The ischaemic cascade is demonstrated in **Figure 1.4** below. Tests which elicit early manifestations of ischaemia, for example coronary microvascular dysfunction (CMVD), are more sensitive, whereas tests which elicit and detect later manifestations, for example, ECG changes, are less sensitive but more specific. The lack of an absolute gold-standard test for ischaemia has resulted in investigators validating one imperfect investigation against another (see **Table 1.1**). Functional tests have been frequently validated against the presence of obstructive CAD at ICA, and anatomical tests against a functional test such as myocardial perfusion scintigraphy. Functional tests can be divided into:

·   Non-invasive: performed on an outpatient basis (section 1.3.1)

·   Invasive: performed during cardiac catheterisation (section 1.4)

1.3.1 Non-invasive functional investigations

1.3.1.1 Exercise ECG testing

Exercise ECG or exercise tolerance testing (ETT), once the cornerstone of functional CAD testing, detects the late stages of the ischaemic cascade. In one meta-analysis of 147 studies (n=24,074) there was wide variability in the sensitivity (68%; range, 23-100%) and specificity (77%; range, 17-100%) (Gianrossi et al., 1989) of ETT relative to ICA. Its use is limited in women (Kwok et al., 1999) and in those with reduced mobility, or uninterpretable ECGs. ETT is now omitted from the 2010 UK NICE guidelines for the assessment of recent onset chest pain (Cooper et al., 2010) and the 2014 European Society of Cardiology (ESC) (Windecker et al., 2014). ETT remains indicated for capable patients (with interpretable ECGs) at intermediate risk of stable CAD according to the 2012 ACC/AHA Guideline for the Diagnosis and Management of Patients With Stable Ischemic Heart Disease, but it is noted that "*stress imaging is estimated to provide a benefit over exercise ECG at a reasonable cost*", "*a result driven chiefly by increased angiography and MACE*" in those with a negative exercise ECG (Fihn et al., 2012).
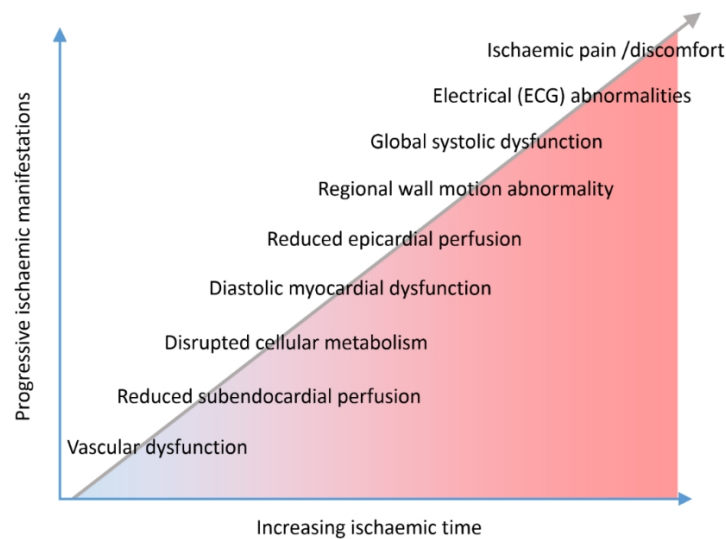
Figure 1.4. The ischaemic cascade.
Increasing ischaemia results in a cascade of functional consequences.
Image, Morris, based on Shaw et al (Shaw et al., 2009)

1.3.1.2 Stress echocardiography

Stress echocardiography detects regional wall motion abnormalities under pharmacological or exercise stress conditions, a late phenomenon in the ischaemic cascade. Sensitivity and specificity vary (70-90% and 77-90% respectively) when compared to either ICA or SPECT as the reference standard (Fleischmann et al., 1998, Imran et al., 2003, Marcassa et al., 2008, Picano et al., 2008).

Accuracy is improved by pharmacological stress induction and with an ultrasound contrast agent. However, accuracy is dependent upon operator expertise and is often limited by patient factors (e.g. obesity and lung disease). Stress echocardiography has a class 1, A recommendation for diagnosing ischaemia in patients with intermediate risk of stable CAD (Windecker et al., 2014). Exercise echocardiography cannot discriminate between epicardial and CMV disease.

1.3.1.3 Myocardial perfusion scintigraphy

Myocardial perfusion scintigraphy (MPS) involves the injection of a radioactive tracer which is taken up by viable myocardium and subsequently detected by either single photon emission tomography (SPECT) or positron emission tomography (PET) under resting and pharmacologically stressed (adenosine infusion or regadenoson bolus) conditions. Diagnosis of ischaemia relies chiefly upon the identification of hypo-perfusion (or transient dilatation or reduced left ventricular ejection fraction) during the stress phase which is not present at rest (hence reversible or inducible) whereas fixed defects represent myocardial scar. SPECT perfusion protocols use a technetium-99m tracer. With ICA as the reference standard, SPECT performs with a sensitivity of 88-91% and a specificity of 75-90% (Fihn et al., 2012). SPECT is limited in obese or large breasted patients. Because SPECT identifies relative reductions in tracer uptake, it is less sensitive in diffuse, 3-vessel disease. Myocardial PET perfusion uses radioactive labelled rubidium or ammonia and provides slightly superior image resolution and accuracy and is less prone to the limitations of SPECT. PET analysis yields additional information regarding myocardial viability. In a meta-analysis including 1442 patients with suspected CAD, PET performed with a sensitivity of 91% and specificity of 85% compared with ICA as the reference standard (Nandalur et al., 2008). PET and SPECT alone detect the preliminary stages of ischaemia but cannot differentiate between small vessel disease and epicardial disease.

1.3.1.4 Perfusion magnetic resonance imaging

Perfusion MR imaging detects myocardial uptake and washout of gadolinium under resting and pharmacologically stressed (adenosine) conditions. The MR-IMPACT II trial demonstrated the superiority of perfusion MR over SPECT in detecting significant CAD in 553 patients (Schwitter et al., 2013). The cardiovascular magnetic resonance and single-photon emission computed tomography for diagnosis of coronary heart disease (CE-MARC) trial represents the largest prospective evaluation of the diagnostic accuracy of MR perfusion to date. This study of 752 patients with suspected CAD demonstrated superior sensitivity (86.5% vs 66.5%, $p<0\cdot0001$) but similar specificity (83.4% vs 82.6%, $p=0\cdot916$) for a multi-parametric MRI protocol consisting of rest and adenosine stress perfusion, cine imaging, late gadolinium enhancement, and MR coronary

angiography (Greenwood et al., 2012). Other advantages of MR include zero ionising radiation, superior resolution, and multiple parameter acquisition in a single study (e.g., ventricular function, perfusion, viability, and coronary anatomy).

1.3.1.5 CT perfusion

Coronary CT perfusion (CTP) is a relatively new technique based upon the concept that intravenously injected contrast agent migrates from the intravascular domain into the myocardial interstitium. The increase in intensity in the myocardium can be quantified by measuring the time-attenuation curve (TAC) determined by the wash-in and wash-out dynamics of the contrast agent interacting with the myocardium. The TAC can be converted into absolute mean blood flow which is territory-specific. CTCA and CTP protocols are simply combined into a single investigation, which means that anatomical and functional data can be acquired simultaneously. However, minimising radiation dose remains a major challenge (Rossi et al., 2014).

1.3.1.6 Hybrid imaging protocols.

Hybrid protocols combine an anatomical imaging modality (CT or MRI) with a functional test such as SPECT or PET. The combination of anatomy and function in a single study, is an attractive proposition and has demonstrated promising early results (Di Carli et al., 2007a, Di Carli et al., 2007b). However, hybrid protocols require further evaluation and technological maturation before the true power of their diagnostic accuracy is known and co-registration between tests can be challenging.

Table 1.1. Summarises the diagnostic accuracy of tests commonly used to identify the presence or absence of stable CAD as reported in the literature.

1.4 Functional invasive coronary artery disease assessment

Invasive functional tests are based physiological indices derived from sensor-equipped guidewire measurement of intracoronary pressure and flow during left heart catheterisation. These indices include: fractional flow reserve (FFR), coronary flow velocity reserve (CFVR), hyperaemic stenosis resistance (HSR), baseline stenosis resistance (BSR) and index of myocardial resistance (IMR). Because these indices are measured during ICA, they can be used to guide directly decisions regarding PCI.

1.4.1 Fractional flow reserve

Myocardial fractional flow reserve (FFR) is defined as: *"the maximal myocardial perfusion during hyperaemia in the presence of a stenosis in the epicardial artery, expressed as a fraction of its normal maximal expected value"* (De Bruyne et al., 1995). FFR is an index of coronary flow but is derived from pressure measurements. FFR is calculated from the ratio of the intracoronary pressure distal to a coronary stenosis (P_d), divided by the proximal intracoronary pressure (P_a), during maximal hyperaemia. FFR objectively quantifies epicardial CAD lesion significance within the context of the remainder of the arterial circulation. Supported by robust outcome data, FFR has quickly emerged as an important diagnostic modality within the armamentarium of interventional cardiologists.

Table 1.1. Diagnostic accuracy of tests commonly used to identify the presence or absence of CAD or IHD.

Modality	For detecting reference standard		Reference standard	Key references	Level of evidence
	Sensitivity (%)	Specificity (%)			
CTCA	95-99	64-83	Obstructive CAD at ICA	(Budoff et al., 2008, Miller et al., 2008, Meijboom et al., 2008a)	A
CTCA	60-83	46-91	Perfusion defect on SPECT	(Tamarappoo et al., 2010, Schuijf et al., 2006b, Hacker et al., 2005)	B
ETT	45-50	85-90	Obstructive CAD at ICA	(Froelicher et al., 1998, Gibbons et al., 2003, Morise and Diamond, 1995)	A
Stress (exercise) echo	80-85	80-88	Obstructive CAD at ICA	(Heijenbrok-Kal et al., 2007)	A
Stress (pharm) SPECT	90-91	75-84	Obstructive CAD at ICA	(Heijenbrok-Kal et al., 2007, Higgins et al., 2006)	A
Stress (pharm) PET	81-97	74-91	Obstructive CAD at ICA	(Mc Ardle et al., 2012, Higgins et al., 2006, Jaarsma et al., 2012)	A
Stress (pharm) MRI	67-94	61-85	Obstructive CAD at ICA*	(Greenwood et al., 2012, de Jong et al., 2012, Nandalur et al., 2008, Hamon et al., 2010, Schwitter et al., 2013)	A
CT perfusion	68-96	62-93	Perfusion defect on MRI or SPECT	(Feuchtner et al., 2011, Wang et al., 2011, Bamberg et al., 2014, George et al., 2014)	B
CT perfusion (+CTCA)	80-94	67-98	Perfusion defect on SPECT or MRI	(George et al., 2011, Wang et al., 2011, Rochitte et al., 2014, Feuchtner et al., 2011, Nasis et al., 2013)	B

*CTCA, computed tomographic coronary angiography; ETT, exercise tolerance testing; pharm, pharmacologically induced; SPECT single photon emission computed tomography; PET, photon emission tomography; MRI, magnetic resonance imaging; CT, computed tomography; CAD, coronary artery disease; ICA, invasive coronary angiography. *CE-MARC 2 will compare Stress MRI with FFR.*

1.4.1.1 Physiological basis of FFR

Young et al (Young et al., 1977) first described the physiological relationship between pressure and flow within a diseased coronary artery in the 1970s but it was Pijls and De Bruyne who developed the concept and described the experimental basis for pressure-derived FFR in 1993 (Pijls et al., 1993). In any hydrodynamic system, the relationship between pressure and flow is a function of the resistance within the system. This relationship is analogous to electrical circuits where, according to Ohms law (where: V = potential difference; I = current; and R = resistance):

$$V = IR \qquad\qquad \text{Eq 1.4.1}$$

In a hydraulic system, V is analogous to pressure (P) and I is analogous to flow (Q), such that:

$$P = QR \qquad\qquad \text{Eq 1.4.2}$$

In the coronary circulation, the resistance of the distal coronary bed is dynamic. Through alterations in vascular tone, the distal coronary microvasculatature (CMV) resistance (CMVR) responds to a combination of neurohumoural, metabolic, endothelial and myogenic signalling pathways in order to:

- maintain constant flow (within a physiological BP range) at times of stable metabolic demand i.e. *autoregulation*
- increase or decrease flow according to the prevailing metabolic demands i.e. *metabolic adaptation* (Tiefenbacher and Chilian, 1998, Mosher et al., 1964) (see **Figure 1.5** below).

The epicardial artery therefore represents just a sub-compartment of a larger, more complex, and highly dynamic circulatory system, any part of which may influence flow through the system. At times of minimal CMVR (maximal CMV vasodilatation), flow is maximal (maximal hyperaemia), and coronary arteriolar regulation of flow is obliterated. At this point, flow becomes dependent on pressure. The experimental basis for using a pressure-derived fractional *flow* reserve (FFR) therefore rests upon the assumption that the resistance of the coronary circulation is both minimal and stable, during maximal arteriolar dilatation. As Pijls et al explain, it is '*intuitively reasonable*' to assess patients under maximal hyperaemia since the '*functional capacity of patients with ischemic heart disease is determined by the maximally achievable blood flow through the stenosis and its dependent myocardium*' (Pijls et al., 1993).
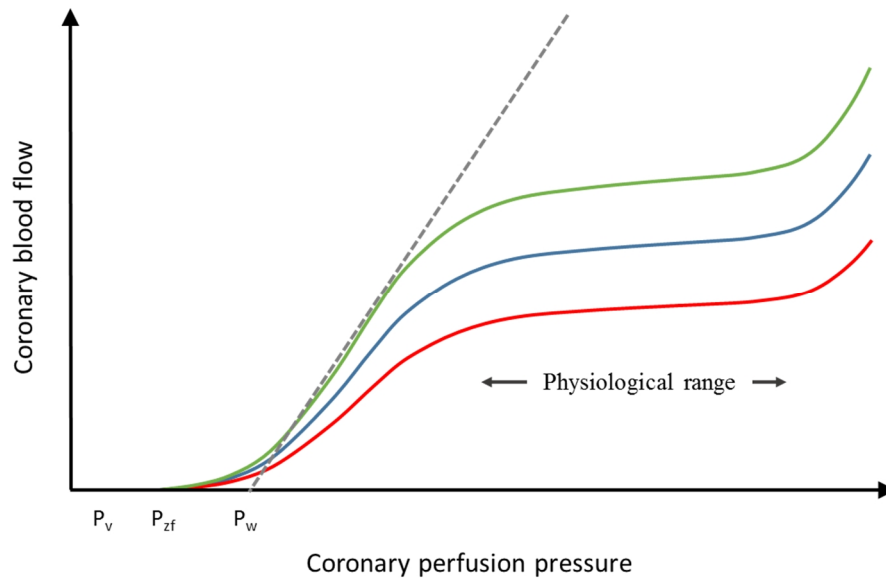
Figure 1.5. Pressure and flow in an unobstructed coronary artery.
The dark blue line represents baseline conditions and the red and green lines represent the influence of autoregulation during decreased and increased metabolic demand. Note the relatively flat section within physiological pressure range. Pressure at zero-flow (P_{zf}) occurs slightly above venous pressure (P_v). The dotted grey line represents the pressure-flow relationship during maximal hyperaemia when flow becomes dependent upon pressure. Linearity is dependent on the absence of stenosis. Note the non-zero intercept corresponding to the wedge pressure (P_w). Adapted from van de Hoef et al (van de Hoef et al., 2013)

1.4.1.2 Derivation of FFR

FFR is an index of flow but is derived purely from pressure measurements. It is therefore important to understand the derivation of FFR along with the assumptions upon which it is based. More comprehensive reviews are reported by Hoffman et al and Pijls et al (Pijls et al., 1993, Hoffman, 2000). By definition, FFR is equal to the ratio of the flow in the presence of a stenosis by the flow in the hypothetical absence of stenosis. In a simple coronary circulation, assuming no collateral flow, the system can be represented as:

15
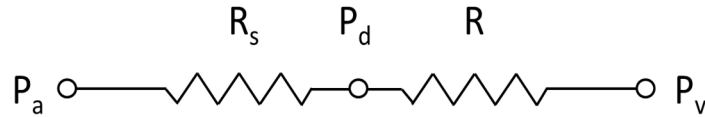
Figure 1.6. Simple coronary circuit
The coronary stenosis and microvasculature act as two resistors arranged in series. The distribution of pressure is determined by the magnitude of these resistances. P_a is the proximal aortic pressure, P_d is the distal pressure, P_v is the venous pressure (assumed to be zero), R_s is the stenosis resistance and R is the resistance of the CMV (CMVR).

Where P_a is the proximal aortic pressure, P_d is the distal pressure, P_v is the venous pressure (assumed to be zero), R_s is the stenosis resistance and R is the resistance of the CMV, then according to Ohm's law:

$$R = \frac{V}{I}$$

and

$$R = \frac{P}{Q}$$

then

$$P_a - P_d = Q R_s$$

and

$$P_d - P_v = QR$$

Therefore, by combining these two circulations:

$$P_a - P_v = Q\ (R_s + R)$$

which can be rearranged to:

$$Q = \frac{P_a - P_v}{R_s + R}$$

FFR, by definition is equal to:

$$\frac{Q_{R_s}}{Q_{R_s=0}}$$

16

i.e. the ratio of flow through the artery (Q_{Rs}) to the flow in the hypothetical situation where there is no stenosis and, thus the resistance is equal to zero ($Q_{Rs=0}$). Therefore:

$$FFR = \frac{P_a - P_v}{R_s + R} \cdot \frac{0 + R}{P_a - P_v}$$

i.e.

$$FFR = \frac{P_a - P_v}{R_s + R} \cdot \frac{R}{P_a - P_v}$$

Which simplifies to:

$$FFR = \frac{R}{R_s + R}$$

Which expands to:

$$FFR = \frac{P_d - P_v}{Q} \cdot \frac{Q}{P_a - P_v}$$

And since the flow cancels out:

$$FFR = \frac{P_d - P_v}{P_a - P_v}$$

Since P_v is assumed to be zero:

$$FFR_{myo} = \frac{P_d}{P_a} \qquad\qquad \text{Eq 1.4.3.}$$

This derivation rests upon the assumption that the resistance (R) will be the same in both in the presence of a stenosis, and in the hypothetical absence of a stenosis.

In a circulation with collateral flow connections the system is better represented as two epicardial 'circuits' arranged in parallel as shown in **Figure 1.7**:
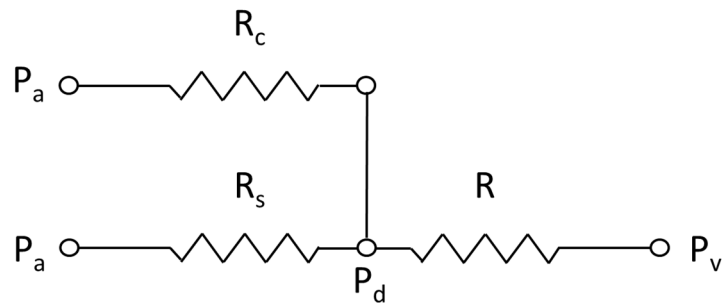
Figure 1.7. Coronary circuit with collateral flow.
R_c is the resistance of the collateral system.

Where R_c is the resistance of the collateral system. The contribution of the collateral circulation to the overall system can be calculated if P_d is measured with the index stenosis (R_s) completely occluded. This can be achieved *in vivo* by positioning the pressure transducer distal to the stenosis while completely occluding (wedging) the stenosis via balloon inflation during PCI. When this occurs the situation can be represented as in **Figure 1.8** below:
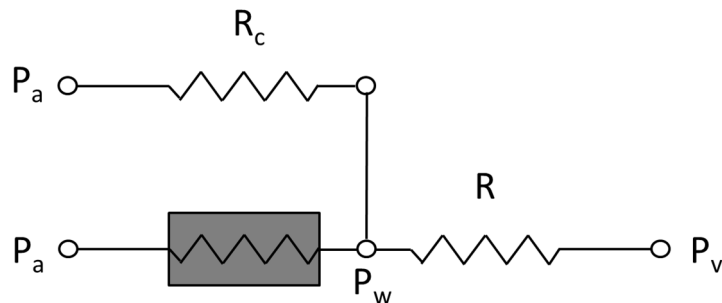
Figure 1.8. Coronary wedge pressure (P_w).
Measured whilst R_s is occluded by the angioplasty balloon.

Note that with the stenosis occluded, P_d becomes the wedge pressure (P_w). Therefore:

$$P_a - P_w = QR_c$$

and:

$$P_w - P_v = QR$$

and so:

$$\frac{\cancel{Q}R_c}{\cancel{Q}R} = \frac{P_a - P_w}{P_w - P_v}$$

1. Flow through the collateral system (Q_c) can be calculated thus:

$$Q_c = \frac{P_a - P_d}{R_c}$$

2. And flow through the stenosis (Q_s) is calculated thus:

$$Q_s = \frac{P_a - P_d}{R_s}$$

3. And total flow through the myocardium (Q) is calculated thus:

$$Q = \frac{P_d - P_v}{R}$$

Therefore, by adding the first two equations, total flow, which is equal to flow through the collateral and stenosis can be calculated:

$$Q = (P_a - P_d)(\frac{1}{R_c} + \frac{1}{R_s})$$

this can be rearranged to:

$$\frac{Q}{\left(\frac{1}{R_c} + \frac{1}{Rs}\right)} = P_a - P_d$$

and

$$Pa - \frac{Q}{\left(\frac{1}{R_c} + \frac{1}{Rs}\right)} = P_d$$

We have already described flow thus:

$$Q = \frac{P_d - P_v}{R}$$

and rearranged:

$$P_d = QR + P_v$$

Therefore:

$$Pa - \frac{Q}{\left(\frac{1}{R_c} + \frac{1}{Rs}\right)} = QR + P_v$$

and:

$$P_a - P_v = Q \cdot \left[R + \frac{1}{\frac{1}{R_c} + \frac{1}{Rs}} \right]$$

Rearranged, this forms the general equation which expresses flow in the presence of collateral flow and a stenosis:

$$Q = \frac{P_a - P_v}{\left[R + \frac{1}{\frac{1}{R_c} + \frac{1}{Rs}} \right]}$$

Since FFR is defined as:

$$FFR = \frac{Q_{Rs}}{Q_{Rs=0}}$$

then:

$$FFR = \frac{P_a - P_v}{\left[R + \frac{1}{\frac{1}{R_c} + \frac{1}{Rs}} \right]} \cdot \frac{R^*}{P_a - P_v}$$

*note that this term reduces to zero since when R_s is equal to zero (as in the hypothetical scenario which defines FFR), $\frac{1}{\infty} = \mathbf{0}$. Therefore, all that remains is R. Since the "P_a-P_v" terms cancel out, we are left with:

$$FFR = \frac{R}{R + \left[\frac{1}{\frac{1}{R_c} + \frac{1}{Rs}} \right]}$$

and if we the divide top and bottom terms by R then we can express FFR in terms of a resistance ratio:

$$FFR = \frac{1}{1 + \left[\frac{1}{\frac{R}{R_c} + \frac{R}{Rs}} \right]}$$

To express this in terms of pressure we need to go back to:

$$Q = (P_a - P_d) \left(\frac{1}{R_c} + \frac{1}{R_s} \right)$$

and

$$Q = \frac{P_d - P_v}{R}$$

20

and so:

$$Q = \frac{P_d - P_v}{R} = (P_a - P_d)(\frac{1}{R_c} + \frac{1}{R_s})$$

rearranged:

$$\frac{R}{R_c} + \frac{R}{R_s} = \frac{P_d - P_v}{P_v - P_d}$$

inverted:

$$\frac{1}{\left[\frac{R}{R_c} + \frac{R}{R_s}\right]} = \frac{P_a - P_d}{P_d - P_v}$$

Substituted into the general equation:

$$FFR = \frac{1}{1 + \left[\frac{P_a - P_d}{P_d - P_v}\right]}$$

If we multiply by $(P_d - P_v)$ then:

$$FFR = \frac{P_d - P_v}{(\cancel{P_d} - P_v) + (P_a - \cancel{P_v})}$$

i.e.

$$FFR = \frac{P_d - P_v}{P_a - P_v}$$

This equation provides the myocardial FFR (FFR$_{myo}$) i.e. the total amount of myocardial flow (Q) in the presence of a stenosis compared with the hypothetical normal artery. Coronary FFR (FFR$_{cor}$) can also be calculated i.e. the total amount of flow through the stenosed artery (Q_s) achievable with the stenosis, compared with the hypothetical normal artery. Calculation of the FFR$_{cor}$ requires a value for the wedge pressure (P_w). Given that:

$$Q = \frac{P_a - P_v}{\left[R + \frac{1}{\frac{1}{R_c} + \frac{1}{R_s}}\right]}$$

then the proportion of flow through the stenosis (Q_s) can be given by:

21

$$Q = \frac{P_a - P_v}{\left[R + \frac{1}{\frac{1}{R_c} + \frac{1}{R_s}}\right]} \cdot \frac{R_c}{R_s - R_c}$$

Note that when R_c is zero, Q_s is zero, and when R_s is zero, Q_s is the same as Q, which is appropriate. FFR$_{cor}$ can therefore be calculated thus:

$$FFR_{cor} = \frac{Q_{S_R}}{Q_{S_{R=0}}} = \frac{\frac{P_a - P_v}{\left[R + \frac{1}{\frac{1}{R_c} + \frac{1}{R_s}}\right]} \cdot \frac{R_c}{R_s - R_c}}{\frac{P_a - P_v}{\left[R + \frac{1}{\frac{1}{R_c} + \frac{1}{R_s}}\right]}}$$

Note that if Rc is zero then the $\frac{1}{\frac{1}{R_c} + \frac{1}{R_s}}$ term reduces to zero. This is further rearranged to:

$$= \frac{1}{1 + \frac{1}{\left[\frac{R}{R_c} + \frac{R}{R_s}\right]}} \cdot \frac{R_c}{R_s - R_c}$$

Going back to the original equations describing flow through the three compartments:

$$Q_c = \frac{P_a - P_d}{R_c} \qquad\qquad Q_s = \frac{P_a - P_d}{R_s} \qquad\qquad Q = \frac{P_d - P_v}{R}$$

then

$$Q = (P_a - P_d)\left(\frac{1}{R_c} + \frac{1}{R_s}\right) = \frac{P_d - P_v}{R}$$

and

$$\left[1 + \frac{R_c}{R_s}\right] = \frac{R_c}{R} \frac{(P_d - P_v)}{(P_a - P_d)}$$

and

$$\frac{R_c}{R_s} = \frac{R_c}{R} \frac{(P_d - P_v)}{(P_a - P_d)} - 1$$

since:

$$\frac{R_c}{R_s - R_c} = \frac{\frac{R_c}{R_s}}{\left[1 + \frac{R_c}{R_s}\right]} = \frac{\frac{R_c}{R}\frac{(P_d - P_v)}{(P_a - P_d)} - 1}{\frac{R_c}{R}\frac{(P_d - P_v)}{(P_a - P_d)}}$$

therefore:

$$\frac{R_c}{R_s - R_c} = 1 - \frac{R}{R_c}\frac{(P_a - P_d)}{(P_d - P_v)}$$

but

$$\frac{R_c}{R} = \frac{P_a - P_w}{P_w - P_v}$$

therefore:

$$= 1 - \frac{(P_w - P_v)}{(P_a - P_w)}\frac{(P_a - P_d)}{(P_d - P_v)}$$

and by multiplying out and cancelling terms:

$$= \frac{(P_a - P_v)}{(P_a - P_w)}\frac{(P_d - P_w)}{(P_d - P_v)}$$

therefore:

$$FFR_{cor} = \frac{\cancel{(P_d - P_v)}}{\cancel{(P_a - P_v)}} \cdot \frac{\cancel{(P_a - P_v)}}{(P_a - P_w)}\frac{(P_d - P_w)}{\cancel{(P_d - P_v)}}$$

Thus coronary FFR is calculated from:

$$FFR_{cor} = \frac{(P_d - P_w)}{(P_a - P_w)} \qquad\qquad \text{Eq 1.4.4.}$$

Myocardial blood flow is the most important physiological parameter. Furthermore, coronary wedge pressure is rarely measured in normal clinical practice. For these reasons, FFR_{cor} is rarely measured. Unless explicitly stated, throughout this thesis, the term FFR refers to the FFR_{myo}.

1.4.1.3 FFR and fluid dynamics

The concept of FFR is based upon the total pressure drop across a stenosis which can be divided into:

· **Poiseuille** pressure losses, which are the viscous losses in a straight tube, associated with fully developed parabolic flow. Poiseuille pressure (*P*) losses increase *linearly* with flow. They are dependent upon blood viscosity (μ), vessel length (*L*), and critically, the fourth power of the radius (*R*) (Westerhof et al., 2010):

$$\Delta P = \frac{8\mu QL}{\pi R^4} \qquad \text{Eq 1.4.5.}$$

· **Bernoulli** losses (**Figure 1.9** below), which are due to convective acceleration of blood flow through stenotic narrowing. These losses increase *quadratically* with flow velocity (V) due to squared velocity term. Where ρ is blood density:

$$\Delta P = \frac{1}{2}\rho(V_2^2 - V_1^2) \qquad \text{Eq 1.4.6.}$$

(neglecting gravitational terms)

The Bernoulli principle predicts pressure full recovery if the vessel diameter is restored. However, in the post-stenotic region high velocity jets cause flow separation, vortex formation and eddy currents. This prevents full pressure recovery (see section 2.2). Within the narrowing part of the stenosis, the conversion of potential to kinetic energy (reduced pressure, increased velocity) is efficient and predictale. In the post-stenotic region, kinetic energy is not converted back to potential energy efficiently, nor fully. Therefore, the laws of Bernoulli and Poiseuille only partly characterise the relationship between vessel geometry, flow and pressure under idealised circumstances. It takes a more sophisticated mathematical (numerical) method to fully describe the haemodynamics in a dynamic 3-D system like the coronary circulation. **Figure 1.9** demonstrates the pressure-flow relationship for three stenoses of increasing severity. This relationship is described by the equation: $\Delta P = K_1 V + K_2 V^2$. Where ΔP is the pressure drop and *V* is blood flow velocity. K_1 and K_2 are coefficients which characterise the stenosis geometry and the rheological properties of blood. These coefficients, uniquely characterise the relationship between flow and pressure on an individual case basis.

As stenosis severity increases (beyond ~50% diameter loss), progressive dilatation (autoregulation) of the distal CMV ensures preservation of myocardial blood flow. This corresponds with the angiographic work of Lance Gould in the 1970's (Gould et al., 1974, Gould et al., 1975) (section

1.2.1). During this phase, the flow reserve is reduced during exercise, but flow at rest is preserved. There comes a point when CMV dilatation is maximal and thus flow reserve is exhausted. During this phase, even a slight increase in either stenosis severity or metabolic demand causes the myocardial demand for flow to exceed supply i.e. myocardial ischaemia occurs. According to Gould et al, this roughly corresponds to a lumen diameter loss of ~85% (Gould et al., 1974, Gould et al., 1975) (see section 1.2.1).
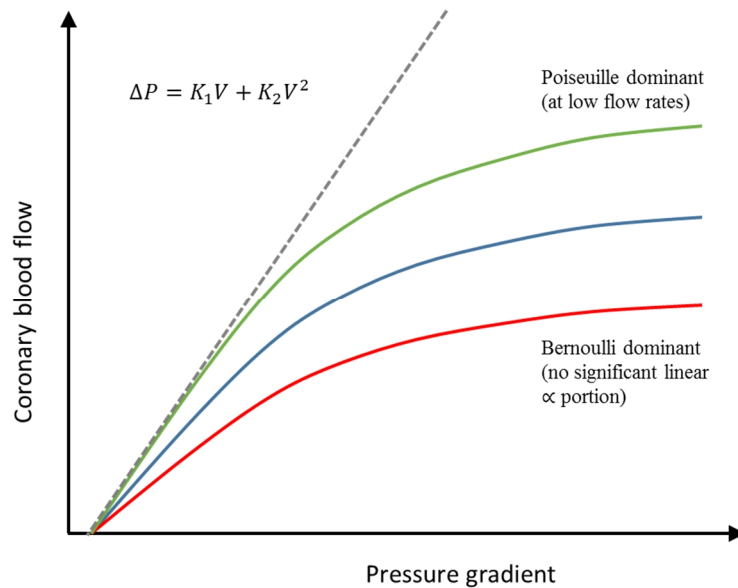
Figure 1.9. Pressure and flow relationship in the presence of stenosis.
In this idealised diagram, the green, blue and red lines represent mild, moderate and severe stenoses. The dotted grey line represents a hypothetical normal artery without stenosis. The equation describes the P-Q plot. Each unique geometry is characterised by different K_1 and K_2 coefficients. Without a stenosis, the equation simplifies to the linear Poiseuille term which explains the interrupted, linear, grey line.

Coronary flow velocity reserve (CFVR) is therefore recognised as an objective marker of stenosis severity, defined as the ratio of mean hyperaemic flow through a stenosis (Q_H^S) to the mean basal flow (Q_B^S):

$$CFVR = \frac{Q_H^S}{Q_B^S}$$

Eq 1.4.7.

CFVR reflects the magnitude of vasodilatory reserve of the CMV. A normal CFVR is a reflection of a healthy epicardial and microvascular circulation whereas an abnormal CFVR (<2.0) indicates an abnormality in either the epicardial or CMV compartments but does not distinguish which.

Furthermore, CFVR is vulnerable to alterations in the prevailing hemodynamic conditions under both baseline and hyperaemic flow (Hoffman, 2000). For example, CFVR is reduced by tachycardia, due to an increase in basal flow and decrease in hyperaemic blood flow (McGinn et al., 1990). A further limitation is that coronary flow is challenging to measure. Doppler ultrasound guidewires are capable of estimating coronary flow velocity. However, the sensor tip may have to be repeatedly re-positioned before the 'maximal velocity' is recorded. Even then it is impossible to know for sure that the wire is aligned with the centreline of the vessel and unless this is the case only a velocity vector is recorded. Doppler signal artefact affecting the velocity envelope is another common problem (Kern, 2000) and even in expert hands inadequate signal acquisition occurs in up to 15% of cases (Kern et al., 2006). These factors have restricted the clinical applicability of CFVR as a decision making aid in the catheterisation laboratory. This is explored further in Chapter 2 and Chapter 6.

As mentioned previously, FFR is based upon pressure measurements during hyperaemia and is therefore not affected by variability in baseline flow dynamics which limits CFVR. The relationship between coronary flow and pressure in the presence of a stenosis is demonstrated in **Figure 1.10** below. The blue line represents the baseline flow condition (Q_b) which, due to autoregulation, is relatively flat within the physiological pressure range. The dotted red and grey lines represent hyperaemic flow with and without stenosis. In the hypothetical non-stenosed artery the *P-Q* relationship is straight (dotted grey line) because (linear) Poiseuille forces are dominant. In the presence of a stenosis, hyperaemic flow is restricted (relative to the hypothetical normal artery) and the line curves towards the pressure axis due to (non-linear) Bernoulli forces (dotted red line). As the severity of the stenosis increases, hyperaemic flow (Q_s) more limited relative to flow in the hypothetical normal artery (Q_n). This decreases the value of both CFVR (Q_s/Q_b) and FFR (Q_s/Q_n). Note that in the context of FFR, distal and proximal pressures are used as surrogates for flow according to the derivation previously described. It should also be noted that the x axis intercept is not at zero but at a value just above venous pressure (P_v) termed pressure at zero-flow (P_{zf}) (also see **Figure 1.5**). The wedge pressure (P_w) is slightly greater and incorporates the influence of collateral flow.

1.4.1.4 FFR measurement and the role of adenosine and minimal CMVR

The clinical protocol for measuring FFR in the cardiac catheter laboratory is described in Chapter 3. FFR measurement necessitates the induction of minimal CMVR, i.e. maximal hyperaemia. This is achieved pharmacologically with parenteral adenosine or, rarely, with papaverine administration. Adenosine is a very potent CMV vasodilator. It is a naturally occurring purine

nucleoside and is involved in endogenous coronary autoregulation and metabolic adaptation. Adenosine is metabolised very quickly, has a plasma half-life <10s and is administered either as a peripheral i.v. infusion at a standardised 140μg/Kg/min rate or as a bolus intracoronary injection of 60μg through the guiding catheter.
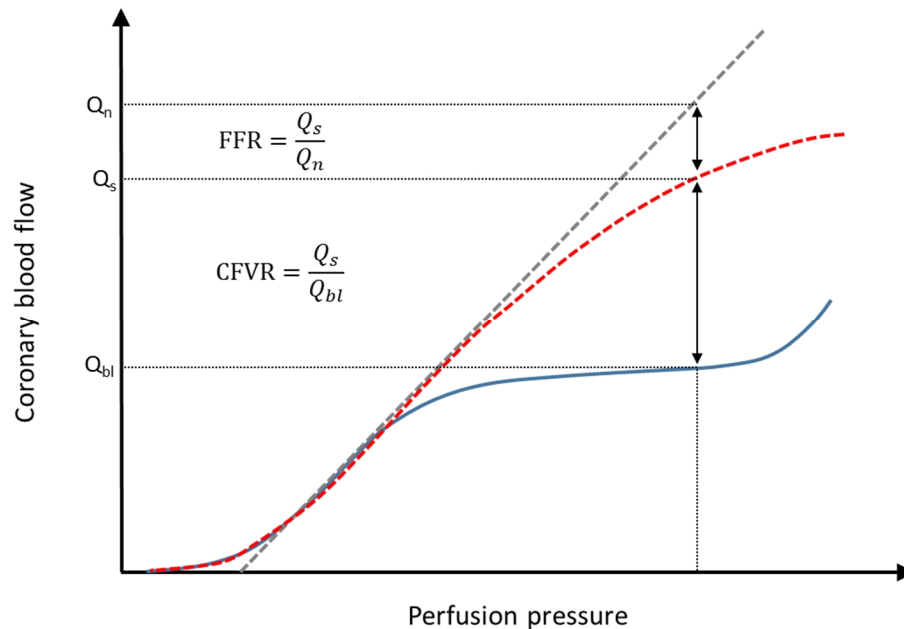
Figure 1.10. Pressure (P) and flow (Q) relationships in CFVR and FFR.
CFVR, coronary flow velocity reserve; FFR, fractional flow reserve; Q_s, trans-stenotic flow; Q_n, flow through a hypothetically normal artery; Q_{bl}, flow at baseline. Legend and explanation in the text immediately above. Adapted from van de Hoef et al (van de Hoef et al., 2013).

The adenosine receptor is widely expressed and so infusion has far-reaching, across multiple organ systems including regulation of the sympathetic nervous system and reduced blood pressure and heart rate. The notion that a single protocol of administration is able to successfully induce maximal and stable minimal CMVR in all recipients, is controversial. Adenosine is one of many influences regulating CMVR. CMVR response to hyperaemic stimulus demonstrates inter-individual (Meuwissen et al., 2001, Chareonthaitawee et al., 2001) and intra-individual variability (between adjacent myocardial territories) (Chareonthaitawee et al., 2001). Furthermore, 'minimal CMVR' implies that CMVR cannot be reduced further, yet several authors have demonstrated that compared with the standard regime, incrementally larger doses of adenosine induce progressively lower FFR values, suggesting that minimal CMVR is not universally attained by a single protocol (De Luca et al., 2011, Rioufol et al., 2005). The currently applied ischaemic thresholds were determined by the standard protocol and validation using higher doses has not been performed. This must be borne in mind when measuring FFR in the cardiac catheter laboratory.

Further uncertainty regarding the measurement of FFR was reported by Petraco et al (Petraco et al., 2013b) who analysed the original DEFER trial data (see section 1.4.1.7) (Bech et al., 2001) and found that, when two consecutive FFR measurements were taken in the same lesion, ten minutes apart, variability was observed over and above measurement error. The probability that the FFR-guided revascularisation strategy would not change if the test was repeated 10 min later was established. Measurements >0.85 or < 0.75 were associated with >95% diagnostic certainty, whereas those falling between 0.77 and 0.83 gave <80% diagnostic certainty. Diagnostic certainty around the 0.80 level fell to ~50%. They reported that "*in clinical practice, [this] means that each time a single FFR value falls between 0.75 and 0.85, there is a chance that the FFR-derived revascularization recommendation will change if the measurement is repeated 10 min later, with this chance increasing the closer the FFR result is to 0.80.*" (Petraco et al., 2013b). Repeatability may be improved by the adoption of the automatic detection of the 'smart minimum' proposed by Johnson et al. In this study the coefficient of variation was just 2.5% but, unlike in the Petraco study, there was no stratified analysis based upon FFR value (Johnson et al., 2015).

1.4.1.5   Ability to detect ischaemia

The ability of FFR to detect ischaemia-causing (functionally significant) lesions has been widely evaluated. Van de Hoef et al reviewed 24 studies investigating the performance of FFR to identify ischaemic heart disease using non-invasive testing (ETT, MPS, DSE, MPS) as the reference standard (see **Table** 1.2) (van de Hoef et al., 2013).

Table 1.2. Summary of studies investigating FFR as a surrogate for myocardial ischaemia.

Method of hyperaemia induction	N patients (lesions)	Optimal FFR cut-off	Diagnostic accuracy (%) (range)
Intravenous adenosine	271 (271)	0.75	87 (76-97)
Intracoronary adenosine	613 (732)	0.74	83 (67-95)
Other protocols (papavarine and mixed protocols)	661 (698)	0.74	81 (69-91)
All studies (average)	*1545 (1701)*	*0.74*	*83*

However, it is important to remember that, in these validation studies, the reference standard was a non-invasive test such as MPS or stress echocardiography. Myocardial ischaemia can be caused by epicardial stenosis or by CMV disease. Non-invasive techniques (e.g. MPS, CMRI) detect the

presence, extent and location of inducible ischaemia caused by either pathology; a positive test result does not distinguish whether the ischaemic aetiology lies within the epicardial or CMV compartments, or whether both are affected. Although FFR is influenced by CMV disease, it only provides information on the flow limiting characteristics of epicardial stenoses i.e. the amount of flow potentially restorable by revascularisation. Since epicardial stenosis is more common than CMV disease, a correlation would be expected between the detection of ischemia by FFR and non-invasive techniques. However, in the absence of a true gold standard reference, there will never be 100% agreeability between modalities.

Whilst it is has been established that FFR can be used to detect significant lesions with a high level of accuracy, some uncertainty remains as to the precise threshold 'cut-off' which can be taken to indicate significance. As highlighted in
Table 1.2 above, several early reports suggest various thresholds with high sensitivity for detecting ischaemia. The landmark DEFER and FAME (Fractional Flow Reserve versus Angiography for Multivessel Evaluation) trials (see below) identified a diagnostic *'grey-zone'* between 0.75 and 0.80. In DEFER, lesions with a FFR>0.75 were safely treated with medical therapy. Indeed, the 0.75 cut-off was associated with a 100% sensitivity for detecting ischaemia (Bech et al., 2001). The later FAME and FAME 2 trials employed a 0.80 cut-off (>90% specificity) but similarly demonstrated clinical efficacy (Pijls et al., 1993, Bech et al., 2001, Tonino et al., 2009, De Bruyne et al., 2012). However, the fact that a single test is unlikely to provide a standard, pre-defined cut-off, suitable for all lesions, in all patients, under all circumstances is perhaps not surprising given the large natural variability in patient anatomy, physiology and pathology. The role of all clinical investigations is to *guide*, not *rule* the physician. Therefore, for FFR values falling within the grey-zone, it may also be important to consider other patient factors which influence the risk-benefit balance such as frailty, exercise tolerance and multi-vessel disease.

1.4.1.6   Clinical decision making

Sant'Anna et al investigated 250 patients (471 lesions), referred for PCI (93% SCAD, 7% unstable angina). Based solely upon the referral angiogram, a panel of three expert interventionists placed each case into 'treat' or 'do not treat' groups. Patients were re-grouped depending on FFR measurement (cut-off of 0.75). FFR changed management in 48% patients (32% lesions). 100 'treat' lesions were subsequently left alone and 44 'do not treat' lesions were subsequently treated (including 7 patients (9 lesions) with surgery) (Sant'Anna et al., 2007). Increased numbers of UK patients referred for diagnostic angiography without prior non-invasive testing provided the rationale for the RIPCORD (Does Routine Pressure Wire Assessment Influence Management

Strategy at Coronary Angiography for Diagnosis of Chest Pain?) study which evaluated the impact of routine FFR measurement in all major coronary artery branches, in patients undergoing diagnostic (cf. PCI) angiography (Curzen et al., 2014). The management plan was altered in 26% of patients: medical therapy increased from 72 to 89 patients, PCI reduced from 90 to 80 patients, CABG increased from 23 to 30 patients and the requirement for additional information reduced from 15 to 1 patient. For 32% of cases, the number of vessels considered to have physiologically significant lesions changed in light of the FFR data. RIPCORD raises challenging questions regarding the future of diagnostic angiography in non-PCI centres. Although scientifically less rigorous, a large registry based study of 1028 patients demonstrated a reclassification of revascularisation strategy (based on FFR result) in 43% of cases (33% a priori medical patients, 56% a priori PCI patients and 51% a priori CABG patients) (see) (Van Belle et al., 2014).

1.4.1.7   Clinical outcome data

In 2007 the landmark Clinical Outcomes Utilizing Revascularization and Aggressive Drug Evaluation (COURAGE) trial was published (Boden et al., 2007). Patients with stable CAD were randomised to OMT (n=1149) or OMT plus PCI (n=1138). After 4.6 years there was no significant difference in the primary endpoint (all-cause mortality or death) between the groups. Although the study had limited applicability (94% subject exclusion rate) and was heavily criticised, some used these data to challenge the benefit of PCI in stable CAD. Of relevance to the current thesis, the demonstration of inducible ischaemia was not an essential inclusion criteria and none of the patients in the PCI group underwent intra-coronary physiological assessment. Since the COURAGE trial, multiple studies have demonstrated benefit from PCI in stable CAD with the greatest benefit observed in those with the most significant ischaemic burden (Davies et al., 1997, Beller and Zaret, 2000, Smith et al., 2006, Erne et al., 2007, Shaw et al., 2008, Wijns et al., 2010). The most compelling validation for the use of any novel technique is through clinical outcome data. Three landmark FFR outcome trials are discussed below.

1.4.1.7.1   DEFER

The 'DEFER' trial (Pijls et al., 2007, Bech et al., 2001) challenged the notion that all angiographically significant coronary lesions should receive PCI. In this trial, patients with functionally insignificant stenoses (FFR>0.75), referred for PCI, were randomized into either the PCI 'perform' group (n=90) or the PCI 'defer' group (n=91). Those with functionally significant lesions (FFR<0.75, n=144) received PCI and were entered into a reference registry. The primary endpoint was a composite of death, MI, CABG, or PCI. Results were reported at two and five years. The five year results, based on follow up of 97% of the original cohort, demonstrated no

significant difference in event-free survival between the PCI or defer groups. Despite PCI, the event-free survival in the reference group was significantly lower than in the 'perform' and 'defer' groups (61%, reference group; versus 73%, perform; 79%, defer group). Furthermore, the rate of cardiac death or MI in the reference group was five times higher than in those with functionally non-significant lesions treated with OMT alone. Although this study was performed before the adoption of drug-eluting stents and patients with multi-vessel CAD were under-represented, the results suggest that:

- OMT and deferral of PCI is a safe strategy in those with physiologically non-significant lesions (FFR>0.75)
- the risk of death in those with physiologically non-significant lesions is <1% and this is not reduced by stenting
- those with functionally significant lesions (FFR<0.75) are associated with the highest risk, even after PCI

1.4.1.7.2 FAME

The Fractional Flow Reserve versus Angiography for Multivessel Evaluation (FAME) trial demonstrated the benefits of FFR in guiding revascularisation. This multicentre study randomised 1005 patients with multi-vessel CAD to either angiographically-guided (n=496), or FFR-guided (n=509) PCI with DES. Baseline and angiographic characteristics were similar between the two groups. Results were reported at one and two years (Tonino et al., 2009, Pijls et al., 2010). In the FFR guided group at one year:

- the number of stents deployed was reduced (1.9 v 2.7, per patient, p<0.001)
- the one year MACE rate (composite of death, MI, repeat revascularisation) was reduced (13.2% v 18.3%, p=0.02)
- the number of patients free from angina were similar (78% v 81%, p=0.20)
- the one-year cost saving was ~$2000 per case (Fearon et al., 2010)

At two years, the rate of mortality or MI was reduced in the FFR group (8.4% v 12.9%, p=0.02) but this was driven mainly by the reduction in MI as opposed to a mortality benefit. There was no difference in angina symptoms or functional status between the groups at two years.

1.4.1.7.3 FAME 2

The FAME 2 trial (De Bruyne et al., 2012) helped answer some of the criticisms of the COURAGE trial. FAME 2 compared OMT versus FFR-guided revascularisation in stable patients with

functionally significant stenoses in a multicentre trial involving 28 European and North American centres. Patients with stable CAD who were being considered for PCI had all coronary stenoses assessed by FFR. Patients with ≥1 functionally significant lesion (FFR <0.80) were randomised to either OMT (n=441) or FFR-guided PCI plus OMT (n=447). Patients with no significant lesions (FFR >0.80) were entered into a registry. The composite primary endpoint was defined as death, MI, or urgent revascularisation. Recruitment was terminated prematurely at 213 days due to a significant, between-group difference in the percentage of patients who experienced the primary endpoint (4.3% in the FFR guided PCI group vs 12.7% in the OMT group, HR 0.2; 95% CI, 0.06-0.30, P<0.001). The percentage of patients experiencing the primary endpoint in the registry group was 3%. The difference between the two groups was driven primarily by a reduction in urgent revascularisation in the FFR group (1.6% vs. 11.1%; hazard ratio, 0.13; P<0.001). Rates of any revascularisation were also reduced in the FFR group (1.7% vs 12.1%, HR 0.14 p<0.0001). It remains unclear whether premature termination of the study precluded the identification of re-stenosis as a late complication in the FFR group. However, it is hard to imagine that this would have had an impact on the sevenfold increase in urgent revascularisation events in the OMT group. Had the study run to completion, it is possible that a mortality benefit may have emerged. A further limitation is that only the PCI group received dual anti-platelet therapy but again, it is hard to imagine that this would have had such a large effect as to cancel out the significant difference between the two groups. This study challenged the findings of the COURAGE trial and suggested that:

- OMT plus *physiologically-guided* PCI is superior to OMT alone in the context of stable coronary disease.

1.4.1.7.4   Other outcome studies

Since these seminal publications, several large, retrospective, observational, registry-based studies have assessed the clinical outcomes of patients undergoing adjuvant FFR-assessment (see

Table 1.3). The lack of a prospectively defined study protocol mean that such studies are inherently prone to variability in clinical protocol and operator practice which, in theory, can dilute any associated positive (or negative effects) of FFR use. Nonetheless, they do report, what might be considered, 'real-world practice'. Furthermore, despite methodological constraints, each of these studies report a positive effect of FFR use. FFR is the subject of several, ongoing, major clinical trials looking at FFR in an extended role beyond assessment of stable CAD including its role in: multivessel disease assessment (NCT01881555), NSTEMI (NCT01764334), assessing

intermediate lesions in comparison to IVUS (NCT01175863), STEMI with multivessel disease (NCT01399736 and NCT01960933), CABG planning (NCT01810224) and its routine use in assessment of chest pain (NCT01070771).

1.4.1.8   Cost benefit economic analysis

Measuring FFR incurs increased 'upfront' costs (approximate) including single-use pressure wire (£550), pressure monitor /transducer (£22,500), technology service contract (£1-2,000 PA), the cost of 20 minutes additional catheter laboratory time per patient (variable) and, where appropriate, additional personnel to administer the hyperaemic drug. Despite these increased costs, FFR-guided PCI is associated with reduced long-term costs ($2,385 dollars less per patient), even as early as twelve months (Fearon et al., 2010). Increasingly, parsimonious healthcare providers require proof of the physiological significance of CAD as a pre-requisite for financial reimbursement. FFR is apposite for this purpose since it is deployed at the time of catheterisation. Although no UK-specific economic analysis has been conducted, a series of conference abstracts analysing potential savings in major European nations (including the UK) in those in whom ICA is indicated suggest that, compared with standard ICA, FFR-guided ICA is associated with cost savings of €300-600 per patient (Bornschein et al., 2011, Siebert et al., 2011a, Siebert et al., 2011b, National Institute for Clinical Excellence, 2015).

Table 1.3. Summary of studies assessing the effect of FFR on clinical outcome.

Author, study, year, reference	Study design	N patients	Resarch question/s	Primary results	Conclusion/s
Bech and Pijls DEFER 2001, 2007 (Bech et al., 2001, Pijls et al., 2007)	Prospective RCT	90 'perform' 91 'defer'	PCI+OMT (perform) vs OMT alone (defer) in pateints with FFR>0.75	Event (death, MI, CABG, or PCI) free survival no different between perform and defer groups at 2 and 5 years. Prognosis worse in those with FFR<0.75, even after PCI.	OMT alone is safe when FFR>0.75. Mortality risk <1%, not affected by PCI
Tonino and Pijls FAME 2009, 2010 (Tonino et al., 2009, Pijls et al., 2010)	Prospective RCT	496 std angio 509 FFR angio	FFR guided PCI versus standard angiography guided FFR	1 year: FFR guidance associated with: less stents deployed (1.9 v 2.7, per patient); reduced MACE (13 vs 18%), cheaper procedure. 2 years: death /MI reduced in FFR group. Symptoms similar between groups.	FFR guided PCI is associated with reduced stent implantation, reduced cost and increased event free survival.
De Bruyne, FAME 2 2012 (De Bruyne et al., 2012)	Prospective RCT	441 PCI 447 OMT	OMT versus OMT+PCI in those with FFR<0.80	Terminated prematurely (213 days) due to reduced event (death, MI, or urgent revascularisation) free survival in the PCI group. Effect driven by increased urgent revascularisation.	In those with FFR <0.80, PCI + OMT superior to OMT alone.
Li Mayo clinic* 2013 (Li et al., 2013)	Single centre registry (retrospective observational)	6268 std PCI, 1090 FFR guided PCI	Is FFR guided PCI superior to std PCI?	MACE (death/MI/rpt revascularisation) less frequent in the FFR-guided group (50 vs 57%, P < 0.001). Repeat revasc' similar (35 vs 36%, P=0.97) after 7years follow up.	FFR-guided PCI superior to standard PCI in terms of long term clinical outcomes in a large cohort of largely unselected CAD pateints.
Van Belle French registry 2013 (Van Belle et al., 2014)	Multicentre regsitry (retrospective observational)	1028 FFR cases across 20 centres	Does FFR assessment change revasc decision compared with std PCI?	Revasc' strategy reclassified (in light of FFR result) in 43% of cases (33% a priori medical patients, 56% a priori PCI patients and 51% a priori CABG patients). 1 year MACE as good in reclassified pateints as in those whose revasc strategy remained unchanged post FFR.	FFR assessment during ICA reclassifies revasc' strategy in 43% cases
Frohlich Pan-London registry* 2014 (Frohlich et al., 2014)	Single city, Multicentre registry (retrospective observational)	37090 std PCI, 2767 FFR cases	Was FFR (or IVUS) guided PCI guidance associated with any clinical benefit?	No mortality difference between std and FFR-guided PCI (HR, 0.88; 95% CI, 0.67-1.16; P=0.37) over 3.3 years. The mean no. stents implanted was lower in the FFR group compared with IVUS and std angio groups (1.1 vs 1.6 vs 1.7, P < .001).	Less stents deployed when FFR used to guide PCI but no mortality advantage versus std PCI

*Only statistically significant differences are reported (at the 95% confidence leve). RCT, randomised controlled trial; PCI, percutaneous coronary intervention; OMT, optimal medical therapy; FFR, fractional flow reserve; MI, myocardial infarction; CABG, coronary artery bypass graft surgery; revasc, revascularisation; std angio, standard angiography. *also included ~10% acute /NSTEMI cases.*

1.4.1.9   FFR in the guidelines

NICE issued a Medtech innovation briefing which describes the currently available FFR technology and reviews the current place of FFR in the management of CAD (National Institute for Clinical Excellence, 2015). Although the briefing reviews the safety, economics, strengths and weaknesses of FFR as described in the literature, its purpose is to inform local decision-making by clinicians, managers and procurement professionals and does not constitute 'guidance' *per se*. **Table 1.4** summarises the recommendations regarding FFR in the major European and US guideline documents.

Table 1.4. Fractional flow reserve in major guideline documents.

Guideline document Recommendation	Class	Level of evidence
2013 ESC guidelines on the management of stable coronary artery disease (Montalescot et al., 2013)		
FFR is recommended to identify haemodynamically relevant coronary lesion(s) when evidence of ischaemia is not available.	1	A
Revascularisation of stenoses with FFR <0.80 is recommended in patients with angina symptoms or a positive stress test.	1	B
Revascularisation of an angiographically intermediate stenosis without related ischaemia or without FFR <0.80 is not recommended.	III	B
2014 ESC guidelines on myocardial revascularization (Windecker et al., 2014)		
FFR to identify haemodynamically relevant coronary lesion(s) in stable patients when evidence of ischaemia is not available.	1	A
FFR-guided PCI in patients with multi-vessel disease.	IIa	B
2012 ACCF/AHA Guidelines for the Diagnosis and Management of Patients With Stable IHD (Fihn et al., 2012)		
FFR <0.80 considered to indicate physiological lesion significance	1	A
CABG /PCI should not be performed to improve survival in patients with stable IHD with ≥1 stenoses that are not anatomically (<70% diameter) or functionally (FFR<0.80, or only mild or absence of ischaemia on non-invasive testing) involve only the LCx or RCA, or subtend only a small area of viable myocardium	III	B

1.4.1.10 Critique of FFR

Although, simple, elegant, and supported by clinical outcome data, FFR is based upon physiological assumptions which are not wholly supported by evidence. The assumption of both minimal and stable CMVR is of paramount importance to the rationale of FFR. Section 1.4.1.4 (page 26) discusses issues affecting the induction of 'minimal' CMVR. The derivation of FFR is based upon the assumption that CMVR is constant with and without a stenosis ($CMVR_s$, $CMVR_N$). This implies that changes in perfusion pressure (e.g. P_d vs P_a) do not affect the CMVR. This may

not be a valid assumption because, as already discussed, distal vascular tone is affected by perfusion pressure (autoregulation). Furthermore, even under hyperaemic conditions, perfusion pressure does affect CMVR. Chamuleau et al demonstrated a positive correlation between lesion severity and CMVR which normalises with PCI (Chamuleau et al., 2003). Verhoeff *et al*, studied 24 CAD cases in conditions of hyperaemia and demonstrated that restoration of P_d by PCI induced a reduction in CMVR below the level of corresponding reference vessels, suggesting that not only does P_d influence CMVR but also that '*microvascular remodelling is induced by long-term exposure to a low-pressure environment*' (Verhoeff et al., 2005). This indicates that more severe lesions will be associated with a lower P_d and thus a higher CMVR. In turn, this would result in an increased P_d thus overestimating the FFR. Consequently, physiologically significant lesions might be inappropriately left untreated.

The mathematical and physiological rationale for FFR is that pressure is a suitable surrogate marker for flow i.e. pressure and flow are linearly related such that, in the presence of a stenosis, distal pressure is reduced in proportion to flow. Pijls and de Bruyne state that '*a direct relation between coronary pressure and flow or flow reserve, however, may be presumed only if coronary resistances remain constant (and minimal) as theoretically is the case during maximum arteriolar vasodilation. In that case, pressure measurements alone theoretically can be used to predict flow and thereby functional stenosis severity*' (Pijls et al., 1993). However, several authors have demonstrated that this is not the case (Spaan et al., 2006, Heusch, 2010, van de Hoef et al., 2012b). Even under maximal hyperaemia, the combined effects of resistance, coronary venous back pressure, collateral flow and myocardial compliance result in coronary blood flow ceasing, not at zero pressure but at approximately 20mmHg (Hanley et al., 1984, Grattan et al., 1986). Although the hyperaemic P-Q relationship becomes approximately linear within the physiological pressure range, this line deviates towards the pressure axis at lower pressures. This has led some authors to describe the relationship as *incremental linear* (van de Hoef et al., 2013).

Taken alone, the information provided by CFVR and FFR are limited. An abnormal CFVR indicates coronary disease but does not distinguish whether this occurs in the epicardial, the CMV, or both compartments. FFR is only capable of providing information about the flow limiting potential of the *epicardial* artery. FFR does reveal any information about the CMV but is heavily influenced by this important component of the coronary circulation. Combined pressure and flow measurement integrated into a single assessment provides a more comprehensive, more detailed and possibly more reliable interrogation of coronary pathophysiology. This is discussed further in section 1.4.2 (page 38) and in Chapter 6. Furthermore, unlike most non-invasive functional tests,

FFR (and CFVR) are unable to quantify the location or extent of ischaemic myocardium, a key determinant of prognosis (Shaw et al., 2008).

Reported variability in the FFR result ranges from 2.5% (Johnson et al., 2015) to 4.8% (de Bruyne et al., 1996) and higher (Petraco et al., 2013b) but the precise figure and impact on the procedure is dependent upon proximity to the 0.80 threshold.. The adoption of a single cut-off value of 0.80 (in itself controversial) as the ischaemic threshold which is applied to all patients, in all cases, in all circumstances is a simplification. Although this approach has had beneficial effects (because using 'some' physiology is better than none), it is likely that either a more sophisticated physiological index, or a more sophisticated application of FFR will better represent the needs of individual circumstances. However, such an approach is yet to be described. FFR is considered independent of haemodynamic conditions (de Bruyne et al., 1996) but this is challenged by Siebes et al who demonstrated, with an electrical analogue model that, for a given stenosis, FFR increases with either increasing IMR or decreasing Pa, an effect which was most prominent in the intermediate range.

1.4.1.11 FFR adoption

The UK and USA have been the most enthusiastic adopters of FFR, but even in these countries, use is well below what might be expected. The British Cardiovascular Interventions Society evaluated total UK catheterisation data (244229 coronary catheter procedures) carried out during 2013. FFR was used in 6.3% of all catheterisations, relatively evenly split between diagnostic cases (6.0%) and PCI cases (6.8%). This represented a 12% increase on FFR use from 2012 and 284% increase over 5 years. UK FFR use is significantly higher than IVUS (3.1%) or OCT (0.4%) as an angiographic adjunct (Ludman. P, 2014). **Table 1.5** outlines a decade of FFR use in the UK. In the USA, Dattilo et al analysed the US CathPCI Registry (includes data from ~85% of US catheter laboratories) over twelve months from 2009-2010 (Dattilo et al., 2012). Analysis was restricted just to those with intermediate (40-70%) stenoses (n= 61,874). FFR was used in 6.1% of cases which is low considering that non-moderate lesions were excluded. IVUS was used in 20.3% and the remaining 73.6% received no adjunctive procedure. FFR cases were more often younger males assessed in University hospitals. The authors attributed underuse of FFR to high cost and low, or zero, reimbursement. A similar CathPCI Registry analysis performed twelve months later (2010-2011) by Dehmer *et al*, studied 1,110,150 patients undergoing cardiac catheterisation (941,248 PCI) (Dehmer et al., 2012). 13% of the PCI cohort had a 40-70% stenosis. Of this highly selected group, FFR was used in 7% of cases (cf. IVUS; 18%). However, there is a

lag phase between large scale epidemiological data collection and publication and Medicare reimbursement for FFR has improved since this time.

Why is FFR used so infrequently, 20 years after its introduction, with such a strong evidence base? First, decisions regarding the mode of revascularisation are usually made at the time of invasive CAG; but this is limited specifically to PCI operators, working in an interventional catheter laboratory, with the time and facilities to perform FFR. Second, the procedure is prolonged, and short-term costs increased, because of the need for a pressure wire and a hyperemic drug. Third, confidence is exhibited by many operators that their own visual assessment is physiologically accurate, allied to a misconception that multiple visual assessments (e.g. in a 'Heart Team' setting), or when supported by a prior non-invasive test of ischaemia, improve their accuracy. Finally, despite the FAME trial data (Tonino et al., 2009, De Bruyne et al., 2012), some clinicians remain sceptical of the value of PCI in the context of stable coronary artery disease which reduces enthusiasm for invasive FFR assessment (Boden et al., 2007).

1.4.2   Other invasive physiological indices

Other invasive physiological indices include instantaneous wave free ratio (iFR), hyperaemic and basal stenosis resistance, and index of microvascular resistance.

1.4.2.1   Instantaneous wave-free ratio (iFR)

Whereas FFR represents the trans-lesional pressure ratio during hyperaemia, averaged over the entre cardiac cycle, iFR measures the pressure ratio from mid to end diastole under resting conditions. iFR makes use of the wave-free, high-flow, diastolic period when CMVR is at its lowest basal level. During this phase, the ratio of Pd to Pa demonstrates high agreeability with FFR (Sen et al., 2012). The central concept of iFR is the notion that resting (diastolic) CMVR is equivalent to the mean hyperaemic resistance, something which remains controversial (Johnson et al., 2013, Berry et al., 2013). Although iFR requires the passage of an intracoronary, pressure-sensitive wire, it does not require induction of hyperaemia which is the key advantage (Petraco et al., 2012). iFR has been demonstrated to have high diagnostic accuracy for the diagnosis of ischaemia causing lesions as defined by an FFR of <0.80 (area under ROC curve = 0.93), with iFR values correlating closely with FFR (r=0.9) in a preliminary study of 118 cases (Sen et al., 2012). In contrast to FFR, iFR was shown to be resistant to spontaneous beat-to-beat variability caused by arrhythmia and ectopic beats because these artefactual anomalies occur predominantly during systole. A hybrid iFR-FFR approach is proposed as an adenosine-saving strategy whereby iFR results <0.86 or >0.93 indicate intervention and deferral, with intermediate results requiring

Table 1.5. A Decade of FFR use in the UK

Year	Total LHCs	PCI cases	Diagnostic cases	FFR centres	Total FFR procedures	Annual % increase	FFRs per LHC (%)	IVUS procedures	IVUS per LHC (%)	OCT cases	OCT per LHC (%)
2004	201380	62780	138600	42	1281		0.6	689	0.3	-	-
2005	205782	70142	135640	53	2089	63	1.0	840	0.4	-	-
2006	215572	73692	141880	68	2829	35	1.3	1089	0.5	-	-
2007	223638	77373	146265	72	3903	38	1.7	2668	1.2	-	-
2008	230028	80351	149677	88	5406	39	2.4	2836	1.2	-	-
2009	235253	83130	152123	92	8775	62	3.7	3857	1.6	-	-
2010	231510	87676	143834	107	9132	4	3.9	4326	1.9	147	0.06
2011	235376	88692	146684	110	10688	17	4.5	5140	2.2	256	0.11
2012	244880	92445	152435	113	13762	29	5.6	6407	2.6	739	0.30
2013	244229	92589	151640	110	15394	12	6.3	7618	3.1	977	0.40

A breakdown of FFR use over the last decade. There were 114 PCI centes and 69 'diagnostic only' centres in the UK as of 2013. IVUS and OCT data are shown for comparison. LHC, left heart catheter; PCI, percutaneous coronary intervention; FFR, fractional flow reserve; IVUS, intravascular ultrasound; OCT, optical coherence tomography; - indicares no data. Source: British Cardiovascular Interventions Society Audit returns (Ludman. P, 2014).

additional adenosine administration for FFR measurement. This approach generated good results in the hybrid iFR study (Petraco et al., 2013a) but less accurate evaluations are reported by other groups (Berry et al., 2013, Johnson et al., 2013). The lack of a true gold-standard method for identifying ischaemia causing lesions has left room for debate as to the relative value of iFR compared with FFR (Jeremias et al., 2014), with some data suggesting that iFR use may even be superior to FFR (Sen et al., 2013). Data from two large outcome trials which together will study iFR and FFR in over 4500 patients are awaited (NCT02053038, NCT02166736).

1.4.2.2   Indices combining pressure and flow

The potential confounding influence of CMVR on FFR and basal flow fluctuations on CFVR (Hoffman, 2000, Pijls et al., 2000, van de Hoef et al., 2013) has led to the investigation of other physiological indices of intracoronary physiology. The ability to measure both pressure and flow within the coronary lumen provides the means by which trans-stenotic and myocardial resistance can be assessed. Thus, ambiguity regarding the relative contribution that these components influence pressure-derived FFR and /or flow-derived-CFVR can be reduced. The velocity-based index of microvascular resistance (IMR) is defined as the ratio of mean distal coronary pressure (venous pressure assumed zero) mean peak blood flow velocity as determined by Doppler during hyperaemic flow conditions (see also Chapter 6.1). Alterations in IMR influence the flow velocity and distal pressure (and thus FFR) in opposite directions. IMR helps to explain discordance in FFR and CFVR (27% cases) (Meuwissen et al., 2001) and adds value to the quantification of FFR by improving the diagnostic accuracy after adjustment for the IMR (van de Hoef et al., 2014b). In 2014 van de Hoef et al investigated the physiological basis and clinical outcome of FFR-CFVR discordance in 157 patients with intermediate lesions in whom revascularisation was deferred (van de Hoef et al., 2014c). Discordance was reported in 37% which was characterised by CMVR measurement. Over 11.7 years, compared with concordant results (normal FFR and CFVR), a normal FFR but abnormal CFVR was associated with an increased MACE rate. Conversely, and abnormal FFR but normal CFVR was comparable to concordant results. This study demonstrates that discordance between CFVR and FFR originates in the CMVR and that increased MACE is determined more by an abnormal CFVR than FFR, thus supporting the measurement of both pressure and flow. Measuring both flow and pressure also allows the epicardial stenosis resistance to be specifically calculated which is also advantageous (see below).

1.4.2.2.1 Hyperaemic stenosis resistance

Hyperaemic stenosis resistance (HSR) (Gould et al., 1975, Logan, 1975, Meuwissen et al., 2002), is defined as the ratio of the mean trans-lesional pressure gradient and average peak flow velocity (APV), under hyperaemic (^{H}) flow conditions:

$$HSR = \frac{P_d^H - P_a^H}{APV^H}$$
<div align="right">Eq 1.4.8.</div>

where; P_d^H is distal pressure, P_a^H is proximal pressure and APV^H is the peak flow velocity, averaged over a cardiac cycle. Meuwissen et al evaluated the predictive power of HSR to identify ischaemia causing lesions (with SPECT as the reference standard) in 151 patients with stable CAD (181 arteries). The HSR ischaemic threshold was optimally defined as 0.8 mmHg/cm, with results higher than this indicating ischaemia causing lesions. HSR outperformed both CFVR and FFR (AUC, 0.90±0.03; 0.80±0.04, p=0.024; 0.82±0.03, p=0.018 respectively) particularly the group with discordant FFR-CFVR results (Meuwissen et al., 2002). In a study similar in design to DEFER, the same group compared the prognostic value of combined FFR and CFVR results in determining lesion non-significance in 186 intermediate lesions, ranked as negative or non-diagnostic for ischaemia by non-invasive testing. Cases were divided into four groups: group A (FFR ≥0.75 and CFVR ≥2.0), group B (FFR≥0.75 and CFVR <2.0), group C (FFR<0.75 and CFVR ≥2.0) and group D (FFR<0.75 and CFVR <2.0). Despite the negative non-invasive results, there was a 31% MACE rate overall. MACE rates were lowest (4.7%) when both FFR and CFVR were negative (group A). In comparison, MACE rates were significantly higher in groups B (21%), C (17%) and D (33%) (p=0.008). These results, particularly the results of the discordant groups (B and C) suggest that reliance upon either FFR or CFVR alone is suboptimal and that a combined (P and Q) index may be superior. The prognostic power of HSR (multivariate analysis) was superior to both FFR and CFVR as an independent predictor of MACE (Meuwissen et al., 2008). The benefits of combined pressure-flow measurement and HSR are re-visited in Chapter 6.

1.4.2.2.2 Basal stenosis resistance

In 2012, van de Hoef et al published an evaluation of baseline stenosis resistance (BSR), defined as the ratio of the pressure gradient across the stenosis to the basal average peak flow velocity (APV) measured under baseline (^{B}) flow conditions, averaged over a cardiac cycle (van de Hoef et al., 2012a):

$$BSR = \frac{P_d^B - P_a^B}{APV^B}$$
<div align="right">Eq 1.4.9.</div>

The ischaemic threshold was optimally determined as 0.66 mmHg/cm/s. The great advantage of this index is that is it a) combines pressure and flow and b) does not require induction of hyperaemia with the associated problems described above.

In a comparison with HSR, FFR and CFVR at detecting ischaemia, as defined by SPECT, BSR was comparable to FFR and CFVR. However, HSR was superior as is demonstrated in **Figure 1.10** (van de Hoef et al., 2012a) where the area under the curve for HSR (0.81, 0.76-0.87) was significantly greater than for BSR (0.77, 0.71-0.83), FFR (0.77, 0.71-0.83) and CFVR (0.75, 0.68-0.81) (p<0.05). In a similar comparison (MPS and HSR combined reference standard), BSR, iFR and FFR all demonstrated similar diagnostic accuracy (van de Hoef et al., 2014a).

In a stenosed coronary artery, the relationship between pressure and flow is curvilinear, described by the equation $\Delta P = K_1 V + K_2 V^2$ (Young et al., 1977, Gould, 1978, Gould, 1985). It is therefore perhaps not surprising that prediction of physiological lesion significance using one out of the two variables might be inferior to an approach which incorporates both. Resistance indices are not dependent upon variability in the magnitude of pharmacological vasodilatation in the coronary catheter laboratory.
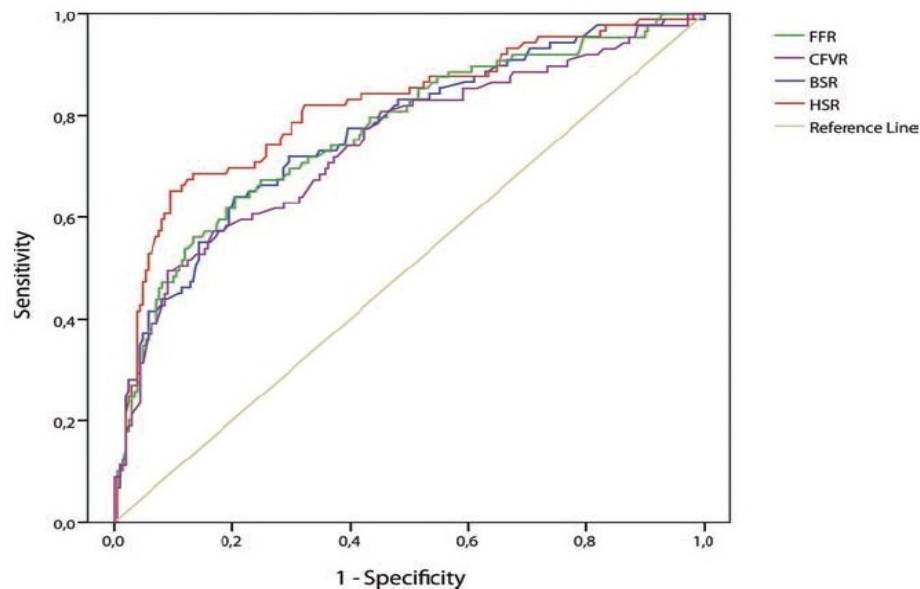
Figure 1.11. Receiver operator characteristic curves of FFR, CFVR, HSR and BSR.
Reprinted with permission from van de Hoef et al (van de Hoef et al., 2012a)

Both HSR and BSR require further clinical validation before they are adopted into routine clinical practice. Furthermore, measuring coronary blood flow velocity with Doppler tipped coronary wires is technically challenging for many operators whereas pressure measurement acquisition is much simpler. For these reasons cardiologists have almost exclusively turned to FFR as their index of choice, but this should not hamper the development of potentially superior physiological approaches and indices.

1.5 What is the best test for diagnosing and assessing CAD?

There is no gold standard investigation for the diagnosis and assessment of stable CAD and there is no standard assessment pathway suitable for all. Pre-test likelihood of CAD broadly determines the choice of investigation/s. If:

- high (61–90%), ICA should be the first-line diagnostic investigation
- moderate (30–60%), functional imaging should be the first-line diagnostic investigation
- low (10–29%), CT calcium scoring (±CTCA) should be the first-line diagnostic investigation

Table 1.6. Recommendations and level of supporting evidence for investigations indicated in the investigation of CAD /IHD.

	Asymptomatic		Symptomatic					
			Pre-test probability of CAD*					
			Low (<15%)		Intermediate (15-85%)		High (>85%)	
Test	Class	Level	Class	Level	Class	Level	Class	Level
ICA	III	A	III	A	IIb	A	I	A
CTCA	III	B	III	C	IIa	A	III	B
Stress echo	III	A	III	A	I	A	III	A
MPS SPECT	III	A	III	A	I	A	III	A
MPS PET	III	B	III	C	I	A	III	B
Stress MRI	III	B	III	C	I	A	III	B

*According to the 2014 European Society of Cardiology (Windecker et al., 2014). ICA, invasive coronary angiography; CTCA, Coronary computed tomography; echo, echocardiography; SPECT, single photon emission computed tomography; PET, photon emission tomography; MRI, magnetic resonance imaging; CAD, coronary artery disease . *See Figure 1.2.1.*

Non-invasive tests such as SPECT, stress echocardiography and CMRI provide information about the location and extent of myocardial ischaemia and detect ischaemia caused by either epicardial or CMV disease but (with the possible exception of CT-perfusion) cannot distinguish between these two aetiologies. **Table 1.6** (above) summarises the European guidelines regarding investigations used in CAD /IHD. Anatomical tests provide detailed information specific to the artery or even an individual lesion but ignore the functional consequences of disease and do not detect CMV disease at all. Catheter laboratory based functional tests have the advantage of providing combined anatomic and functional data at an artery-, or even lesion-specific level. Importantly, indices such as FFR reveal the potential *value* of revascularisation, a key factor in clinical decision making. However, they cannot estimate the myocardial ischaemic burden. Because these tests are deployed in the catheter laboratory during invasive angiography, they can also be used to directly guide decisions about the mode and strategy of treatment. The literature is confusing because of wide variability in terms of which investigation is used as the reference (gold) standard, the criteria used to define significant CAD and whether the reported accuracy is defined on a per-patient or per-vessel basis. For example, some studies evaluate accuracy against SPECT and some against ICA. Even for those using ICA, some define significance as a stenosis >50% and others >75%. Per-patient analysis enhances sensitivity at the expense of the specificity whereas the opposite is true of per-vessel analysis.

The value of an individual test is determined by a wide range of individual, patient-specific factors (e.g. clinical stability, age, frailty, gender, comorbidities, mobility, heart rate, arrhythmia, body mass index) which must be weighed against a wide range of heterogeneous investigation-specific factors (e.g. radiation exposure, invasiveness, habitus, sensitivity and specificity) and other considerations such as the strength of supporting evidence, available resources, cost, and local expertise. Although guideline documents are helpful, these case-specific factors are often underrepresented. **Table 1.7** summarises some of the key considerations of the major investigations used in the diagnosis and assessment of stable CAD.

1.6   Chapter One: Key Clinical Considerations

Revascularisation should be targeted to ischaemia causing lesions. In terms of coronary assessment, physiology should supersede anatomy. Within the cardiac catheter laboratory, FFR has become adopted as the standard of care in terms of physiological lesion significance. FFR-guided PCI is associated with improved clinical outcomes, reduced stent insertion and reduced healthcare costs. FFR remains underused due to a number of procedural, economic and operator-

related issues. Other physiological indices that incorporate both pressure and flow provide a more comprehensive physiological assessment and may provide superior diagnostic and prognostic data with which to better guide treatment. Because coronary flow remains difficult to measure, operators have mostly adopted pressure-derived FFR as their index of choice.

There is a need for a method which can deliver the advantages of intracoronary physiological assessment which is not limited by the factors which restrict use of the invasive technique. *All* patients undergoing assessment for proven or suspected CAD should be afforded the benefits of physiological coronary assessment, not just a small minority. This thesis describes the development, optimisation and preliminary validation of such a method.

Table 1.7. Practical and methodological considerations (pros and cons) of the major investigations used in IHD.

Investigation	Radiation exposure	Coronary anatomical data	Myocardial functional data (detects ischaemia)	Capable of guiding PCI	Invasive	Applicable to a largely unselected patient cohort	Discriminates epi- from endocardial disease	Total positive (/7)
Invasive anatomical tests								
ICA	Yes	Yes	No	Yes	Yes	Yes	No	3
CTCA	Yes	Yes	No	No	No	No	No	2
Non-invasive functional tests								
Exercise ECG	No	No	Yes	No	No	No	No	3
Stress echo	No	No	Yes	No	No	No	No	3
MPS (SPECT)	Yes	No	Yes	No	No	Yes	No	4
MPS (PET)	No	No	Yes	No	No	Yes	No	4
Perfusion MRI	No	No	Yes	No	No	Yes#	No	4
CT perfusion	Yes	Yes*	Yes	No	No	No	Yes*	4
ICA based functional tests								
FFR	Yes	Yes	Yes	Yes	Yes	Yes	No	4
CFVR	Yes	Yes	Yes	Yes	Yes	Yes	No	4
HSR	Yes	Yes	Yes	Yes	Yes	Yes	Yes	5

*Practical and methodological considerations (pros and cons) of the major investigations used in IHD. Red and green shading indicates positive and negative attributes. *Potentially, if performed as hybrid procedure with CTCA protocol. #Standard uncommon MRI exclusions (claustrophobia and ferromagnetic prostheses)*

Chapter two:

Technical Background

2.1 Introduction

The basic haemodynamic laws such as those of Bernoulli and Poiseuille (described in section 1.4.1.3) are a simplification of reality. Poiseuille's law, for example, is based upon the balance between the pressure gradient and the viscous stresses and assumes fully developed flow within a straight tube, neither of which are consistent with coronary arterial physiology. Although the Bernoulli equation predicts pressure loss into a coronary stenosis (vena contracta), it cannot accurately predict the degree of pressure recovery distal to a coronary lesion. These simple laws cannot capture the complex haemodynamic effects of vessel tortuosity (variation in three dimensional space); nor do they capture the effects of dynamic (pulsating) vascular flow. Although these simplifications may yield useful clinical predictions, for example for determining the severity

of obstruction in stenotic valve disease, they do not provide satisfactory results in the context of predicting intracoronary physiology from measures of lesion length and percentage stenosis using quantitative coronary angiography, IVUS and OCT measurements (Koo *et al.*, 2011b, Ben-Dor *et al.*, 2012, Ben-Dor *et al.*, 2011, Gonzalo *et al.*, 2012, Bartunek *et al.*, 1995). Accurate intracoronary physiological simulation requires a more sophisticated model which can adequately capture the haemodynamic characteristics of blood flow through a diseased coronary lumen. Computational fluid dynamics (CFD) modelling meets these requirements.

2.2 Coronary haemodynamics

Pressure drives flow through the vascular system according to Ohm's law (see section 1.4.1.2). However, in contrast to other circulations, coronary flow is reduced in systole when driving pressure (Pa) is increased and is augmented in diastole when driving pressure falls. This occurs because of extravascular compression of the CMV during myocardial contraction. Resistance to flow is therefore increased during systole and reduces to baseline during diastole. Both epicardial and myocardial coronary vessels offer resistance to flow and the sum of these two resistances determines flow at a given pressure. It is the pressure gradient across the system which drives flow. However, it is widely accepted that the coronary venous pressure is low enough to regard as zero (although this results in P_d/P_a (FFR) slightly exceeding $Q_{stenosis}/Q_{norm}$) (Siebes et al., 2002). The relative influence of these two resistances is key to understanding and interpreting physiological indices of coronary flow such as FFR, CFVR, HSR and IMR.

2.2.1 Translesional energy loss

When blood flows across an epicardial coronary stenosis a reduction in pressure occurs. The magnitude of the pressure drop is incorporated into the calculation of both FFR and HSR. There are two primary contributors to the pressure drop along a stenosed vessel. The first, and generally most significant, is captured by the Bernoulli equation (section 1.4.1.3). As the flow accelerates into the vena contracta within (or just beyond) the stenotic region, the kinetic energy increases and, as a consequence, the hydrostatic energy (associated with the static pressure) falls. The process of conversion of hydrostatic energy into kinetic energy is efficient and generally the Bernoulli equation provides a good estimate of the static pressure drop between the inlet and the throat of the stenosis (the vena contracta). Flow decelerates distal to the lesion, where kinetic energy is lost and the Bernoulli equation predicts a concomitant increase in hydrostatic energy i.e. pressure. However this conversion is not efficient, and typically there is a significant non-recovery of the static

pressure. A number of factors explain this including: flow separation, vortex formation, and, under some conditions, turbulence; and viscous energy losses. Conservatively, it might be assumed that there is no pressure recovery; certainly full pressure recovery is unlikely in real systems. The second source of pressure loss is the viscous loss associated with the normal, undisturbed, flow of fluid in tube, described by the Poiseuille equation (section 1.4.1.3 and **Figure 2.1** below). Relative to the Bernoulli loss, this is likely to be significant only in less severe stenoses. Poiseuille losses increase linearly with flow ($\propto Q$), whereas Bernoulli losses are related quadratically with flow ($\propto Q^2$). Total pressure loss can be described the quadratic equation:

$$\Delta P = K_1 Q + K_2 Q^2$$
Eq 2.1

Where K_1 and K_2 are case-specific coefficients of the geometry in question and the rheological properties of blood. The first term accounts for Poiseuille losses and the second term Bernoulli losses. In the absence of stenosis, the equation reduces to the Poiseuille term alone and the ΔP-Q plot becomes linear. Analytical solutions such as Poiseuille and Bernoulli represent only a crude estimation of reality. Poiseuille assumes steady, fully developed, laminar flow within a motionless, straight tube.
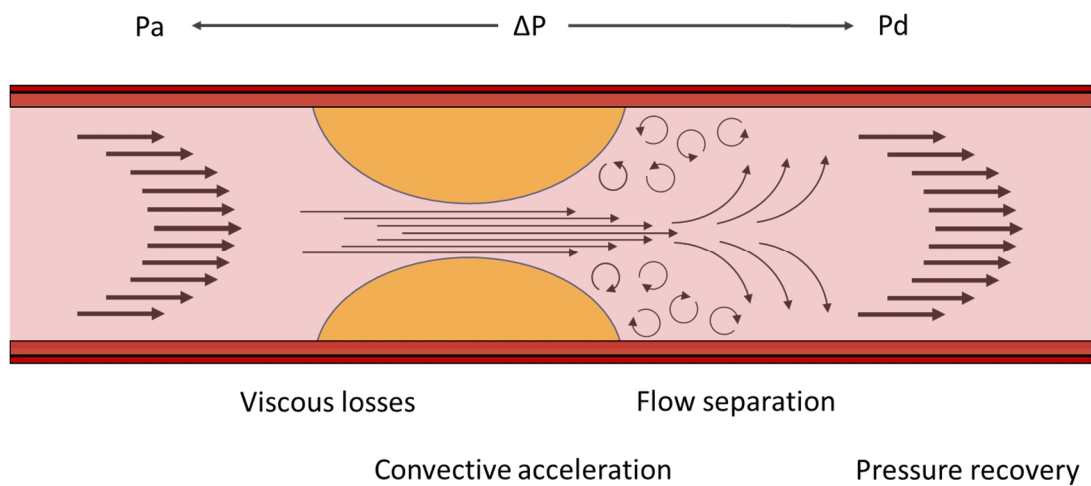
Figure 2.1. Trans-stenotic flow dynamics
Developed (parabolic) flow accelerates across a stenosis. The vena contracta is demonstrated diagrammatically in the neck of the stenosis. The position of the vena contracta can extend beyond the point of minimal stenosis. The position and dimensions of the vena contracta are not easily predicted. Flow separation, vortices and eddy currents occur in the post-stenotic region resulting in energy losses. Pressure recovery is therefore not complete, thus the Bernoulli equation fails to accurately predict the translesional pressure gradient. P_d is also influenced by the distal CMV physiology which is not represented in this diagram.

49

Coronary flow is pulsatile, not fully developed (depending upon the Womersley number), in some pathological cases turbulent, and follows a dynamic and tortuous course. This is likely to explain why the aforementioned approaches which were based on analytical solutions have failed to predict physiological indices such as FFR and demonstrates why a numerical solution is required (see section 2.4.1 also).

2.2.2 Laminar and turbulent flow

The Reynolds number is a dimensionless number which defines the ratio of inertial (momentum) forces to viscous forces:

$$Re = \frac{inertial\ forces}{viscous\ forces} = \frac{\rho VD}{\mu} \hspace{2cm} \text{Eq 2.2.}$$

Where ρ is density, V is fluid velocity, D is hydraulic diameter and μ is dynamic viscosity. Laminar flow is associated with low Reynolds numbers where viscous forces dominate. However, in a straight tube, at Re >2300, inertial forces dominate and laminar flow breaks down to transition into chaotic, turbulent flow at Re $\geq$4000. Re numbers in the 2300 - 4000 range are known as critical Re numbers where laminar flow transitions into turbulent. From the previous sections above, it is clear that turbulence is not essential for the generation of pressure loss but, when present, it is associated with additional energy and pressure loss in the decelerating post-stenosis flow. For a coronary diameter of 3 mm and mean baseline flow velocity of 7 cms^{-1} the Re = 60. At a mean peak velocity of 40 cms^{-1}: Re = 343. Within a 75% diameter stenosis, the luminal diameter falls to 25% and thus the velocity increases sixteen-fold, resulting in Re = 1371. Two additional effects must also be considered. First, flow is pulsatile, thus velocities reach higher peak values. Second, the calculation of the Reynolds number assumes a straight tube; it is recognised that Re is influenced by alterations in geometry, and sudden and abrupt alterations in diameter in particular. This is the situation at the entrance and exit from a stenosis and critical Re numbers can be reached at human vascular length scales (Brown, 2012). The Bernoulli equation describes the pressure loss into the vena contracta. Several processes including, flow separation vortices, eddy current formation, and, at higher Re numbers, turbulence may compromise pressure recovery.

2.3 CFD modelling in the cardiovascular system

CFD is a specialist area of mathematics and a branch of fluid mechanics. It is used routinely in the design of many safety-critical systems subject to hydro- and aero-dynamic forces including aircraft and vehicle design. CFD uses computer processors to solve differential equations to analyse and simulate fluid flow in two or three dimensions. Almost all CFD analyses are based upon solving the governing equations of fluid motion namely, the Navier-Stokes and continuity equations (Eq 2.3.1 below). The Navier-Stokes equations are non-linear, partial differential equations based upon the principles of conservation of mass and momentum (derived from Newton's 2nd law of motion), which provide relationships between the velocity field and pressure gradients. Simplifications yield familiar formulae such as those of Bernoulli or Poiseuille.

$$\rho \frac{\partial u}{\partial t} + \nabla \cdot (\rho u \boldsymbol{U}) = -\frac{\partial p}{\partial x} + \frac{\partial \tau_{xx}}{\partial x} + \frac{\partial \tau_{yx}}{\partial y} + \frac{\partial \tau_{zx}}{\partial z}$$

$$\rho \frac{\partial v}{\partial t} + \nabla \cdot (\rho v \boldsymbol{U}) = -\frac{\partial p}{\partial y} + \frac{\partial \tau_{xy}}{\partial x} + \frac{\partial \tau_{yy}}{\partial y} + \frac{\partial \tau_{zy}}{\partial z}$$

$$\rho \frac{\partial w}{\partial t} + \nabla \cdot (\rho w \boldsymbol{U}) = -\frac{\partial p}{\partial z} + \frac{\partial \tau_{xz}}{\partial x} + \frac{\partial \tau_{yz}}{\partial y} + \frac{\partial \tau_{zz}}{\partial z}$$

$$\nabla \cdot \boldsymbol{U} = 0$$

Eqs 2.3.1.

Where ρ is fluid density, u, v and w are the components of velocity in the x, y and z direction; p is the pressure; t is time; $\boldsymbol{U}$ is the velocity vector and τ is the shear stress. The Navier Stokes equations are non-linear, partial differential equations which are transformed into a system of non-linear algebraic equations which are solved iteratively. The momentum equations can be derived by applying Newton's second law to the principles of fluid dynamics. Nonlinearity, due to convective acceleration (uU term), makes the numerical solution for these equations extremely challenging. The first term in each equation accounts for the acceleration in either the $\boldsymbol{x}$ ($\rho \frac{\partial u}{\partial t}$), $\boldsymbol{y}$ or $\boldsymbol{z}$ direction. The second term ($\nabla \cdot (\rho u \boldsymbol{U})$) is the velocity vector accounting for convective acceleration in the appropriate direction. In simple 1-D model constructs, this term can be simplified into the Bernoulli equation. The third term ($-\frac{\partial p}{\partial x}$) refers to the pressure gradient in the given direction and the final three components ($\frac{\partial \tau_{xx}}{\partial x} + \frac{\partial \tau_{yx}}{\partial y} + \frac{\partial \tau_{zx}}{\partial z}$) account for viscous losses which, in simple 1-D constructs, may be simplified to the Poiseuille equation. The first, second and third equations together account for the conservation of momentum in the $\boldsymbol{x}$, $\boldsymbol{y}$ and $\boldsymbol{z}$ direction. The final equation assures conservation of mass, or continuity. The Navier-Stokes equations are

applicable to a diverse range of physical and industrial systems including blood flow within the cardiovascular system. Specialised software applications, known as CFD 'solvers', are used to solve the Navier-Stokes and continuity equations, which are transformed into a series of non-linear algebraic equations prior to their solution. For complex geometries analytical solutions typically do not exist and so computation is used to achieve an 'approximate' numerical solution. Non-linearity due to convective fluid acceleration makes this challenging, especially in 3-D models and as a result CFD analyses require time and significant computational power. Cardiovascular CFD model construction and solution can broadly be described in seven stages:

1. Clinical imaging

A range of medical imaging modalities can be used, including ultrasound, computed tomography (CT), magnetic resonance imaging (MRI) and X-ray angiography (de Vecchi et al., 2014, Gasser et al., 2014, Rengier et al., 2014, Bossers et al., 2014, Tu et al., 2014, Villa-Uriol et al., 2011). Imaging must provide sufficient anatomical and physiological detail, in an appropriate format and quality, to enable segmentation and data extraction (Weese et al., 2013, Cimen et al., 2014).

2. Segmentation & reconstruction

Segmentation methods identify vascular geometry from medical images which can be reconstructed into 3-D geometric representations *in silico* and support the extraction of physiological data. The segmented geometry defines the physical bounds of the region of interest in the model. Images acquired over a cardiac cycle must either track anatomical motion or be acquired during a uniform cardiac phase (i.e. ECG gated). Segmentation algorithms have evolved considerably over the last two decades and a range of manual, semi-automatic and automated protocols are now available to clinicians and scientists (Barber and Hose, 2005, Steinman, 2002, Taylor and Steinman, 2010, Zhao. Feng and Xie. Xianghua, 2013).

3. Discretisation

Spatial discretisation, or 'meshing', divides the geometry into a number of discrete volumetric elements or cells. Temporal discretisation divides the solution into discrete time steps. The accuracy and numerical stability of the analysis are influenced by both spatial and temporal refinement (Löhner, 2008). The fabrication of the mesh, and the level mesh refinement are influenced by case- and context-specific factors. The mesh and timestep (i.e. spatio-temporal discretisation) must be refined enough to capture the important haemodynamic behaviour of the modelled compartment (the final solution should be independent of mesh parameters), but without excessive refinement because this impacts negatively on computational resource and solution time.

4. Boundary conditions

Although it is impossible, and perhaps unnecessary, to model in 3-D the c5 billion vessels in the entire cardiovascular system, the region to be analysed must have at least one inlet and one outlet. To enable CFD analysis, the physiological conditions at the wall, inlet and outlet boundaries must be specified. Boundary conditions are a set of applied physiological parameters (which may vary over time) that define the physical conditions at the inlets, outlets and walls. They may be based on patient-specific data, population data, lower order physical models (see 2.3.1.1 and Chapter 3) or assumptions. The process of coupling together models of different dimensions or length scales is known as multi-scale modelling. Multi-scale modelling allows detailed analysis of a region of interest but does not waste high levels of temporal and spatial refinement on areas beyond. Instead, these regions may be represented by reduced order models (Brown et al., 2012a).

5. Simulation

A computer file defining the physical parameters of the model is written. In addition to geometric, discretisation and boundary condition data, this file must define properties including: blood density and viscosity (i.e. the characteristics of the fluid model), the initial conditions of the system (e.g. whether the fluid is initially static or moving), time discretisation information (time step length and numerical approximation schemes) and the desired output data (e.g. number of cardiac cycles to be simulated). This information instructs the CFD solver to solve the Navier-Stokes and continuity equations, proceeding incrementally towards a final solution (convergence'). A typical 3-D cardiovascular simulation involves >1 million elements run over several cardiac cycles, each divided into hundreds or thousands of individual time-steps. For linear systems the equations can be solved directly at every time step. For nonlinear systems such as those generated by the Navier-Stokes equations the solution is generated by an iterative process in which the application of a solution algorithm leads to a reduction in error at each iteration until the equations are satisfied, within some pre-defined tolerance, after which the time step is incremented and the process repeated. In some cases the error does not reduce to the required tolerance, and this is referred to as non-convergence. In some cases the error grows at each iteration, and this is divergence. The number of iterations required for convergence at each time step depends on many things, including the timestep itself, but typically for the problems that are addressed in this thesis it is of the order of 10. Typically three cycles are simulated, with a timestep of 1 ms. Thus of the order of four million equations are solved thirty thousand times. 3-D CFD modelling is therefore time-consuming and computationally demanding. CFD simulates laminar flow with high degrees of accuracy. The length and time-scales of turbulent flow demand impractically fine mesh elements and time-step refinement for full resolution of the fields (Direct Numerical Simulation, DNS).

There are approximations that are used to model turbulence by solving additional equations representing the statistical processes, but none of these models have been explicitly designed for the transitional Reynolds numbers typical of certain arterial flows. In a challenge to the community issued by the FDA (Stewart et al., 2013), one such method, the Shear Stress Transport turbulence model was successfully applied by most CFD practitioners. In this thesis turbulence has not been considered, because the Reynolds numbers are below critical zone. The issue of turbulence in the context of CAD pathophysiology is explored in more detail in Chapter 6.

6. Post-processing

Typically, the solver produces pressure and velocity fields for each element at each time-step. The sheer volume of data is too much for a human to interpret, and so some post-processing is required to ensure relevant data are extracted and presented appropriately. For the FFR studies in this thesis, it is possible to extract just one characteristic measure, the FFR, although other details such as the pressure variation along the centreline throughout the arterial system or the flow streamlines to illustrate the nature of the flow might also be of interest.

7. Validation

It is vital that modelled results are validated against an acceptable standard. Commonly, this involves comparison with either values measured within an *in vitro* phantom or acquired during *in vivo* assessment. Validation generates confidence in the accuracy and reliability of a CFD model.

Collectively, the steps one to six outlined above are known as a *workflow* or *toolchain*. Although there are many specialised software applications facilitating the construction and operation of CFD-based workflows, considerable skill and experience are required at each stage to ensure reliability of results.

2.3.1.1 Model design and tuning

Rather than specifying a pressure or flow signal at a boundary, an additional, lower-order (simpler) model may be coupled to the 3-D solver to generate more realistic physiological representations proximal and distal to the simulation domain. Electrical circuit models are often used. These models lack spatial dimensions and are referred to as lumped-parameter, or zero-dimensional since the variables (flow, pressure, concentration) are spatially uniform within each compartment, varying only in time. In some cases the model representing the distal boundary also provides input for the proximal boundary. Such closed-loop models or system models, require very careful tuning. Coupling a lower order model is efficient as it allows detailed analysis in the 3-D region without
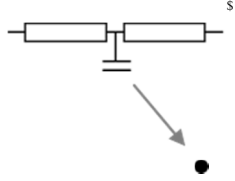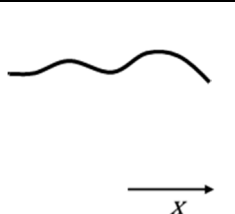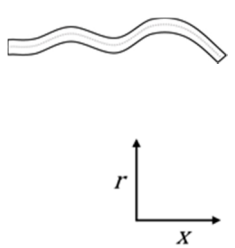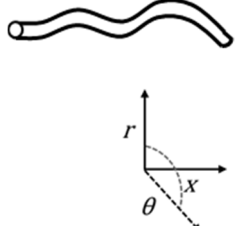
wasting high temporal and spatial refinement on regions beyond this. Because the 0-D models do not recognise any spatial distribution at the boundary with the 3-D model, which does contain this information on the boundary, an averaging process is required. There is a long history of simplification of the governing equations to lower spatial dimensions. **Table 2.1** summarises the relationship between these approaches and provides clinical examples of their use. 2-D analyses typically assume symmetry of the solution about the central axis, 1-D models capture variation of the solution along the axial direction only, and 0-D representations lump the behaviour of vascular regions into a model with no spatial dimensions, hence the term 'lumped-parameter models' (Shi et al., 2011, van de Vosse and Stergiopulos, 2011). Care must be taken to ensure that the formulation of the coupling deals appropriately with this discontinuity, but the mathematical details of this are beyond the scope of this thesis.

2.3.1.2 Assumptions

CFD analyses usually rely on a number of assumptions. First, many CFD models assume that the segmented region has rigid walls. Although untrue in the cardiovascular system, this approximation is considered to be acceptable for some applications (Jeays *et al*., 2007). Compliance allows vessels to store blood during systole and release it during diastole. At the system level this results in a finite speed of pressure-wave transmission and tends to reduce the peak pressures associated with the inertial acceleration of the blood. Compliance tends to reduce shear stresses because the vessels are slightly larger when peak flow occurs. It is possible to model the deformation of the wall in response to fluid pressure using fluid-solid interaction (FSI) models. However, these are far more complex to solve, boundary conditions are a challenge, many wall parameters remain unknown and, largely because of the uncertainty of individual arterial properties, it is yet to be established if FSI approaches improve accuracy in patient-specific simulations.(Brown et al., 2012b) An alternative is to impose wall movement derived from imaging data (e.g. gated MRI). There are exciting developments in the use of data assimilation techniques in which sparse clinical data, e.g. from 4-D imaging, are integrated with the analysis process so that material properties of tissues in individual patients are recovered as the simulation progresses (Bertoglio *et al*., 2014). Second, in biomedical workflows it is assumed the boundaries of the fluid geometry are smooth, yet medical images may not generate smooth surfaces due to poor resolution or imaging artefacts. Instead, structures may be smoothed *in silico* after segmentation. Third, blood is a non-Newtonian fluid. The viscosity depends on the shear rate: for low shear rates the viscosity is high, but as the shear rate increases the viscosity reduces rapidly, and is asymptotic to a value of about 3.5 times the viscosity of water. This must be considered for flow in small capillaries, whereas in larger vessels, in which the shear rate is higher and the

viscosity approaches the asymptotic limit, the non-Newtonian behaviour of the fluid is often neglected.

Table 2.1. Summary of the orders of CFD modelling applied to the cardiovascular system.

Model	Figure	CFD solution	Description /examples	Solution time[*]
0-D	[$]	No spatial dimension. Physiological variables such as pressure (P), flow (Q) and resistance (R) are assumed spatially uniform within the model, varying only as a function of time (t) e.g. $$P_{(t)} = Q_{(t)} \cdot R_{(t)}$$ Solved with ordinary differential (0-D NS) equations	Lump together distributed physiological systems into a single description. They describe the global behaviour of the modelled segment. The 0-D Windkessel model (pictured) (Westerhof et al., 2009) is often used to represent the compliant and resistive nature of the arterial circulation.(Kim et al., 2010a) 0-D models are frequently used to model components of the cardiovascular system or to improve boundary conditions for 3-D models of, arterial, ventricular or venous pathophysiology. (Morris et al., 2013, Lucas, 1984, Biglino et al., 2013, Kim et al., 2009, Zervides and Giannoukas, 2013)	Immediate solution
1-D	X	Physiological variables are solved as a function of a single spatial variable, typically length (x) e.g. $$P_{(x,t)} = Q_{(x,t)} \cdot R_{(x,t)}$$ Solved with partial differential (1-D NS) equations	Used to represent wave propagation characteristics and wave reflection. 1-D models may also be used to provide boundary conditions for higher order models in order to increase refinement of the solution, especially where the effects of wave reflection are significant. (Reymond et al., 2012, van de Vosse and Stergiopulos, 2011, Shi et al., 2011)	Seconds (static) Minutes (transient)
2-D	r X	Physiological variables are solved as a function of two spatial variables, typically length and distance from centreline (r) e.g. $$P_{(x,r,t)} = Q_{(x,r,t)} \cdot R_{(x,r,t)}$$ Solved with axisymmetric NS equations	Able to resolve the solution in 2-D. Used less often now than previously due to ready availability of improved computer processing and 3-D solvers.(Xiong et al., 2011) Examples include the simulation of para-prosthetic valve haemolysis and improvement of the assessment of the proximal flow convergence zone in the clinical evaluation of regurgitant valve disease.(Garcia et al., 1996, Rodriguez et al., 1992, Rodriguez et al., 1993)	
3-D	r X θ	Physiological variables are solved as a function of all three spatial variables, including the angle around the centreline axis (θ) e.g. $$P_{(x,r,\theta,t)} = Q_{(x,r,\theta,t)} \cdot R_{(x,r,\theta,t)}$$ Solved with full 3-D NS equations	Full 3-D CFD can resolve the physiological solution in all dimensions including time. Examples are more widely reviewed in the main body of the text.	Minutes for steady-state Hours or days for transient

[$]*Hydro-electrical analogue diagrams are often used to describe physiological components such as resistance, pressure (voltage), compliance (capacitance) and flow (current).* [*]*Solution times vary according to complexity of the model and the mathematical solution. The times presented are approximate and are based on a model of coronary physiology.(Morris et al., 2013)*

56

2.3.1.3 Benefits of cardiovascular CFD modelling

The wider benefits of CFD modelling in the cardiovascular system are beyond the scope of this thesis. However, CFD modelling has already proven beneficial in the context of device design (Yoganathan *et al.*, 2005) (Farag *et al.*, 2014); simulating disease process (Morlacchi and Migliavacca, 2013); analysis of wall shear stress (Chien, 2007, LaDisa *et al.*, 2005); less invasive diagnostic tools (Lungu *et al.*, 2014) and personalised assessment and risk assessment (Venkatasubramaniam et al., 2004, Martufi and Gasser, 2013).

2.4 Computational fluid dynamics modelling and FFR

The economic and clinical benefits of FFR have driven a number of investigators to explore the possibility of computing FFR using *in silico* models based on anatomical imaging methods. In fact, the goal of attaining a single, non-invasive assessment which delivers both anatomical and physiological detail has been described as the '*holy grail*' of non-invasive imaging (St. Goar *et al.*, 2012). At the outset of this thesis, there were no publications that derived FFR from CFD analysis. More recently, several papers including those by the current author describing techniques whereby CFD modelling, allied to anatomical models based upon coronary imaging, are used to compute FFR, without passage of a pressure wire. This is becoming known as 'virtual' or computed FFR (vFFR). In a relatively short period of time vFFR has undergone rapid development. Two broad categories of approach have emerged: FFR derived from CTCA imaging data (vFFR$_{CT}$) and FFR derived from ICA imaging data (vFFR$_{ICA}$).

2.4.1 Analytical models

Many investigators have attempted to infer FFR from simple 2-D and 3-D QCA measurements using analytical mathematical models based on Bernoulli energy loss calculations. Although there is broad correlation between QCA parameters and FFR, results have been universally disappointing (Brown et al., 1977, Bartunek et al., 1995, Fischer et al., 2002, Sun et al., 2012, Yong et al., 2011, Christou et al., 2007). The results from similar analyses using OCT (Belkacemi *et al.*, 2013, Gonzalo *et al.*, 2012) and IVUS (Koo *et al.*, 2011b, Ben-Dor *et al.*, 2011, Ben-Dor *et al.*, 2012, Koh *et al.*, 2012) have demonstrated similar results. This is explained by two main factors: (i) the inability of the Poiseuille and Bernoulli equations to capture the complex haemodynamics within a diseased coronary artery (see section 2.2) and (ii) studies based purely upon 2- and even 3-D QCA do not represent the patient-specific physiological conditions of the distal small vessels

within the myocardium. These influence the distal pressure and thus are critical to determining the FFR in a particular case.

2.4.2 CT derived FFR

A single group has pioneered vFFR$_{CT}$: HeartFlow Inc. (Redwood City, CA). Building upon previous theoretical and development work (Taylor and Figueroa, 2009, Taylor and Steinman, 2010), in December 2011, Koo *et al* published the DISCOVER-FLOW (Diagnosis of ISChemia-Causing Stenoses Obtained Via NoninvasivE FRactional FLOW Reserve) study (Koo *et al*., 2011a), the first major evaluation of vFFR. CTCA data were used to segment coronary luminal anatomy. This prospective, multicentre study, funded by HeartFlow, compared the diagnostic performance of CTCA (stenosis ≥50%) against CT derived vFFR (vFFR$_{CT}$≤0.80) in predicting myocardial ischaemia as defined by an invasively measured FFR of ≤0.80. One hundred and fifty nine vessels with ≥50% stenosis (by CTCA) were studied in 103 patients. A broad range of FFR values were observed, particularly within the challenging 0.70-0.90 range. vFFR$_{CT}$ was found to be more accurate than CTCA alone in predicting a measured FFR ≤0.80. The area under the receiver operating characteristics curve (AUC) was 0.90 for vFFR$_{CT}$ and 0.75 for CTCA (p=0.001). For dichotomised data, accuracy, sensitivity, specificity, PPV, and NPV were 84.3%, 87.9%, 82.2%, 73.9%, 92.2% for vFFR$_{CT}$ and 58.5%, 91.4%, 39.6%, 46.5%, 88.9%, for CTCA respectively. vFFR$_{CT}$ led to a 70% reduction in false positive diagnoses, a two-fold increase in true negatives and a 25% increase in overall diagnostic accuracy. These results demonstrated the potential for CFD modelled vFFR and paved the way for further investigation.

In a follow-up study of 252 patients (407 vessels), the same group attempted to demonstrate the effectiveness of vFFR$_{CT}$ according to pre-defined standards of accuracy (Min *et al*., 2011). The primary endpoint of the Determination of Fractional Flow Reserve by Anatomic Computed Tomographic Angiography (DeFACTO) study assessed if vFFR$_{CT}$ plus CTCA could predict ischaemia (FFR ≤0.80) on a per-patient basis, such that the lower boundary of the 1-sided 95% confidence interval for diagnostic accuracy was >70% (Min *et al*., 2011). The study did not achieve this pre-defined target. Per-patient diagnostic accuracy for vFFR$_{CT}$ plus CTCA was 73% (95% CI, 67-78). Sensitivity, specificity, PPV, and NPV were 73% (67- 78), 90% (84-95), 54% (46-83), 67% (60- 74), and 84% (74-90) respectively. Although DeFACTO did not meet its accuracy-driven primary endpoint, improved diagnostic utility of using physiological data computed using CFD was demonstrated. In a sub-study analysis, Nakazato *et al* performed a sub-group analysis of 150 intermediate vessels (30-69% stenosis by ICA) from the DEFACTO cohort (Nakazato et al., 2013). Unlike DeFACTO, analysis was similar to DISCOVER-FLOW, in that the diagnostic

performance of vFFR$_{CT}$ was compared with CTCA in predicting an invasively measured FFR of ≤0.80. For intermediate lesions, on a per-patient basis the accuracy, sensitivity, specificity, PPV and NPV for $_{CT}$FFR were 71%, 74%, 67%, 41% and 90%, compared with; 63%, 34%, 72%, 27% and 78% for CTCA. The discriminatory power of vFFR$_{CT}$ was superior to CTCA with an AUC of 0.81 vs. 0.50, P = 0.0001. Most recently, the same group published the NXT trial (Analysis of Coronary Blood Flow Using CT angiography: Next Steps) (Gaur *et al.*, 2013, Norgaard *et al.*, 2014). Using "*updated proprietary software*", "*improved image segmentation*", "*refined physiological models*", "*increased automation*" and "*stricter adherence*" to CTCA guidelines, vFFR$_{CT}$ demonstrated improved diagnostic power in terms of predicting FFR≤0.80. These trials demonstrate superior diagnostic power value of vFFR$_{CT}$ when compared with CTCA alone. In addition the marked increase in specificity and high values of NPV (perhaps a reflection of the nature of CTCA) allow this tool to provide evidence to exclude even more patients from unnecessary invasive catheterisation. **Table 2.2** (below) summarises the findings of these key vFFR$_{CT}$ studies.

A particular strength of vFFR$_{CT}$ is that the computational methods work on standard image algorithms and do not require any additional images or techniques. A criticism common to the vFFR$_{CT}$ studies is that average error is not reported; only dichotomised FFR data (< or > 0.80) predictions are presented. A Bland-Altman plot is included in the NXT trial manuscript which demonstrates a slight positive bias (mean delta) for vFFR$_{CT}$ (0.03, SD 0.074) and limits of agreement (± 2SD) from -0.115 to +0.175. A disadvantage of vFFR$_{CT}$ is the long list of contraindications for the technique (Gaur *et al.*, 2013). Nonetheless, vFFR$_{CT}$ adds value to CTCA. vFFR$_{CT}$ has become the most advanced tool of its kind and, subsequent to the aforementioned studies, HeartFlow Inc. has gained FDA approval for the use of vFFR$_{CT}$ as a class II Coronary Physiologic Simulation Software Device (Food and Drug Administration, 2014, USA).

More recently, in a study similar in design to RIPCORD (section 1.4.1.6), Curzen *et al* demonstrated the influence of vFFR$_{CT}$ on treatment in the FFR$_{CT}$ RIPCORD study (Curzen et al., 2015) by reviewing 200 CTCA cases from the HeartFlow NXT study. Consensus agreement decided best treatment from four options: OMT, PCI+OMT, CABG+OMT, or more information from performing invasive FFR. After vFFR$_{CT}$ data were made available, the cardiologists altered their decision in 36% of cases. **Table 2.3** demonstrates the overall results. 18% of vessels selected for PCI were re-categorised post vFFR$_{CT}$. 11.8% and 26.3% of patients in the 'more information' and 'OMT' categories, went on to require revascularization post vFFR$_{CT}$. Conversely, 29.8% of patients selected for PCI moved to the OMT group.

Table 2.2. Summary of the key vFFR$_{CT}$ studies to date.

	Patients	Method used to predict FFR of ≤0.80	Sens	Spec	PPV	NPV	Acc	AUC
	Vessels	Basis of analysis						
DISCOVER FLOW	103	vFFR$_{CT}$ ≤0.80	88%	82%	74%	92%	84%	0.9
(Koo *et al.*, 2011a)	159	Per-vessel analysis						
DeFACTO	252	CTCA ≥50% + vFFR$_{CT}$ ≤0.80	90%	54%	67%	84%	73%	0.81
(Min *et al.*, 2012)	407	Per-patient analysis						
DeFACTO substudy	-	vFFR$_{CT}$ ≤0.80	74%	67%	41%	90%	69%	0.79
(Nakazato et al., 2013)	150	Per vessel analysis						
HeartFlow NXT	254	vFFR$_{CT}$ ≤0.80, Per-patient (top)	86%	79%	65%	93%	81%	0.90
(Norgaard *et al.*, 2014)	484	Per-vessel (middle)	84%	86%	61%	95%	86%	0.93
		235 intermediate (30-70%) stenoses (bottom)	85%	79%	63%	92%	80%	

FFR, fractional flow reserve; sens, sensitivity; spec, specificity; PPV, positive predictive value; NPV, negative predictive value; acc, accuracy; AUC, area under receiver operating characteristic curve.

Table 2.3. Results from the vFFR$_{CT}$ RIPCORD study.

Treatment option	CTCA alone	CTCA + vFFR$_{CT}$	% Change
OMT	33.6%	56.5%	+23%
OMT+PCI	43.5%	39.0%	-5%
OMT+CABG	4%	4.5%	+0.5%
More information required	19%	0%	-

OMT, optimal medical therapy; PCI, percutaneous coronary intervention; CABG, coronary arterial bypass graft surgery. (Curzen et al., 2015)

2.4.2.1 vFFR$_{CT}$ method

The vFFR$_{CT}$ computational workflow begins with the segmentation of CTCA images using proprietary software in order to extract the geometry of the aortic root and the topology of the coronary arterial tree. The luminal surface is reconstructed and a volumetric mesh is generated. Zero-dimensional models are used to represent the proximal and distal boundary conditions (see **Figure 2.2**). Zero-D model parameters are tuned so that *"cardiac output matches that computed from an allometric scaling law, and the computed mean aortic pressure matches the patient's measured mean brachial pressure"*(Taylor et al., 2013). Distal coronary boundaries (represented by Windkessels) are tuned so that *"a relationship between pressure and flow based on a model of the coronary microcirculation is enforced"* (Taylor et al., 2013). The derivation of these parameters is based on Murray's law of constant shear-stress which states that flow (Q) through a vessel is proportional to the cube of the diameter (Murray, 1926):

$$Q \propto D^3$$

Murray's law explains anatomical adaptation whereby blood vessels continuously remodel in order to homeostatically maintain shear stress. From Poiseuille's law, constancy of wall shear stress implies that vessels must remodel in order to maintain constant shear-stress when exposed to chronic alterations in flow conditions. Thus low flow conditions result in diameter reduction and vice versa. Since:

$$P = QR \quad \text{and} \quad Q \propto D^3 \quad \text{(for constant shear)}$$

$$R \propto D^{-3}$$

Baseline coronary is flow is calculated from myocardial mass derived from CTCA. Resistance values are predicted from flow and pressure is derived from mean cuff (brachial arterial) pressure. The calculation of the resistance (R) of each coronary outlet is based upon morphometric laws ($R \propto$

61

D^{-3}), where D is vessel diameter, and resistance is inversely related to individual vessel diameter. The wall boundary is represented by a no-slip condition for viscous fluids. Hyperaemic flow conditions are simulated on the assumption that during standard adenosine infusion, total coronary resistance reduces to 24% of baseline. This is based on work by Wilson *et al* (Wilson *et al*., 1990).

Limitations of vFFR$_{CT}$ include those of CTCA such as blooming artefacts arising from calcification, motion, arrhythmia and tachycardia. Artefacts cause ambiguity in identifying the true bounds of the coronary lumen which impairs segmentation, even in the hands of experienced CTCA doctors (Rollano-Hijarrubia *et al*., 2009). Previous PCI remains a contraindication. Boundary condition tuning and the application of generic (population-based) boundary conditions is explored further in Chapter 3 and Chapter 5. Overestimating CMVR results in underestimating lesion significance (falsely elevated FFR) and vice versa. CMVR is variable between individuals and between perfusion territories in an individual heart. Furthermore, the CMVR fluctuates according to metabolic adaptation and autoregulation. The assumption that there can be a 'predictable reaction to hyperaemia' (Koo *et al*., 2011a) is also debatable considering the highly variable response to adenosine already described above. Although the scientific basis of vFFR$_{CT}$ is described by Taylor et al (Taylor et al., 2013), and summarised above, the precise details of the algorithms and individual case tuning have not been disclosed.

2.4.3 ICA derived FFR

ICA provides images of coronary luminal anatomy with superior temporal and spatial resolution and routinely measures the aortic pressure which is equivalent to the proximal boundary conditions. It therefore offers a platform upon which a 3-D CFD model of the coronary physiology could potentially be built. This approach circumvents some of the limitations of vFFR$_{CT}$ but, inevitably, introduces fresh challenges. Although ICA is invasive, it does offer the opportunity to perform PCI during the same procedure, offering a complete single assessment and management tool for CAD. This would significantly simplify the currently crowded and complicated assessment algorithms. As mentioned previously, at the time of commencing this thesis, no papers on CFD modelled vFFR from ICA had been published. Morris et al was the first to publish details of such a model in 2013 and this work forms the basis of Chapter 3 (Morris et al., 2013). Subsequently, in 2014 two alternative models with broad overlap to the work in this thesis were described. Tu *et al* developed a method based on 3-D CFD in order to predict vFFR (Tu *et al*., 2014). Arterial segmentation was from CAG images (QAngio XA 3D research edition 1.0 Medis Special BV, Leiden NL) (Tu *et al*., 2012). Steady-state CFD simulation was used which converged to a result
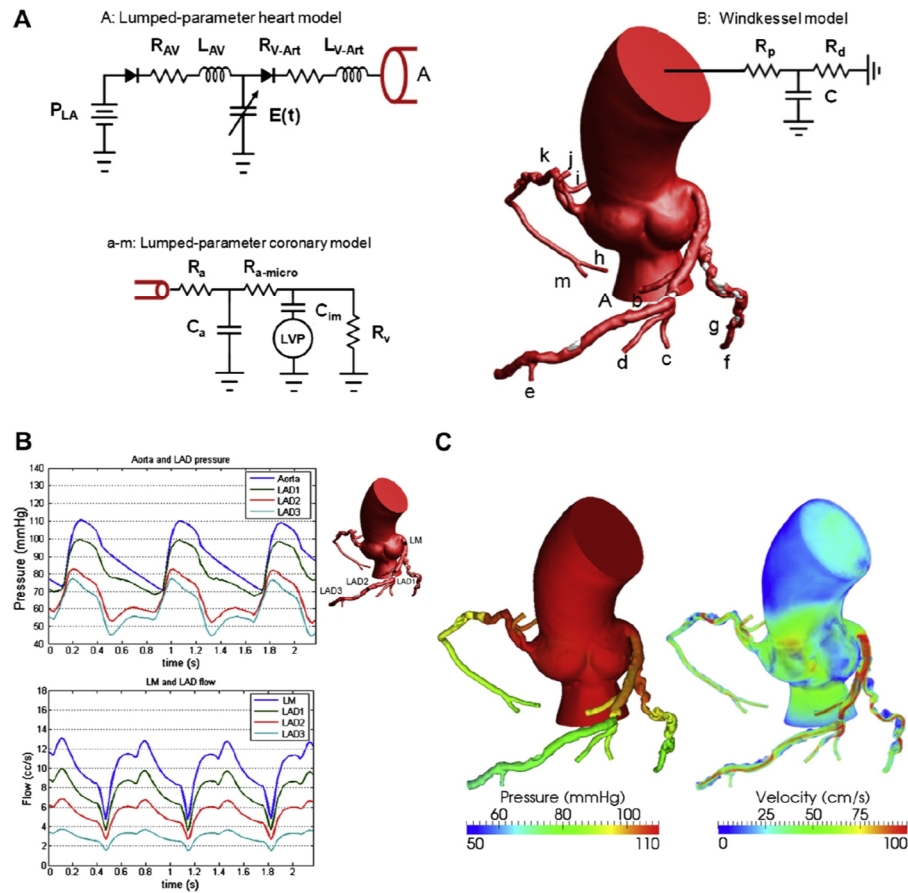
Figure 2.2. Mathematical modelling of vFFR_CT.

(A) Zero-dimensional, lumped parameter models are used to represent the heart (model input), the non-coronary vessels, and the coronary outlets. (B) Transient pressure and flow waves reflect high pressure and reduced flow in response to CMVR during systole. (C) The result of transient CFD analysis are demonstrated graphically with pressure and flow colour maps. P, pressure; R, resistance; C, capacitance; L, inductance; E(t), elastance as a function of time; LA, left atrium; AV, atrioventricular; V-Art, ventricle-arterial; p, proximal; d, distal; a, arterial; im, intermyocardial, V, venous. From Taylor et al, with permission from Elsevier (Taylor et al., 2013).

63

within approximately 5 minutes. Flow boundary conditions were used. This is advantageous because if hyperaemic flow is known then no further assumptions are required to aid tuning. However, coronary flow is difficult to measure, even with invasive intra-coronary instrumentation and so mean hyperaemic flow was derived from Thrombolysis In Myocardial Infarction (TIMI) frame by counting the rapidity of the flowing contrast wavefront within the coronary arteries during injection. This is advantageous since this can be estimated during routine angiography. However, this method was originally developed for use in identifying the coronary no reflow phenomenon in the context of acute myocardial infarction (indicating abnormal tissue perfusion) (Eeckhout and Kern, 2001). Validation data are absent from the paper (and from the literature) in respect of the precision to which this method estimates true mean flow velocity. A disadvantage of the method is that it still requires induction of hyperaemia (another potential factor contributing to FFR under-use) and, because it is only an estimation of mean flow, the method can only easily be applied to steady-state CFD analysis. Nevertheless, their vFFR model provided reasonable diagnostic accuracy in 77 intermediate (40-70% DS) cases (68 patients) with physiological lesion significance (FFR > or ≤ 0.80) being determined with 88.3% accuracy (AUC, 0.93) and agreeability between vFFR and FFR reported with 97% of cases falling within the Bland-Altman limits of agreeability (mean ±delta vFFR values not reported). **Figure 2.3** and **Figure 2.4** (below) demonstrate elements of the workflow and results. More recently, the same group have described methods for using a similar approach to bifurcation lesions which although promising requires further validation prior to implementation (Tu et al., 2015).

Papafaklis *et al* reported a new computationally-derived parameter; the virtual functional assessment index (vFAI) for fast functional assessment of intermediate coronary lesions (Papafaklis *et al.*, 2014). 3D-QCA was performed, and FFR measured in 139 intermediate (30-70% DS) cases (120 patients). Segmentation from ICA allowed 3-D reconstruction with proprietary software (CAAS QCA-3D, Pie Medical Imaging, Maastricht, NL). CFD simulation was used to construct the pressure gradient to be plotted against flow (ΔP-Q curve) for each case. Unlike vFFR$_{CT}$ CFD boundary conditions were specified (paired steady-state analyses at 1 and 3 ml/s with P_a set to 100 mmHg). The quadratic relationship was defined and vFAI was computed based upon the ratio of distal to proximal pressure over the lesion for flows in the range zero to 4 ml/s, normalised by the ratio over this range for a normal artery.
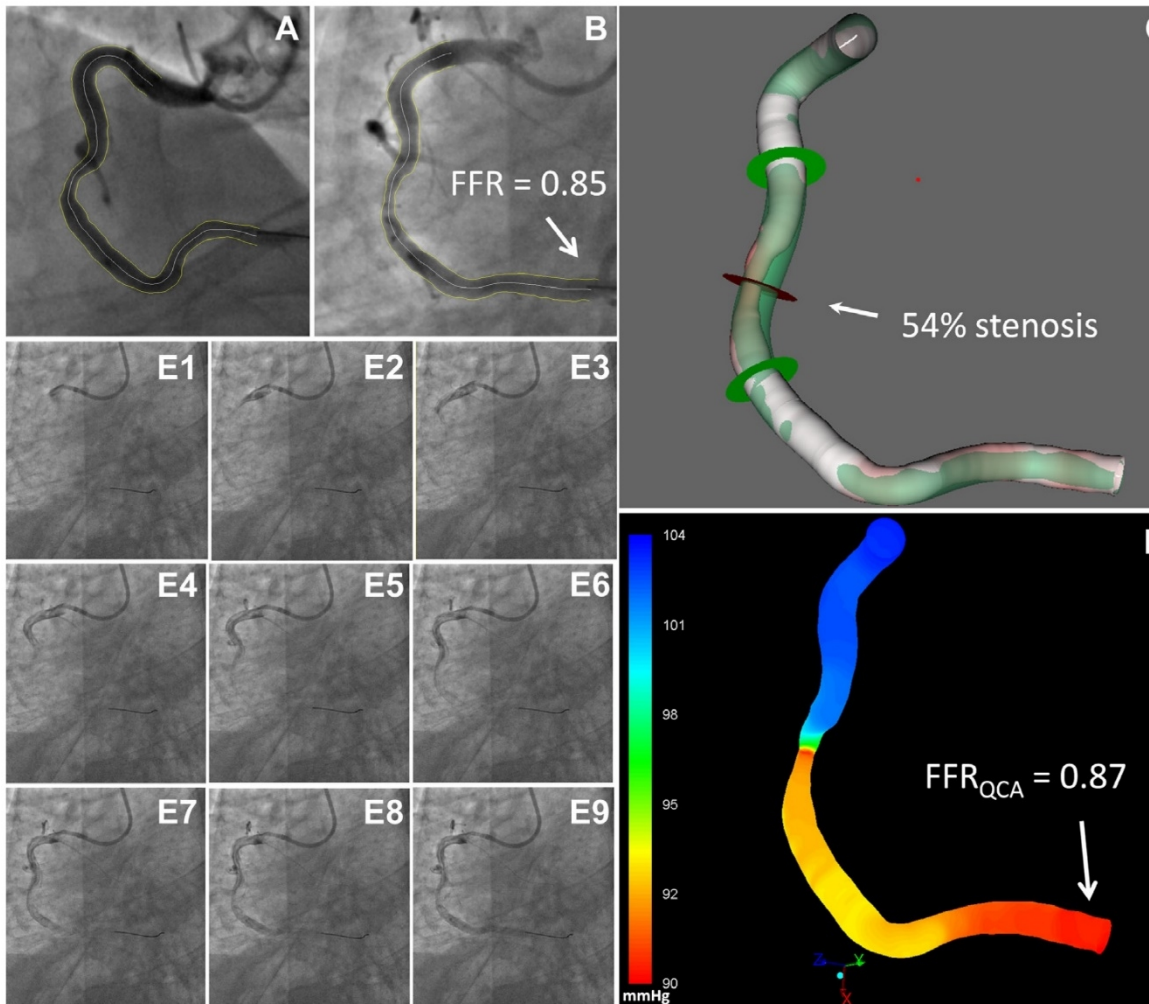
Figure 2.3. Computing vFFR_{ICA} using TIMI derived flow

(A&B) demonstrate coronary luminal segmentation in the context of a right coronary artery stenosis. (C) 3-D reconstruction with superimposed 'normal' arterial contours. (D) Steady flow CFD result based on TIMI derived flow (panels E1-E9) demonstrating FFR_{QCA} of 0.87. From Tu et al with permission from Elsevier (Tu et al., 2014).
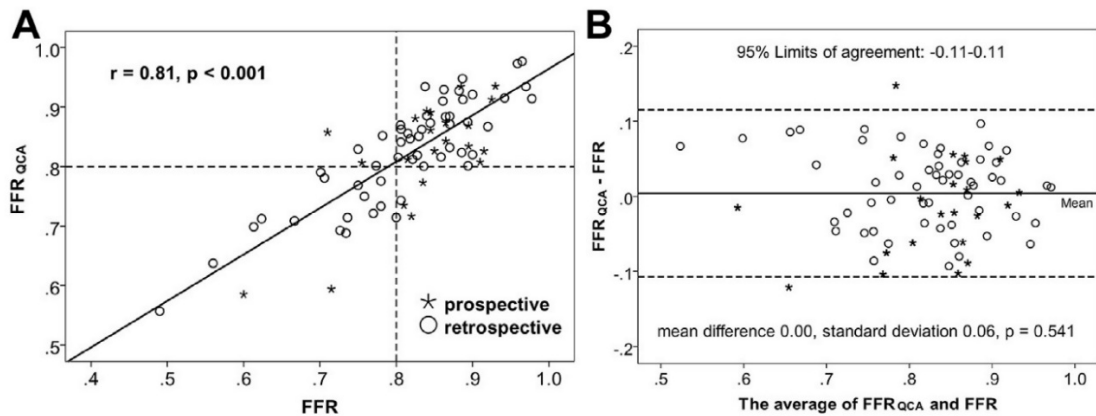
Figure 2.4. Correlation (A) and agreement (B) between FFR and vFFR$_{ICA}$ ('FFR$_{QCA}$')
Note that the limits of agreement (±2SD) roughly correspond to those of vFFR$_{CT}$ (section 2.4.2). From Tu et al with permission from Elsevier (Tu et al., 2014).

The optimal vFAI threshold for significance was ≤0.82. vFAI discriminated physiological lesion significance (FFR≤0.80) with an area under the receiver operator characteristic curve: 0.92 (95% CI: 0.86-0.96). Overall diagnostic accuracy, sensitivity and specificity for vFAI were 88%, 90% and 86%, respectively. Virtual-FAI performed better than 3D-QCA–derived % area stenosis (AUC: 78% [95% CI: 70-84%]; p<0.0001 compared to vFAI). vFAI was correlated with FFR (r=0.78, p<0.0001) and the mean delta between vFAI and FFR was −0.0039 ±0.085, p=0.59. The results in terms of correlation with fractional flow reserve (FFR) are impressive for this medium-sized cohort study.

However, certain aspects of the methodology raise concern. First, the vFAI is computed based upon the ratio of distal to proximal pressure over the lesion for flows in the range zero to 4 ml/s, normalised by the ratio over this range for a normal artery. The pressure ratio as a function of flow is described as a quadratic equation with coefficients determined by steady-state computational fluid dynamics analysis at two flow rates (1 and 3 ml/s). Although it is not explicitly stated, the vFAI is numerically equal to the average of the computed pressure ratio over this flow range and this seems to be a simple way to describe the parameter and gives it a physiological interpretation. Second, the vFAI is entirely a function of the geometry of the stenosis. It is likely to be better than QCA because the geometric description is transformed into a more physiologically relevant measure, namely pressure ratio, by the computation of the relationship between pressure ratio and flow. However vFAI can never be a surrogate for FFR because the point of FFR is that it measures the pressure ratio in the context of the patient-specific physiology. The vFAI will always be low,

66
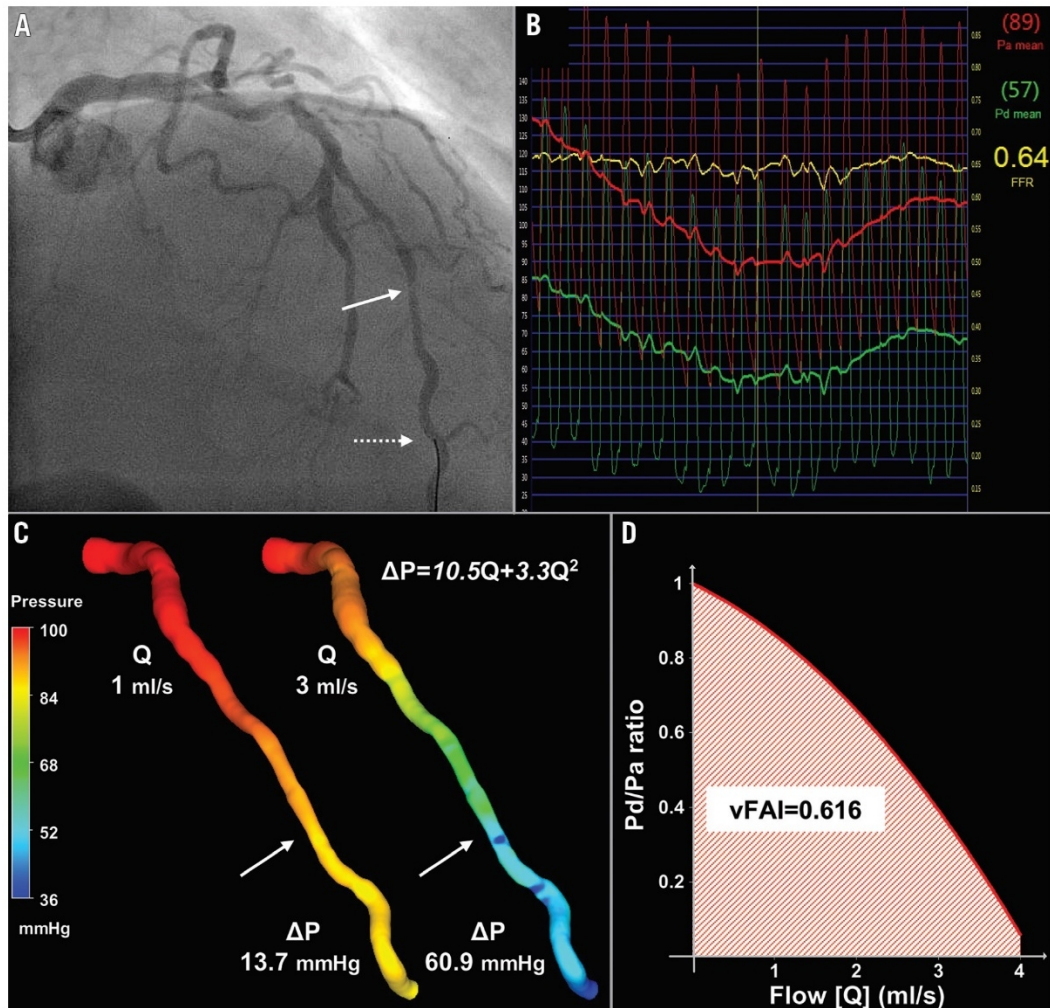
Figure 2.5. Example of vFAI computation.
(A) Coronary angiogram demonstrating a left anterior descending artery with moderate stenosis (arrow). (B) fractional flow reserve is measured at 0.64 with pressure wire (dashed arrow). (C) Reconstructed coronary lumen with CFD results at 1 and 3 ml/s with the quadratic ΔP–Q relationship described. (D) Pd/Pa pressure ratio is plotted against flow, and vFAI is calculated at 0.62. From Papafaklis et al with permission from EuroIntervention (Papafaklis et al., 2014).

indicating the need for intervention, if the lesion is geometrically significant, whilst the FFR could be high or low for the same lesion depending on the overall physiology, and in particular on the status of the coronary microvasculature. Although on average there is a correlation between vFAI and FFR, simply because the pressure ratio is likely to be lower when the lesion is more geometrically significant, large differences can occur when the impedance of the microvasculature deviates significantly from the norm, and these are exactly the circumstances that are captured by the FFR. This may explain the sometimes high deviation of the vFAI measure from the FFR, as illustrated in the Bland-Altman plot; and would risk incorrect diagnosis of the physiological importance of the lesion in certain circumstances.

The methods and findings of the key vFFR trials (as of July 2015, excluding published work included in this thesis) are summarised in **Table 2.5** (page 48).

2.4.4 $vFFR_{CT}$ 'versus' $vFFR_{ICA}$

The development of FFR_{CT} and FFR_{ICA} reflects the desire to introduce the clinical and economic benefits of physiological lesion assessment into previously anatomical tests. However, these two approaches are neither competitive, nor exclusive. $vFFR_{CT}$ is associated with high levels of specificity and NPV and is therefore apposite for outpatient cases where the pre-test probability of significant IHD is low or intermediate. In this scenario, FFR_{CT} can be used as a 'gatekeeper' for ICA in order to minimise unnecessary left heart catheterisations. Furthermore, prolonged computational protocols (c 5 hours) (Kim et al., 2010b, Taylor et al., 2013) are not convenient in the outpatient setting. FFR_{ICA} is better suited to higher risk cases where vFFR can be used to guide revascularisation decisions directly. All patients undergoing PCI or CABG undergo an ICA. However, for $vFFR_{ICA}$ techniques to become truly useful, they must provide results within tractable timescales. **Table 2.4** (below) compares the key elements of $vFFR_{ICA}$ and $vFFR_{CT}$.

2.5 Summary

Simple haemodynamic constructs provide only a crude estimation of coronary haemodynamics which are challenging due to:
- Pulsatility: which flattens the flow profile (according to Womersley number)
- Vascular curvature: which, due to centrifugal forces, introduces asymmetry of flow and WSS
- Frequent bifurcations: before flow is fully developed

- Transitional Reynolds numbers which occur in the context of hyperaemic flow within diseased arteries

3-D CFD provides an ideal platform upon which to base a predictive model of intra-coronary physiology.

Table 2.4. Comparing vFFRI$_{CA}$ with vFFR$_{CT}$.

Factor	vFFR$_{ICA}$	vFFR$_{CT}$
Invasive	Yes	No
Contraindications	Few	Many
Accuracy	Depends on technique	High specificity and NPV
Imaging	Good resolution	Artefact can limit image quality
Segmentation	Less well developed algorithms	Well developed proprietary algorithms
Boundary conditions	Individualised tuning scheme required*	Individualised tuning scheme required
Simulation	Prolonged*	Prolonged
Ideal subject	High risk of CAD	Low-intermediate risk of CAD

Unless hyperaemia induced and TIMI flow used.

2.6   Thesis hypothesis, aims, objectives

The hypothesis underpinning this thesis is that ***intracoronary physiology can be computed from invasive coronary angiography using computational fluid dynamics (CFD)***.

The aim of this thesis is to ***develop, validate and optimise a method which can deliver the clinical and economic benefits of physiological lesion assessment that is not associated with the factors which restrict use of the current invasive methods***.

2.7   Thesis outline

Chapter 3 describes the development of the initial CFD model of intracoronary physiology which is capable of computing trans-lesional pressure gradients and thus FFR and validates the model within a clinical trial.

Chapter 4 focuses on model acceleration and describes two novel methods for computing 3-D CFD in timescales which rival invasive FFR measurement.

Chapter 5 focuses on the design tuning of model boundary conditions and describes a novel approach for patient-specific tuning of the distal (outlet) boundary conditions.

Chapter 6 investigates whether the model can usefully be used to compute coronary flow from measured pressures and with an experimental validation performed using 3-D printed, patient-specific arterial phantoms.

Chapter 7 brings the work of the preceding chapters together and explores future opportunities and strategies for clinical translation and commercialisation.

Table 2.5. Summary of methodology and precision of models of vFFR (excluding arising from subsequent work in the current thesis).

vFFR model /study reference	Pt Vessels	Imaging modality	CFD simulation	Boundary condition strategy	Other	Diagnostic accuracy$	AUC$	Agreeability	Pearson correlation coefficient	Bias ±SD	Approximate run time
						Versus invasively measured FFR					
CTCA-FFR DISCOVER-FLOW (Koo et al., 2011a)	103 159	CTCA	3-D CFD	Based on vessel diameter and myocardial mass	Coupled lumped parameter model at outlets. (HeartFlow software version 1.0)	84% (per-vessel)	0.90	Not reported (94% of results within Bland-Altman limits of agreement)	0.68 (p<0.0001)	0.02±0.116	Remote core lab computation (c.5 hrs)
CTCA-FFR DeFACTO (Min et al., 2012)	252 407	CTCA	3-D CFD	Based on vessel diameter and myocardial mass	Coupled lumped parameter model at outlets (HeartFlow software version 1.2)	69% (per-vessel)	0.81 (per-patient)	Not reported. No Bland-Altman plot	0.63	0.06 (SD not reported)	Remote core lab computation (c.5 hrs)
vFAI* (Papafaklis et al., 2014)	120 139	CAG	Steady-state 3-D	Flow	Derived from ΔP-flow curve	87.8%	0.92	Not applicable*	0.78	0.00±0.085	7 minutes
CTCA-FFR HeartFlow NXT ((Norgaard et al., 2014)	251 484	CTCA	3-D CFD	Based on vessel diameter and myocardial mass	Coupled lumped parameter model at outlets (HeartFlow software version 1.4)	86% (per-vessel)	0.93 (per-vessel)	Not reported	0.82	0.02±0.074	Remote core lab computation (c.5 hrs)
FFR$_{QCA}$ (Tu et al., 2014)	68 77	CAG	Steady-state 3-D	Mean flow (derived from TIMI frame count)		88.3%	0.93	Not reported (97% cases within Bland-Altman limits of agreement)	0.81	0.00±0.06	5 minutes

Based on the best interpretation of published literature. vFAI = virtual functional assessment index is a surrogate marker of functional lesion assessment. $Diagnostic accuracy in diagnosing physiological lesion significance of an invasively measured FFR of < or > 0.80.
vFFR = virtual fractional flow reserve; CFD = computational fluid dynamics; ROC = receiver operating characteristic; SD = Standard deviation; mFFR = invasively measured fractional flow reserve; vFFR = virtual fractional flow reserve; CAG = invasive coronary angiography; CTCA = computed tomographic coronary angiography; TIMI = thrombolysis in myocardial infarction; AUC, area under receiver operating characteristic curve.

71

Chapter Three:

Model Development and Validation

3.1   Introduction

This chapter describes the development and validation of the initial computational model, 'VIRTU-1'. The purpose of the model was to test the hypothesis that it is feasible to compute 'virtual' fractional flow reserve (vFFR) from invasive coronary angiography. At the time of commencing development no other models of vFFR were described in the literature. Therefore, in this initial period, many of the decisions regarding design and construction were made based upon the clinical and technical experience of the current group. Many well-constructed *in silico* models of human physiology lack either direct clinical application or suitability for use in the clinic. Therefore, a key priority in the current project was to maintain a focus on developing a useful and practical model.

3.2   Aims and objectives

The aim of the work described in this chapter was to design, construct, and validate a system capable of simulating clinically relevant physiology. The objectives were threefold:

1. design and implement an *in silico* prototype for computing vFFR using routine clinical data
2. test the workflow in a small clinical pilot study
3. identify the major challenges of modelling vFFR in order to guide further work

3.3   Model development

The development of VIRTU-1 proceeded in line with the generic steps of a typical CFD workflow as outlined in Chapter 2 (section 2.3).

3.3.1   Segmentation and reconstruction

Segmentation from invasive coronary angiography (ICA) has already been described (Liao et al., 2010) but proves challenging due to both the small length scales involved in CAD, and cardiac motion. Clinical segmentation and reconstruction protocols have become more established in the context of CTCA, where images are acquired, according to the phase of the cardiac cycle, by ECG-triggered gating. This is not possible in ICA. The local cardiac catheter laboratory (South Yorkshire Cardiothoracic Centre, Sheffield Teaching Hospitals NHS Foundation Trust (STH), Sheffield, UK) is a Philips Healthcare reference centre equipped with the facility to perform single-axis rotational coronary angiography using the Philips Allura Xper Swing system (Philips Healthcare, Best, NL). Rotational CA (RoCA) is a relatively new method of angiographic image acquisition, originally conceived and developed for imaging cerebral vessels, to overcome the limitations of conventional multiple single plane angiography described in section 1.2.1 (Cornelis et al., 1972, Thron and Voigt, 1983, Tu et al., 1996). In RoCA, 121 individual X-ray images are acquired as the X-ray C-arm sweeps around the patient (transverse axis) in a 120° arc at a rate of 30° per second (**Figure 3.1**). Once the images have been acquired, the 3-D coronary luminal anatomy can be reconstructed and visualised using the Philips XtraVision 3D-CA software (Philips Healthcare, Best, NL). Using this system, the operator selects two images from a single rotational acquisition. Using a semi-automatic process, the system enables the operator to segment the luminal surface from both projections, following which reconstruction (including the addition of branches) is performed. The result is a branching 3-D coronary luminal surface. The Philips system

is adapted so that 3-D quantitative coronary angiography (3-D QCA) can then be performed and the 'TrueView' function, which calculates the best view with least foreshortening, can be used to select the optimal view with which to assess 3-D coronary anatomy and pathology. This is demonstrated in **Figure 3.2**.
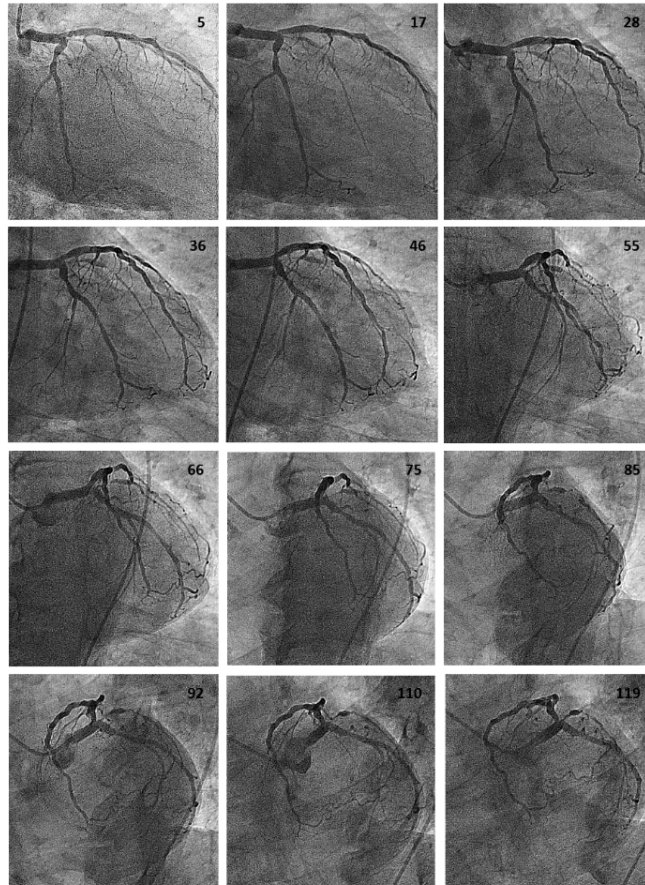
Figure 3.1. Rotational coronary angiography.
Representative frames from a rotational angiogram of a LAD artery.
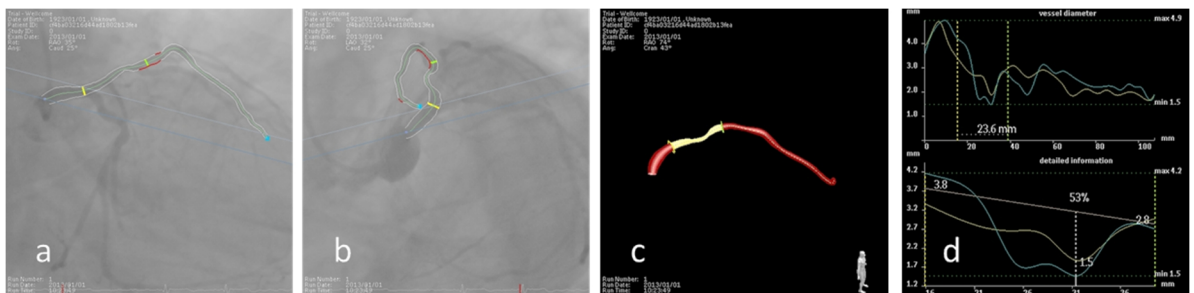
Figure 3.2. Segmentation and reconstruction using the Philips system.
An LAD artery is segmentation in the first (a) and second (b) planes. The reconstruction (c) and 2-D QCA function (d).

RoCA was developed to help circumvent the limitations of multiple single-plane (standard angiography) whereby operators are required to recall the appearance of previous angiographic runs and reconstruct 3-D anatomy using their 'mind's eye'. In the context of diagnostic angiography, RoCA is associated with a reduction in the volume of contrast agent used and the total radiation dose delivered to the patient (Horisaki, 2008a, Raman et al., 2004, Maddux et al., 2004, Rigattieri et al., 2005). More recently, work by the current author has demonstrated that RoCA may also have a role in planning coronary revascularisation because, compared with conventional ICA, RoCA augmented assessment of 3-D bifurcation anatomy, vessel calibre and improved operator confidence when assessing lesion length and stenosis, but did not affect X-ray dose, contrast agent volume, or procedure duration (Morris et al., 2015a).

A priority was to develop a model of vFFR that could rapidly enter clinical practice, with as many components as possible already externally validated (including segmentation and reconstruction). For this reason, and because it was already installed and available at STH, the Philips 3DRA system was therefore used as the first step in the workflow. The standard Allura 3DRA system exports image data from RoCA studies (in binary form) to the 3-D station where segmentation and reconstruction are performed. In the normal mode of operation, 3-D reconstructions can be visualised in viewing software but the 3-D virtual reality modelling language (VRML - *.wrl) files are not exportable. A formal arrangement was reached with Philips Interventional X-ray (see acknowledgements) whereby a prototype PC enabled the export of VRML files was built and provided to the Medical Physics Group, the University of Sheffield (UoS).

3.3.2 VRML import and geometric definition

The Medical Physics group had experience working with an open source software platform called Graphical Interface for Medical Imaging Analysis and Simulation (GIMIAS, 2015), originally developed within the Universitat Pompeu Fabra (Barcelona, ESP), and latterly within the Centre for Computational Image and Simulation Technologies in Biomedicine at the University of Sheffield. GIMIAS is an open source workflow-oriented software environment for processing biomedical imaging and physiological simulations and is well-suited for the development of academic and clinical workflow prototypes.

As the available library of image analysis tools accessible to GIMAS was not sufficiently comprehensive for the needs of the current workflow additional functionality in the form of software plugins, coded in C++ was developed locally (by RL and DR) and incorporated into the GIMAS framework

3.3.3 "Load a coronary VRML" plugin

GIMIAS processed geometric data in the Visualization Toolkit (*.vtk) format. The bespoke Philips workstation produces a *.vrml file which defined the 3-D coordinates of the luminal surface and the centreline/s (skeleton). The Philips system does not produce a single surface representation of the branching tree structure and, instead, regarded the centre lines and lumens of each of the branches as separate entities. This plugin was required to; (i) convert *.vrml into *.vtk, (ii) close the surface, (iii) merge the centrelines, and (iv) merge the luminal surfaces thus eradicating internal vessel overlap.
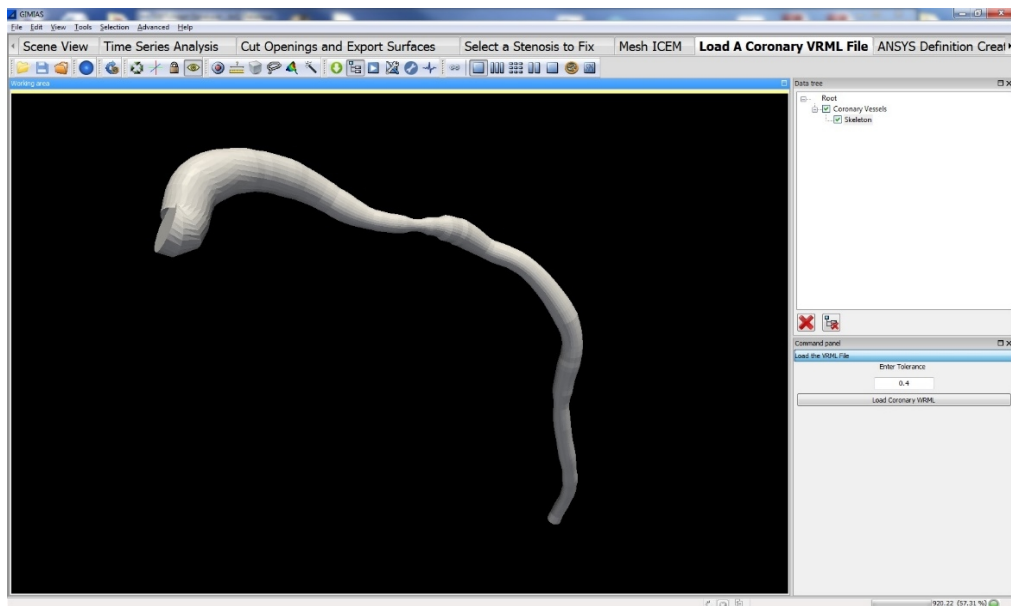
Figure 3.3. The VRML import function incorporating the left main stem and left anterior descending artery of patient #1.
Note the proximal reconstruction inconsistency at the left main stem ostium introduced by the Philips reconstruction software (see section 3.7 below).

3.3.4 "Cut openings and define inlets /outlets" plugin

The next plugin was developed in order to identify and extract the region of interest, and then to define the boundary regions of the luminal surface. A 'ring cut' was performed tangential to the skeleton at points defined by the operator as corresponding to the inlet and outlet/s. These, locations were then defined as 'inlet' or 'outlet'. The 'region of interest' and the inlets and outlets were then extracted as a single entity but saved as separate *.vtk files as 'extracted surface'.
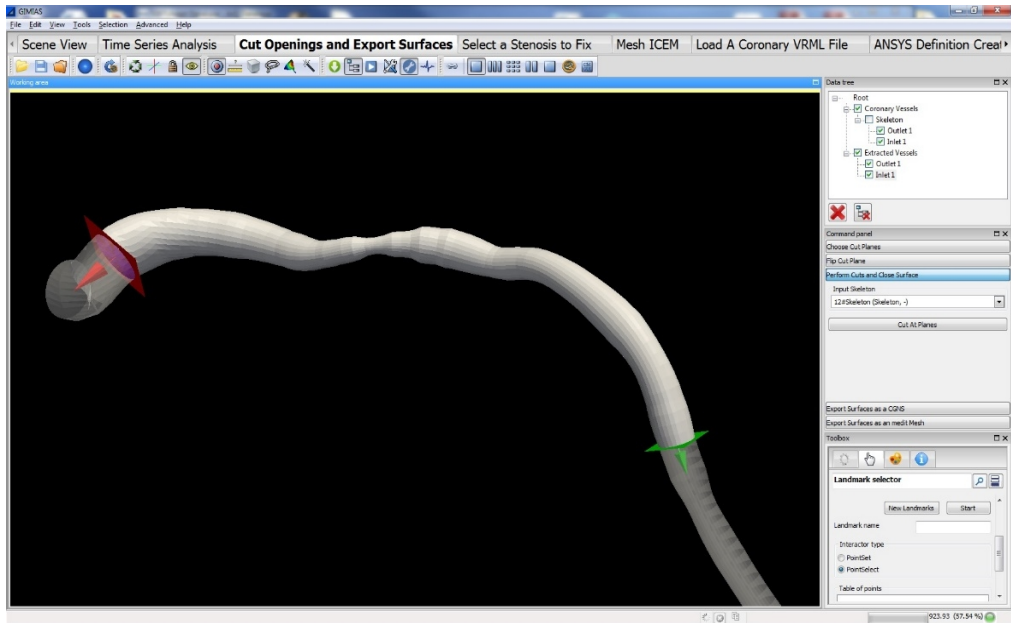
Figure 3.4. Cut openings and export surfaces
The inlet (red plane) and outlet (green plane) were defined, and the region of interest was extracted as a *.vtk surface. The proximal inconsistency at the origin of the left main coronary artery was eliminated.

3.3.5   "Mesh vessel" plugin

High quality volumetric meshes can now be produced with a variety of proprietary codes. ANSYS ICEM CFD (ANSYS, Inc. PA, USA) was selected for inclusion in the current workflow. ICEM mesh generation was a semi-automatic process whereby the operator defined the mesh parameters and the mesh was then fabricated and saved in a working directory. In order to streamline the workflow, a CFX command language (*.ccl) prompt was implemented as a plugin within the GIMIAS framework. In VIRTU-1 a tetrahedral mesh approximating 1-1.5 million elements was implemented based upon previous group experience, reinforced by mesh sensitivity testing on representative cases (see **Figure 4.1**).

3.3.6   "Time series analysis" plugin

This function processes and averages physiological data to be processed and averaged in order to derive boundary conditions. Pressure and flow data were exported from the catheter laboratory via optical disc. Data were loaded into software (ComboMap Study Manager), provided courtesy of Volcano Corps (Zaventem, BE, EU) which enables study data to be exported as a text file
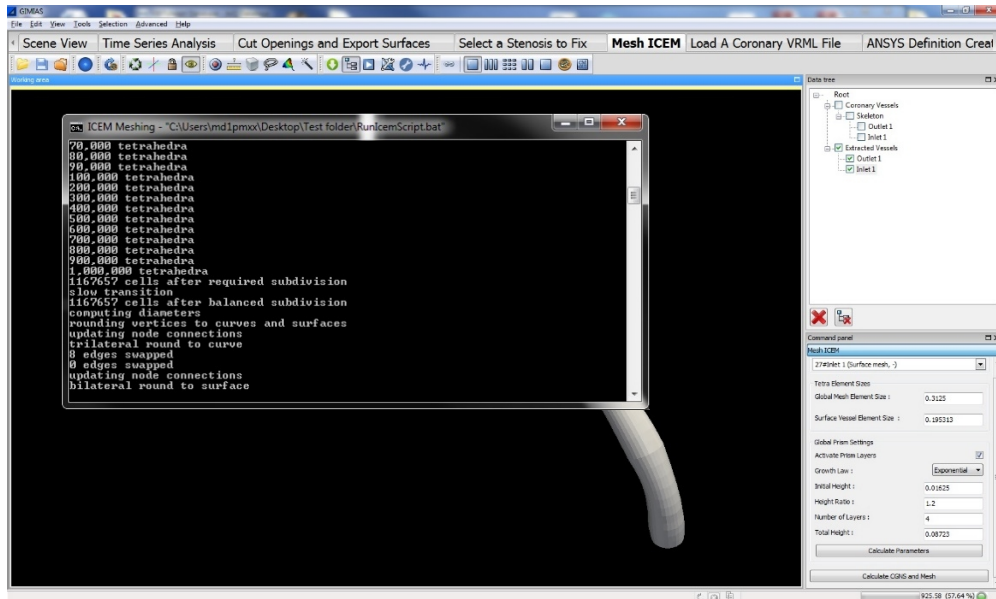
Figure 3.5. Fabricating the volume mesh.

GIMIAS instructed ICEM to fabricate the mesh according to the parameters chosen in the command panel (lower right). The DOS window (upper left) describes the meshing process progress in real time.

comprising; proximal (catheter tip) pressure, distal (wire) pressure, Doppler flow velocity, and electrocardiogram curve data (including an R wave trigger), all as a function of time, in 5 ms increments. The plugin enabled these text data to be loaded, visualised and processed. First, the period of clinical measurement was identified and selected ('raw data windowing', **Figure 3.6**, panel a). The selected data could then be used to calculate the FFR for that period. Second, the signals within the period of interest were divided into individual cycles according to a signal and threshold value of the operator's choice ('cycle selection', **Figure 3.6**, panel b). The ECG R wave was identified as the optimal signal for splitting signals according to cardiac phase. Errant cycles with poor signal and artefact were then excluded or merged in order to ensure precise cycle division. Finally, the included cycles were ensemble-averaged into a single cycle representative of the period of measurement minus any errant cycles ('averaged', **Figure 3.6**, panel c). Output data included; cycle length, minimum, mean and maximum pressure values for each pressure trace (P_a and P_d) including errors (as plotted on the pressure traces in panel c) and the facility to save each signal as a text document.

Figure 3.6. Workflow physiological signal processing. Legend on next page.

Figure 3.6 (previous page). *Panel (a) demonstrates a period of hyperaemia from 22 min 01 s - 22 min 44 s recorded by the Volcano ComboMap system and displayed in the workflow environment. ECG curve (top), proximal (blue) and distal (green) pressure traces (middle row) and flow signal (bottom) are displayed. The plugin automatically calculated the FFR and /or CFVR averaged over the selected period which was defined visually or by manual time entry. Panel (b) demonstrates cycle selection. The signal has been split into individual cycles (periods) according to the ECG R wave trigger (top right). Individual cycles were deleted or merged (using the right middle panel controls) to ensure signal artefact did not pollute the final process of averaging the signals. Panel (c) demonstrates the ensemble averaged data as a single cardiac cycle (period). The mean error is plotted on the signals and detailed in the information panel (right). Minimum, maximum and mean values for all signals and cycle length (s) were detailed, along with corresponding error values.*

3.3.7 Boundary condition selector plugin

A separate plugin was developed which ascribed (via CFX command language) the boundary conditions after the relevant volumetric mesh file (*.msh) was loaded. The arterial wall function was set to default as a rigid wall; an acceptable approach in this context (Zeng et al., 2003, Zeng et al., 2008). Inlets and outlet boundary conditions were defined as transient or steady, pressure or flow. Transient data were imported, plotted and selected as text files (as a function of time). Once all boundaries were defined, a file comprising these data was written (file extension *.bcs) and saved which informed simulation definition (see 3.3.8).
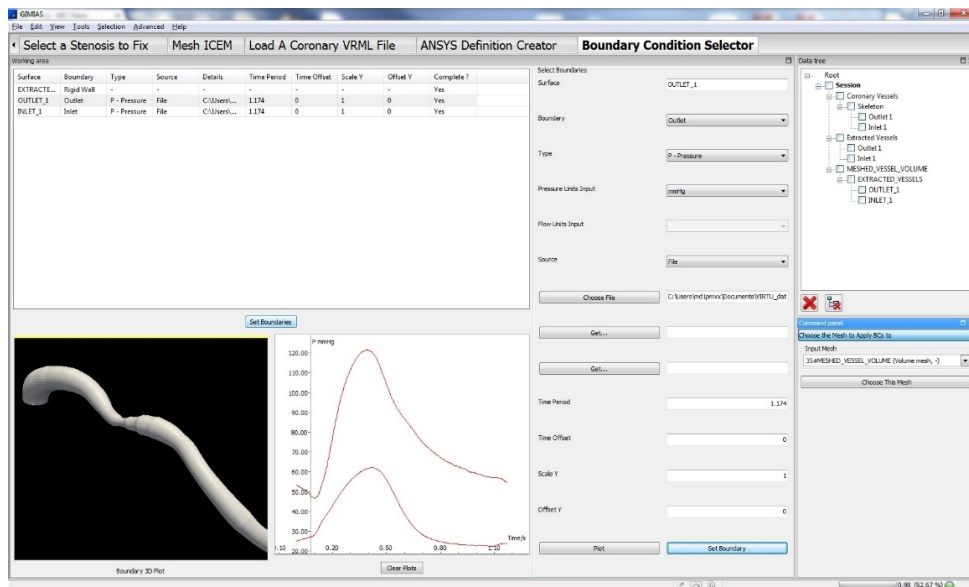
Figure 3.7. Selecting and specifying boundary conditions
The grey panel (middle right) enables pressure or flow (steady or transient), or a zero-dimensional model to be applied at the boundaries according to operator selection. The top left panel demonstrates what conditions have been specified to which boundary and which are complete or incomplete. The bottom left panel displays the arterial geometry. In this case, pressure boundary conditions have been applied at the proximal and distal boundaries and the selected traces are plotted.

3.3.8   "Definition file creator" plugin

The final step within the GIMIAS workflow was to set up the ANSYS CFX files. The relevant volume mesh and boundary conditions files were selected and loaded. This plugin enabled a variety of ANSYS CFX Pre commands to be defined including:

· Time control: time-step (period /n), total time (period * nCycles)

· Solution control; convergence criteria, residual target, minimum and maximum coefficient loops (number of iterations per time-step)

· Fluid properties; Newtonian /non-Newtonian, rheological parameters (density and viscosity)

· Output control: nature and volume of output data, transient folders

· Units; pressure and flow converted to Pascals and m^3s^{-1}.

· Volumetric mesh information; region (inlets, outlets, wall) definitions

Once the above parameters had been selected /defined, the plugin wrote a CFX Pre case file (*.cfx), a CFX command language text file (*.ccl) and a CFX definition file (*.def).
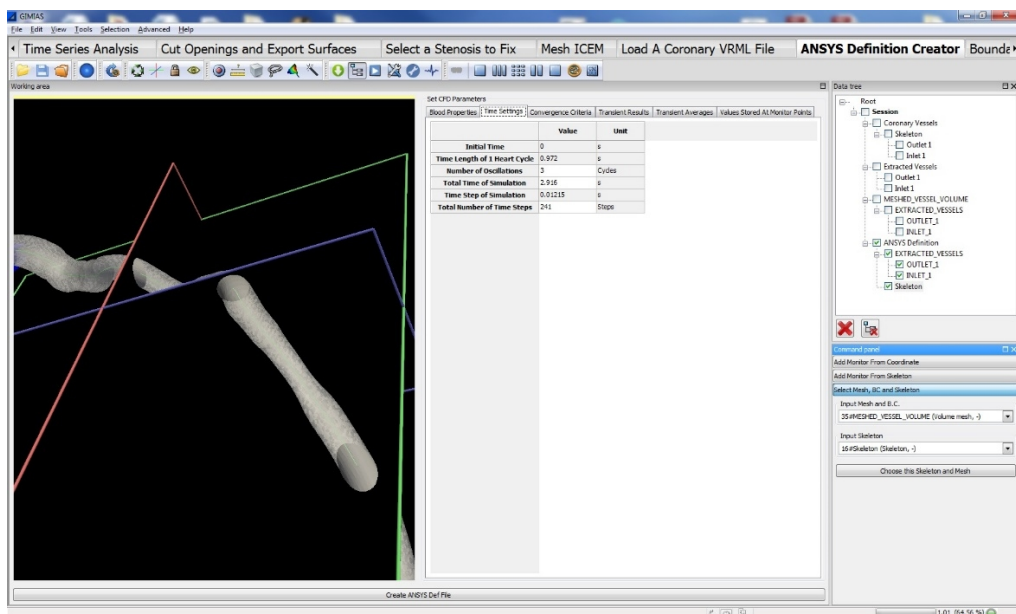
Figure 3.8. CFX Definition file creator
All of the major blood, time, convergence and output parameters were defined at this stage according to the tabs at the top of the display. The command panel (bottom right) specifies the selected mesh and prompts the user to select the appropriate boundary condition files (.bcs).*

3.3.9   ANSYS CFX Pre, Solver Manager and Post

Within CFX Pre, the mesh and regions were visualised and the simulation details (defined in 3.3.8) checked. Once the simulation setup was verified, the simulation was compiled. Once compiled, the simulation proceeded within ANSYS CFX Solver Manager until completion, whereupon a results file (*.res) and an 'out' file (*.out) were written. The results were exported from the solver manager as a comma separated values file (*.csv) into Microsoft Excel where results could be analysed.

3.3.10   Boundary conditions

Accurately representing the physiological behaviour at the boundaries is critical to model accuracy. Even if an appropriate boundary model is applied, a challenge common to all human biological CFD modelling is to understand how to tune ('parameterise') this on an individual case basis. Parameterisation strategy is critical to model output accuracy, but requires detailed knowledge of a variety of physiological metrics in the proximal or distal circulations which may be either challenging to measure or, in the case of the coronary model, not measured at all in a truly predictive model. Often these conditions display wide heterogeneity in both healthy and diseased states and thus should not be assumed or based on population-averaged data. It is important to understand the sensitivity of model outputs to individual input parameters such as boundary conditions, so that effort can focus on the dominant factors (see Chapter 5). It is necessary to determine which are the most influential, which can be assumed, or averaged, and which require individual-patient tuning. This facilitates scaling back of unnecessary model complexity (although simplicity should be balanced against accuracy). Relatively simple models (by technical engineering standards) can be surprisingly valuable and effective in biological modelling (Brown et al., 2012). Within this thesis, the design and tuning of the distal boundary condition are explored and revisited both here, and in Chapter 5. As *in silico* modelling of vFFR has developed over the last three years, the distal boundary condition has emerged as the single greatest challenge facing accurate vFFR prediction (Morris et al., 2015b). The greatest challenge is to accurately represent the physiological behaviour at the distal boundary in a way which supports predictive modelling of the pressure distal to a coronary lesion (P_d) and thus vFFR. Both the model and the parameters applied at the distal boundary had to be determined.

3.3.10.1 Proximal boundary condition

During ICA, the pressure at the catheter tip is monitored continuously, and hence the patient-specific proximal boundary pressure condition is readily available. Knowledge of hyperaemic flow would be ideal because this would fully define the simulation but, unless specifically recorded,

coronary flow is not known during ICA. Mean flow can be inferred from the speed of travel of the wave-front of injected contrast along the coronary lumen (Tu et al., 2014). However, the 'wave-front' is actually unclear due to mixing with the blood, baseline flow is variable (a limiting factor for CFVR) and hyperaemic flow requires pharmacological induction which is to be avoided, because this is a limitation of the current invasive FFR measurement technique.

3.3.10.2 Wall boundary condition

The epicardial coronary arteries were studied after intracoronary (i.c.) glyceryl trinitrate (GTN), and the vessels were considered to be maximally dilated. Although un-diseased epicardial arteries are compliant, this was considered negligible and the arteries were simulated as rigid tubes. This is an acceptable approximation if the capacitance of the epicardial vessels themselves is negligible, one of the consequences being that any phase shifts associated with wave transmission within the artery itself is not captured. This approach has been used and validated in a number of cardiovascular simulations including coronary (Zeng et al., 2003, Jeays et al., 2007, Zeng et al., 2008, Brown et al., 2012). Coronary segmentation was performed at end diastole since this is when maximal coronary flow occurs.

3.3.10.3 Distal boundary condition: modelling

In the context of vFFR modelling, neither flow nor pressure distal to the lesion are known. Because the inlet pressure condition can be known (as above) and the arterial wall is assumed to be rigid, model accuracy at the distal boundary represents a critical factor when predicting P_d and thus vFFR. This boundary represents the physiological behaviour of the coronary microvasculature (CMV), i.e. all the distal coronary vessels (arterioles, capillaries, venules and veins) which penetrate and drain the myocardium. It is possible to reduce the entire CMV compartment into a single, lumped-parameter, zero-dimensional, model which can be coupled to the distal outlet/s of the 3-D domain. In such models, flow, pressure, vascular compliance, viscous energy losses (Poiseuille law) and the inertial properties of flowing blood are represented as current, potential difference (voltage), capacitance, resistance and inductance in electrical analogue constructs. A limitation of zero-dimensional, lumped-parameter models is that the pressure and flow vary as a function of time but there is no concept of spatial variation within the compartment. The advantage is that it is possible to discretise the cardiovascular system into a number of lumped models according to the segmental arrangement of the cardiovascular system, in the form of a distributed model (Westerhof *et al.*, 2010). The Windkessel model has been used for over 100 years to represent compliant arterial physiology. Frank's two-element Windkessel comprised a resistance component (representing the smaller distal resistance vessels) and a capacitance component (representing elastic compliance of

the proximal larger arteries) arranged in parallel (Frank, 1899). This arrangement neglects the veins which are considered as 'far field' elements, at zero pressure. The arterial system is pulsatile, which is analogous to electrical alternating current (AC). The typical flow and pressure signals have a fundamental frequency of about 1 Hz (period 1 second), but higher frequency components, up to 10Hz and beyond, are significant. The simple two-element Windkessel model is known to perform poorly in the higher-frequency range (Wetterer, 1940) and this can be addressed by addition of a further resistance element (Z_c) arranged in series, forming the three-element, Z_c-C-R configuration representing the system impedance (Landes, 1943). The Z_c component represents the characteristic impedance, defined as the ratio of oscillatory pressure and flow when no reflected waves are present (unit: Ohms) (Nichols *et al*., 2011), with the sum of R and Z_c equal to the total systemic vascular resistance in the previous RC model. This improves higher frequency performance and has been widely used for cardiovascular simulation (Westerhof et al., 1969, Westerhof et al., 1971, Westerhof and Elzinga, 1991). Further elements can be added to the Windkessel model (Shi et al., 2011, van de Vosse and Stergiopulos, 2011) to improve particular characteristics of the performance, but of course each extra parameter needs to be tuned to represent the patient. Furthermore, all of these models are passive in that they represent the pressure/flow relationship into an elastic vessel, and there are special issues with respect to coronary flow, associated with pressurisation within the ventricle of the endocardial vessels and with the contraction of the ventricle causing the active squeezing of the intra-myocardial coronary vessels. This is discussed in the next paragraphs. Ultimately, the important test of the model is that it is able to reproduce adequately the measured responses of the system. For the current work the three-element Windkessel, modified to represent ventricular loads on the CMV, is shown, in Chapter 5, to have acceptable performance for the characterisation of the pressure/flow relationship in the distal coronary vasculature.
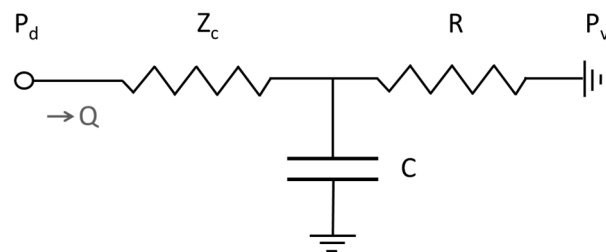
Figure 3.9. Three element Windkessel model.
Zero-dimensional, lumped parameter model used to represent the compliant and resistive properties of the CMV. P_d, pressures distal to stenosis; Z_c characteristic impedance; C, capacitance; R, resistance; P_v coronary venous pressure

The passive 3 element Windkessel model is unable to represent the dependency of the CMVR on the phase of the cardiac cycle; failing to capture realistic diastolic flow predominance – an acknowledged physiological phenomenon of coronary physiology. To this end, the compressive effects of ventricular systole on the CMV were represented by the addition of a dynamic 'backpressure' and thus a dynamic voltage was added to the distal side of the capacitor to drive flow from the coronary microvasculature into the larger coronary arteries and veins. Essentially this represents the loads imposed by the ventricle on endocardial and intra-myocardial coronary vessels. Other groups have described the adoption of a similar approach previously (Keijsers, 2012, Bessems, 2007). For the purpose of this model a backpressure function has been defined with a shape that is broadly representative of the temporal distribution of the ventricular pressure. There is a rise of pressure, followed by a plateau and then a reduction back to the ventricular filling pressure (taken to be zero). The function is smooth, with rise and fall both represented as a sigmoid shape. The model is described by four parameters, representing the amplitude, the period of pressure increase, the period of the plateau and the period of the decay. Thus the final model has seven parameters – two resistances, one compliance, and four representing the direct ventricular load.
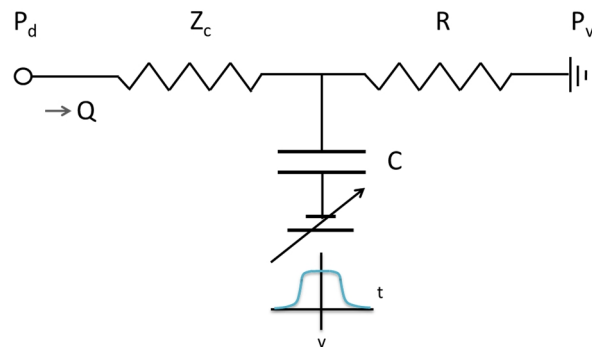
Figure 3.10. Modified (seven element) coronary Windkessel
*In this model, a time (t) dependent voltage (v) is applied to the capacitor in order to represent the rise and fall of intramyocardial pressure during systole and diastole. Other labels as in **Figure 3.9**.*

P_d is distal pressure (analogous to voltage), Q is flow, R_c is characteristic impedance, C is capacitance, R is resistance, P_v is the venous pressure, taken to be zero although any other value could be specified. Total resistance can be calculated by the ratio of mean P_d and mean Q. In **Figure 3.3**, the capacitor has a variable potential applied to the distal plate as shown.

3.3.10.4 Distal boundary condition; tuning

The physiological parameters of the CMV (total resistance in particular) are heterogeneous in both healthy and disease states (Meuwissen et al., 2001), and these directly influence FFR (Hoffman, 2000, Verhoeff et al., 2005). Therefore, the Windkessel model parameters should, ideally be tuned

on an individual patient basis to ensure accuracy on an individual case basis. Paradoxically, this requires knowledge of invasive measurements which we seek to avoid. There is no accepted scheme for deriving these parameters non-invasively. For this reason, in VIRTU-1 a generic set of parameters were applied based on averaged values derived from a sub-group of 6 RCA and 6 LCA cases. Initially, and as a starting point in the passive system (no active backpressure), the Windkessel parameters were derived using the following strategy:

1. The patient-specific coronary arterial volume mesh was simulated using *in vivo* measured pressure values as inlet and outlet boundary conditions (transient analysis)

2. The simulated pressure-flow relationship was extracted, as a function of time

3. Assuming that coronary venous pressure drains to zero, then Z_c + R (total resistance) was calculated from $\overline{P}_d / \overline{Q}$

4. C was calculated by matching the decay exponential to the diastolic distal pressure profile. The calculated exponent of the fit is equal to -1/RC (Stergiopulos et al., 1995).

5. Z_c is often considered as 0.1·R but it can be calculated explicitly from (fluid density)(wave speed)/area where wave speed is calculated from $(\Delta Q)/(\Delta A)$ where A is area (Westerhof et al., 2010, O'Rourke, 1982).

Unlike in other models, such as the aorta, this scheme was inappropriate for the coronary because, (i) there is no zero inlet flow phase and (ii) the addition of the active component (backpressure) means that the capacitance value and the distribution of resistances becomes dominated by the active squeeze phenomenon. Therefore, to tune the active model and derive values for the ventricular backpressure curve, an analytical solver representing the Windkessel model, was encoded in Matlab (by DRH) (MathWorks, UK). A manual optimisation process was then performed in order to identify the parameters which produced the best agreement (least squares (RMS) fit) between extracted flow and the flow solution calculated by the forward solver.

Table 2.1. Generic 0-D parameters

Parameter	RCA	LCA (main outlet)	LCA (minor outlet)
Passive (Windkessel)			
R_{total} (Pa.s/m^3)	3.29E+09	3.29E+09	5.21E+09
Active (backpressure)			
Ventricular amplitude (Pa)	4000	6000	6000
Ramp up*	0.20	0.20	0.20
Flat section*	0.25	0.25	0.25
Ramp down*	0.20	0.20	0.20

*RCA, right coronary artery; LCA, left coronary artery; R_{total}, total resistance; C, capacitance; Z_c, characteristic impedance. *as a fraction of the period. #
fraction Z_c of R_{total} (Z_c+R). All simulated over 5 cycles*

In the predictive model the seven-element Windkessel model was coded as an external function in User Fortran. The 3D-CFD model is coupled to the 0-D Windkessel model at each arterial outlet. In the implementation used for this pilot study, at the completion of each individual time-step the CFD solver (CFX) passes the computed outlet flow solution to the Windkessel function. The (analytical) Windkessel uses the flow solution to compute the corresponding pressure which is passed back to the 3-D solver where the value is used as the outlet pressure for the next iteration. This is known as explicit coupling. The generic parameters applied for all simulations in the pilot study are shown in **Table 2.1**:

3.4　Model validation

The VIRTU-1 model workflow was validated in a pilot study, against a clinical reference standard of invasively measured FFR. The aims of this section were to evaluate the diagnostic accuracy and precision of computed vFFR against invasively measured FFR in a population of patients with stable coronary disease and to investigate the feasibility of this approach as a potential tool for use in the cardiac catheter laboratory.

3.4.1.1　Study design and location

This was an observational, analytical study. Clinical data collection was performed at the South Yorkshire Cardiothoracic Centre, Northern General Hospital, Sheffield Teaching Hospitals NHS Foundation Trust, Sheffield, UK. Data analysis and workflow operation was performed within the Medical Physics Group, Department of Cardiovascular Science, UoS.

3.4.1.2　Ethics and governance

The VIRTU-1 study protocol and all supporting documentation and proformas were approved by the National Research Ethics Service (REC #08/H108/193) and by Sheffield Teaching Hospitals Research and Development board (STH15740)

3.4.1.3　Study population

Patients with known stable CAD were identified from elective PCI referrals from the South Yorkshire region (total catchment population: 1.8 million), to the two clinical operators (JPG and ACM) involved in the study. Patients were eligible if they were older than 18 years of age and had angiographically confirmed CAD, considered suitable for elective PCI. Referrals were screened and cases with relatively simple, native vessel disease consistent with the ACC/AHA classification of coronary lesions category of 'Type A' lesions (Maier et al., 2001) were selected. Exclusion

criteria were: serious comorbidity; previous MI; inability to provide informed consent; significant (>30%) left main stem disease; chronic total occlusion; acute presentation in the previous 60 days; intolerance of intravenous adenosine, nitrate or iodine based contrast media; previous coronary artery bypass graft (CABG) surgery or PCI; or were too obese for RoCA to be performed.

3.4.1.4   Recruitment and data collection

Patients received a letter of invitation and a patient information sheet by post prior to attending for their procedure. On the day of the procedure, the patient was counselled about the study and informed consent was gained. Clinical data regarding inclusion and exclusion criteria, age, gender, comorbid conditions, medication, height, weight, body mass index, smoking status were documented onto the data collection sheet. During the procedure, data were documented according to; coronary anatomy, details of angiographic and rotational runs, precisely when and where FFR was measured and the treatment delivered. SYNTAX (SYNergy between PCI with TAXus and cardiac surgery) scoring (Serruys et al., 2009) was performed and documented after the procedure.

3.4.1.5   Angiographic protocol

Angiography was performed using single axis RoCA, using the Allura XperSwing system (Philips, Best, NL) (Horisaki, 2008b) after iso-centering in posterior-anterior (PA) and lateral planes. Each RoCA acquisition recorded 21 images, at 12.5 frames per second in a standard 512 by 512 pixel matrix. For right coronary artery (RCA) cases image acquisition was from LAO 55° to RAO 55° **with** 25° **of** cranial tilt. For left coronary artery (LCA) cases, images were acquired from LAO 55°, RAO 55°, with both 25° of cranial and 25° degrees of caudal angulation. Intra-coronary glyceryl trinitrate (GTN) was administered immediately prior to RoCA. RoCA was performed during a breath-hold, with a hand injection of 15-20mls of contrast agent through a 6F guiding-catheter ensuring optimal vessel opacification. After the procedure, stenosis severity was assessed visually, and lesions were categorised according to percentage diameter stenosis (<30%, 30-70%, >70%). Other vessel characteristics were also documented at the time of angiography including the SYNTAX (SYNergy between PCI with TAXus and cardiac surgery) score (Serruys et al., 2009) and whether the target lesion was tortuous, was long or diffuse, or affected a bifurcation.

3.4.1.6   Invasive measurement of fractional flow reserve and percutaneous coronary intervention

All arteries with disease affecting ≥50% vessel diameter, judged by visual estimation, were interrogated with a pressure and (Doppler) flow sensitive ComboWire® XTPressure angioplasty wire using the ComboMap® Pressure and Flow System (Volcano Corp, Rancho Cordova,

California) (Volcano Corp, 2001). Hyperaemia was induced by an intravenous infusion of adenosine 140 mg/kg/min. Intracoronary pressure and (Doppler) flow were recorded throughout the study. FFR was measured in the diseased vessels according to the method described by Pijls and De Bruyne *et al* (Pijls et al., 1993, Pijls et al., 1995, Pijls et al., 2000). The position of the wire was recorded as an angiographic run each time a physiological measurement was taken. Stent implantation proceeded according to the operator's normal practice, based upon both the angiographic appearance and the FFR. If a stent was implanted, RoCA and physiological assessment were repeated.

3.4.1.7 Data management

Patient identifiable data were removed from the digital studies within the Xcelera viewing software (Philips, Best, NL), following which RoCA data were exported to the Philips XtraVision 3D-CA PC within the cardiac catheter laboratory. From here, the studies were exported onto DVD. Physiological data were archived from the ComboMap® transducer hard drive onto CD. Discs and datasheets were then transported to the computer research laboratory at the University of Sheffield for analysis.

3.4.1.8 Segmentation and reconstruction

Segmentation and reconstruction was performed using the custom PC built for the project by Philips fitted with the Philips XtraVision 3D-CA software. Two 2-D images are selected from the RoCA acquisition (121 in total). There must be $\geq 60°$ angle separation between the two projections and ideally, images should be chosen from the same phase of the cardiac cycle. A semi-automatic edge detection protocol is then used to delineate the luminal surface in both projections. The system co-registers these luminal segments and reconstructs an axi-symmetric luminal surface geometry in 3-D with a vessel centreline. Although this system is available commercially (integrated into catheter laboratory hardware), the bespoke prototype PC provided by Philips Healthcare was used since this supported export of the 3-D reconstructed arteries (including the un-closed surfaces and branch centre lines) in virtual reality modelling language (*.vrml) format.

3.4.1.9 Workflow operation and the computation of vFFR

The VRML file was imported into the workflow. VRML files were converted to VTK, the surfaces were closed and the centrelines of any branches were merged. The tolerance (in mm) was manually adapted to ensure successful merger of branches without inappropriately joining overlapping branches. Importantly, the branch-merging algorithm eliminated any internal projections (overlap) between the parent vessel and the branch. Landmarks along the centreline (known as the skeleton)

were selected and designated as the inlet and outlet boundaries. The vessel was then cut at these points and planes were inserted at each boundary, perpendicular to the skeleton. The surface was re-closed and the extracted surface defined the region to be modelled. The extracted surface was then spatially discretised using ICEM CFD v14.5 (ANSYS Inc, Canonsburg, USA) via the developed meshing plugin. A virtual tetrahedral mesh was fabricated within the extracted surface. The plugin enabled the global mesh, and surface vessel mesh element size (GMES and SVES) to be varied which directly influences the spatial refinement of the volumetric mesh. In this initial validation study, GMES and SVES edge lengths of 0.125 mm and 0.06 mm were chosen respectively. This yielded a mesh with between 1 and 1.5 million elements in all cases. In later work an improved mesh structure featuring prism layers at the wall boundary was developed, but the pilot study reported in this chapter used only tetrahedral elements.

In the predictive model, the patient-specific zero-dimensional parameters are unknown; so generic, averaged parameters were applied from a cohort of 6 RCA and 6 LCA cases. The proximal boundary condition was estimated using an average of the inlet (i.e. aortic) transient pressure (i.e. pressure as a function of time) waveform, measured via the coronary catheter for RCA and LCA cases (described in section 3.3.10.1). The transient pressure data were added (text file) as a function within ANSYS CFX Pre. Each of the distal outlets were coupled with a zero-dimensional, modified three-element Windkessel model as described in section 3.3.10.3. Windkessel elements were parameterised according to the method in section 3.3.10.4. This approach sacrifices vFFR accuracy compared with using individually tuned parameters, but demonstrates most effectively the predictive capability of the model with minimal personalized data. An *a posteriori* correction was also calculated in a subgroup, which incorporates the distal impedance as per the measured data. This provides an indication of the accuracy that would be achievable if the Windkessel parameters could, in future, be effectively personalised. The correction is based on the assumption that the distal impedance remains unchanged after revascularisation. The developed software automatically saves the meshed arterial geometry which was imported into into ANSYS-CFX Pre. Within ANSYS CFX Pre, the rheological properties of blood were defined and the time-step was defined. The target residual (i.e. a measure of the error by which the computed results at each timestep fail to satisfy the governing equations) was set to RMS 10 e^{-6}. **Table 3.1** outlines the definition file parameters applied.

The Windkessel was coded in User Fortran (by DR/DRH) and applied to the CFX file as a user routine, which had to be individually compiled prior to simulation. The definition file also had to be compiled before simulation. Simulation was performed using a Dell desktop PC using 4 cores. Solution stability was monitored using ANSYS CFX Solver Manager. ANSYS-CFX writes an

output file and a transients folder (containing all of the transient results) upon completion. A separate script file was written (by DR) in order to calculate the pressure and flow at the inlet and outlet, averaged over the cross-sectional area of the boundary (inlet or outlet/s). These transient data were exported into MS Excel, within which the data were divided into individual cycles and analysed. The vFFR was calculated from the ratio of mean outlet pressure (P_d) to mean inlet pressure (P_a) over the last period.

Table 3.1. Parameters used in the predictive simulation

Parameter	Value
Rheological properties of blood	
Blood viscosity	0.0035 Pa·s
Density	1066 kgm^{-3}
Time constraints	
Timestep (tstep)	Period /80ms
Timesteps per period	80
Total analysis time	241*timestep
Solution control	
Target residual	10 e^{-6}
Maximum iterations per timestep	100
Minimum iterations per timesep	2

3.4.1.10   Statistical analysis

Both measured and virtual FFR (mFFR and vFFR) data were dichotomised according to whether they were ≤ or > 0.80; the threshold of physiological significance. The ability of vFFR to predict whether mFFR was ≤ or > (i.e. the diagnostic accuracy of the workflow) was evaluated by calculating sensitivity, specificity, positive predictive value (PPV), negative predictive value (NPV) and overall accuracy. 95% confidence intervals for sensitivity, specificity, PPV and NPV were calculated using the exact binomial test (Harper and Reeves, 1999). Agreeability between mFFR and vFFR was assessed by calculating the bias (mean delta, vFFR-mFFR) and the standard deviation (SD) of the differences. A Bland-Altman plot was drawn (Bland and Altman, 1986) and the average absolute error was calculated. The correlation between vFFR and mFFR was assessed using Pearson's correlation coefficient (R).

3.5   Results

3.5.1.1   Patient and clinical characteristics

Twenty patients were recruited. One patient was subsequently found to have had a previous MI (NSTEMI: diagnosed on basis of chest pain and mild troponin rise) and was therefore excluded in

accordance with the exclusion criteria (section 3.4.1.3). Nineteen patients were therefore included in the final analysis. Baseline characteristics of the included patients are presented in **Table 3.2**. The mean age of the group was 64 (range 45 to 81) years. Twelve patients were male (63%). Sixteen patients had hypertension (84%), and 19 patients had treated hyperlipidemia (100%). One patient had type 2 diabetes mellitus (5%). None had prior stroke or peripheral vascular disease. Of the 19 patients included, 13 received PCI (6 LCA, seven RCA), and six patients had physiologically non-significant stenoses (four LCA, five RCA) that did not receive PCI. Three patients had stenoses in both the LCA and RCA. Therefore, the total number of datasets analysed in the study was 35 (two for each stent case [before and after intervention], one for each non-stent case, and three cases that included both RCA and LCA stenoses). **Table** 3.3 provides details of the lesion characteristics.

3.5.1.2   Computation.

Generic boundary conditions were applied in all cases. CFD solutions were successfully obtained in all 35 cases. The CFD simulation time was between 24 and 48 hours. The solution in eight cases was unstable at the default time-step (50 ms) and did not settle, even by the end of the first period. These cases were re-simulated at a reduced time-step of 10 ms which improved solution stability and convergence in all but two cases which required further time-step reduction down to 5 ms to ensure solution stability.

3.5.1.3   Diagnostic accuracy of vFFR

Lesions were stratified into two groups: those with an invasively measured FFR ≤ 0.80; and those with an FFR > 0.80. The computed vFFR was stratified in the same way, and the results were compared. There was a high level agreement between mFFR and vFFR. Diagnostic accuracy of vFFR was evaluated as follows; sensitivity 86% (95% CI : 0.48 to 0.97), specificity 100% (0.87 to 1.00), positive predictive value 100% (0.60 to 1.00), and negative predictive value 97% (0.82 to 0.99). The overall diagnostic accuracy was 97%. Applying the more stringent and more traditional threshold of physiological lesion significance for FFR (≤ 0.75) (see section X), the sensitivity was 71% (2 false negatives), specificity 100%, PPV 100%, NPV 93% and overall diagnostic accuracy 94%. **Table 3.4** and **Table 3.5** demonstrate the accuracy of vFFR based on dichotomised data.

Table 3.2. Baseline characteristics of the included patients

General demographics	
Mean age, years (range)	64 (45-81)
Male	12 (63)
Mean body-mass index	29
Comorbidities	
Hypertension	16 (84)
Hyperlipidaemia	19 (100)
Diabetes	1 (5)
Current smoker	4 (21)
Prior myocardial infarction	1 (5)
Stroke	0 (0)
Peripheral vascular disease	0 (0)
Medication	
Aspirin	17 (90)
Beta-blocker	15 (79)
Nitrate	3 (16)
Statins	19 (100)
ACE inhibitors	11 (58)
Calcium-channel blockers	6 (32)
Clopidogrel	19 (100)
ARBs	0 (0)

Values are mean (range) or n (%). ACE, angiotensin-converting enzyme; ARB, angiotensin receptor antagonist.

3.5.1.4   Quantitative accuracy of vFFR.

There was a strong correlation between vFFR and mFFR values (Pearson's correlation coefficient; $R = 0.84$) (**Figure 3.11**). However, correlation is no indicator of agreement, because it is possible to achieve 100% correlation with 0% agreement (see Chapter 6). A Bland-Altman plot is shown in **Figure 3.12**. Each individual mFFR is compared with its corresponding vFFR in **Figure 3.11**.

The quantitative accuracy of the workflow is described in **Table 3.6**. The mean difference (bias) between mFFR and vFFR was + 0.02 (SD 0.08). The average absolute error of vFFR, when compared with mFFR, was ± 0.06 (± 8.1%).

Table 3.3. VIRTU-1 lesion characteristics.

Patient	Dominance	Vessel	% diameter stenosis	Bifurcation	Tortuous	Long	Diffuse	SYNTAX	Stented
1	R	RCA	>70	N	N	N	N	2	Y
2	R	LAD	30 - 70	N	N	N	N	5	Y
3	R	LAD	30 - 70	N	N	Y	N	7	N
4	R	RCA	30 - 70	N	N	Y	N	3	N
5	R	LAD	>70	N	N	Y	N	9	Y
6	R	RCA	30 - 70	N	N	N	N	2	N
7	R	RCA	>70	N	Y	Y	Y	6	Y
8	R	LAD	30 - 70	N	N	N	N	7	N
9	R	LAD	30 - 70	N	N	N	N	7	Y
10	R	RCA	>70	N	N	Y	N	3	Y
11	R	LAD	30 - 70	N	N	N	N	7	Y
12	R	RCA	30 - 70	N	N	N	N	2	N
12	R	LAD	30 - 70	N	N	Y	N	5	Y
13	R	RCA	30 - 70	N	Y	N	N	4	Y
14	R	RCA	30 - 70	N	N	N	Y	6	N
15	R	LCX	30 - 70	N	N	N	N	3	Y
16	R	RCA	30 - 70	N	N	N	N	2	N
16	R	LAD	30 - 70	N	N	Y	N	8	N
17	R	LAD	30 - 70	Y	N	N	N	10	Y
18	R	LAD	30 - 70	N	N	N	N	7	N
19	R	RCA	>70	N	N	Y	N	3	Y
19	R	OM	>70	N	N	N	N	2	N

Percentage diameter stenosis was assessed visually. Values are n (%) unless stated otherwise. The average SYNTAX (SYNergy between PCI with TAXus and cardiac surgery) score of the vessels studied was 4.9. Twelve of the 22 vessels had a measured fractional flow reserve (FFR) > 0.80 and were not stented. LAD, left anterior descending artery; LCX, left circumflex artery; RCA, right coronary artery; OM, obtuse marginal; R, right; N, no; Y, yes.

3.5.1.5 Doppler flow

In the majority of cases, the ComboWire® XTPressure angioplasty wire did not return reliable flow velocity profiles during hyperaemia. The use of flow data in this study was therefore abandoned.

Table 3.4. True and false positives.

	vFFR ≤ 0.80	vFFR > 0.80	Total
mFFR ≤ 0.80	6	1	7
mFFR >0.80	0	28	28
Total	*6*	*29*	

Table 3.5. Diagnostic accuracy (all cases).

All cases	%	95% CI
Sensitivity	86%	0.48-0.97
Specificity	100%	0.87-1.0
Positive predictive value	100%	0.60-1
Negative predictive value	97%	0.82-0.99
Overall diagnostic accuracy	*97%*	
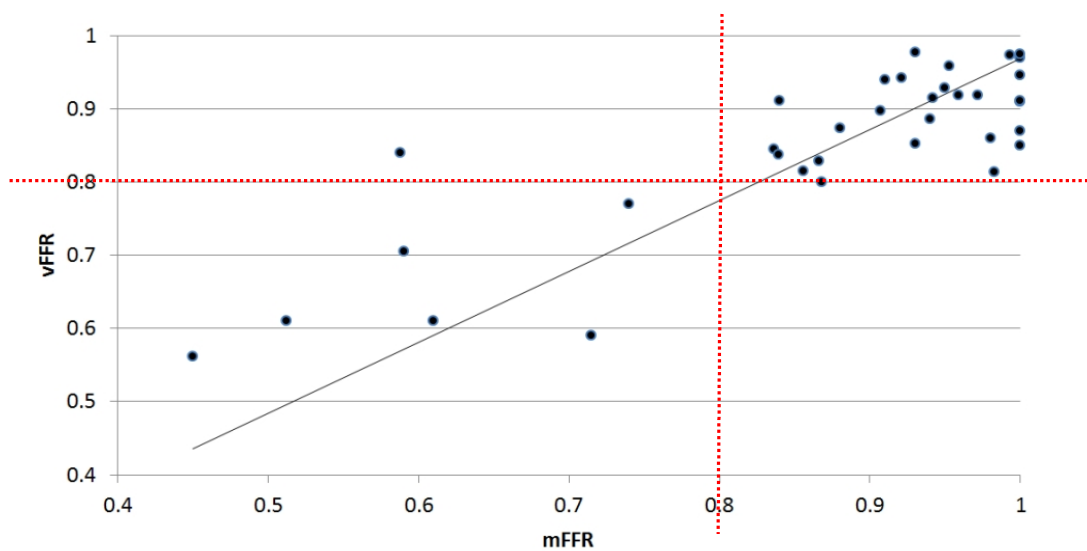
Figure 3.11. Measured FFR plotted against virtual FFR for all 35 datasets
Pearson's correlation coefficient (R) is 0.84. The grey line indicates the line of best fit for the correlation. The dotted red lines indicate the 0.80 threshold for intervention. From a treatment perspective, cases falling in the bottom left or top right quadrant are correctly categorised, whereas those in either of the other two quadrants are incorrectly categorised.
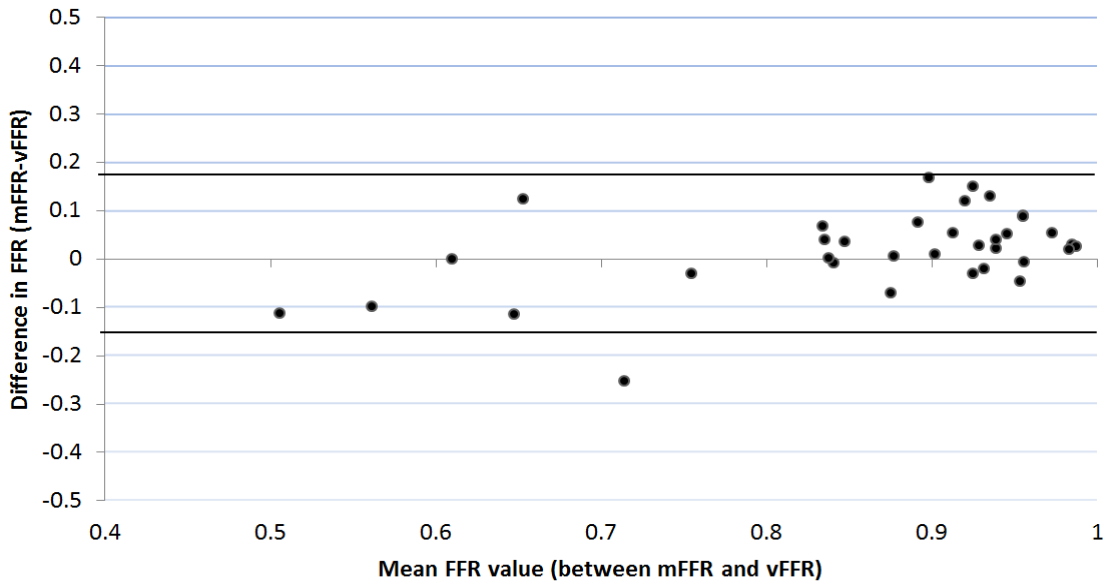
Figure 3.12. Bland Altman plot for all cases.

Dark lines represent the limits of agreement (mean ± 2 SD)

3.5.1.6   Sub-group analyses

Right versus left coronary cases

A typical RCA case, shown in the CFD workflow (ANSYS CFX Post, post-processing) environment, is demonstrated in **Figure 3.14**. For RCA cases the mean difference between vFFR and mFFR was + 0.03 (SD 0.08). The average absolute error of vFFR when compared with the mFFR was ± 0.07 (± 8.5%). A typical LCA case, shown in the CFD workflow environment, is demonstrated in **Figure 3.15**. For LCA cases the mean difference between vFFR and mFFR was + 0.01 (SD 0.09). The average absolute error of the vFFR when compared with the mFFR was ± 0.06 (± 7.8%).

Pre- versus post-PCI cases

To investigate whether accuracy was consistent across all values of FFR we compared the agreeability of vFFR and mFFR, excluding data from post-stent cases. This enabled us to focus on the cases with lower mFFR values, i.e. those of most clinical interest. There was a small non-significant increase (0.01) in the average absolute error, ± 0.07, p=0.41. **Table 3.6** summarises the accuracy of vFFR for all cases and for the subgroup analyses described immediately above.

A posteriori correction

This correction was applied to the pre- and post-PCI cases. The correction re-calculated the pressure distal to the lesion when individualised, patient specific Windkessel parameters were applied as calculated from simulation using the invasive pressure data as boundary conditions. The correction reduced the average absolute error from ± 0.070 to ± 0.035.

Table 3.6. Quantitative accuracy of vFFR: all cases and sub-group analysis.

Measure of quantitative accuracy of vFFR	RCA cases n = 16	LCA cases n = 20	Post-stent cases excluded n = 22	Total cases n = 35
Mean difference (bias)	0.03	0.01	0.01	0.02
Standard deviation	0.08	0.09	0.1	0.09
Average absolute error	± 0.07	± 0.06	± 0.07	± 0.06
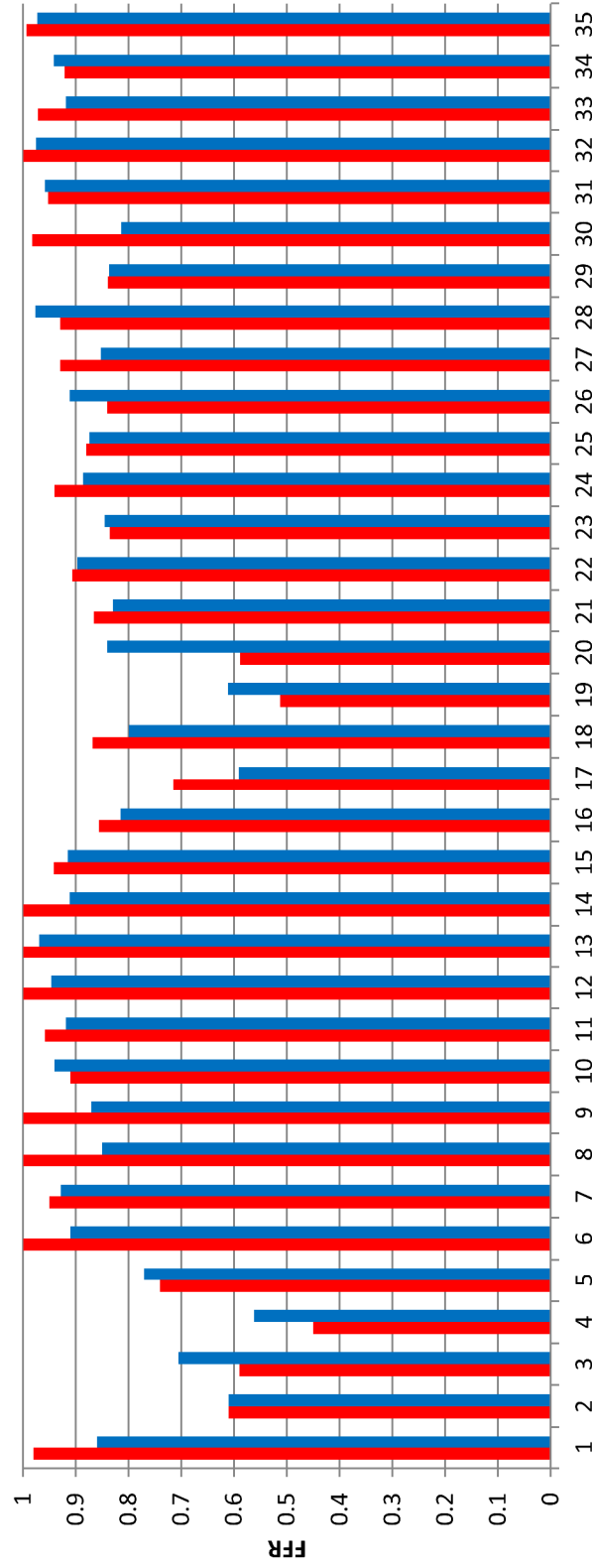
Figure 3.13. Measured fractional flow reserve (mFFR) (red) compared with virtual fractional flow reserve (vFFR) (blue). 1 – 15: RCA cases, 16 - 35 LCA cases.
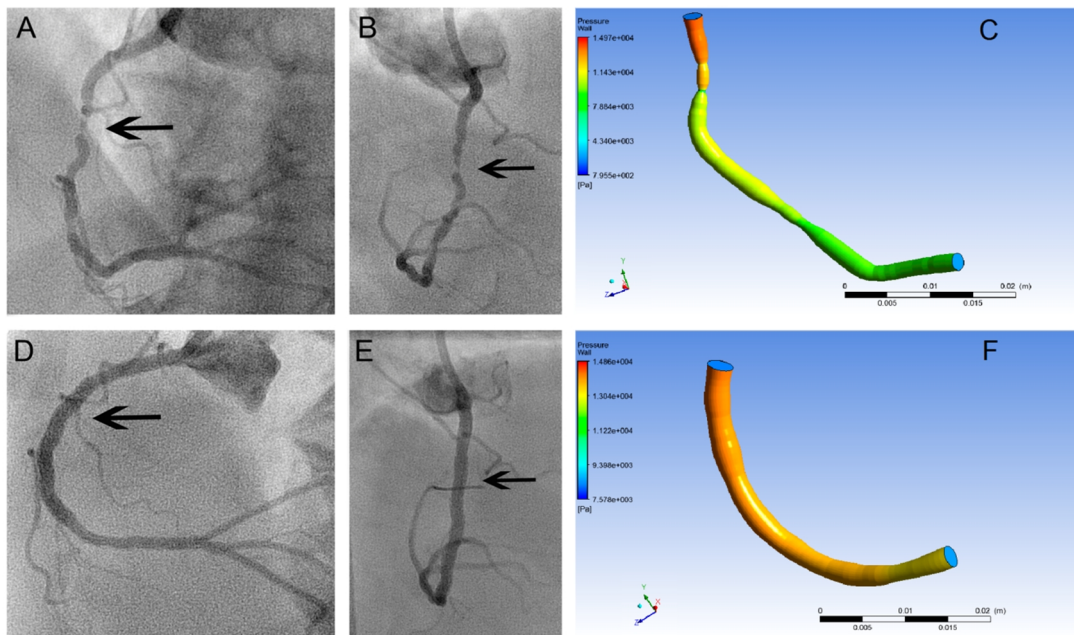
Figure 3.14. Example of vFFR in a right coronary artery case.

Images from Patient #10, a 63-year-old woman with chronic stable angina and a stenosis in the RCA. A single rotational angiogram was recorded with cranial tilt. (A and B) Single frames from that rotation, in the left anterior oblique (A) and right anterior oblique (B) projections. The arrows identify the stenosis. The baseline mFFR was 0.45. The angiographic data were processed for anatomic and physiological reconstruction, which is displayed in C. The colours represent pressure (Pa) according to the scale shown. The vFFR was 0.56. A 3*38 mm stent was implanted. The rotational angiogram was repeated, and the mFFR was 1.0. The corresponding images, taken from the post-implantation angiogram and the reconstruction, are shown in D, E, and F. The vFFR post-implantation was 0.91
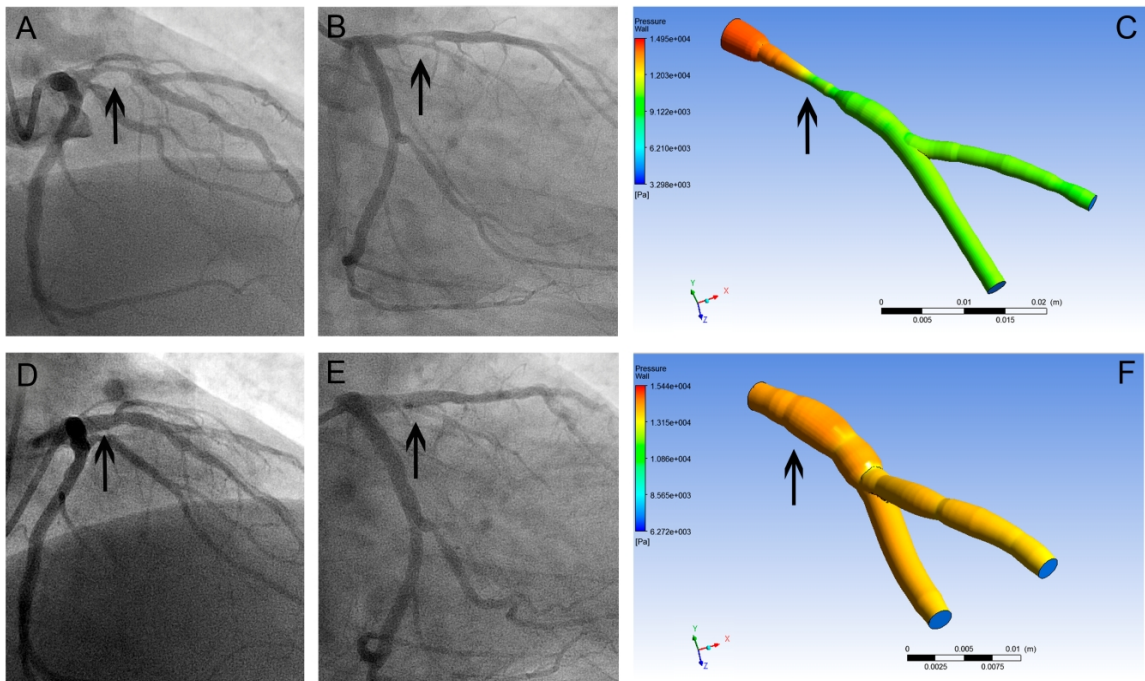
Figure 3.15. Example of vFFR in a left coronary artery case.

Images from Patient #11, a 50-year-old man with chronic stable angina and a stenosis in the proximal LAD artery. Two RoCAs were recorded, 1 with cranial, and the other with caudal tilt. (A and B) Single frames from the cranial rotation, in the posteroanterior (A) and right anterior oblique (B) projections. The arrows identify the stenosis. The baseline mFFR was 0.51. The angiographic data were processed for anatomic and physiological reconstruction, which is displayed in C. The colours represent pressure (Pa) according to the scale shown. The vFFR was 0.60. A 4*12 mm stent was implanted. The rotational angiogram was repeated, and the mFFR was 0.95. The corresponding images, taken from the post-implantation angiogram and the reconstruction, are shown in D, E, and F. The vFFR post-implantation was 0.96.

3.6   Discussion

The VIRTU-1 workflow demonstrated the feasibility of using the combination of image analysis and 3-D CFD modelling to predict clinically useful physiological measures within a diseased coronary circulation solely from angiographic images. The workflow has been developed to create a simplified, 3-D virtual coronary tree from a single RoCA. With a CFD solver, and with generic boundary conditions, the pressure and flow solution are calculated. The results enable assessment of 1 or more stenoses *in silico*. The vFFR values agree well with the measured values, with an overall average deviation from the measured values of ± 0.06. Lesions requiring PCI (mFFR <0.80) were identified from non-significant lesions (mFFR >0.80) with 97% accuracy. This level of accuracy is excellent considering the small number of patients in this study. Furthermore, the coefficient of variation of mFFR itself is reported as $\pm 4.8\%$ (de Bruyne et al., 1996).

3.6.1.1   Advantages of modelled physiology

There are several advantages offered by using physiological measures derived from our CFD workflow. The model only requires knowledge of vessel geometry. There is no need for the induction of hyperaemic flow, additional procedure time, the inconvenience (or hazard) of passing an intracoronary wire, or additional equipment, training, or cost i.e. all factors which have limited uptake of the invasive FFR technique. A computational tool such as this would therefore improve operator and patient access to physiologically guided decision making with potential impact on clinical outcomes and cost. A further advantage of vFFR is that the effects of multiple lesions or, indeed, collateral vessels can be included in the simulation. Moreover, this technique is able to provide a pressure (and flow) solution at point within the modelled region in a single analysis which is superior to the invasive technique which provides a single-point FFR unless a pullback procedure is performed. Finally, *in silico* techniques enable the virtual arterial geometry to be manipulated in order to simulate stenting. Virtual stenting provides a means by which the physiological impact of various PCI strategies can be simulated and predicted thus enabling the optimal strategy (which balances the maximum physiological result for least intervention) to be selected prior to delivery of treatment *in vivo*.

3.6.1.2   Comparison with FFR_{CT}.

Papers by Koo, Min and Nakazato et al. (Min et al., 2012, Koo et al., 2011a, Nakazato et al., 2013) report the calculation of FFR from CCTA. Both the CCTA and this angiographic study succeed in inferring the physiological significance of coronary lesions by applying CFD to reconstructed cardiovascular anatomy. There are similarities in how this is achieved. Both approaches apply a

lumped parameter model at vessel branches, and both model blood as a Newtonian fluid with the incompressible Navier Stokes equations. However, unlike vFFR$_{CT}$, VIRTU-1 relies on vessel geometry alone from ICA and does not involve an estimation of myocardial mass from CT. Furthermore, the results of this study appear more accurate than those reported in these articles. However, it is important to note that whilst the greater accuracy of these results may reflect the superior resolution of ICA over CCTA it may simply be related to the small patient cohort in the current study. Koo et al. describe the DISCOVER-FLOW (Diagnosis of Ischemia-Causing Stenoses Obtained Via Noninvasive Fractional Flow Reserve) study as being based upon three key principles: 1) as patients with rest angina were excluded in their study, coronary supply met myocardial demand at rest, enabling calculation of total resting coronary flow relative to ventricular mass; 2) resistance of the microcirculation at rest is inversely, but not linearly, proportional to the size of the feeding vessel; and 3) microcirculation reacts predictably to maximal hyperaemic conditions in patients with normal coronary flow. An explicit comparison of the current method with theirs is not possible, since precise details of their simulation and the parameters used to inform their model are not disclosed. Disadvantages of vFFR$_{CT}$ include the requirement for a separate test (many patients will require ICA anyway), and that CTCA overestimates lesion severity in calcific CAD and is limited in those with irregular heart rhythm, tachycardia or motion artefact. Ultimately, just as CTCA and ICA serve different purposes in different populations, vFFR$_{CT}$, which is useful in low-moderate risk patients and vFFR$_{ICA}$, which is useful in guiding directly interventional management, should be regarded as complementary rather than competing technologies.

3.6.1.3 Comparison with other studies

Other investigators have attempted to predict the physiological significance of CAD from luminal geometry. Quantitative coronary angiography, intravascular ultrasound (IVUS) and, more recently, optical coherence tomography (OCT) have all been used to predict indexes of intracoronary physiology but with disappointing results (Koo et al., 2011b, Ben-Dor et al., 2011, Gonzalo et al., 2012). Gonzalo *et al* compared the use of OCT and IVUS in predicting an FFR of<0.8. There was no significant difference between OCT and IVUS, and diagnostic accuracy was described as "modest" (sensitivity 82%, specificity 63%). Rather than applying simplified haemodynamic laws such as the Poiseuille drop and statistical regression techniques to measures, such as minimum lumen diameter, minimum lesion area, or lesion length (or combinations of these), the current methodology employs 3-D CFD which better characterises the complexity of 3-D flow. Similar to previous studies, the current method requires geometric knowledge of the vessel. However, vFFR uses the segmented geometry of the diseased artery, employs generic boundary conditions (on the basis of multiple arterial resistance and compliance measurements and a Windkessel model), and solves the 3-D unsteady Navier-Stokes and continuity equations (CFD) for multiple heart cycles.

This gives a fuller physical picture of the time-varying pressure and flow velocity profiles in the artery. Calculations also include assumptions with regard to the upstream pressure and downstream resistance and compliance, transiently, over a full heart cycle.

3.6.1.4 Doppler flow velocity

In the majority of cases, the ComboWire® XTPressure angioplasty Doppler wire did not provide reliable signal (as interpreted by the primary operator) and had to be abandoned. However, this issue is widely reported by interventionalists and explains the low clinical uptake of Doppler wires relative to pressure wires. The limitations of the Doppler wire are further explored in Chapter 6.

3.7   Methodological challenges and limitations

3.7.1.1 Study limitations

The number of cases included in this preliminary study was modest, and deliberately prioritised simple lesions in stable patients for this proof-of-concept study. Therefore the results were hypothesis-generating. The high level of diagnostic accuracy obtained for this small sample of 35 datasets may have included an element of serendipity. Nevertheless, the results were encouraging, and the data sufficient to warrant further investigation. Although the majority of lesions were intermediate by visual assessment, (**Table 3.3**), only a limited subgroup of cases (n = 9) had an mFFR falling between 0.70 and 0.90, the range that is of greatest clinical interest, representing the lesions which cause most doubt regarding the need for intervention. This was unfortunate given the unbiased patient selection, but further supports the fact that physiology cannot be inferred from visual angiographic analysis alone.

3.7.1.2 Methodological challenges

A major limitation of the method, at this point, was the time required to compute a result (24-48 hrs). 99% of this time was dedicated to CFD simulation. It was clear that this had to be improved in order to make the workflow viable as a clinical tool. The workflow required significant computational expertise (i.e. a PhD student or computer scientist) to operate and involved five separate programs. Systems instability lead to frequent crashes with associated loss of processed data. A typical analysis (without crashing) took approximately 5-10 minutes to segment and reconstruct (Philips), 10 minutes to prepare (GIMIAS), 5-10 minutes to mesh (ICEM via GIMIAS), 10 minutes to set up the simulation (ANSYS ± ssh client), 24-48 hours to run the simulation (ANSYS) and 15 minutes to post process the result. Clearly, this process required significant

rationalisation and development before the workflow can be deployed as a clinical tool, for example, in a clinical trial. CFD is accurate, and its use is well established for a wide range of safety-critical industrial applications. The precision of the VIRTUheart™ model is therefore dependent upon two main factors: accuracy of the segmentation and application of boundary conditions. Both areas require further development.

The image segmentation and reconstruction software used in this study (Philips) was associated with numerous procedural, methodological, and even commercial challenges. Procedurally, compared with standard angiography, RoCA was associated with:

· procedure prolongation due to protracted patient set up – necessary to avoid frequent proximity alarm activations which terminates image acquisition

· achieving good opacification throughout the entire acquisition

· default caudal and cranial angulation settings (25°) compromise and constrain the quality of the images, relative to standard angiography

Moreover, the hardware and software required to perform RoCA is available in only a minority of centres in the UK and even fewer globally. If VIRTUheart™ is to be used more widely, reliance upon RoCA will limit the potential applicability and commercial viability of the VIRTUheart™ system.

Vessel reconstruction is also currently inadequate as a clinical tool. As mentioned previously, coronary segmentation is inherently challenging due to cardiac motion and the small length scales involved within the coronary stenoses. When the project started, the Philips system was the only proprietary system which segmented and reconstructed coronary arterial luminal surfaces. However, the VIRTU-1 study identified numerous limitations of the technique. First, only two images are used for reconstruction from a possible 121. This means that, not only is the majority of data discarded, but the system generates an axisymmetric geometry and any eccentricity of plaque within the luminal circumference ignored. Although the Philips system requires both images to be from the same cardiac phase (end diastole) in order to eliminate potential artefacts introduced by the beating heart, not all patients are able to achieve breath hold, thus the heart moves with ventilation. There is no correction for this. Third, it was observed that during the first and last 20% of the 3 second acquisition the vessel lumen was poorly opacified, relative to the middle 60%. This is important because the quality of the reconstruction is influenced by the angle of separation between the two selected images used which is constrained if the first and last images are sub-optimally opacified. Fourth, choice of images is significantly constrained. This is because images must be selected from the same cardiac phase and RoCA is completed within three seconds.

Therefore, there are only ever 2-4 segments of the acquisition that can be used. In short, there are conflicting priorities when selecting the two images for segmentation. Major priorities include ensuring; good opacification, minimal overlap (difficult with fixed RoCA caudal-cranial angulation), minimal foreshortening, that the stenosis is clearly seen, and that images are from the same cardiac phase. Given the rapidity of the rotation and the limited number of cardiac cycles recorded, satisfying even two of these criteria was a challenge, and any more was impossible. Finally, one projection image cannot identify the 3-D co-ordinates of a point: its location must be identified in two images. An epipolar line is the line in a second projection image on which a point identified in a first projection image must lie. Errors were introduced when segmentation of the second image proceeded parallel (or close to parallel) to the epipolar line from the former image. This is understandable and logical but was impossible to avoid, particularly in the context of RCA cases since course of the RCA deviates through approximately 180°. It is therefore impossible to maintain perpendicular epipolar lines through the entire course when segmenting from just two images. All these issues are being resolved in work carried out in parallel to the current project but are beyond the scope of the current thesis (Cimen et al., 2014).

It is clear that the microcirculatory impedance presents a significant challenge. FFR represents the fraction of the normal maximal myocardial flow that can be achieved despite the epicardial stenosis. Alterations in the resistance or impedance of the downstream CMV limit the rise in hyperaemic blood flow and restrict the corresponding pressure drop distal to the stenosis in the epicardial artery (Pijls et al., 1996, Hoffman, 2000, De Bruyne et al., 1995). The developed model makes universal assumptions about the downstream resistance applying a "one-size fits all" approach. Consequently, in cases with abnormally high CMVR, or when maximal hyperaemia has not been achieved, the vFFR will overestimate lesion significance whereas, in cases with abnormally low CMVR, vFFR will underestimate physiological lesion significance. If deployed clinically, this risks unnecessary revascularisation, or inappropriate deferral of treatment. It is recognized that mFFR might be less reliable in cases with microvascular damage, and an important future challenge is to represent this in the model, with patient information to inform the distal resistance model. The reduction in error observed when the *a posteriori* correction was applied suggests that a better appreciation of the factors governing the coronary microcirculatory resistance, on an individual patient basis may, in the future, enable improvements to be made to the tuning of the distal Windkessel. This is likely to result in an even closer estimation of mFFR and is the focus of Chapter 5.
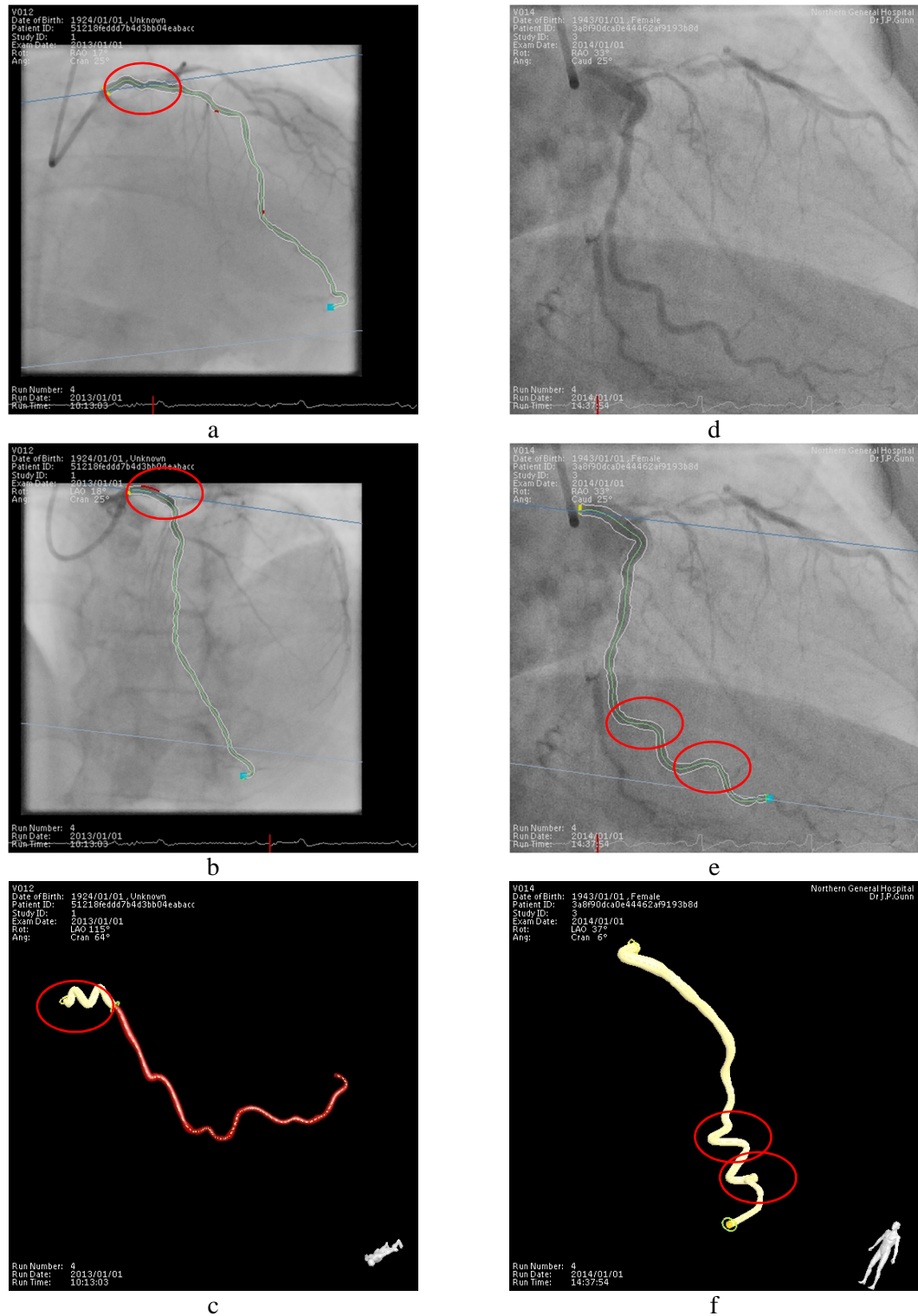
***Figure 3.16. Examples of errors introduced when epipolar lines are approximately parallel to the
local vessel centreline***
*In the left column, two images (a and b) are selected for segmentation and reconstruction (c). The
left main stem falls almost parallel to the epipolar (blue) lines. This introduces artefact in the final
model (c) in this region. The right column (d, e and f) demonstrates the same phenomenon in a distal
LAD.*

106

3.8   Conclusions and subsequent work

The developed workflow uses images from a RoCA, segments and reconstructs the luminal surface, meshes and applies 3-D CFD analysis, and calculates vFFR to identify physiologically significant coronary lesions with 97% accuracy. The model quantifies FFR with an accuracy of $\pm$ 0.06 on average. This is the first *in vivo* study to report such accurate CFD-based measurements within the coronary circulation. The potential advantages of this approach justify further investigation and development. Subsequent sections of this thesis focus on optimising the accuracy, speed and usability of the model with greater patient numbers and with more complex cases.

Further work will focus on the major limitations of the technique which are fivefold. First; the workflow operates too slowly for use in the cardiac catheter laboratory where results are needed quickly in order to guide treatment decisions. This limitation is dealt with in the following chapter (Chapter 4). Second; the use of generic boundary conditions limits accuracy in patients whose coronary microvascular impedance diverges from the average value applied. This risks unnecessary intervention when the impedance is underestimated and inappropriate not intervening if the impedance is over-estimated. A strategy for circumventing this problem is described in Chapter 5. Third; the method of segmentation is key to accuracy. Significant limitations have been identified with use of the Philips system deployed in this study. Although, the development of an alternative segmentation and reconstruction method is beyond the scope of the current thesis, collaborative work performed in parallel has provided two alternative methods which are resolving the issues raised above. Fourth; the CFD calculations of flow are impossible to validate due to the absence of an adequate Gold Standard. Chapter 6 investigates this further and describes an experimental model suitable for this purpose. Fifth; the current workflow is unstable with frequent crashes. Furthermore, it involves expertise in using five separate programs. A graphical user interface (GUI) is needed to streamline the workflow to make it easier to use without losing functionality. GUI development is described in Chapter 5.

Chapter Four:
System Acceleration

4.1   Introduction

VIRTU-1 demonstrated the feasibility of computing coronary physiology from coronary angiography despite relatively crude methods of segmentation, reconstruction, boundary condition application and meshing. It is important that the generated result is not dependent upon simulation run time, nor the refinement of the spatial discretisation process. It is also important to ensure that the run time and mesh refinement are not unnecessarily long, nor overly refined because this prolongs simulation time beyond what is necessary. This chapter, includes a sensitivity analysis to ensure an asymptotic result for the least appropriate computation time. In VIRTU-1, the time

taken to compute results ranged from 24 to 48 hours, and 99% of this time was taken up by CFD analysis. This is far from apposite for a clinical tool where speed is proportional to clinical applicability. Measuring FFR invasively during angiography takes a minimum of an extra10 minutes in most cases and this is reported as a contributory factor for the current under-use of FFR, even in the context of PCI (Morris et al., 2015b). Whilst a tool which takes c24 hours to compute may be acceptable for an outpatient test, such as CTCA, it is not for suitable for an invasive test such as ICA because decisions regarding revascularisation therapy are often made during ICA. For practical reasons, a vFFR tool should ideally compute a result within the period which allows decisions to be made while the patient remains on the angiography table. In practical terms this would be approximately 5-10 minutes. Real-time, or close to real-time, on-table results are therefore the standard to which to aspire if clinical applicability of vFFR is to be maximised. System acceleration is therefore a key priority. The aims of this chapter were to:

1. Optimise the mesh and CFD solution to ensure an asymptotic solution;

2. Explore, and investigate, methods for accelerating VIRTUheart™ solution time;

3. Develop and validate a method which accelerates VIRTUheart™ to within a tractable timescale for use in the cardiac catheterisation laboratory i.e. an accurate result in ≤ 10 minutes.

4.2 Mesh sensitivity analysis

Haemodynamic models of the cardiovascular system require relatively complex, refined volumetric meshes. In addition to capturing the key geometric features (via segmentation and reconstruction), it is important that the design, and refinement, of the fabricated mesh is appropriate for capturing the haemodynamic behaviour and physiology of the vascular compartment being simulated (flow and pressure fields) at the required length-scales. The fully converged result should be independent of the operator-dependent meshing parameters selected. Highly refined meshes with increased element density result in more accurate results, especially in regions with high pressure and flow gradients (stenoses) but simulation times are increased. Conversely, coarser meshes compute quickly but may not capture fully the haemodynamics thus generating an inaccurate result. There comes a point where further increasing mesh refinement sacrifices computational speed without significant additional increase in accuracy; there is a trade-off between mesh refinement and speed of computation. For this reason, it is beneficial to perform a mesh sensitivity analysis in order to identify the minimal degree of mesh refinement associated with an acceptable level of accuracy so as to avoid the redundancy of excessive mesh refinement. Mesh refinement does not necessarily have to be homogeneous throughout the domain. Fluid velocity decreases non-linearly from the luminal centre, towards the wall due to viscous friction.

In no-slip simulations, the velocity immediately adjacent to the wall is zero with the largest velocity gradients within regions closest to the wall. Boundary (or wall) inflation layers can be designed and implemented so that thinner elements (usually prisms) close to the wall can accurately capture these gradients.

4.2.1 Method

The most challenging cases are those with the greatest pressure and flow gradients, i.e. those with the tightest stenoses. In Chapter 3, the most severe arterial stenosis was case 15, pre-PCI (FFR = 0.36). This case was therefore selected to perform the mesh sensitivity analysis. The meshes were constructed in ANSYS ICEM (ANSYS, Canonsburg, PA, USA) by means of a parameterised script file as discussed previously.

4.2.1.1 Tetrahedral elements

In Chapter 3, a homogenous tetrahedral mesh (without boundary prism layers) with a surface volume element size (SVES) of 0.125mm and global mesh element size (GMES) of 0.06mm was used (LaDisa et al., 2003, Shrestha, 2010). This produced a 1-1.5 million element mesh in all cases. In this analysis, the same GMES and SVES parameters were used as the starting point and a purely tetrahedral mesh (without prisms) was evaluated. Relative to the starting point, the GMES, and then the SVES, were reduced to 50% (halved) and then increased to 200% (doubled). The effects of this on the number of elements, simulation wall clock time, and whether the pressure results were asymptotic were recorded over 40 periods (i.e. 40 cardiac cycles), transient, 3-D CFD analysis.

4.2.1.2 Tetrahedral elements with prism layers activated

Tetrahedral elements are inefficient for capturing and resolving the physical solution at the boundary whereas prisms better resolve the physics perpendicular to the boundary wall where the viscous blood and the vessel wall come into contact. Activating prism layers generates thinner (prism) elements adjacent to the wall surface allowing more calculations per unit distance and is, therefore, more efficient and realistic resolution of the surface numerics, without increasing the total number of surface elements. This produces a more accurate, realistic, and quicker solution, without the need for a very fine tetrahedral mesh (ANSYS Inc, 2011). Prism layers were activated. The chosen starting parameters were: growth law, exponential; initial height, 0.01625mm; height ratio, 1.2; layers, 10; giving a total height of 0.422mm. The GMES was then reduced to 75% and increased to 125% relative to the starting point. The SVES was reduced to 75% and 62.5% (i.e. a

further 75% reduction) and increased (relative to the starting point) to 125% and to 162.5% (i.e. a further 25% increase).

4.2.1.3   Prism layers

Within ANSYS ICEM it is possible to manipulate the growth law (exponential or linear), initial height, height ratio and number of layers of prisms. The number of layers was varied and the effect on: the number of elements; simulation wall clock time; and the point at which the pressure and FFR solution became asymptotic were recorded. Simulations were run for 40 cardiac cycles to ensure that the asymptote was reached.

4.2.2   Results

4.2.2.1   Tetrahedral mesh

The results of this experiment (see **Table 4.1**) show that, for a purely tetrahedral mesh, the finer the mesh the better the convergence of the FFR solution. The solution converges towards the asymptote from above. Complete mesh independency was not achieved with a homogeneous tetrahedral mesh, and for this reason, prism layers were activated.

4.2.2.2   With Prism layers

The results of the second analysis are presented in **Table 4.2**. Once prism layers are activated, the solutions converged from below. In addition, the asymptote was reached, and the GMES, SVES and prism parameters chosen as the reference appear to be converged and can be considered reliable.

Table 4.1. Tetrahedral mesh evaluation.

	Start	**Varying GMES**		**Varying SVES**	
Alteration	Reference	50% GMES	200% GMES	50% SVES	200% SVES
GMES (mm)	0.25	0.125	0.5	0.25	0.25
SVES (mm)	0.125	0.125	0.125	0.0625	0.25
Elements (n)	$6.91 \times 10^{5*}$	2.12×10^6	6.32×10^5	2.76×10^6	2.65×10^5
Distal Pressure (Pa)	3915	3820	3871	2884	4595
FFR	0.350	0.342	0.346	0.270	0.411
Time (min)	2549	4739	2348	7221	599
Time (days)	1.77	3.29	1.63	5.01	0.42

*Coupled analysis with a specified proximal pressure and a distal Windkessel. GMES, global mesh element size; SVES, surface vessel element size. *Nodes in the reference mesh = 141687.*
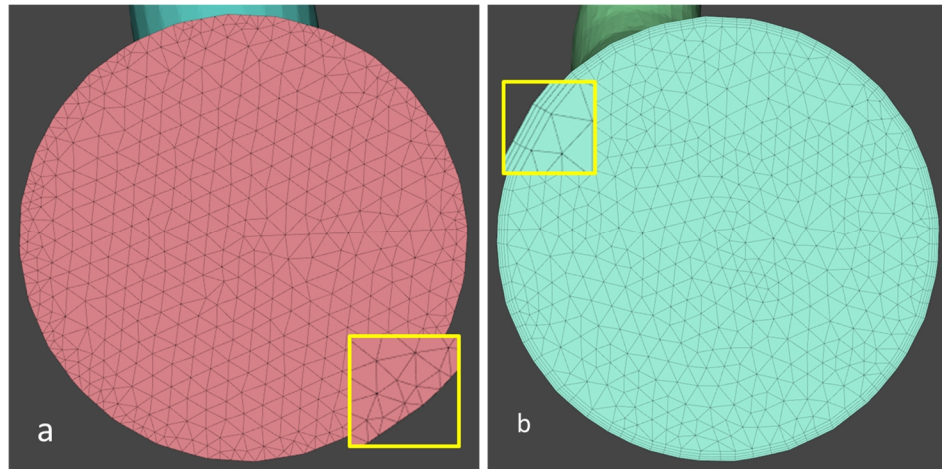
Figure 4.1. Examples of the mesh arrangement at the inlet boundary.

(a) demonstrates a purely tetrahedral mesh and (b) demonstrates a tetrahedral mesh with prism layers at the wall. The yellow boxes are a 'zoom in' to emphasise the wall.

Table 4.2. Varying the GMES and SVES with prism layers activated.

	Start	Varying GMES		Varying SVES			
Alteration	Reference	75%	125%	75%	56.25%	125%	156.25%
GMES (mm)	0.25	0.1875	0.3125	0.25	0.25	0.25	0.25
SVES (mm)	0.125	0.125	0.125	0.09375	0.070313	0.15625	0.195313
Initial Height (mm)	0.016	0.016	0.016	0.016	0.016	0.016	0.016
Height ratio	1.2	1.2	1.2	1.2	1.2	1.2	1.2
Layers (n)	10	10	10	10	10	10	10
Total Height (mm)	0.422	0.422	0.422	0.422	0.422	0.422	0.422
Tetrahedra (n)	309550	1052602	310099	674827	1381938	557375	294336
Prisms (n)	9.97×10^5	10.0×10^5	9.96×10^5	1.77×10^6	3.15×10^6	6.40×10^5	4.10×10^5
Elements (n)	1.3×10^6	2.1×10^6	1.3×10^6	2.4×10^6	4.5×10^6	1.2×10^6	0.7×10^6
Distal Pressure (Pa)	2603	2618	2608	2639	2636	2598	2507
FFR	0.2339	0.2343	0.2335	0.2362	0.2359	0.2325	0.2244
Time (mins)	5882	8400	4680	9555	11670	2399	1230
Time (days)	4.08	5.83	3.25	6.64	8.10	1.67	0.85

GMES, global mesh element size; SVES, surface vessel element size

4.2.2.2.1   Prism Elements

In the final stage of this analysis, the prism layer parameters were manipulated to understand the influence upon the computation time and results. Results are demonstrated in **Table 4.3**.

Table 4.3. Evaluation of prism layers

	Start	**Reducing prism layers**		
Alteration	**Reference**	**5 layers**	**4 layers**	**3 layers**
GMES (mm)	0.25	0.25	0.3125	0.3125
SVES (mm)	0.125	0.125	0.195313	0.195313
Initial height (mm)	0.01625	0.01625	0.01625	0.01625
Height ratio	1.2	1.2	1.2	1.2
Layers (n)	*10*	*5*	*4*	*3*
Total height (mm)	0.422	0.121	0.097	0.059
Tetrahedra (n)	309550	462171	535037	554519
Prisms (n)	996851	499045	164192	123144
Elements (n)	1.31×10^6	9.6×10^5	7.0×10^5	6.8×10^5
Distal Pressure (Pa)	2603	2639	2571	2650
FFR	0.233	0.236	0.230	0.237
Time (min)	5882	2189	988	928
Time (days)	4.09	1.52	0.69	0.64

GMES, global mesh element size; SVES, surface volume element size

4.2.3   Conclusion

On the basis of the analysis, the following mesh parameters were deemed to provide a reasonable balance between execution time and accuracy of computation: GMES, 0.3125; SVES, 0.195313; type, exponential; initial height, 0.01625; ratio, 1.2; layers, 4; total height, 0.08723.

4.3   Number of simulated cardiac cycles

The nature of the fully transient 3-D CFD solution (with coupled Windkessel) is such that as successive cardiac cycles are simulated the, global solution approaches, or converges, towards the final result, i.e. the solution is approached in a time-dependent manner. If the solution is plotted as a function of time, an exponential shape is observed. Therefore, it is essential that solution

simulation continues until the asymptote is reached, i.e. the point at which the curve towards convergence approaches linear and the solution space is flat. At this point, further simulation yields no significant improvement and the result is considered independent of the solution time. VIRTU-1 arbitrarily simulated physiological dynamics over ten cardiac cycles. It is observed that cases with more severe stenosis cases take longer to converge than those with mild stenoses. It is important that the final result, which is expected to be periodic, is not polluted by a dependence on the initial conditions.

4.3.1.1   Method

Four cases were selected to assess the effect of lesion severity on the number of simulated cycles required to reach the asymptote. The cases chosen represented a range of severities including: severe (vFFR = 0.36), significant (vFFR = 0.61), borderline (vFFR = 0.81), and mild stenosis (vFFR = 0.90). Each case was run for 40 cycles. The asymptote was determined stringently as the point at which there was a difference of $< 5\ e^{-5}$ between the FFR solution for two successive cardiac cycles. In addition, a less stringent, more pragmatic approach was taken which defined the point at which the time of simulation no longer affected the FFR. This was taken as the point at which there was a difference of $< 4\ e^{-3}$ between the FFR solution for two successive cardiac cycles.

4.3.1.2   Results

Table 4.1 summarises the number of periods the simulation needed to run before reaching the asymptotic result. To reach the asymptote, the severe case (vFFR = 0.36) took 25 periods, the significant case (vFFR = 0.61) 23 periods, the borderline case (vFFR = 0.81) 21 cycles, and the mild case (vFFR = 0.90) 19 cycles to reach the asymptote. At the less stringent level of defining the asymptote, the severe case took 17 periods, significant 14, borderline lesion 13 cycles and the mild lesion 11 periods. **Figure 4.3** demonstrates the convergence of the severe case. The longest total simulation time was the severe case (vFFR = 0.35) at 79 hours.

Table 4.4. The number of periods taken to reach the asymptote

Case	FFR	N cycles (delta $5\ e^{-5}$)	N cycles (delta $4e^{-3}$)
Severe	0.35	25	17
Significant	0.61	22	14
Borderline	0.81	21	13
Mild	0.89	19	11

N cycles indicates the number of periods taken to reach the asymptotic result according to the delta criteria, between successive cycles.

For both thresholds, the FFR was plotted against the number of cardiac cycles taken for the simulation to reach the asymptote. The line of best fit (linear) reflects the number of simulated periods required to reach the asymptote for a given FFR (see **Figure 4.2**).
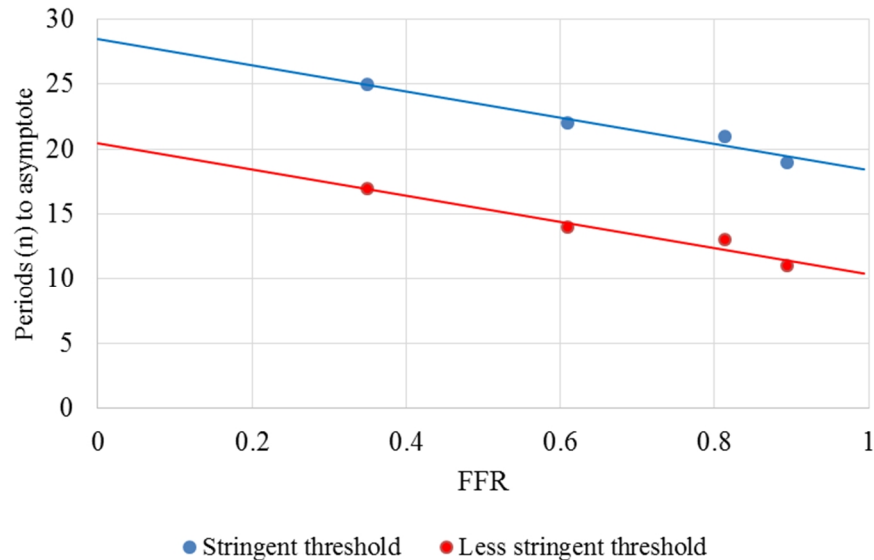
Figure 4.2. Number of periods to reach asymptote with extrapolated line of best fit.

4.3.2 Conclusion

In the current analysis, the number of cycles required for a simulation to reach full convergence (asymptote) is dependent upon the severity of the lesion and the criteria by which the asymptote is defined. Very severe lesions require approximately twice the number of cycles than very mild stenoses. According to the stringent criterion, approximately 30 cycles are needed to ensure a fully asymptotic result. However, the focus of this project is to develop a practical clinical tool. On that basis, the less-stringent criterion indicates that very severe lesions require approximately 20 - 21 cycles to reach full convergence. However, in terms of dichotomised data prediction (FFR $<$ or $\geq$ 0.80), the borderline region (FFR 0.75 – 0.85) is where accuracy matters most. In this region, 13 cycles produced an acceptable result. Outside this region, small differences in result will not influence the revascularisation decision. Furthermore, very severe lesions with $>90\%$ stenosis by visual criteria do not require FFR measurement (Tonino et al., 2010). Either way, when applying the current method of CFD simulation (fully transient 3-D with coupled 0-dimensional model), 10 cycles is not sufficient to give confidence that a fully converged result has been achieved. This extends rather than decreases computation time relative to VIRTU-1.
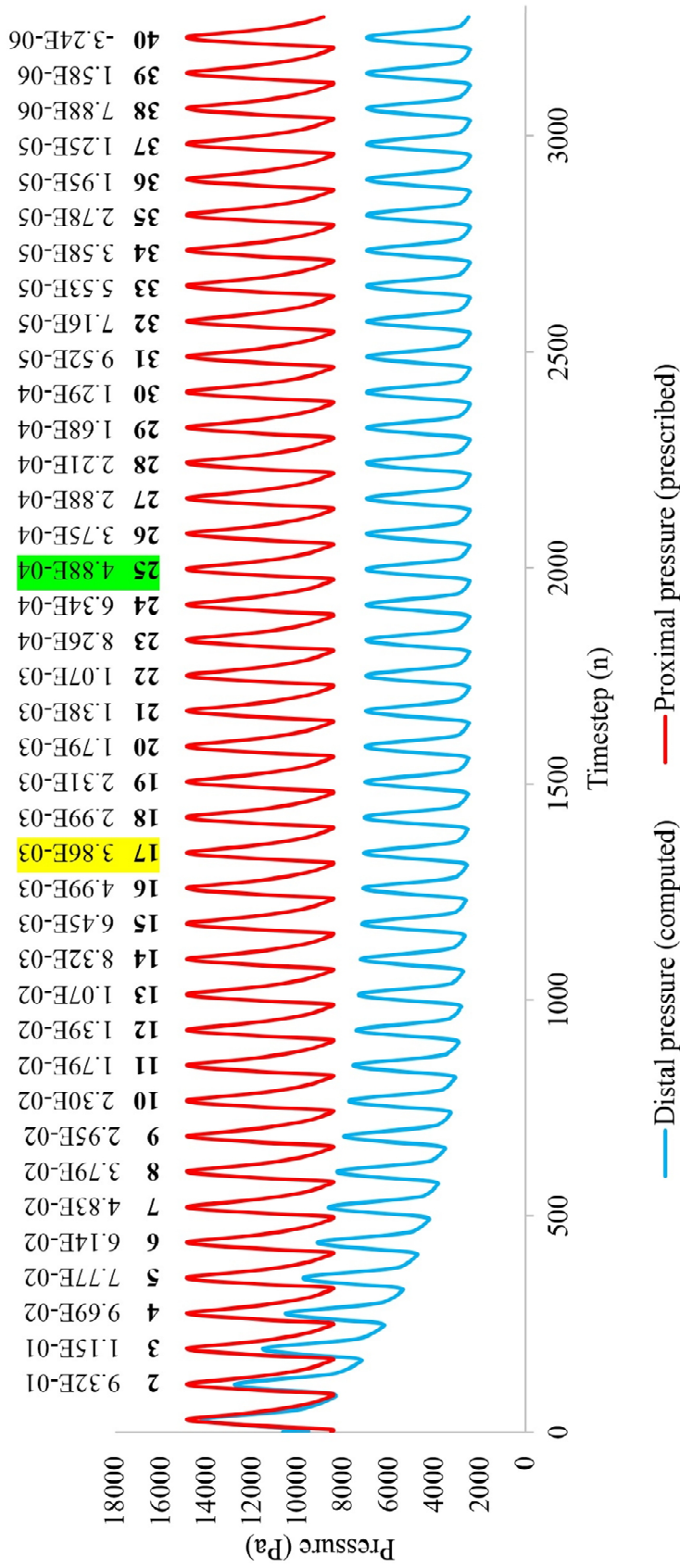
Figure 4.2. Convergence of case 15 (severe lesion) over 40 periods.

The numbers above the cycles indicate the cycle number and the corresponding delta value between the FFR of that cycle and the previous cycle. The yellow and green highlighted figures indicate when the pragmatic and stringent thresholds for reaching the asymptote were reached

4.3.3 Richardson's extrapolation

Since convergence towards the asymptote follows an exponential, it may be possible to extrapolate the asymptote from the results of the initial cardiac cycles thus predicting the fully converged result without completing the full simulation. The Richardson extrapolation (Roache, 1994, Roache, 1997) is a sequence acceleration method which allows the estimation /prediction of the asymptote from the relationship between earlier interval observations. Given an exponential relationship such as is shown in **Figure 4.4** (below), where X_1, X_2 and X_3 are three, equally spaced (i.e. $h_1 = h_2$) early observations (cycle solutions). The predicted final, asymptotic result (y_0) can be calculated according to:

$$y_0 = \frac{y_1 y_3 - y_2^2}{y_1 - 2y_2 + y_3} \qquad \text{Eq 4.1}$$

It is expected that later observations will yield more accurate predictions of the final result. A 40 cycle 3-D CFD simulation was run using the same four cases used in the mesh sensitivity analysis (section 4.3). A range of cardiac cycle solutions were substituted into the equation in order to predict the fully converged result.
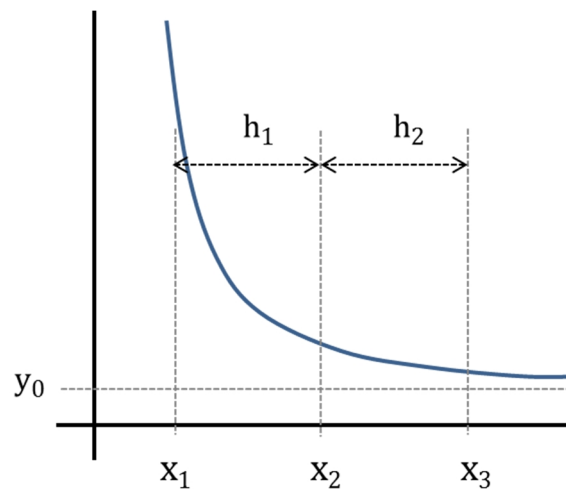
Figure 4.4. CFD solution convergence
See text for explanation

4.3.3.1 Results

Table 4.5 outlines the results of this evaluation. The results demonstrate that it is possible to predict the final asymptote from early interval observations. These results are consistent with the hypothesis in that later observations would yield more accurate results; the number of the last cycle

used in the calculation was inversely proportional to the magnitude of error between the predicted and actual results (Pearson's correlation coefficient = 0.72, p=0.018). In this preliminary evaluation, using cycles 6, 7 and 8 generated < 1.0% error in all cases and cycles 7, 8 and 9 were associated with <0.50% error in all cases.

4.3.3.2 Conclusion

This novel application of the Richardson extrapolation provides a reliable estimation of the fully converged result without the need to run a simulation to full, periodic, convergence. This could be integrated into the final model in order to reduce computation time. It may also be deployed in a manner which provides a pre-determined level of confidence according to whether the priority for a given case is speed or accuracy. For example if a vFFR result of 0.45 was predicted from the results of cycle 4, 5 and 6, even a 10% error margin would give an accurate assessment of the physiological significance of the given lesion. In this provisional evaluation on a small number of representative cases, using cycles 7, 8 and 9 generated an appropriately accurate prediction of the final solution in all cases. Therefore, although successful in reducing the total time of computation from 20 or 30 cycles (depending on the desired level of accuracy – see section 4.3) down to just 8 or 9 periods, this is almost identical to the number used in Chapter 3 which was associated with very protracted simulations. Whilst successful and of potential use in other fields of CFD analysis, this novel use of the Richardson's extrapolation is not a viable option for VIRTUheart™.

Table 4.5. Demonstrating the extrapolated /predicted result from early cycle solution interval observations.

	Case 1 vFFR=0.363		Case 2 vFFR=0.816		Case 3 vFFR= 0.895	
Cycles used	Extrapolated result	Error	Extrapolated result	Error	Extrapolated result	Error
1,2,3	0.2041	-43.78%	0.7941	-2.64%	0.8357	-6.62%
2,3,4	0.3275	-9.79%	0.7646	-6.25%	0.8381	-6.36%
3,4,5	0.3495	-3.71%	0.7989	-2.04%	0.8786	-1.83%
4,5,6	0.3544	-2.38%	0.8075	-0.99%	0.8882	-0.77%
5,6,7	0.3557	-2.01%	0.8105	-0.62%	0.8910	-0.45%
6,7,8	0.3608	-0.60%	0.8136	-0.25%	0.8936	-0.15%
7,8,9	0.3613	-0.46%	0.8144	-0.15%	0.8944	-0.07%
1,3,5	0.3152	-13.15%	0.7440	-8.78%	0.8194	-8.45%
3,6,9	0.3534	-2.63%	0.8060	-1.17%	0.8865	-0.95%

vFFR values refer to the final result after 40 cycles. Error indicates the percentage difference between the predicted result and the asymptote.

4.4 Reasons for prolonged computation

The coronary circulation is a dynamic, 3-D, pulsatile system. In order to best characterise this, VIRTU-1 implemented a transient, 3-D CFD simulation. However, this method involves solving, for several millions of degrees of freedom, a set of non-linear, partial differential equations (Navier-Stokes), simultaneously and repeatedly, thousands of times each cardiac cycle. Even using a high performance desktop PC (Intel Xeon processor, 32GB RAM), this takes considerable time. The optimal CFD simulation method for computing vFFR has yet to be established. In order to accelerate result generation, VIRTUheart™ requires either an increase in computing power, or an alternative, reduced-order method of computing the result.

4.4.1 Potential methods for acceleration

Upscaling computational power remains one option for accelerating CFD simulation but this is not easily accommodated within traditionally parsimonious healthcare systems. Nowadays, this problem can be resolved by accessing high performance computing (HPC) within a cloud service. The feasibility of this approach was tested. A simple ANSYS definition file was written and a workflow was designed within the Taverna Workbench Core (v2.5.0, School of Computer Science, University of Manchester, UK) (Taverna Workbench 2015) to read the definition file to the Amazon Cloud (Amazon Web Services, Inc. USA), via VPH-Share infrastructure. The simulation ran in the cloud and the results and *.out files were written back to the VPH-Share filestore. With a simple simulation (300 000 element straight tube, steady-state analysis, residual target (RMS) $\leq 10^{-4}$), the process took >15 minutes to return results, the majority of which was taken up by file transfer. Therefore, simulation speed aside, this is impractical for a clinical tool. Furthermore, in a clinical application, sensitive clinical data would need to be exported beyond hospital firewalls into a proprietary web service; this associated with a wide range of separate issues. Remote computation has been adopted by HeartFlow, Inc (Redwood City, USA) where physicians upload anatomical data (standard CCTA protocols) to the secure HeartFlow system. HeartFlow perform their patent-protected CFD analysis on high-performance computers and return a result with a color-coded 3-D model of the coronary arteries showing vFFR. However, prolonged computation times are less crucial for CT-derived FFR because of the intervening time period between the non-invasive CT scan and the invasive CAG. Whether or not the clinical community (and hospital management) have an appetite for this is yet to be determined. A system which allows real-time processing within software integrated into local catheter-laboratory systems is likely to be more desirable.

If major reductions in simulation time are to be made, an alternative, reduced order model or method is required. The remainder of this chapter focuses on alternative methods for computing vFFR.

4.5 1-D CFD modelling

In the context of VIRTU-1, the excessive simulation times are a consequence of the transient 3-D CFD analysis. It is therefore logical to either reduce the dimensions of the model to a 1-D transient (this section) model, or change to an analysis based upon a 3-D steady-state method (see section 4.6). The operation of a 1-D model on sixteen cases from the VIRTU-1 dataset is reported in the MSc thesis of Jeroen Feher (Feher, 2014). This work is summarised in this section, culminating in the comparison, in **Figure 4.8**, of JF's 1-D results with the 3-D results reported in Chapter 3 of this thesis. Clinical data was generated by Morris. Simulations and analysis were done in collaboration

In 1-D wave propagation models, the motion of blood is resolved by the axisymmetric (1-D) form of the Navier Stokes equations, whereas the motion of the elastic vascular walls is governed by the equations of equilibrium (Shi *et al*., 2011). 1-D models require significantly less computational expense than higher order CFD models because the 3-D domain is reduced simply to a measure of vessel radius as a function of vessel length. Zero- and 1-dimensional (0-D and 1-D) models are often used to represent the principal cardiovascular components, such as the heart, valves, and vessels. 0-D and 1-D models are frequently coupled to more complex multi-scale models where their role is to represent the boundary conditions. The great advantage of 1-D models is that they typically solve in seconds or minutes. The disadvantage is that they only represent the vessel radius as a function of length, thus ignoring the complex 2-D and 3-D effects of coronary arterial anatomy. Furthermore, blood flow in the radial direction is assumed to be zero; this is not the case in the post-stenotic region. The hypothesis in this section is that a 1-D model will provide faster, but less accurate, results than a 3-D model.

4.5.1 The model

A 1-D wave propagation model of coronary physiology was developed during the course of this project with JF and was based upon a circulation model by Keijsers *et al* (Keijsers, 2012b). The model consists of three types of elements; a heart contraction model element, a 1-D wave propagation element representing the large (systemic and coronary) arteries, and, similar to VIRTU-1, a set of 0-D lumped parameter elements to represent the distal boundary conditions. The model is outlined in**Figure 4.5.**

Detailed descriptions of the one-fibre heart model (Bovendeerd et al., 2006), 1-D wave propagation models of the arterial segments (Kroon et al., 2012), coupled Windkessels (Feher, 2014), valves, (Mynard et al., 2012), parameterisation (Cox et al., 2009), stenosis element (Bessems et al., 2007) and generation of geometric data (Stergiopulos et al., 1992) can be found in the referenced manuscripts (Keijsers, 2012b).
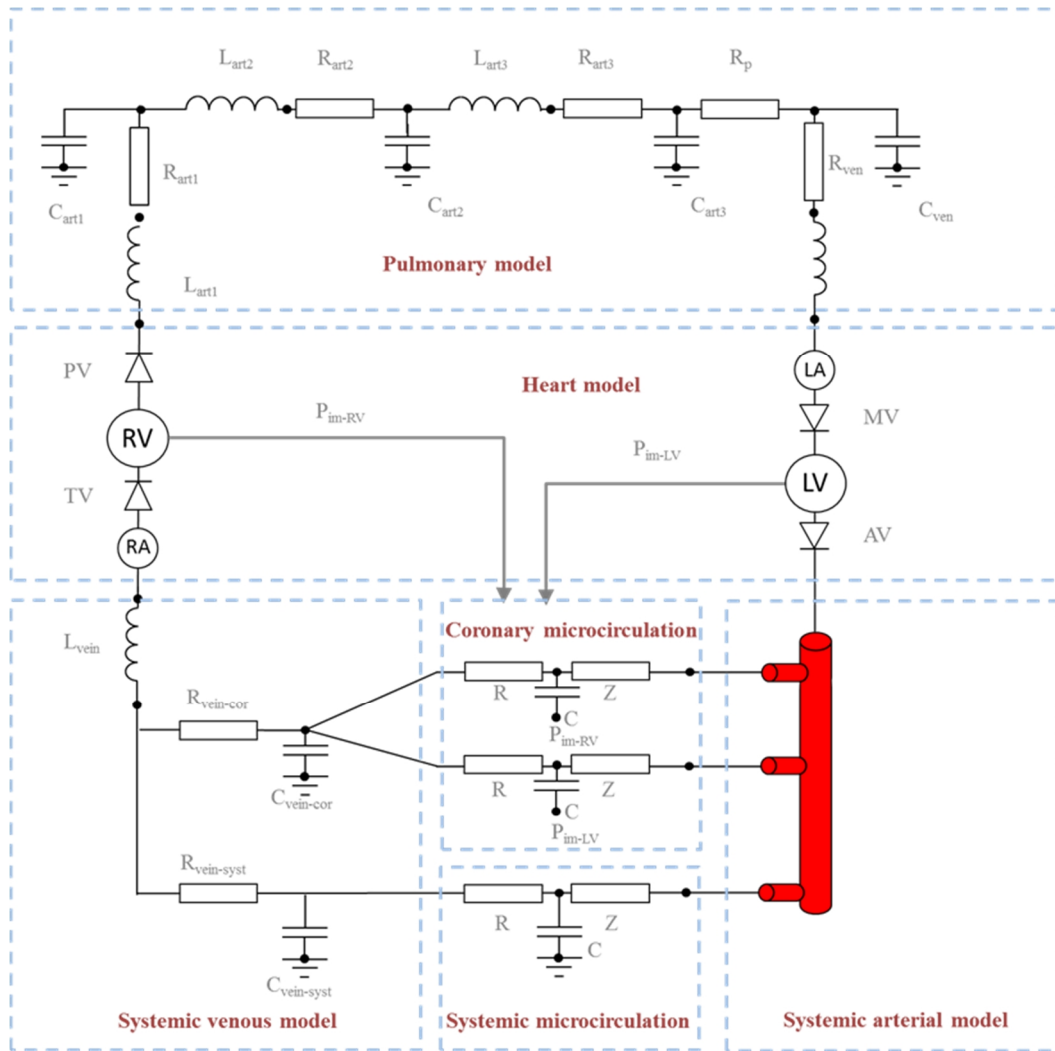
Figure 4.5. The full circulation model from Keijsers et al (Keijsers, 2012a)
The model comprises a 1-D arterial model coupled to zero-dimensional elements grouped into a heart, pulmonary, microcirculation and venous models. The focus in this section was on patient specific modelling of diseased coronary arteries with the remainder of the model providing boundary conditions. The ventricles in the heart model provide input to the coronary microcirculation. L, inertance; R, resistance; Z, impedance; C, capacitance; TV, tricuspid valve; PV, pulmonary valve; AV, aortic valve; MV, mitral valve; LV, left ventricle; RV, right ventricle; $P_{im\text{-}RV}$ and $P_{im\text{-}LV}$, intramyocardial pressure of right and left ventricles.

4.5.2 Method

In this analysis the relevant coronary element was replaced with a 1-D topology informed by patient-specific data. In order to provide a comparison with the model used in VIRTU-1, the same generic Windkessel parameters and the same arterial geometry data were used as for VIRTU-1 (segmented and reconstructed from rotational angiography) to construct the patient-specific 1-D models. A script file was coded in Matlab (DR) which (i) skeletonised the 3-D files encoding the extracted vessel and (ii) computed the radius at each point along the centerline. The output comprised a set of radii and relevant axial coordinate in 3-D (x, y, z) space (*.vtk). The 3-D coordinates were reduced to a 1-D description by calculating distance between each axial coordinate and plotting the cumulative distance against radius, thus radius versus arterial length could be plotted. The stenosis model was limited to representation of a single stenosis, on the assumption that the most significant pressure drop would be associated with the major stenosis. The stenosis is represented by a smooth cosine wave (defined below). The numerical solution assumes laminar flow. The remainder of the non-stenosed artery was represented as a smooth tapered tube with decreasing radius.

Patient specific arterial data were plotted in MS excel. The position of the stenosis according to length along the centerline, stenosis length and severity were determined visually and used to define the stenosis element geometry (see below). Thus, the non-stenosed regions were defined, and by fitting a linear regression best-fit to these data, the normal vessel radius, true length of the modelled segment and the proximal and distal radii were defined. Stenosis severity (S_v) was defined according to:

$$S_v = \left(1 - \frac{a_s}{a_0}\right) \cdot 100$$

Eq 4.2.

Where, a_s is the minimum luminal cross sectional area and a_0 is the normal, non-diseased area according to the linear regression fit.

These data (vessel length, proximal radius, distal radius, stenosis severity, position and length) were then used as input functions to inform the model which is implemented in Matlab (MathWorks, UK). For cases without stenoses (post-PCI), the stenosis severity was programmed as 0%. Stenosis geometries were defined by radii according to **Figure 4.6** and Eq 4.3 based on an inverse cosine wave. **Figure 4.7** demonstrates an example of the raw and resulting 1-D modelled data.
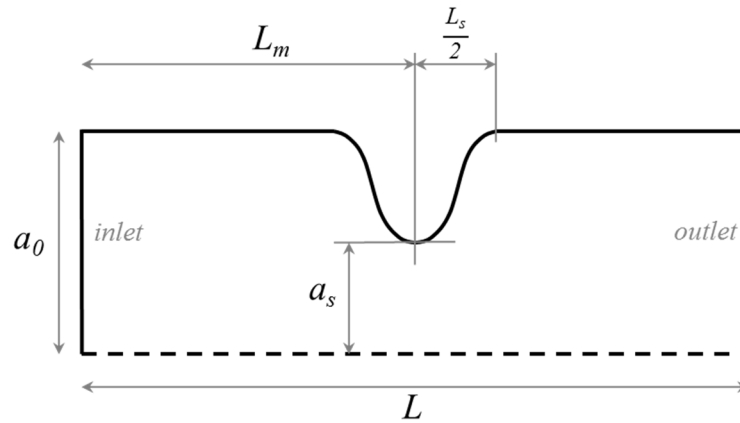
Figure 4.6. Stenosis geometry
L_m, length to the middle of the stenosis; L_s, stenosis length; a_0, normal area; a_s, area of the stenosis; L, length

$$r = a_0 - \frac{a_0 - a_s}{2}\left[1 - \cos\left(2\pi\frac{z - L_m - L_s/2}{L_s}\right)\right]$$

Eq 4.3.
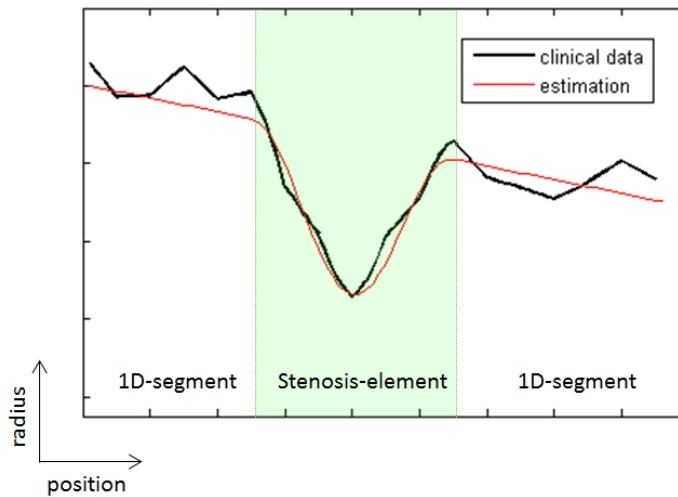
Figure 4.7. Raw data and 1-D estimation
Patient-specific clinical data are used to inform the 1-D radius-length model

The remaining coronary arteries and parameters remain the same as in the normal condition case. The parameters for the coronary microcirculation Windkessel elements were used as in Chapter 3. This enables comparison between the $vFFR_{3-D}$, and $vFFR_{1-D}$.

4.5.3 Results

The 1-D model results computed considerably more rapidly than the 3-D model. Mean 1-D computation time was 556.5 s (9.3 min) (SD, 27 s; range, 534 – 624 s). 3-D computation times were all in excess of 24 hours. The 3-D model categorised (FFR $\geq$ or $<$ 0.80) all cases correctly, whereas, even on this small dataset, the 1-D model computed 3 false negatives. The 1-D model had a positive bias (mean delta) of +0.09 (SD 0.12) whereas the 3-D model was associated with a small negative bias of -0.04 (SD 0.08). Mean error was also greater for the 1-D model ($\pm$ 0.085 (SD 0.11) vs $\pm$ 0.070 (SD 0.05)). This difference was not statistically significant on this small dataset but, the worst results from the 1D model were associated with the more physiologically significant cases. There was a strong correlation between mFFR and the 1-D model results (r= 0.85), but this was not as strong as the correlation between mFFR and 3-D model results (r=0.90).

There are limitations to this study. First, the number of cases was modest. Second, the proximal boundary condition differed from that used in VIRTU-1. However, using an already established model was more convenient than developing a model *de novo*, especially in the context of a small pilot study. Moreover, subsequent work has demonstrated by the use of sensitivity analysis that the vFFR model (1-D and 3-D) is relatively insensitive to even large differences in the input pressure (see Chapter 5). Third, the representation of the coronary artery lumen and stenosis remains a simplification compared with the 3-D model.

4.5.3.1   Conclusion

The results are consistent with the hypothesis in that a 1-D wave propagation model would provide far quicker but less accurate results. Even 10 minutes might be too slow for a clinical application for use in the cardiac catheter laboratory (although it is likely that the code and processing could be optimised further). Furthermore, without significantly more work, the current implementation of the code restricts modelling to a single stenosis which is not consistent with real-world interventional cardiology. 1-D modelling represents a promising method. 1-D development lies outside of the scope of the current thesis but work on this is continuing at the Technical University of Eindhoven, NL. Even in the current form, the 1-D model may provide a useful and expedient method of tuning the distal Windkessel parameters and analysing model output sensitivity to input parameters variation without expending significant time computing 3-D simulations.
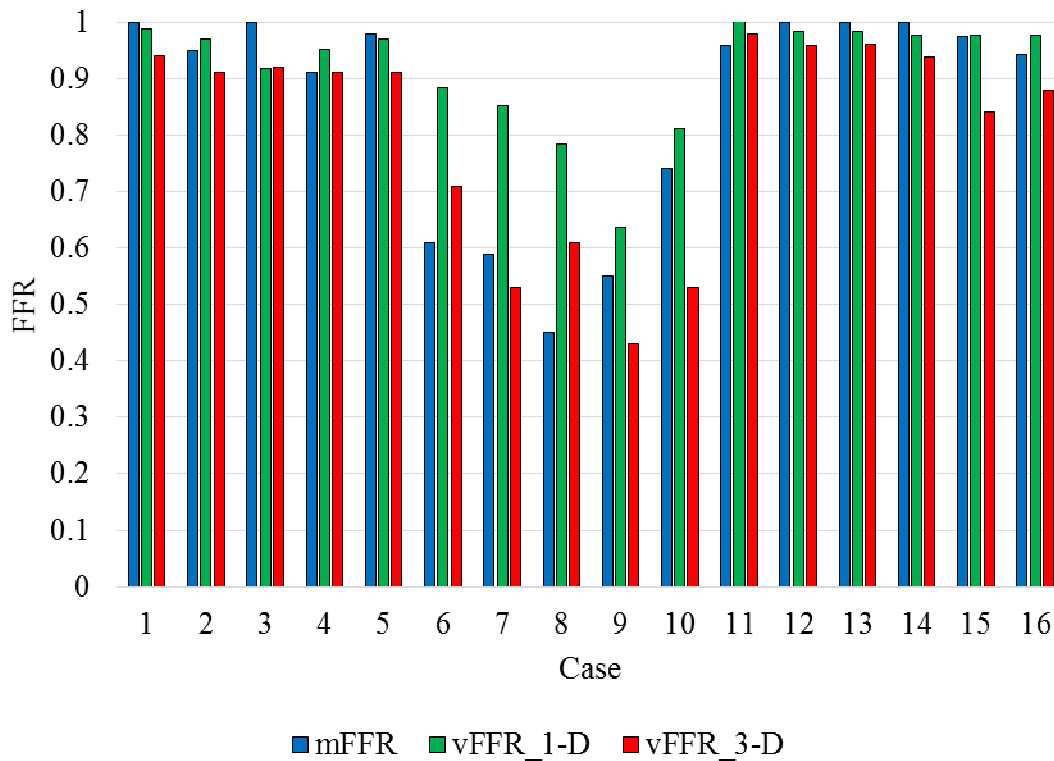
Figure 4.8. vFFR1-D and vFFR3-D results plotted against the measured FFR
Note the wider discrepancy between 1-D and measured FFR (mFFR) in the physiologically more significant cases

4.6 Steady-state analysis

Steady-state CFD analyses run several orders of magnitude more quickly than transient analyses. Steady-state analysis cannot characterise the accelerative /de-accelerative, time-dependent behaviour of pulsatile blood flow in the context of coronary arterial physiology, but it remains to be determined whether it can be used to calculate FFR, which by definition is a time average measure.

4.6.1.1   Steady-state assumptions in pulsatile cardiovascular systems

In 1951 Gorlin and Gorlin proposed an equation which could be used to predict cardiac orifice area in the context of the cardiac valves, patent ductus arteriosus, ventricular septal defect and atrial septal defect. Their equation was notable because it incorporated mean (steady) flow and ignored flow pulsatility (Gorlin and Gorlin, 1951). Where A is orifice cross-sectional area in cm^2; Q is flow rate in C.C. per second; C is an empirical constant; g is gravitational acceleration and h is pressure gradient across the orifice in mmHg, then:

$$A = \frac{Q}{C\left(\sqrt{2gh}\right)}$$

Eq 4.4.

Accurate predictions for numerous valve and orifice areas were made. The authors themselves expressed surprise at the results: "*considering that the equations were derived from systems of steady flow through fixed orifices, the surprise was that the equations worked at all!*" (Gorlin, 1987).

Nevertheless, the implication was that accurate predictions of cardiac anatomy, namely orifice area, could be made assuming and applying measures steady flow and ignoring dynamic, pulsatile behaviour. Many years later Cochrane *et al* proposed replacing cardiac output (CO) with stroke volume/systolic duration as the flow parameter (or diastolic duration for the atrioventricular valves) because CO is the product of stroke volume and rate, and is affected by valvular regurgitation. The accuracy of their predictions was independent of heart-rate, stroke volume, and changes in peripheral resistance (Cochrane et al., 1991):

$$EOA = \frac{Q}{6.96 \times P_d^{1/2}} - 0.7$$

Eq 4.5

Where *EOA* is effective orifice (cross-sectional) area; Q is mean flow over systole in L min^{-1} and P_d is the pressure drop over systole.

Predicting pulsatile vascular physiology on the basis of steady flow assumptions is, thus not entirely without precedent. However, the coronary circulation is distinct in that vascular dimensions are an order of magnitude smaller (coronary arterial diameter ~3mm versus mitral valve diameter ~3cm); stenoses are fixed and immobile (cf. cardiac valves), and the course of the arteries is far more tortuous and dynamic throughout the cardiac cycle.

4.6.1.2 Steady state CFD analysis in the context of intra-coronary physiology

Tu *et al* developed a 3-D steady-state model in order to predict vFFR. Arterial segmentation was from ICA images. CFD simulation was completed within *circa* 5 minutes. However, coronary flow is difficult to measure even with invasive intra-coronary instrumentation. The authors circumvented this by deriving mean hyperaemic flow from Thrombolysis In Myocardial Infarction (TIMI) frame counting the rapidity of the flow wave-front within the coronary arteries during contrast injection. This is advantageous because this can be estimated during routine angiography. However, this method was originally developed for use in identifying the coronary no reflow phenomenon in the context of acute myocardial infarction (indicating abnormal tissue perfusion)

(Eeckhout and Kern, 2001). Validation data are absent from the paper (and from the literature) in respect of the precision to which this method estimates true mean flow velocity. A disadvantage of this method is that it requires induction of hyperaemia (another potential factor contributing to FFR under-use) and, because it is only an estimation of mean flow, the method can only easily be applied to steady-state CFD analysis thus generating cycle-averaged, mean physiological results. Nevertheless, their vFFR model provided respectable diagnostic accuracy in 77 cases with FFR > or ≤ 0.80 being determined with 88.3% accuracy (area under ROC curve, 0.93). Agreeability was not quantitatively reported but 97% of vFFR results fell within the Bland-Altman limits of agreeability (**Table 2.4**).

Papafaklis *et al* developed a novel parameter, the '*virtual functional assessment index (vFAI) for fast functional assessment of intermediate coronary lesions*' which was also based upon steady-state analysis (Papafaklis et al., 2014). vFAI was computed based upon the ratio of distal to proximal pressure over the lesion for flows in the range 0-4 ml/s, normalised by the ratio over this range for a normal artery. The pressure ratio as a function of flow is described as a quadratic equation with coefficients determined by steady-state CFD analysis at two flow rates (1 and 3 ml/s). vFAI is numerically equal to the average of the computed pressure ratio over this flow range. Although this is likely to be superior to QCA-derived functional lesion assessment (because the geometric description is transformed into a more physiologically-relevant measure, namely pressure ratio, by the computation of the relationship between pressure ratio and flow), reasonable diagnostic accuracy was reported (n=139; diagnostic accuracy, 87.3%; AUC, 0.92) and CFD results were processed within 7 minutes. However, vFAI is entirely a function of the geometry of the stenosis and as such it can never be a surrogate for FFR because FFR measures the pressure ratio in the context of the patient-specific physiology. The vFAI will always be low, indicating the need for intervention, if the lesion is geometrically significant, whilst the FFR might be high or low for the same lesion depending on the overall physiology, and in particular on the status of the coronary microvasculature. Although on average there is expected to be a correlation between vFAI and FFR, simply because the pressure ratio is likely to be lower when the lesion is more geometrically significant, large differences would occur whenever the impedance of the microvasculature deviates significantly from the norm, and these are exactly the circumstances that are captured by FFR. This is likely to explain the occasionally high deviation of vFAI from FFR in the Papafaklis' paper, as illustrated in the Bland-Altman plot. This error risks incorrect diagnosis of the physiological significance of a lesion in certain circumstances.

4.6.2 System development

The starting point for developing a system capable of predicting vFFR using only steady-state CFD analysis was based upon the assumption that the relationship between flow (Q) and pressure gradient (ΔP) across any given coronary stenosis is quadratic, as demonstrated in **Figure 4.9**.
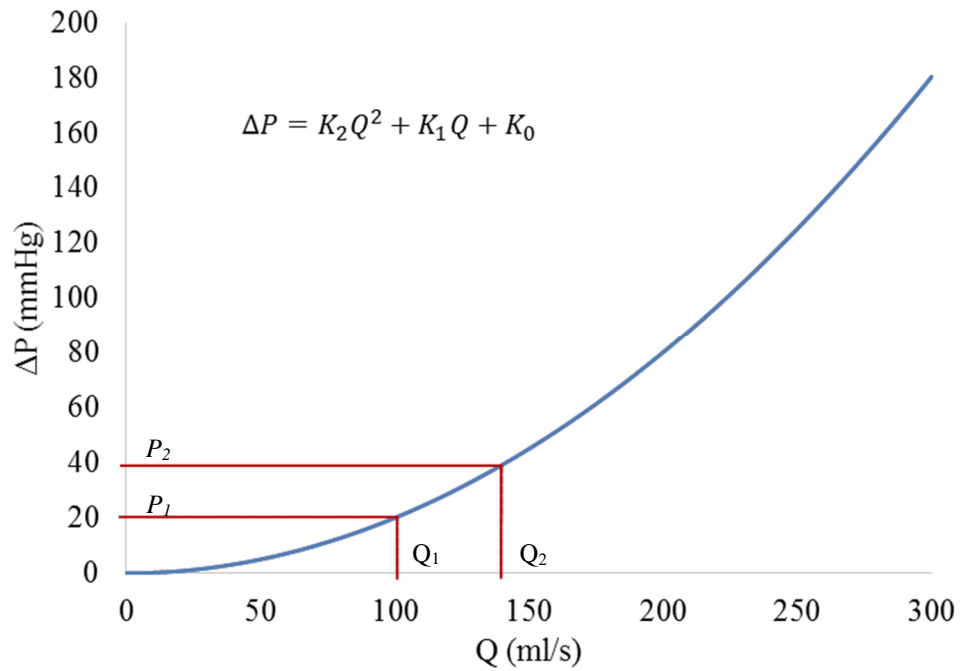
Figure 4.9. Relationship between translesional blood flow and pressure gradient
The ΔP-Q relationship is quadratic, as defined by the equation. Only a small segment of this line
will represent the physiological range for a given lesion.

The relationship between pressure gradient and flow is thus defined as:

$$\Delta P = (K_2 \cdot Q^2) + (K_1 \cdot Q) + K_0 \qquad \text{Eq 4.6}$$

The linear term $(K_1 \cdot Q)$ represents the Poiseuille pressure loss and the quadratic term $(K_2 \cdot Q^2)$ represents the Bernoulli losses. The two constants (K_1 and K_2) are derived from 3-D CFD analysis. Since a zero intercept is assumed, K_0 can be dropped from the equation. Therefore, according to **Figure 4.9**:

$$dP_1 = (K_2 \cdot Q_1^2) + (K \cdot Q_1) \qquad \text{Eq 4.6.1}$$

and

$$dP_2 = (K_2 \cdot Q_2^2) + (K_1 \cdot Q_2) \qquad \text{Eq 4.6.2}$$

In order to calculate K_1 and K_2 one of the constants must first be eliminated. Therefore, by dividing Eq 4.6.1 by Q_2^2 and then multiplying by Q_1^2 :

$$\frac{dP_2 \cdot Q_1^2}{Q_2^2} = (K_2 \cdot Q_1^2) + \frac{K_1 \cdot Q_2 \cdot Q_1^2}{Q_2^2} \qquad \text{Eq 4.6.3}$$

By subtracting equation 4.6.3 from equation 4.6.1:

$$dP_1 - \frac{dP_2 \cdot Q_1^2}{Q_2^2} = ((K \cdot Q_1^2) + (K_1 \cdot Q_1)) - \left((K_2 \cdot Q_1^2) + \frac{K_1 \cdot Q_2 \cdot Q_1^2}{Q_2^2}\right) \qquad \text{Eq 4.6.4}$$

This eliminates K_2 and becomes:

$$dP_1 - \frac{dP_2 \cdot Q_1^2}{Q_2^2} = (K_1 \cdot Q_1) - \frac{K_1 \cdot Q_2 \cdot Q_1^2}{Q_2^2} \qquad \text{Eq 4.6.5}$$

Which simplifies to:

$$dP_1 - \frac{dP_2 \cdot Q_1^2}{Q_2^2} = (K_1 \cdot Q_1) - \frac{K \cdot Q_1^2}{Q_2} \qquad \text{Eq 4.6.6}$$

Therefore, K_1 is equal to:

$$K_1 = \frac{\left(dP_1 - \frac{dP_2 \cdot Q_1^2}{Q_2^2}\right)}{\left(Q_1 - \frac{Q_1^2}{Q_2}\right)} = \frac{(dP_1 \cdot Q_2^2 - dP_2 \cdot Q_1^2)}{(Q_1 Q_2^2 - Q_1^2 Q_2)} \qquad \text{Eq 4.6.7}$$

And once K_1 is known, K_2 can also be solved for:

$$K_{2=} \frac{dP_1}{Q_1^2} - \frac{K_1 \cdot Q_1}{Q_1^2}$$

<div align="right">Eq 4.6.8</div>

Once K_1 and K_2 are known then the flow at any known pressure gradient can be calculated and *vice versa*.

Therefore, paired steady-state analyses, run at different pressure gradients (or flow rates), should, in theory, yield all the data required to determine both coefficients (K_1 and K_2) and thus define the case-specific quadratic ΔP-Q relationship. This allows the flow to be computed from any known pressure gradient. Since the pressure gradient is known throughout the cycle, flow can be calculated for the entire cycle. The two constants characterise the ΔP-Q relationship on a case-specific basis, acting like a unique fingerprint for an individual case. This is significant because if the stenosis section is characterised in this way, and if the model is coupled to an impedance (Windkessel) with assumed zero distal pressure, and if the parameters of the Windkessel are known, then the system effectively represents two non-linear impedances in series with known pressure at both ends which can be used to calculate flow and pressure at the middle node, distal to the lesion, and thus the FFR, without the need for performing transient analysis. To the best of the current author's knowledge, this has not been attempted or described previously.

4.6.2.1   Proof of concept experiment

Before developing a system which predicts vFFR purely on the basis of steady-state analysis, a proof of concept experiment was devised. The premise of this experiment was to evaluate whether realistic pulsatile flow could be accurately predicted from measured pressure gradients using steady-state analysis from data in the physiological range.

4.6.2.1.1   Methods: Computing flow curves using transient 3-D CFD analysis

As previously described, volumetric coronary flow is challenging to measure *in vivo*. Coronary flow velocity was measured during initial development of VIRTU-1 using a Volcano Combowire (Volcano Corps, San Diego, CA, USA) but significant artefact and poor Doppler windowing made these measured data sub-optimal and unreliable for use. For the purposes of this experiment, transient flow was computed using transient 3-D CFD analysis applying patient-specific, measured time-dependent pressure signals as the boundary conditions.

In this analysis, RoCA and physiological data were collected from 12 patients with stable CAD. VIRTU-1 cases were not used since data collection for the Wellcome Trust /Department of Health,

Health Innovation Challenge Fund (HICF) grant had commenced and these newer cases provided a richer dataset. Data collection was consistent with the methods described in Chapter 3. Data were collected pre-PCI and in those with treated, physiologically significant lesions, post PCI. All datasets were segmented using the Philips 3DCA segmentation software as previously described (Chapter 3) (Philips Healthcare, Best, NL). The cases were simulated using full transient 3-D CFD with measured pressure boundary conditions consistent with the workflow described in Chapter 3. Rather than applying a lumped-parameter model at the outlet, measured pressure data were applied as the boundary condition. Inlet and outlet pressure boundary conditions were derived using the VIRTU-1, GIMIAS-based workflow as follows:

1. Pressure data (P_a and P_d) were selected from the appropriate section of the analysis (Volcano study files were exported as text files).

2. The workflow plugin was used to divide the signal into individual cardiac cycles, defined by the electrocardiographic R wave signal trigger automatically recorded by the Volcano ComboMap software.

3. Individual pressure cycles contain significant artefact, and /or regions of unreliable signal were eliminated.

4. The remaining pressure data were ensemble-averaged into a single time dependent P_a and P_d signal, representative of all included data within the period of interest. These 'trace data' were applied as proximal and distal boundary conditions to the inlet and outlet of the volumetric mesh respectively, saved as a batch compiler specification (BCS or .bcs) file.

5. Simulations were performed using ANSYS-CFX. **Table** 4.6 outlines the simulation setup parameters used to define each simulation.

6. Output data (P_{in}, P_{out}, Q_{in}, Q_{out}) were exported from the ANSYS-CFX Solver Manager and a CFX results file was written.

7. This was repeated for each case under baseline and hyperaemic conditions, pre- and post-PCI where appropriate.

The output from the 3-D CFD analysis (P_a, P_d and Q_{in} and Q_{out}) was tabulated in MS Excel. The pressure gradient across the modelled segment, over the cardiac cycle was calculated from these data. This enabled each data-set to be plotted according to
Figure 4.10.

Table 4.6. Def file set up for computing flow

Category	Parameter/s	Value	Units
Volumetric mesh	Patient-specific geometry	See section 4.2	mm
Boundary conditions	Inlet pressure	Patient-specific	mmHg
	Outlet pressure	Patient-specific	mmHg
	Arterial wall	Rigid wall	-
Blood properties	Dynamic viscosity	0.0035	Pa.s
	Density	1066	kg m^{-3}
	Molar mass	1	kg Kmol^{-1}
Time settings	Initial time	0	s
	Period	Patient-specific	s
	Number of oscillations	3	cycles
	Total simulation time	3 · period	s
	Time step	Period / 80	s
	Total no. of time-steps	241	steps
Convergence criteria	Min no. of iterations	2	iterations
	Max no. of iterations	100	Iterations
	Residual target	10 e^{-6}	RMS

4.6.2.1.2   Steady-state analysis

To construct the quadratic curve, at least two steady-state analyses are required. Because simulations should ideally proceed within the physiological range, initially case-specific pressure gradients were used to compute flow. Two schemes were initially proposed to produce paired flow results. Analyses could be run with pressure gradients corresponding to the following points in the cardiac cycle:

1.   maximum P_a and maximum dP
2.   maximum dP and half maximum dP

Both strategies were evaluated on all cases. Steady-state analysis was performed applying the values of P_a and P_d as the boundary conditions. The same mesh and blood parameters were applied as in the transient analysis and detailed in **Table** 4.6. A small analysis of 10 cases revealed that there was <0.1% difference in the flow result between steady-state results computed at residual targets (RMS) of 10 e^{-6} and 10 e^{-5}. Therefore, in the interests of system acceleration, convergence criteria was set to a RMS of 10 e^{-5}. All steady-state analyses were performed on 10 cores on a Dell Precision T5600 desktop PC (Intel Xeon processor, 32GB RAM).
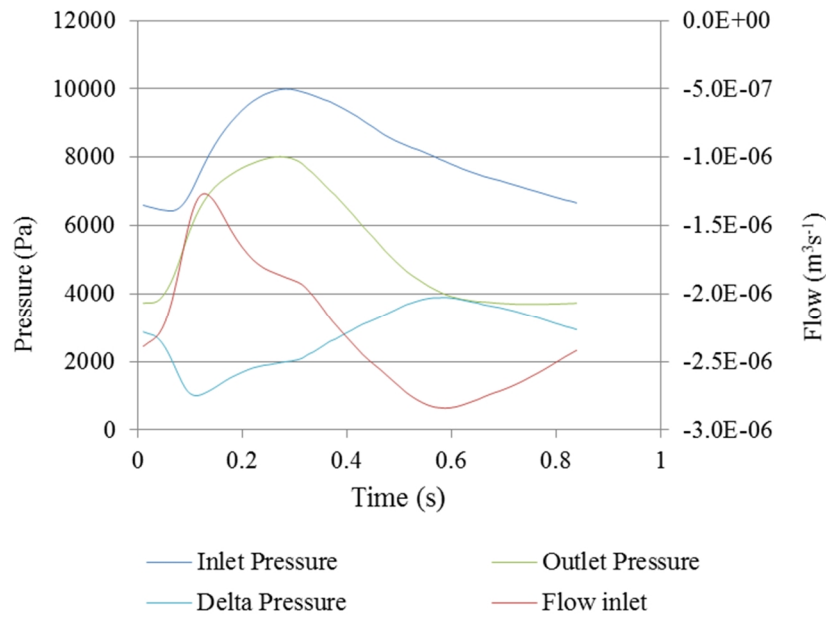
Figure 4.10. Transient 3-D CFD output data.
Data from a left anterior descending arterial case from study patient 1. Inlet flow is considered negative.

Equations 4.6.7 and 4.6.8 were used to calculate both coefficients from the pressure and case-specific flow result. Once the coefficients are known, measured dP was used to calculate flow for all time points. Thus, 'pseudo-transient' flow is calculated based upon steady-state analyses (Q_{ss}). This can then be compared to flow computed by the transient 3-D method which is based on measured data (Q_{trns}). **Figure 4.11** demonstrates an example Q_{ss} result plotted against Q_{trns}.

4.6.2.1.3   Quantifying agreeability between the two methods

The precision to which Q_{ss} approximated Q_{trns} was evaluated by calculating two statistical measures. First, the delta Q was calculated at each of the 80 time points over a cardiac cycle, from which, the root mean square (RMS) was calculated. The root mean square was normalised by dividing by the average (mean) Q_{trns} and multiplying by one hundred, thus transforming this measure into a percentage error; 'instantaneous (RMS) error'. Instantaneous (RMS) error is the most stringent, measure of time-dependent precision. However, FFR is calculated as the ratio of P_d/P_a *averaged* over the *entire cardiac cycle*.
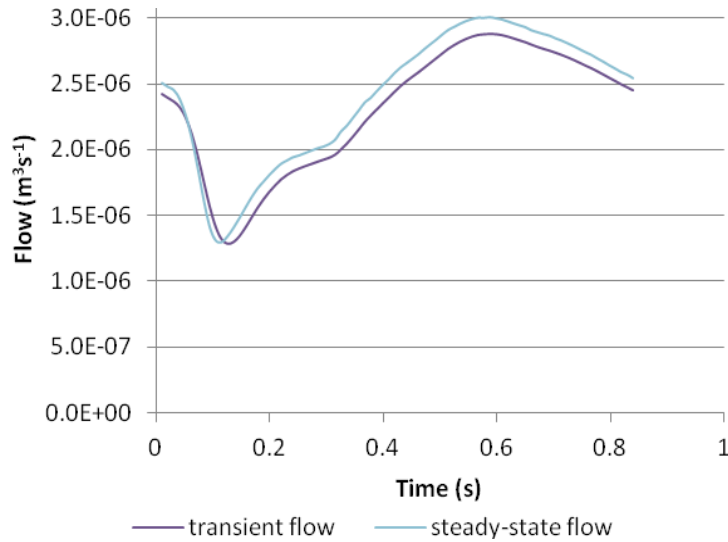
Figure 4.11.   Transient flow versus pseudo-transient flow derived from paired steady-state analyses.
In this case, data are from a pre-PCI, left anterior descending artery case, under hyperaemic conditions, from study patient 1.

A second method was thus used to calculate the percentage difference between Q_{ss} and Q_{trns} averaged over cycle because this is more indicative of FFR. This is referred to as 'cycle averaged' precision. Unless stated otherwise, data are presented as mean ($\pm$ SD, range). 1-tailed Pearson's correlation coefficient is used to demonstrate the strength of any correlation.

4.6.2.2   Results

4.6.2.2.1   Case mix and analysis details

12 patient cases yielded 62 individual arterial datasets. Transient 3-D CFD analysis successfully computed in all cases. Steady-state analyses were performed at maximum P_a, maximum dP, and at half maximum dP for all cases. A total of 248 3-D CFD analyses were performed; 186 steady-state, and 62 transient. All CFD analyses ran to successful completion. Mean FFR value was 0.87 (± 0.14, range; 0.35 – 1.00). 26 cases had an FFR value below 0.90 i.e. in the region of clinical interest. The arterial case mix is described in **Table 4.7**.

4.6.2.2.2   Computation time

The average time to compute the paired steady-state CFD results was 140.5 s ($\pm$ 38 s, range 29 – 208 s). The average time for computing the transient 3-D results was 2.23×10^4 s ($\pm 1.51 \times 10^4$ s, range; 4.03×10^4 - 5.77×10^4 s). This is not entirely indicative of predictive vFFR computation

which involves solving over many more cycles with a coupled-lump parameter model at the outlet/s (>24 hrs in VIRTU-1, Chapter 3).

Table 4.7. Characteristics of the arterial datasets included in the proof of concept study.

Case type	Number
Right coronary artery	19
Left anterior descending artery	30
Diagonal artery	3
(Left) Circumflex artery	6
Left main coronary artery	4
Pre-PCI	28
Post-PCI	26
No-PCI	8
Baseline conditions	29
Hyperaemic conditions	33

Total cases included = 62

4.6.2.2.3   Steady-state pairings

Two strategies were trialled for predicting transient flow. The first used the results from computing steady-state flow results at maximum P_a and maximum dP. (strategy 1). The second, used the results from computing steady-state flow results at maximum dP and half maximum dP (strategy 2). There were problems with strategy 1. In six cases, $P_d > P_a$ at this point in the cardiac cycle producing a negative pressure gradient and therefore flow. In one case, the value of dP at maximum P_{in}, by chance, was very similar to the value of maximum dP which of course is unhelpful when determining the quadratic relationship between pressure gradient and flow. Due to unreliability, strategy 1 was dropped at this point. Strategy 2 computed results successfully in all cases.

4.6.2.2.4   Agreeability between steady-state and transient analysis

In all cases, Q_{ss} was plotted against Q_{trns}. Examples of good and bad instantaneous agreement are demonstrated in

Figure 4.12. For all cases, mean instantaneous (RMS) error was 37.1% ($\pm$68.8%, range; 1.43% - 348.0%). Accuracy was significantly worse for less severe cases (higher FFR value). Not only was the FFR value correlated with instantaneous (RMS) error (r = 0.37, p=0.0015) but the error was significantly lower for cases where the FFR was < 0.90, compared with cases where FFR $\geq$ 0.90 (6.82% $\pm$4.01% vs 59.64% $\pm$84.42%, p<0.001). Considering the cases of most clinical

importance, i.e. the pre-PCI, hyperaemic cases, mean instantaneous (RMS) error was similarly low at 6.12% (±4.26, range; 1.43% - 18.7%). These data are summarised in **Table 4.8**.

Table 4.8. Instantaneous (RMS) precision of Q_{ss} in matching Q_{trns}

	All cases	FFR < 0.90	FFR ≥ 0.90	Pre-PCI, hyper'mic
N	62	26	36	15
Norm RMS error (±SD)	37.1% (±68.8)	6.82% [*](±4.01)	59.64% (±84.42%)	6.12% (±4.26) [#]
Minimum error	1.43%	1.43%	8.35%	1.43%
Maximum error	348.0%	18.71%	348.0%	18.7%

[*]p<0.001 compared with FFR > 0.90. [#]p<0.001 compared with all other cases. Pre-PCI hyper'mic indicates pre-PCI under hyperaemic flow conditions

Over all cases, the mean error of the cycle average was ± 9.41% (± 12.07). Overall, the Q_{ss} method tended to underestimate (bias) Q_{trns} by -4.40%. The mean error of the cycle average was ± 4.68% (± 2.26) in cases where the FFR < 0.90, compared with ± 12.83% (± 14.88%) in cases where FFR ≥ 0.90. In pre-PCI cases under hyperaemic conditions, the mean error of the cycle average was ± 4.47% (± 2.02). These data are summarised in **Table 4.9**.
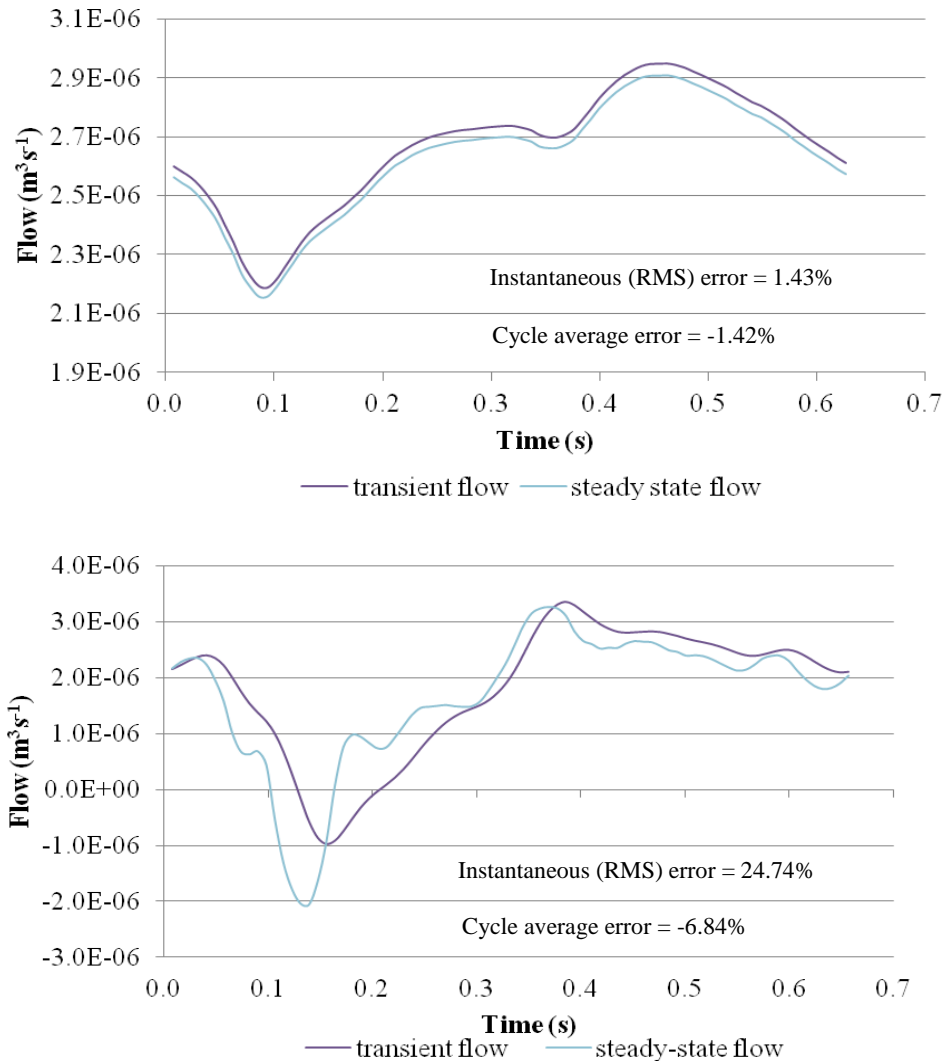
Figure 4.12. An example of good and poor instantaneous agreement.
The example of good instantaneous agreement (top) comes from study patient 9, a left anterior descending artery case with a low FFR (0.35) under hyperaemic conditions. The example of poor agreement comes from the same case but after PCI, under baseline conditions when the FFR was 0.96. Note that despite poor instantaneous (RMS) accuracy of the second case, the mean error of the cycle average is much better.

137

Table 4.9. Cycle averaged precision of Q_{ss} in matching Q_{trns}

	All cases	FFR < 0.90	FFR ≥ 0.90	Pre-PCI, hyper'mic
N	62	26	36	15
Cycle average error (SD)	±9.41% (12.07)	±4.68%* (2.26)	±12.83% (14.88%)	±4.47%[#] (2.02)
Bias (SD)	-4.40% (14.69)	-3.98% (3.38)	-4.71 (19.18)	-3.14 (10.59)
Minimum error	-44.72%	-11.09%	-44.72%	-8.84%
Maximum error	+73.82%	+4.54%	+73.82%	+4.54%

$p < 0.001$ compared with FFR > 0.90. #$p < 0.001$ compared with all other cases.

4.6.2.3   Discussion and conclusion

This proof-of-concept analysis demonstrated the feasibility of deriving realistic coronary physiology from a plurality of steady-state analyses. Furthermore, 'pseudo-transient' flow data was derived without performing transient analyses. The steady-state analyses ran in just over two minutes. Whilst overall instantaneous accuracy (as defined by norm RMS error) was poor it was significantly better in cases with a lower FFR under hyperaemic conditions i.e. the clinically relevant group. This is likely to be due to the fact that these cases provided the greatest pressure gradients, thus the lowest dP error. Greater accuracy might therefore be achieved, if paired steady-state analyses were run at higher flow rates, rather than the current pairings (max dP and half max dP). A further positive consideration is that the cycle averaged flow predictions were consistently superior, likely because regions of flow under-estimation were balanced by regions of over-estimation which, at least partly, cancelled over the entirety of the cardiac cycle. Due to the nature of FFR calculation (similarly averaged over a cycle), this maybe a more practical measure by which to judge the validity and ultimate utility of this novel approach.

Using steady-state analyses to compute a pseudo-transient flow appears feasible and advantageous but a more sophisticated scheme to derive the individual case ΔP-Q coefficients is required to minimise error.

4.7 Steady state method development

Simulating steady-state flow from patient-specific pressure gradients was not an advantageous approach because for two reasons. First, although this was guaranteed to be physiological, in many cases, the pressure gradients were often low (high FFR values) which is associated with increased error. Second, in a truly predictive model, the actual pressure gradients would be unknown. Therefore, the same geometric meshes were run at a series of steady-state flow rates in order to

compute the corresponding pressure gradients. These data could then be used to derive the ΔP-Q coefficients as in 4.6.2.

4.7.1.1 What flow rate pairings should be used?

Coronary arterial flow under baseline conditions in a single main vessel is approximately 60 ml min^{-1} but this increases up to fourfold during exercise or physiological (or pharmacological) stress (i.e. from ~1-5 ml s^{-1}) (Morris et al., 2015a). This increase is limited by epicardial coronary stenosis; the phenomenon upon which coronary flow reserve (CFR) is based. Therefore, it would not be physiological to expect coronary flow to increase 4-fold in a severe lesion, although this is feasible using CFD simulation. However, this range does provide a physiological envelope which can be investigated. Furthermore, selecting purely physiological pressure gradients limited accuracy during the proof-of-concept phase. This approach is similar to that used to compute vFAI (Papafaklis et al., 2014). In computing vFAI, Papafaklis *et al* simulated steady-state flow at 1 and 3 ml s^{-1} in order to construct the quadratic and extract the linear and quadratic terms (K_1 and K_2). In order to reduce the chance of narrowly missing the most useful flow range, it was decided to simulate each mesh at a steady-state flow of 0.5, 1, 1.5, 2, 3, 4 and 5 ml s^{-1}. This is incorporates and extends just beyond the physiological range.

4.7.1.2 Methods

The 32 unique patient specific arterial meshes used in the proof-of-concept evaluation were each simulated under steady-state flow conditions at 0.5, 1, 1.5, 2, 3, 4 and 5 ml s^{-1}. Unlike in the proof-of-concept evaluation, flow rate was controlled and pressure gradient was computed. Distal outlet pressure was set to zero. All other parameters are similar to the previous section including performing the simulation on the same PC. Any two of the seven results can be paired to compute pseudo-transient flow from the measured pressure gradients. Individual pairings were compared in terms of instantaneous accuracy and (as defined by norm RMS error) and by cycle averaged data consistent with the previous section. Individual pairings evaluated were: 0.5 and 1 ml s^{-1}; 1 and 1.5 ml s^{-1}; 1 and 2 ml s^{-1}; 1 and 3 ml s^{-1}; 1 and 4 ml s^{-1}; 1 and 5 ml s^{-1}; and 0.5 and 5 ml s^{-1}.

4.7.1.3 Results

224 individual steady-state analyses were performed. All completed successfully. Average simulation time was 128.7 s (SD 22 s). FFR ranged from 0.35 – 1.0 (mean = 0.827 ±0.145). The majority of cases had a FFR<0.90 (n=20). Computed pressure gradients ranged from 19.34 Pa (0.15 mmHg) – 168468 Pa (1266.7 mmHg), i.e. from sub- to supra-physiological levels.

In terms of instantaneous (RMS) accuracy, the single best pairing overall was 0.5 and 5 ml s^{-1}. In terms of cycle-averaged error, the single best pairing was 1and 5 ml s^{-1} (**Table 4.10** and **Table 4.11**). As predicted by the previous evaluation, the instantaneous (RMS) error was higher than the average cycle error. It is noteworthy that, the majority of cases (n=16) had a relatively flat solution space whereby the specific flow pairing had little effect upon the accuracy of prediction. 14 cases demonstrated a pattern whereby predictive accuracy improved at higher flow separations; a rising profile. Conversely, two cases demonstrated worse predictive accuracy at higher flow separations.

Table 4.10. Instantaneous (RMS) error of the seven flow pairings.

	Flow rate pairings (ml s^{-1})						
	0.5 & 1	**1 & 1.5**	**1 & 2**	**1 & 3**	**1 & 4**	**1 & 5**	**0.5 & 5**
Min error (%)	2.36	1.48	1.17	0.91	0.68	0.19	0.43
Max error (%)	354.20	353.70	354.06	354.87	355.69	356.48	284.99
Mean (SD) (%)	30.37 (65.10)	29.37 (65.30)	29.04 (65.49)	28.65 (65.74)	28.44 (65.95)	28.38 (66.14)	26.13 (55.30)

The optimal flow pairing was 0.5 and 5 ml s^{-1} (green highlight).

Table 4.11. Average cycle error of the seven different flow pairings (all cases).

	Flow rate pairings (ml s^{-1})						
	0.5 & 1	**1 & 1.5**	**1 & 2**	**1 & 3**	**1 & 4**	**1 & 5**	**0.5 & 5**
Min error (%)	-21.53	-20.86	-20.60	-20.07	-20.79	-21.68	-52.80
Max error (%)	12.49	11.38	10.98	10.04	9.36	8.89	14.63
Mean error (SD) (%)	±7.78 (5.22)	±6.61 (4.91)	±6.14 (4.71)	±5.43 (4.59)	±4.96 (4.65)	±4.60 (4.81)	±4.89 (9.93)
Bias (SD)	-6.82 (6.45)	-5.50 (6.16)	-4.93 (6.00)	-4.06 (5.86)	-3.55 (5.84)	-3.14 (5.90)	-3.02 (10.67)

The optimal flow pairing was 1 and 5 ml s^{-1} (green highlight).

Once again, both the instantaneous (RMS), and the cycle averaged error were significantly better in the group of 20 patients where FFR was <0.90 (**Table 4.12** and **Table 4.13**):

· Best mean instantaneous error; 5.49% (4.38) vs 26.13% (55.30)

· Best cycle averaged error; ±1.66% (2.12) vs ±4.89 (9.93)

Table 4.12. Instantaneous (RMS) error in the 20 cases where FFR<0.90

	Flow rate pairings (mls s^{-1})						
	0.5 & 1	1 & 1.5	1 & 2	1 & 3	1 & 4	1 & 5	0.5 & 5
Min (%)	2.36	1.48	1.17	0.91	0.68	0.19	0.43
Max (%)	18.72	18.28	18.06	17.95	17.85	17.85	18.17
Mean (SD) (%)	8.91 (4.83)	7.41 (4.29)	6.88 (4.14)	6.29 (3.99)	5.92 (4.01)	5.78 (4.05)	5.49 (4.38)

The optimal flow pairing was 0.5 and 5 ml s^{-1} (green highlight).

Table 4.13. Average cycle error in the 20 cases where FFR<0.90.

	Flow rate pairings (ml s^{-1})						
	0.5 & 1	1 & 1.5	1 & 2	1 & 3	1 & 4	1 & 5	0.5 & 5
Min (%)	-12.29	-9.82	-8.45	-6.31	-5.82	-5.92	-7.24
Max (%)	2.08	3.58	4.23	5.13	5.63	5.98	6.79
Mean (SD) (%)	±6.47 (3.43)	±4.93 (2.47)	±4.42 (2.01)	±3.64 (1.66)	±3.16 (1.64)	±2.81 (1.87)	±1.66 (2.12)
Bias (SD)	-6.24 (3.85)	-4.53 (3.18)	-3.95 (2.86)	-3.05 (2.64)	-2.54 (2.55)	-2.15 (2.65)	-0.79 (2.60)

The optimal flow pairing was 0.5 and 5 ml s^{-1} (green highlight).

These results suggest that selecting a flow pairing on either 0.5 and 5 ml s^{-1}, or 1 and 5 ml s^{-1}, is optimal. Severe cases aside, this is close to a physiological range and is also roughly consistent with the work of Papafaklis *et al* (Papafaklis et al., 2014). Whilst it might seem tempting to evaluate other pairings, it should be borne in mind that the solution space for the majority of cases was relatively flat. Furthermore, the predictive accuracy of certain cases actually worsened as flow separation increased. 1 and 5 mls s^{-1}, appeared to be the best pairing overall, whereas 0.5 and 5 appeared to be the best pairing for cases where FFR < 0.90. Once again, it is clear that accuracy was improved in the group of most clinical interest i.e. those with a FFR <0.90, which is reassuring.

4.8 Paired steady-state analyses to predict vFFR

Of all the methods piloted in this chapter, the steady-state method appears to demonstrate the most promise in terms of accelerating the computation of vFFR. However, the method described in section 4.6.2.1 and 4.7 has no immediate practical use because it cannot be used to determine vFFR. Therefore, the method was developed so that vFFR could be predicted from data routinely available during diagnostic angiography, namely the arterial geometry and the proximal catheter pressure.

Two methods were developed (see below) both of which are based on the results of paired steady-state analyses to compute the linear and quadratic coefficients (K_1 and K_2) which characterise the pressure-flow relationship for a given coronary artery. In this section, both novel methods are more formally tested against the current vFFR simulation method i.e. fully transient, 3-D CFD coupled to a lumped parameter Windkessel as described in VIRTU-1, Chapter 3. The aims of the current study were twofold:

- to develop two novel methods for computing vFFR, based upon steady-state analysis, which are practical for use in the cardiac catheter laboratory
- to validate these methods using clinical data and compare computation time against the transient method

4.8.1.1 Methods

This was an observational, analytical, single-centre study in which two novel accelerated methods for computing vFFR were developed and validated against both invasive FFR measurement and against fully transient CFD analysis. All work was approved by the local ethics committee. 20 patients were studied. Patients were recruited from the Wellcome Trust and Department of Health, HICF study as detailed in Chapter 3. Patients were eligible for recruitment if they had proven CAD and were awaiting assessment for elective PCI. Apart from chronic total occlusion, all patterns and severities of stable CAD were eligible for recruitment. Exclusion criteria were: acute presentation within 60 days; intolerance to intravenous nitrate, adenosine or iodine based contrast media; coronary artery bypass graft (CABG) surgery, or obesity which precluded ICA.

The clinical protocol for RoCA and FFR measurement were identical to the description in Chapter 3. To ensure a diverse and wide ranging case mix, RoCA and physiological measurements were repeated post-PCI and under baseline and hyperaemic conditions. The RoCA images were segmented and reconstructed into 3-D *in silico* geometric representations using the Philips Allura 3D-RA system (Philips Healthcare, Best, NL). A 1-2 million element volumetric mesh was fabricated in ICEM (ANSYS, PA, USA) for each unique arterial geometry using the optimised mesh parameters described in section 4.2. The proximal physiological boundary condition was the patient-specific pressure measured from the guiding catheter. The distal boundary condition was derived from the distal pressure measured by the pressure wire (Volcano), which is reflective of the state of the coronary microvasculature (CMV). Based upon the work by Lungu et al (Lungu et al., 2014), a semi-automatic optimisation algorithm was developed within Matlab (Mathworks Inc, MA, U.S.A) to derive the parameters of the CMV from invasively measured values (more detailed description in Chapter 5). These parameters included the CMV impedance, resistance and

compliance, along with four parameters reflecting the amplitude and timing of intra-myocardial systolic pressure as described in Chapter 5. Computation and all simulations were performed using ANSYS-CFX (PA, USA) (ANSYS, 2009) on a Dell Precision T5600 computer (Intel Xeon processor, 32GB RAM). Steady-state CFD analyses were performed on each arterial geometry at 0.5, 1, 2, 3, 4, 5 ml/s. Although the optimal pairing had been investigated (section 4.7), the full range of flow rates were re-evaluated in order to identify the flow pairing which optimally characterised the K_1 and K_2 terms in this larger, more representative patient cohort.

4.8.1.1.1 Computing 'pseudo-transient' vFFR results

The computed pressure gradient and corresponding flow from paired analyses were used to derive the linear and quadratic coefficients (K_1 and K_2) that characterise the ΔP-Q relationship for each unique arterial geometry, as described in section 4.6. Pseudo-transient vFFR (vFFR$_{ps-trns}$) is a function of nine parameters: the transient proximal pressure trace, K_1 and K_2 coefficients, CMV resistance, CMV compliance, CMV impedance, and the parameters describing the myocardial systolic contraction including pressure rise, magnitude, plateau, decay and amplitude. The mathematical derivation of the vFFR$_{ps-trns}$ analytical solution is described below. The vFFR$_{ps-trns}$ workflow is outlined in **Figure 4.13**. In this section and the next, the analysis protocol was developed in discussion with my supervisor (DRH), who first wrote down the detailed mathematics and did the coding. The execution on the cohort and subsequent data analysis were performed entirely by the author of this thesis.
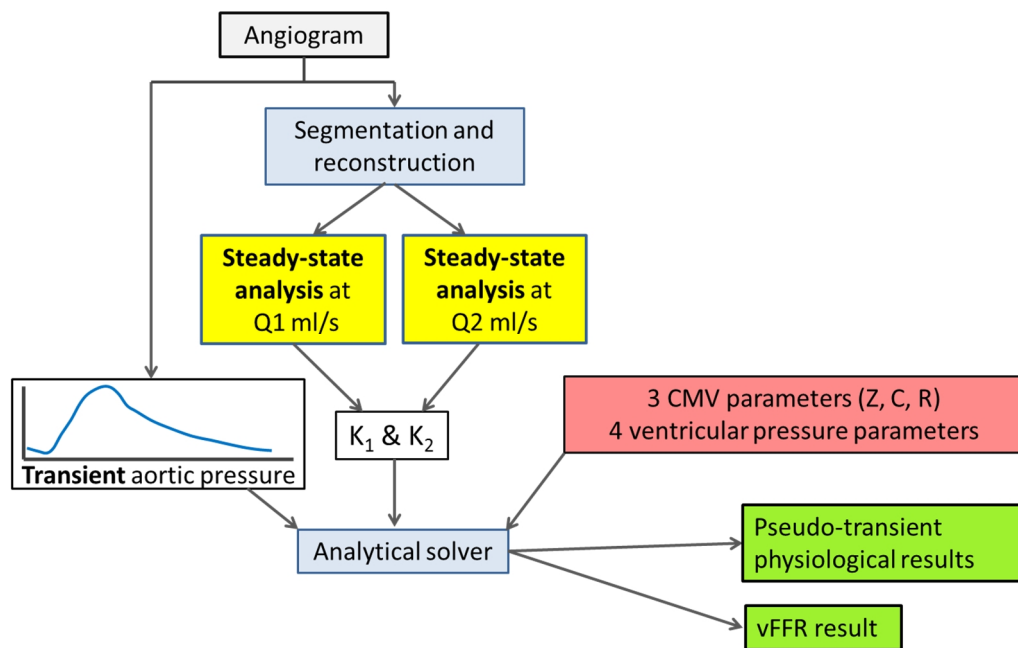
Figure 4.13. Workflow for pseudo-transient vFFR (vFFRps-trns).

Model input parameters are the linear and quadratic coefficients (K_1 and K_2); transient proximal pressure; distal coronary microvascular resistance (R), impedance (Z) and compliance (C); along with the intra-myocardial pressure rise, plateau, decay and amplitude. Parameters in the red box are unknown, all others are known or can be derived. This workflow outputs a vFFR results and pseudo-transient physiological data.
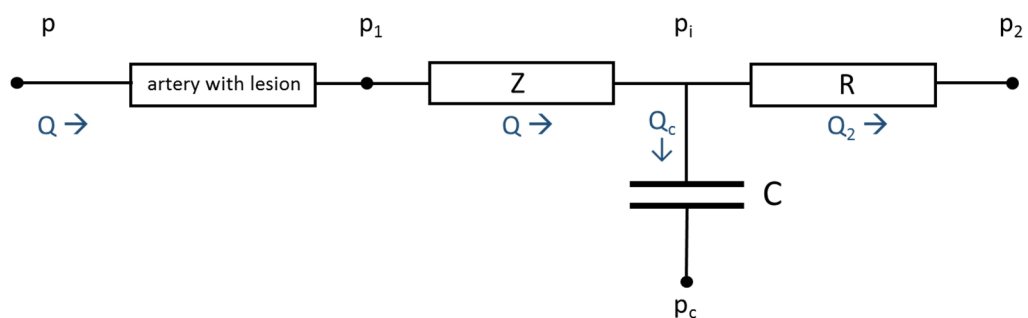
Figure 4.14. Electrical analogue model of the epicardial and myocardial circulations
P, pressure; Q, flow; Z, impedance; R, resistance; C, capacitance

According to **Figure 4.14**, the derivation of vFFR$_\text{ps-trns}$ is as follows:

$$K_2\mathbf{Q}^2 + K_1\mathbf{Q} + \mathbf{ZQ} = \mathbf{p} - \mathbf{p}_i \qquad \text{Eq 4.7}$$

$$\mathbf{RQ}_2 = \mathbf{p}_i - \mathbf{p}_2 \qquad \text{Eq 4.8}$$

$$\mathbf{Q}_i = \mathbf{C}\frac{d(\mathbf{p}_i - \mathbf{p}_C)}{dt} \qquad \text{Eq 4.9}$$

$$\mathbf{Q} - \mathbf{Q}_2 - \mathbf{Q}_i = \mathbf{0} \qquad \text{Eq 4.10}$$

Eliminating $\mathbf{Q}_i$:

$$\mathbf{Q} - \mathbf{Q}_2 = \mathbf{C}\frac{d(\mathbf{p}_i - \mathbf{p}_C)}{dt} \qquad \text{Eq 4.11}$$

Derive differential equation for Q given: $\mathbf{p}=\mathbf{p(t)}$, $\mathbf{p_2}=\mathbf{0}$, $\mathbf{p_C}=\mathbf{p_C(t)}$:

Eliminate $\quad \mathbf{Q}_2 = \frac{\mathbf{p}_i}{\mathbf{R}} = \frac{\mathbf{p} - K_2\mathbf{Q}^2 - (K_1 + \mathbf{Z})\mathbf{Q}}{\mathbf{R}} \rightarrow$

$$\mathbf{Q} - \frac{\mathbf{p} - K_2\mathbf{Q}^2 - (K_1 + \mathbf{Z})\mathbf{Q}}{\mathbf{R}} = \mathbf{C}\frac{d(\mathbf{p} - K_2\mathbf{Q}^2 - (K_1 + \mathbf{Z})\mathbf{Q} - \mathbf{p}_C)}{dt}$$

$$\text{Eq 4.12}$$

$$\mathbf{C}K_2\frac{d(\mathbf{Q}^2)}{dt} + \mathbf{C}(K_1 + \mathbf{Z})\frac{d\mathbf{Q}}{dt} + \frac{K_2\mathbf{Q}^2}{\mathbf{R}} + \left(1 + \frac{(K_1 + \mathbf{Z})}{\mathbf{R}}\right)\mathbf{Q} = \mathbf{C}\frac{d(\mathbf{p} - \mathbf{p}_C)}{dt} + \frac{\mathbf{p}}{\mathbf{R}}$$

$$\text{Eq 4.13}$$

$$\frac{2K_2}{(K_1 + \mathbf{Z})}\mathbf{Q}\frac{d\mathbf{Q}}{dt} + \frac{d\mathbf{Q}}{dt} + \frac{K_2\mathbf{Q}^2}{(K_1 + \mathbf{Z})\mathbf{RC}} + \left(\frac{K_1 + \mathbf{Z} + \mathbf{R}}{(K_1 + \mathbf{Z})\mathbf{RC}}\right)\mathbf{Q} = \frac{1}{K_1 + \mathbf{Z}}\frac{d(\mathbf{p} - \mathbf{p}_C)}{dt} + \frac{\mathbf{p}}{(K_1 + \mathbf{Z})\mathbf{RC}}$$

$$\text{Eq 4.14}$$

Numerical Solution

First order Forward Euler to solve for Q given p:

$$\left(\frac{2K_2}{(K_1 + Z)}\mathbf{Q}_j + 1\right)\frac{(\mathbf{Q}_{j+1} - \mathbf{Q}_j)}{\mathbf{dt}} + \frac{K_2\mathbf{Q}_j^2}{(K_1 + Z)\mathbf{RC}} + \left(\frac{K_1 + \mathbf{Z} + \mathbf{R}}{(K_1 + \mathbf{Z})\mathbf{RC}}\right)\mathbf{Q}_j$$

$$= \frac{1}{(K_1 + \mathbf{Z})}(\mathbf{dp})_j - \frac{1}{(K_1 + \mathbf{Z})}(\mathbf{dp_C})_j + \frac{\mathbf{p}_j}{(K_1 + \mathbf{Z})\mathbf{RC}}$$

<div align="right">Eq 4.15</div>

where: $\qquad\qquad (\mathbf{dp})_j = \left(\frac{dp}{dt}\right)_j \quad ; \quad (\mathbf{dp_C})_j = \left(\frac{dp_C}{dt}\right)_j$

$$\mathbf{Q}_{j+1} = \mathbf{Q}_j + \frac{\mathbf{dt}}{\dfrac{2K_2}{(K_1 + \mathbf{Z})}\mathbf{Q}_j + 1}\left(-\frac{K_2\mathbf{Q}_j^2}{(K_1 + \mathbf{Z})\mathbf{RC}} - \left(\frac{K_1 + \mathbf{Z} + \mathbf{R}}{(K_1 + \mathbf{Z})\mathbf{RC}}\right)\mathbf{Q}_j + \frac{((\mathbf{dp})_j - (\mathbf{dp_C})_j)}{(K_1 + \mathbf{Z})} + \frac{\mathbf{p}_j}{(K_1 + \mathbf{Z})\mathbf{RC}}\right)$$

<div align="right">Eq 4.16</div>

These equations were coded in Matlab in order to generate and plot pseudo-transient and vFFR results.

4.8.1.1.2   Computing non pseudo-transient vFFR results

Because FFR is a ratio of pressures, averaged over the cardiac cycle, a simpler method was developed and evaluated whereby mean inlet pressure was used and the 7-element Windkesssel was reduced to a single resistance value. Thus the simpler method computed 'steady' vFFR (vFFR$_{steady}$) as a function of just three parameters: mean proximal pressure, coefficients K_1 and K_2, and total distal CMV resistance (R_{total}). The proximal boundary condition was the mean, case-specific, catheter pressure. The workflow for this method is demonstrated in **Figure 4.15**. The derivation of the equation for calculating vFFR$_{steady}$ is described below. Because vFFR$_{steady}$ is calculated using mean inlet pressure it is only capable of predicting the mean pressure gradient. Although this is sufficient for generating a vFFR result, vFFR$_{steady}$ is not capable of generating pseudo-transient results.
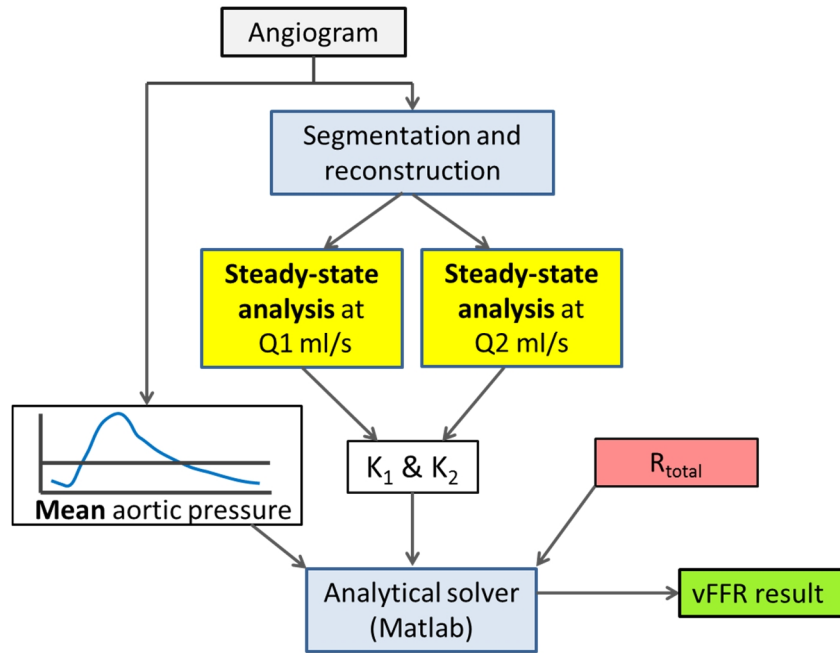
Figure 4.15. Workflow for steady vFFR (vFFR_{steady}).
*Model inputs parameters are reduced (compared with **Figure 4.13**) to K_1 and K_2; mean proximal pressure; and the total distal coronary microvascular resistance (R_{total}). Parameters in the red box (R_{total} only) are unknown, all others are known or can be derived.*

vFFR_{steady} was derived as follows:

$$P_a - P_d = K_1 \cdot Q + K_2 \cdot Q^2 \qquad \text{Eq 4.17}$$

Because $\Delta P = QR$ (where R is resistance) then:

$$P_a - (R_{CMV} \cdot Q) = K_1 \cdot Q + K_2 \qquad \text{Eq 4.18}$$

Where R_{CMV} is the total resistance of the coronary microvasculature. By deducting $K_2 \cdot Q$:

$$K_2 . Q^2 + (K_1 + R_{CMV}) Q - P_a = 0 \qquad \text{Eq 4.19}$$

Eq 4.20

And thus: $$Q = \frac{-(K_1 + R_{CMV}) + \sqrt{(ZK_1 + R_{CMV})^2 + (4 \cdot K_2 \cdot P_a)}}{2 \cdot K_2}$$

Therefore:
$$FFR = \frac{P_d}{P_a} = \frac{Q \cdot R_{CMV}}{P_a}$$
Eq 4.21

Since P_a is known and Q can be derived as above, *FFR* can be calculated as long as the value of R_{CMV} can be approximated. Again, these equations were coded in Matlab (by DRH) in order to generate and plot vFFR$_{steady}$ results

4.8.1.1.3   Computing vFFR using transient analysis

The precision and speed of vFFR$_{steady}$ and vFFR$_{ps-trns}$ solutions were compared with the fully transient, 0-D coupled vFFR model used in VIRTU-1 (vFFR$_{trns-0D}$) in a subset of cases. In order perform an appropriate comparison between the steady-state (vFFR$_{steady}$, vFFR$_{ps-trns}$) and transient coupled (vFFR$_{trns-0D}$) methods, on a case by case basis:

- the same volumetric meshes were used (using optimised parameters – see section 4.2)
- the same 0-D parameters representing the CMV were used
- the same case-specific proximal pressure was applied as the proximal boundary condition

Otherwise, vFFR$_{trns-0D}$ was computed consistent with the methods described in the VIRTU-1 trial (Chapter 3).

4.8.1.1.4   Statistical analysis

The diagnostic accuracy of the workflow (ability of vFFR to predict FFR < or >0.80) was assessed by calculating the sensitivity, specificity, positive predictive value, negative predictive value and overall accuracy. The agreeability between vFFR and FFR was assessed by calculating the bias, mean delta and standard deviation of the mean delta and was demonstrated graphically as a Bland-Altman plot (Bland and Altman, 1986). Time-dependent error between transient and pseudo-transient results is expressed as the instantaneous error expressed as the normalised root mean square (RMS norm). Because FFR is calculated using cycle mean values, the cycle averaged error between the means is also expressed. Pearson's correlation coefficient is used to demonstrate the strength of correlation between two variables. Unless stated otherwise, data are presented as mean (SD).

4.8.1.2 Results

4.8.1.2.1 Patient and clinical characteristics.

Data were collected from 20 patients. Their baseline characteristics are summarised in **Table 1**. In total 73 unique arterial datasets were studied which comprised: 34 left anterior descending, 21 right coronary, 3 diagonal, 7 left circumflex and 8 left main coronary arteries. 39 cases were pre-PCI, 25 cases were post-PCI and 9 cases did not receive a stent. 41 cases were under hyperaemic conditions and 32 were baseline measurements. The mean SYNTAX score was 10.45 and mean New York risk score was 0.22.

Table 4.14. Baseline characteristics.

Baseline characteristics	
Mean age, years (range)	66 (51-87)
Male	70%
Mean body-mass index (kg/m^2)	29.6 (3.4)
Comorbidities	
Hypertension	60%
Hyperlipidaemia	90%
Diabetes	30%
Current smoker	0%
Prior myocardial infarction	45%
Stroke	0%
Peripheral vascular disease	15%
Medication	
Aspirin	90%
Beta-blocker	65%
Nitrate	60%
Statins	90%
ACE inhibitors	45%
Calcium-channel blockers	25%
Clopidogrel	75%
ARBs	20%

Unless otherwise stated, all values are %. ACE = angiotensin-converting enzyme; ARB = angiotensin receptor antagonist.

4.8.1.2.2 Optimal flow steady-state flow pairing

438 steady-state simulations were performed (73 cases, each at 0.5, 1, 2, 3, 4, 5 ml/s), and each pairing combination was assessed. Consistent with the findings in section 4.7, when comparing error between the steady-state method (pseudo-transient) with measured FFR, the best overall accuracy was produced when K_1 and K_2 were derived from steady-state flows simulated at 0.5 and 5 ml/s (vFFR mean error vs measured values ±0.0043 (0.004)). However, neither of these flow-rates are physiological in the context of physiological significant CAD. Furthermore, at a flowrate

of 5 ml/s, one steady-state analysis became unstable and failed to converge to a satisfactory result due to excessively high Reynolds number (unrealistic physics for biological flow through a tight stenosis). For this reason, flow rate pairings of 1 and 3 ml/s were adopted for use in the vFFR$_{steady}$ and vFFR$_{ps-trns}$ workflows and all subsequent analyses are based on this pairing. This pairing is more representative of the prevailing underlying physiology, converged to a satisfactory result expediently in all cases, and was associated with an error which was only mildly higher than that of the 1 and 5 ml/s pairing (mean error ±0.0069 (0.005)).

4.8.1.2.3   Steady-state CFD analysis time

Using the 1 and 3 ml/s flow pairings, all 73 steady-state flow pairings converged successfully, at the first attempt, with no alteration to the protocol. The mean total time for paired steady-state analysis (the basis for the pseudo-transient and steady vFFR workflows) was 189.3 s (SD 34 s).

4.8.1.2.4   Accuracy of pseudo-transient vFFR

Agreement between vFFR$_{ps-trns}$ and measured FFR was high. In percentage terms, relative to measured values, mean vFFR$_{ps-trns}$ error was ±0.86% (0.60). These data are summarised in **Table 4.15** and a Bland-Altman plot is shown in **Figure 4.16**. vFFR$_{ps-trns}$ correlated closely with measured FFR ($R^2 = 0.998$, p<0.001). vFFR$_{ps-trns}$ achieved 100% sensitivity, specificity, positive predictive accuracy, negative predictive accuracy and overall diagnostic accuracy for diagnosing physiological lesion significance (FFR < or > 0.80). Aside from the computation of vFFR, pseudo-transient results were compared with those derived from measured values for goodness of fit i.e. instantaneous accuracy. An example of a measured transient versus pseudo-transient result is demonstrated in **Figure 4.17**. Over all 73 datasets the RMS norm between the pseudo-transient results and measured data was 0.37 (0.49). However, this was significantly better in the cases where FFR was <0.90 (RMS norm 0.15 (SD 0.34)).

4.8.1.2.5   Accuracy of vFFR$_{steady}$

Agreement between vFFR$_{steady}$ and measured FFR was also high (**Table 4.15**). A Bland-Altmann plot is shown in **Figure 4.16**. In percentage terms, relative to measured values, mean error was ±0.50% (0.40). vFFR$_{steady}$ correlated closely with measured FFR ($R^2 = 0.998$, p<0.001) and also achieved 100% sensitivity, specificity, positive predictive accuracy, negative predictive accuracy and overall diagnostic accuracy when diagnosing physiological lesion significance (FFR < or > 0.80).

4.8.1.2.6   Comparison with transient results

For comparison, the complex, 0-D coupled, fully transient method was compared with the $vFFR_{ps\text{-}trns}$ and $vFFR_{steady}$ methods. The mean time for the completion of the fully transient CFD analyses was 26 hours and 48 minutes (range: 6-48 hrs). The steady-state method therefore processed more than 500 times faster, in 0.20% of the time of fully transient analysis. Unlike the steady-state analyses, the transient CFD analyses often became unstable, necessitating reductions in the simulation time-step (at the expense of increasing computation time). Mean error for the transient method ($\pm$ 1.0%) was not statistically significantly different to $vFFR_{ps\text{-}trns}$ and $vFFR_{steady}$ methods in a small subset of 6 transient cases.

Table 4.15. Mean error, bias and error range of the pseudo-transient and steady vFFR methods relative to measured FFR values.

Group Method	N =	Mean error (SD)	Bias (SD)	Max error range*
All cases				
Pseudo-transient	73	$\pm$0.0070 (0.0045)	-0.0051 (0.0065)	-0.018 – +0.013
Steady	73	$\pm$0.0044 (0.0044)	$-6e^{-4}$ (0.0062)	-0.011 – +0.022
FFR <0.90				
Pseudo-transient	37	$\pm$0.0094 (0.0038)	-0.0080 (0.0063)	-0.018 – +0.013
Steady	37	$\pm$0.0050 (0.0049)	$-9.7e^{-5}$ (0.0070)	-0.011 – +0.022
FFR 0.70 – 0.90				
Pseudo-transient	29	$\pm$0.0098 (0.0037)	-0.0090 (0.055)	-0.018 – +0.013
Steady	29	$\pm$0.0048 (0.0045)	$-3.1e^{-4}$ (0.0067)	-0.011 – +0.022

Indicates worst underestimation – worst overestimation.

4.8.1.2.7   Areas of clinical interest

FFR is typically used to help determine the best course of action in borderline cases. Accuracy of both steady-state vFFR methods was therefore also assessed in the sub-groups of cases in which FFR was <0.90 (n=37) and FFR 0.70 - 0.90 (n=29) (**Table 4.15**). There was no statistically significant difference in the accuracy of either method when deployed in either sub-group or when deployed in all cases.

4.8.1.2.8   Generic boundary conditions

The influence of CMV resistance was further demonstrated by re-analysing all cases applying a generic (averaged) value of CMV resistance as the distal boundary condition. The effect this had on vFFR error is demonstrated in **Table 3**. Accuracy improved as the averaged value for CMV applied at the distal boundary better and more specifically reflected the coronary arterial sub-grouping.
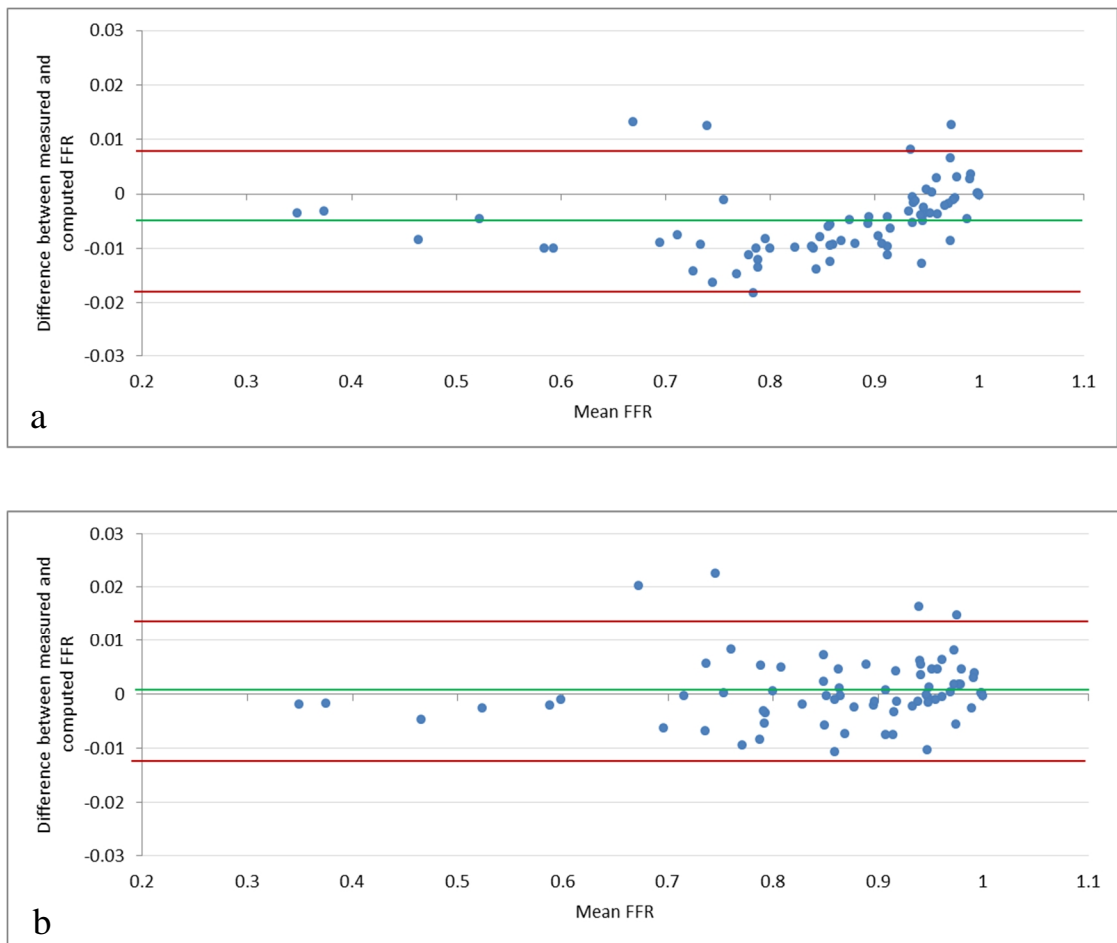
Figure 4.16. Bland-Altman plots demonstrating agreement between vFFR and measured FFR.
Panel A demonstrates agreement for vFFRps-trns and panel B demonstrates agreement for vFFR_{steady}. *The green lines indicate bias (mean delta, mFFR-FFR) and the red lines represent the limits of agreement (± 2 SD). Note the high number of cases in the clinically important FFR range from 0.7-0.9 (cf. VIRTU-1).*
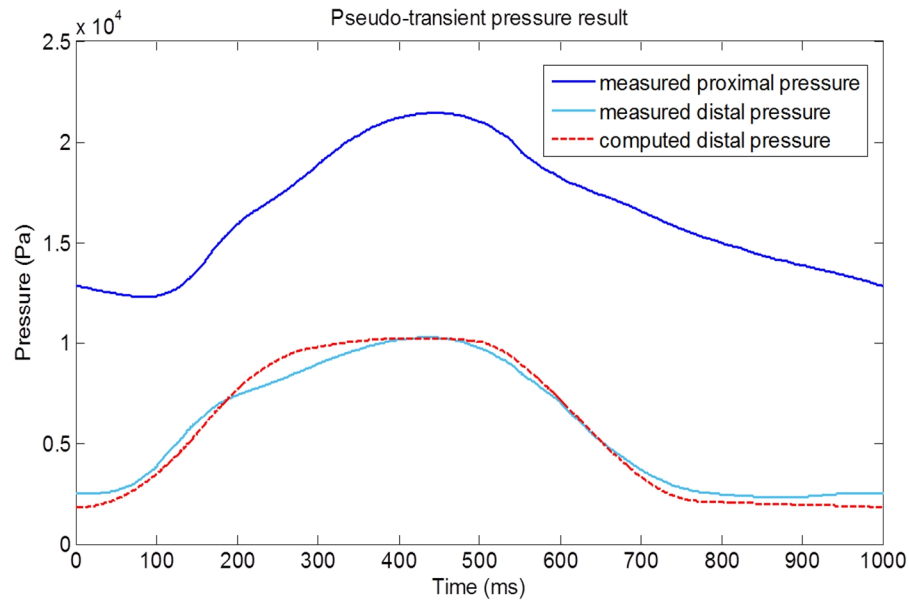
Figure 4.17. Pseudo-transient FFR results

An example of a pseudo-transient pressure result from a left anterior descending arterial case. Invasively measured FFR was 0.350 and the computed vFFR was 0.346. The pseudo-transient result closely matches the invasively measured result (RMS norm 0.026) despite no transient data being used in its computation.

Table 4.16 .The effect of applying generic (averaged) boundary conditions on quantitative and diagnostic error (vFFR$_{steady}$).

Basis upon which subgroup CMVR$_{total}$ averaging was performed	N datasets	Mean error (SD) of vFFR result	Bias (SD) (mean delta)	Diagnostic accuracy
All cases	73	±0.11 (0.12)	0.11 (0.12)	75%
Baseline and hyperaemic conditions	73	±0.096 (0.096)	0.088 (0.104)	52.1%
Right and left coronary arteries (under hyperaemic conditions)	40	±0.078 (0.079)	0.046 (0.102)	80%
Artery specific (LAD, RCA, DX, LMCA, LCX) (under hyperaemic conditions)	40	±0.0050 (0.0046)	-2.6 e^{-5} (0.0068)	82%
Case specific (no averaging)	73	±0.0044 (0.0044)	-6.0 e^{-4} (0.0062)	100%

CMVR$_{total}$, total coronary microvascular resistance; SD, standard deviation; LAD, left anterior descending artery; RCA, right coronary artery; DX, diagonal artery; LMS, left main coronary artery; LCX, left circumflex artery.

153

4.8.1.3 Discussion and chapter conclusions

In this chapter, two new methods were developed for the fast and accurate computation of vFFR. Both methods rely upon performing two steady-state CFD analyses to derive the linear and quadratic terms which characterise the relationship between pressure and flow for each unique arterial case. Both methods ran in approximately three minutes on a standard desktop PC (Dell Precision T5600, Intel Xeon processor, 32GB RAM) and, given an accurate measure of distal resistance, both methods quantified FFR with <1% error and were 100% accurate in diagnosing physiological lesion significance. These results suggest that time-consuming, high-powered computer processing for complex transient CFD analysis is not necessary for the computation of vFFR. Furthermore, steady-state analysis was more robust and reliable than full transient analysis which repeatedly became unstable in a number of cases. The magnitude of this acceleration means that vFFR can be computed in less time than it takes to measure FFR invasively with a pressure-sensitive wire. Both methods are the subject of a UoS patent application. CFD analysis is now no longer the rate limiting step in vFFR computation. Rather, segmentation, pre- and post-processing protocols are now the time-critical processes.

The ability to predict transient values without performing transient analysis is also a significant development. The quality of the fit between pseudo-transient and actual values is dependent upon the accuracy of the Windkessel parameters applied (CMV resistance, impedance, compliance and intra-myocardial systolic pressure). For methodological reasons, parameter derivation is improved when there is a greater difference between proximal and distal pressure signals. It is therefore, unsurprising that pseudo-transient agreement with values derived from measured values was better for cases where the FFR was lower. The accuracy and value of the pseudo-transient method are impressive and are applicable to a wide range of engineering applications (with, but not necessarily limited to, models with similar length-scales and Reynolds numbers) beyond the cardiovascular system and even beyond biological modelling. The pseudo-transient method retains the high temporal and spatial resolution of the transient analysis but relies upon faster and more robust steady-state analysis. The major drawback of the pseudo-transient method is that, in addition to K_1 and K_2, it requires the application of 7 parameters (impedance, resistance, compliance and 4 parameters describing the timing and amplitude of intramural myocardial systolic pressure), whereas the steady method only requires resistance (**Figure 4.13** and **Figure 4.15**). Deriving these parameters may be simple in non-biological modelling, but remains a significant challenge for the current application.

Apart from lesions causing chronic total obstruction, all patterns and severities of CAD including LMS disease were included in this study. The current study therefore reflects 'real world' working practice and is widely applicable which is unlike VIRTU-1 which focused primarily on simple, type A lesions. A further strength of the current methods was that they can be applied to any arterial geometric reconstruction including CAG and CCTA.

Now that feasibility has been demonstrated and acceleration of the simulation method has been achieved, the primary limitation of the model is the tuning of the distal boundary condition. In this study the parameters of the CMV were inferred from a process relying upon invasive measurement. The application of completely generic boundary conditions yielded inferior accuracy. When we applied sub-categorised averages based upon arterial sub-type, accuracy improved, supporting the notion that the precision of the CMV resistance is critical to computing physiological lesion significance. In a truly predictive study, where invasive measurement is avoided, these would not be known. This was appropriate in the current study because the aim was to develop and validate a method of vFFR computation which could operate within timescales which are practical for real-time use in the cardiac catheter laboratory. Tuning the boundary conditions to reflect CMV physiology now represents the single greatest challenge for vFFR prediction. For this reason, the success of $vFFR_{steady}$ in particular is encouraging because this method is associated with just a single unknown parameter, as opposed to $vFFR_{ps-trns}$ which is associated with 7 unknown parameters. The tuning of the distal boundary condition is the focus of Chapter 5.

Chapter Five:

The Distal Boundary Condition

5.1 Introduction

In Chapter three I demonstrated the development and validation of an *in silico* model capable of simulating intracoronary physiology and predicting vFFR. Three major limitations of the model were identified; (i) prolonged computation times, (ii) methodological imprecision of the segmentation and reconstruction algorithm and (iii) the lack of personalisation in the design and tuning of the 0-D model used to represent the distal boundary condition. In Chapter four I demonstrated the development and validation of a novel method based upon paired steady-state analyses for accelerating the CFD simulation enabling the computation of results within timescales

which are tractable for use in making treatment decisions in the cardiac catheter laboratory. Collaborative work being performed in parallel to this thesis is focusing on the development of improved segmentation protocols (Cimen et al., 2014). Optimising the segmentation algorithms is achievable but is beyond the scope of the current thesis. The tuning of the boundary conditions therefore represents the final major limitation and challenge of the VIRTUheart™ model.

In the VIRTUheart™ model, the proximal inlet condition is known because pressure is continuously monitored from the catheter tip during ICA. The arterial wall is a boundary, and this condition is regarded as a rigid wall. This approach has been demonstrated to be acceptable in certain contexts including the coronary circulation (Zeng et al., 2003, Zeng et al., 2008, Jeays et al., 2007, Brown et al., 2012). Therefore, the major challenge lies in tuning the distal boundary condition. I have already demonstrated the improvement in accuracy using patient-specific tuning of the distal boundary conditions, versus the application of generic tuning (Chapter 3). The design and tuning of the distal boundary condition at an individual patient level represents, universally, the principal challenge facing the vFFR modelling community at the current time (Morris et al., 2015).

This chapter is divided into three sections: the first (section 5.2) focuses on the appropriateness of the design of the model used to represent the distal boundary condition; the second section (section 5.3) explores the importance of patient-specific tuning of the distal boundary; and the final section (section 5.4) describes the development of a novel method for patient-specific model tuning.

5.2 Modelling the distal boundary condition

Before a strategy for tuning the parameters of the distal boundary condition is developed, it is important that the design and implementation of the applied model is appropriate. Because it is impossible to represent the many myocardial micro-vessels within the 3-D domain of the model, VIRTU-1 applied a zero-dimensional (0-D), lumped parameter model at the arterial outlets/s to represent the distal physiological conditions.

5.2.1 Zero-dimensional models

0-D models incorporate a number of distributed physical schemes into a single, concise, simplified physical description. They lump all the parameters within a particular compartment of the cardiovascular system together to characterise the global behaviour of the entire compartment within a single relationship. The more physical compartments which are incorporated into a single

representation, the greater the number of assumptions which are made, and the greater the simplification of reality. This global characterisation lacks spatial dimensions (hence the terms 'lumped parameter' and 'zero-dimensional') because the variables (e.g. flow, pressure, capacitance, concentration) are regarded as spatially uniform, varying only in time. Coupling a lower order model to a 3-D model such as in VIRTUheart™ is efficient because it allows detailed analysis in the 3-D region without the need for high temporal and spatial refinement on regions beyond this. In the context of vFFR, this approach is ideal because the spatial distribution of physiological parameters within the CMV is not of clinical interest or methodological importance. Rather, it is the global influence that this compartment has on the pressure distal to a coronary lesion within the 3-D domain which is critical, and this is precisely what this model design provides. Furthermore, from a clinical perspective, CMV pathophysiology is described, characterised and investigated globally, for example, in terms of coronary microvascular resistance (CMVR) which is a marker of coronary microvascular dysfunction and a key influence upon FFR (Knaapen et al., 2009) (see section 5.4.1.2).

5.2.1.1 Lumped parameter modelling: the arterial Windkessel

The 0-D Windkessel (air chamber) model is most commonly used to represent compliant arterial physiology and is described in Chapter 3.3. Rather than representing the entire CMV within a single compartment, it is possible to discretise the system into a number of lumped parameter models according to different segments or branches of the arterial system in a distributed manner (Westerhof et al., 2010). This is the approach taken in preceding chapters and also by Taylor et al in modelling vFFR$_{CT}$ (Taylor et al., 2013).

5.2.2 What is the best Windkessel design?

As described previously, the coronary circulation is unique in that the resistance varies with the phase of the cardiac cycle due to compression of the CMV during systole. Numerous previous modelling studies of coronary physiology have ignored this phenomenon within models which, in the main, prescribe rather than predict coronary flow (Santamarina et al., 1998, Berry et al., 2000, Myers et al., 2001, Zeng et al., 2003, Boutsianis et al., 2004, Gijsen et al., 2008, Zeng et al., 2008) or which use idealised geometries with low mesh resolution (Lagana et al., 2005, Migliavacca et al., 2006). The influence of myocardial contraction must be represented within the model if realistic flow profiles are to be modelled. Thus far, VIRTUheart™ has represented this phenomenon by applying a transient pressure (voltage) at the terminal node of the capacitor in the three-element (Z_c-C-R) Windkessel model. Taylor et al describe a more complex five-element Windkessel model used to represent the CMV in a 3-D model of coronary physiology which is

similarly deployed within a hybrid 3-D, 0-D (Z_c-C_1-R_1-C_2-R_2) model (Kima et al., 2010, Taylor et al., 2013). In this model, the back-pressure (P_b) is applied at the second capacitor arranged in series. Theoretically, the five-element model may better reproduce CMV physiology because the additional elements allow the coronary arteriolar and venous physiology to be individually simulated. However, the overall effects on predicted coronary flow remain unknown. **Figure 5.1** demonstrates the three- and five-element Windkessel model designs. This first section of the current chapter focuses on determining an appropriate 0-D design for representing the CMV in the context of vFFR modelling.

a

b
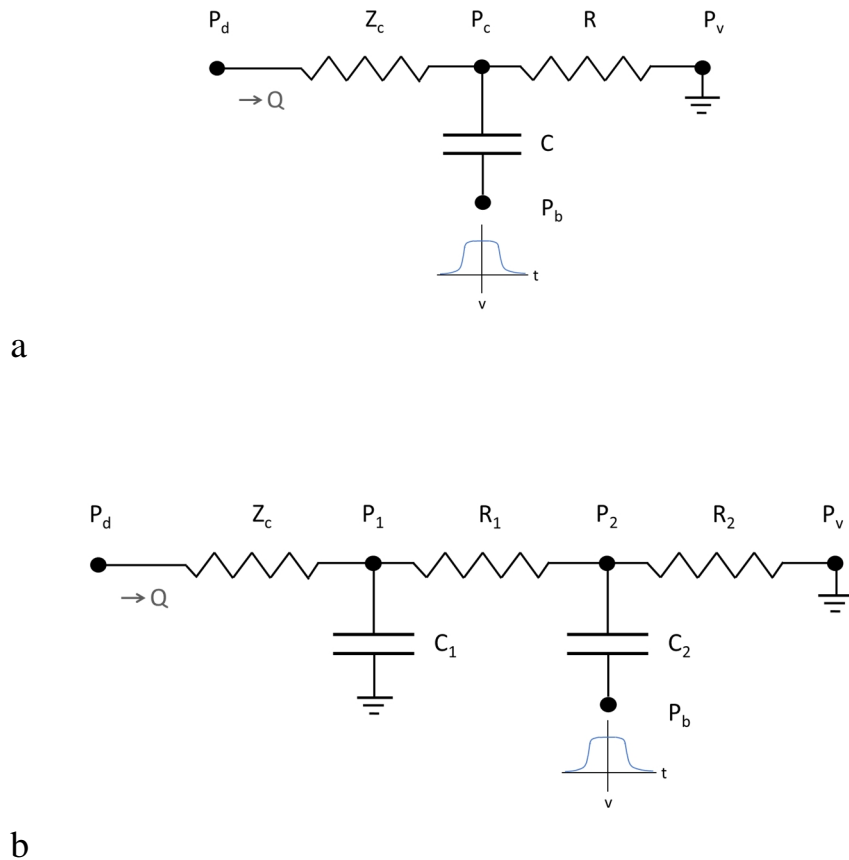
Figure 5.1. The simple and complex Windkessel models
(a) The simple three-element model applies the ventricular back-pressure (Pb) at the terminal node of the capacitor. (b) In the complex five-element model, the first capacitor (C1) discharges to earth whereas the ventricular back-pressure is applied to the second capacitor (C2). Pd, distal pressure; Zc, characteristic impedance; Pc, pressure at the capacitor; R, resistor; Pv, venous pressure; Q, flow.

5.2.3 Method

There is no established or recognised method for evaluating the precision of a 0-D model in representing distal CMV physiology. It was therefore proposed that a Windkessel model could be evaluated by its ability to reproduce realistic coronary flow profiles, especially in the context of the coronary circulation where the myocardium complicates the P-Q relationship. A good Windkessel design will produce a realistic flow profile, whereas a poor Windkessel will fail in this regard. The ability to reproduce realistic coronary flow and the ability to generate an accurate vFFR result are not mutually exclusive. This has already been demonstrated in Chapter 4 with the vFFR$_{steady}$ method which represented the CMV as single resistance element. Whilst this method estimates vFFR and mean coronary flow accurately, it is unable to replicate transient flow physiology which may yield additional information about coronary physiology.

A scheme was developed whereby an analytical solution was formulated for the 0-D domain. This was used to compute transient coronary flow (Q$_{optim}$) from the transient pressure measured by the pressure-sensitive angioplasty wire during ICA. The goodness of fit (least squares, RMS error, similar to Chapter 4) was then calculated relative to the actual coronary flow at this point. However, because transient volumetric coronary flow is very challenging to measure *in vivo*, the reference standard was provided by CFD computed flow (Q$_{3-D}$) consistent with the methods demonstrated in **Figure 5.2** below and as described in Chapter 3 and 4. The hypothesis for this strategy was that an appropriate 0-D model would provide an analytical solution similar (least RMS error) to transient 3-D transient analysis.

However, in order to generate the best fit, the system requires the appropriate parameters to be programmed. It is important that the parameters applied are first, accurate for the particular patient case and second, applied consistently between models when making comparisons. In Chapter 3, a manual parameter optimisation process was used within Matlab to tune Z_c, C and R according to a least squares fit. This is labour-intensive and imprecise. Therefore an optimisation process was developed which extracted the optimal parameters for the least squares fit between the analytical and 3-D solutions.
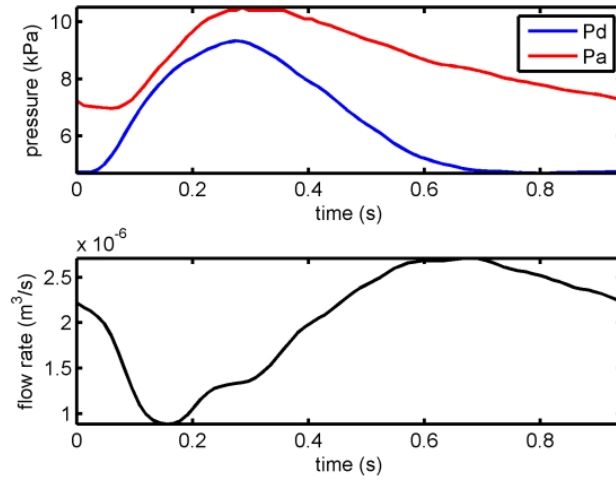
***Figure 5.2. An example of computed flow (Q3-D) derived from measured pressure
boundary conditions***
*For a borderline left anterior descending coronary arterial case (mFFR = 0.78).
(a) Measured proximal (P$_a$) and distal (P$_d$) pressures are used as boundary
conditions for the 3-D CFD analysis. (b) Computed flow (Q$_{3-D}$) demonstrating
systolic flow predominance (time 0 corresponds to the ECG R wave).*

5.2.3.1   Parameter optimisation: extracting the boundary conditions

An optimisation scheme was developed which identified the optimal combination of 0-D
parameters that together, returned the flow profile (Q$_{optim}$) that was closest approximation (i.e.
minimal error) to the flow derived from the 3-D analysis (Q$_{3-D}$). The developed scheme was based
upon the work of Lungu *et al* in which Windkessel parameters were derived for a model of
pulmonary arterial hypertension (Lungu et al., 2014). The developed model comprised a genetic
algorithm (GA), followed by a local gradient descent (GD). The GA is a class of stochastic
searching strategies, modelled on Darwinian evolutionary mechanisms, a popular strategy to
optimise non-linear systems with a large number of variables. The GA searches quickly through a
large, diverse combination of parameters analogous to a randomly generated 'population' of
parameter combinations. For each combination of parameters, Q$_{optim}$ is evaluated relative to Q$_{3-D}$
via the least squares fit:

$$RMS\ error = \sqrt{\sum_{t=1}^{n} \left(Q_{3-D}(t) - Q_{optim}(t) \right)^2} \qquad \text{Eq 5.1}$$

The best combinations are then selected and then crossed with other selected combinations in order
to produce, in theory, a population of even 'fitter' offspring combinations carrying forward the best
traits from each parent combination. This process is then repeated over a number of generations
until the best combination is selected with the cost function being the RMS error. This combination

provides the input to the second routine, the gradient descent algorithm which refines the output of the GA by searching for local minima in the RMS error within the solution space. Both the GA and the GD were implemented in Matlab using the optimisation toolbox. The output was the single best combination of 0-D parameters for that particular case along with the RMS error associated with that combination, relative to Q_{3-D}.

5.2.3.2 Ventricular back-pressure

As demonstrated in **Figure 5.2**, coronary blood flow predominates during ventricular diastole due to the increased CMVR during systole. In the 0-D model this is represented as a back-pressure (P_b) which is applied to the terminal node of the capacitance. The back-pressure is defined according to five parameters: *amplitude*, *sine curve power*, *ramp up, plateau*, and *ramp down* (see **Figure 5.3**). The amplitude of the back-pressure is defined as a fraction of P_a and the latter three parameters are defined as a fraction of the period. The curve power is fixed at two (i.e. $\sin^2$). Therefore, there are four variables used to define the back pressure on an individual case basis.
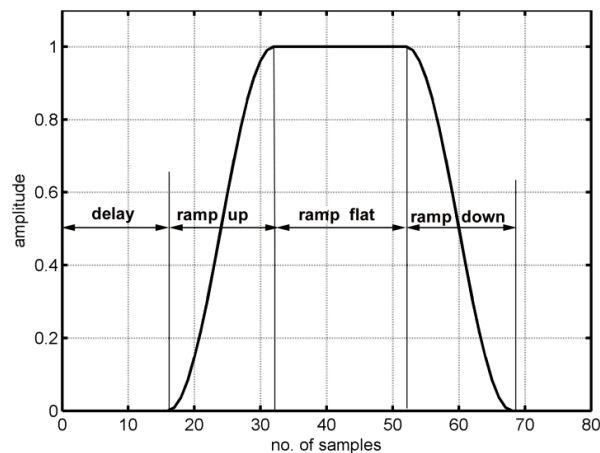
Figure 5.3. Ventricular back-pressure (P_b)
Ventricular back-pressure is defined by the amplitude, ramp up, plateau and ramp down. The amplitude is informed by the mean systolic P_a trace whilst the aortic valve is open and the optimisation algorithm optimises $P_{amp\text{-}fraction}$ which, when multiplied by P_{amp} defines the amplitude of the ventricular back-pressure.

In Chapter 3, a generic back-pressure was applied for right and left coronary cases based upon averaged data. In the current analysis, these four parameters of ventricular backpressure were optimised along with Z_c, C and R. Therefore, the three-element Windkessel was in fact comprised of seven (variable) elements, all of which require optimisation. Any case- or patient-specific information which can be used to inform the tuning of the Windkessel parameters should be

exploited. Since the P_a signal reflects intraventricular pressure during systole, this can be used as a guide to the back-pressure amplitude. However, the Pa signal only reflects intra-myocardial physiology when the aortic valve is open. Early attempts to use ECG timing to define this period were fruitless, likely due to inter-individual variability in cardiac electromechanical coupling. Instead, this period was identified from the Pa pressure trace as the period commencing when Pa begins to rise (corresponding with aortic valve opening) until the dicrotic notch (corresponding with aortic valve closure). Because the pressure data were derived from ensemble averaging the dicrotic notch was smoothed and difficult to identify. Therefore, the dicrotic notch was identified as the point when the polynomial interpolation (used to approximate complicated curves) of the Pa time derivative reaches its minimum (see **Figure 5.4**). The amplitude (P_{amp}) is calculated as the mean value of the aortic pressure between aortic valve opening and closing. The value of the back-pressure applied to the 0D model (P_b) is calculated as:

$$P_b = P_{amp} \cdot P_{amp\_frac} \hspace{2cm} \text{Eq 5.2}$$

In this way, readily available patient-specific data from the ICA procedure were used to inform the 0-D model parameters. This routine was algebraically coded in Matlab by PDR.
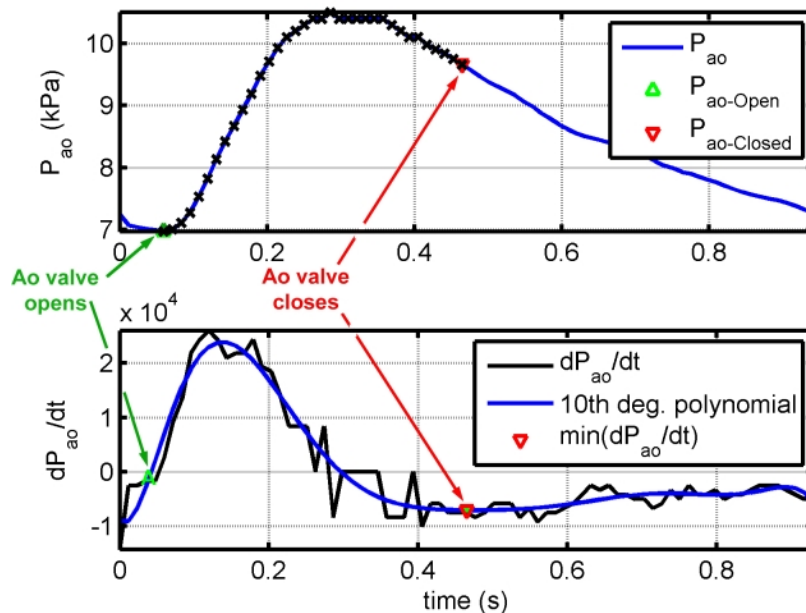
Figure 5.4. Identifying aortic valve opening and closure
The top diagram demonstrates the P_a trace and the points of aortic valve opening and closure. The bottom panel demonstrates the time derivative of P_a (dP/dt) along with the polynomial. The minimum point of the polynomial (min dP_{ao}/dt) corresponds to aortic valve opening.

5.2.3.3 Evaluation

An analytical solution was derived for the three- and five-element Windkessel models. In each case, this was implemented in Matlab as a direct solver (coding by PDR). Analytical solutions were tested against the numerical solution method which were based on the backward Euler method. Because the underlying phenomenology is periodic in time, a Fourier series representation of each analytic solution was used.

The inputs to the optimisation algorithm were the two pressure waveforms (P_a and P_d) and the transient volumetric flow rate through the lesion simulated by the 3-D model using *measured* pressure boundary conditions ($Q_{3\text{-}D}$). The number of parameters optimised depends upon the model in question; three plus four for the simple (Z_c, R and C plus P_{amp}, ramp up, flat and ramp down) and five plus four for the complex model (Z_c, C_1, R_1, C_2 and R_2 plus P_{amp}, ramp up, flat and ramp down). However, total resistance (R_{total}) is known because of Ohms law:

$$R_{total} = (Z_c + R)_{simple} = (Z_c + R_1 + R_2)_{complex} = \frac{\overline{P_d}}{\overline{Q}} \qquad \text{Eq 5.3}$$

Because $\overline{Q}$ is known from the $Q_{3\text{-}D}$ solution, the number of parameters which need optimising is reduced by one in each model. However, in both models, four parameters characterising the back-pressure are also required. Therefore, the simple model is in fact a seven element optimisation and the complex model a nine-element model. The GA allowed the range of possible results for each parameter to be constrained in a sensible manner in order to narrow the solution space in which the GA searches. In addition to evaluating the simple and complex model, a delay function was also evaluated (see **Figure 5.3**). This additional parameter allowed the commencement of the ventricular back-pressure signal to be varied and optimised in each case

Patient data from the Wellcome Trust and Department of Health HICF study (section 5.4.2, page 183) were collected. Data from 20 patients with stable CAD were collected. 3-D arterial geometries were segmented and reconstructed from ICA as previously described (Chapter 3). Transient flow was simulated with measured pressure boundary conditions for all arterial datasets under baseline and hyperaemic flow conditions and pre- and post-PCI where appropriate. These data were used to compute the amplitude of P_{amp} as described in section 5.2.3.2. All cases were then processed with the optimisation protocol described above. The boundary condition parameters were extracted, as was the RMS error in each case (relative to $Q_{3\text{-}D}$).

5.2.4 Results

An example set of results for the simple and complex model, with and without delay, in each of the physiological states for a LAD artery case is demonstrated in **Figure 5.5** and in **Figure 5.6** overleaf (legends are below).

Figure 5.5 (next page). An example of the optimisation results for the simple (Z_cRC) and complex (Z_cRCRC) models with (-D) and without (-ND) delay, under baseline and hyperaemic flow conditions for a single case (for case V001, LAD, same as Figure 5.5 & Figure 5.6), pre-PCI

In the top row of each case, the P_a and P_d pressure traces are seen along with the optimised back-pressure trace. In the bottom row, the flow computed from measured values and the flow computed by the direct solver with the optimised parameters are plotted alongside each other. The RMS error is displayed in each case.

Figure 5.6 (subsequent page). An example of the optimisation results for the simple (Z_cRC) and complex (Z_cRCRC) models with (-D) and without (-ND) delay, under baseline and hyperaemic flow conditions for a single case (for case V001, LAD, same as Figure 5.5 & Figure 5.6), post-PCI

*The results of the same case as **Figure 5.5** are demonstrated post-PCI. Note the increased RMS errors indicating inferior goodness of fit after revascularisation, especially under baseline flow conditions in the simple model (red outline). This is likely to be due to decreased dP when computing the 3-D flow with measured pressure boundary conditions. Abbreviations same as **Figure 5.5**.*
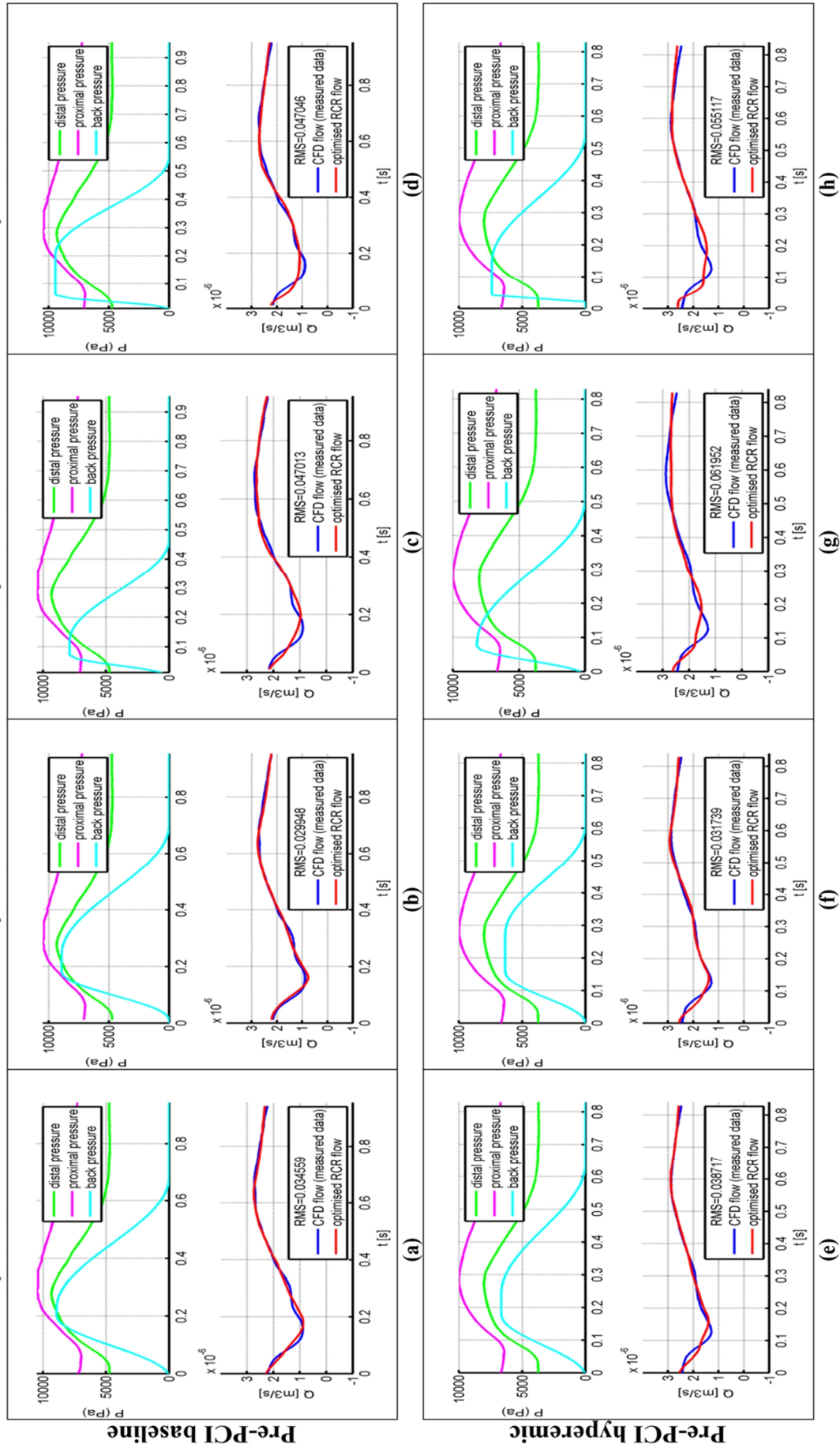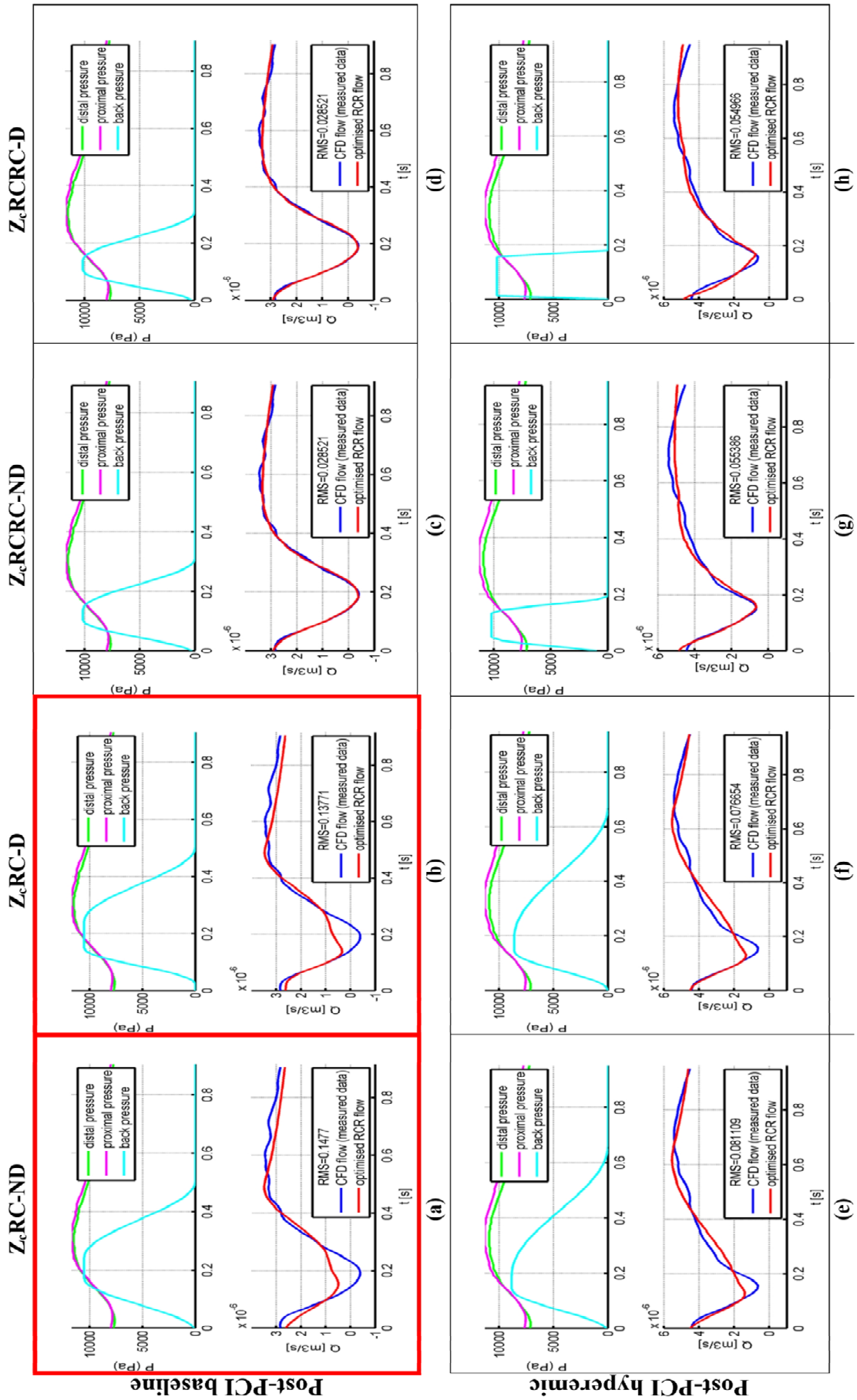
5.2.4.1.1   Constraining the model and the solution space

During preliminary testing it was observed that, without constraint, model parameter results were optimised to supra- or sub-physiological levels in some cases.   Although these parameter combinations were often associated with advantageous RMS errors, since the aim was to develop a physiological, rather than a phenomenological model individual model parameters were constrained within physiological limits.   Initially, the five-element model returned results with significantly higher RMS error than the three-element model.   The level of error was reduced when parameter constraints were manipulated on an individual case basis but this was a time-consuming process.   Stability of the solution was demonstrated by optimising a single case 100 times for each model and assessing the coefficient of variation (SD/mean) of each parameter.   The results are demonstrated below in **Table 5.1**and **Table 5.2**.

Table 5.1. Coefficient of variation of each optimization parameter of the simple model after 100 runs

	Z_c	C	R	$P_{amp-frac}$	Rp up	Rp flat	Rp down	RMS
Coefficient of variation	5.9e-7	4.5	0.6	0.03	0.07	0.5	0.09	0.1

for case V001 LAD, same as Figure 5.5 & Figure 5.6

Table 5.2. Coefficient of variation of each optimization parameter of the complex model after 100 runs

	Z_c	R_1	R_2	C_1	C_2	$P_{amp-frac}$	Rp up	Rp flat	Rp down	RMS
Coefficient of variation	0.11	0.7	0.6	7.9	3.8	0.07	0.4	0.6	0.13	0.19

*for case V001 LAD, same as **Figure 5.5** & **Figure 5.6***

In both models, the impedance was stable.   In the simple model, capacitance was least stable.   The situation was more complex in the five-element model where the variation in R_1, R_2, C_1 and C_2 is significant.   The optimisation algorithm did not 'know' how to distribute these values between the elements.

Once constraints were individually manipulated, the complex model appeared to cope better with the low flow region during diastole in the post-PCI cases than the simple model which struggled in this region (see **Figure 5.6** a, b, c and d).   As discussed previously, it is not practical to manually tune parameter constraints for every case, especially since the only advantage was in cases of least clinical importance i.e. post-PCI cases where there is little separation of pressure during the systolic pressure ramp-up phase.   For this reason, the five-element model was not considered further.

5.2.4.1.2   Results from the simple model

Twenty patient cases were analysed. These yielded 74 individual datasets which comprised a mixture of coronary artery cases and physiological states as outlined in **Table 5.3**. Patient and angiographic details are described in **Table 5.4**.

Table 5.3. Case-specific characteristics of the Windkessel analysis

Case Description	Number
Coronary Artery	
LAD	12
RCA	7
Diagonal	1
Circumflex	3
Left main stem	4
Physiological state	
Pre-PCI	37
Post-PCI	26
Baseline Flow	29
Hyperaemic Flow	40
Total Cases	*74*

Table 5.4. Baseline characteristics of the patients studied

General demographics	
Mean age, years	67 (9)
Male	80%
Mean body-mass index, Kg m^{-2}	30.1 (4.0)
Comorbidities	
Hypertension	60%
Hyperlipidaemia	65%
Type 2 Diabetes Mellitus	30%
Current smoker	0%
Prior myocardial infarction	50%
Angiographic details	
Dominance	85% right
	5% left
	10% co-dominant
SYNTAX	10.8 (6.8)
New York Risk Score	0.31 (0.39)

Values are mean (SD) unless stated as % .

The effect of adding the delay function is demonstrated in **Table 5.5**. As expected, the delay function had a significant effect upon the 'ramp-up' fraction (0.27 (0.090) vs 0.19 (0.093), p=0.01),

without effect upon any other parameter. More specifically, as there was no beneficial effect upon bias, mean or RMS error the delay function was not considered further.

Table 5.5. Comparing parameter values and precision of the simple model with and without delay.

	Mean value (Z_cCR – delay)	Mean value (Z_cCR + delay)	Significance P=
Parameters			
Z_c	1.73 e10 (5.4E10)	1.73E10 (5.4E10)	0.99
C	1.95 (1.68E2)	1.32E-3 (6.1E-3)	0.32
R	1.62E9 (6.1E9)	1.62E9 (6.1E9)	1.0
$P_{amp-frac}$	8.61E-01 (0.19)	8.61E-01 (0.19)	0.91
Ramp up	0.27 (0.090)	0.19 (0.093)	0.01*
Ramp flat	0.20 (0.080)	0.20 (0.088)	0.58
Ramp down	0.20 (0.128)	0.21 (0.128)	0.80
Delay	NA	0.032 (0.016)	
Precision			
Bias	1.40E-3 (2.77 e-3)	1.25E-3 (2.77E-3)	0.69
Mean error	2.31E-3 (2.05 e-3)	2.24 (2.0E-3)	0.78
RMS error	0.21 (0.25)	0.20 (0.25)	0.86

Data presented as mean (SD). Z_c, Impedance; C, capacitance; R, resistance

Again, the effect of running the optimisation 100 times was assessed to see if stability was increased. Due to time constraints, this was done on the first 60 arterial datasets (patients 1 – 12). The results are presented in **Table 5.6**. There was no effect upon result stability or any marker of precision. The three element model was therefore considered stable.

Results across all cases and for patient subgroups for the three-element model are presented in **Table 5.7**. In comparing the FFR < 0.90 and FFR ≥ 0.90 groups, resistance and $P_{amp-frac}$ were both higher in the FFR ≥ 0.90 group (1.60E+08 vs 2.97E+09, p=0.046) whereas the ramp-down duration was decreased in the FFR ≥ 0.90 group (0.247 vs 0.156, p=0.02). The most important difference between the groups was the increase improvement (decrease) in RMS error in the FFR < 0.90 group (0.073 vs 0.333, p = <0.0001). The effect upon accuracy of the mean flow result was negligible (2.14E-03 vs 2.46E-03, p = 0.51). When comparing pre- versus post-PCI cases, there was a small but statistically significant increase in impedance (7.11E+09 vs 1.88E+10, p = 0.02), resistance (4.03E+08 vs 1.97E+09, p = 0.007) and $P_{amp-frac}$ (0.801 vs 0.936, p=0.009). Ramp-down fraction was significantly shorter post-PCI (0.231vs 0.164, p = 0.036). RMS error was significantly reduced in the group with the more significant pressure drop (0.113 vs 0.331, p = <0.001) whereas error in the computed mean flow was similar (2.13E-03 vs 2.49E-03, p= 0.51).

Table 5.6. Comparing a single optimisation run with the single best from 100 runs

Factor	Value from a Single run	Best (SD) value 100 runs	Significance P=
Parameter			
Z_c	1.96E+10 (5.89E+10)	1.96E+10 (5.89E+10)	0.99
C	6.25E-04 (4.04E-03)	2.06E+02 (1.64E+03)	0.17
R	1.92E+09 (6.61E+09)	1.96E+09 (6.60E+09)	0.96
$P_{amp-frac}$	8.66E-01 (1.95E-01)	8.66E-01 (1.94E-01)	0.99
Ramp up	2.13E-01 (9.51E-02)	2.16E-01 (9.83E-02)	0.83
Ramp flat	1.93E-01 (8.72E-02)	1.89E-01 (8.23E-02)	0.69
Ramp down	2.03E-01 (1.33E-01)	2.13E-01 (1.30E-01)	0.55
Precision			
Bias	1.40E-03 (2.82E-03)	1.31E-03 (2.79E-03)	0.81
Mean error	2.29E-03 (2.15E-03)	2.21E-03 (2.15E-03)	0.75
RMS error	2.23E-01 (2.63E-01)	2.65E-01 (2.65E-01)	0.91

Table 5.7. Optimised parameters for the three-element Windkessel

Group	N	Z_c (Pa.s/m³)	C	R (Pa.s/m³)	$P_{amp-frac}$	Ramp up	Ramp flat	Ramp dwn	Bias	±Mean Error	RMS error
All cases	74	1.72E+10 (5.41E+10)	19.48 (167.61)	1.60E+09 (6.08E+09)	0.857 (0.196)	0.224 (0.084)	0.200 (0.086)	0.200 (0.128)	1.40E-03 (2.76E-03)	2.31E-03 (2.06E-03)	0.207 (0.247)
Non-PCI BL	4	1.20E+11 (2.19E+11)	360.46 (720.93)	1.25E+10 (2.49E+10)	0.899 (0.124)	0.155 (0.059)	0.222 (0.131)	0.080 (0.044)	7.25E-04 (3.60E-03)	2.95E-03 (1.43E-03)	0.351 (0.432)
Non-PCI hyp	6	6.11E+09 (4.14E+09)	2.32E-04 (3.28E-04)	3.59E+08 (6.10E+08)	0.843 (0.137)	0.207 (0.013)	0.235 (0.081)	0.240 (0.145)	1.24E-03 (2.56E-03)	2.20E-03 (1.61E-03)	0.164 (0.250)
Pre-PCI BL	16	1.03E+10 (5.85E+09)	4.99E-05 (7.39E-05)	7.67E+08 (8.38E+08)	0.907 (0.180)	0.241 (0.103)	0.176 (0.095)	0.176 (0.112)	1.43E-03 (1.66E-03)	1.77E-03 (1.25E-03)	0.153 (0.135)
Pre-PCI hyp	22	4.78E+09 (2.47E+09)	4.24E-04 (7.92E-04)	1.38E+08 (2.75E+08)	0.724 (0.233)	0.230 (0.076)	0.201 (0.091)	0.272 (0.105)	1.80E-03 (2.29E-03)	2.39E-03 (1.63E-03)	0.084 (0.070)
Post-PCI BL	12	2.44E+10 (3.81E+10)	4.74E-06 (1.64E-05)	2.60E+09 (4.29E+09)	0.979 (0.072)	0.236 (0.055)	0.200 (0.069)	0.112 (0.083)	2.11E-03 (1.00E-03)	2.15E-03 (9.20E-04)	0.356 (0.317)
Post-PCI hyp	14	1.40E+10 (2.14E+10)	3.37E-04 (8.04E-04)	1.43E+09 (2.44E+09)	0.899 (0.165)	0.213 (0.112)	0.202 (0.079)	0.209 (0.153)	3.96E-04 (4.78E-03)	2.79E-03 (3.83E-03)	0.311 (0.304)
FFR <0.90	36	5.41E+09 (3.30E+09)	4.28E-04 (7.73E-04)	1.60E+08 (3.40E+08)	0.754 (0.221)	0.238 (0.091)	0.198 (0.092)	0.247 (0.106)	1.63E-03 (2.10E-03)	2.14E-03 (1.56E-03)	0.073 (0.043)
FFR ≥0.90	38	2.84E+10 (7.42E+10)	37.94 (233.90)	2.97E+09 (8.30E+09)	0.955 (0.099)	0.211 (0.077)	0.201 (0.082)	0.156 (0.133)	1.19E-03 (3.28E-03)	2.46E-03 (2.45E-03)	0.333 (0.291)
	P	0.07	0.33	**0.046**	**<0.001**	0.18	0.88	**0.002**	0.49	0.51	**<0.0001**
Pre-PCI	38	7.11E+09 (5.00E+09)	2.66E-04 (6.27E-04)	4.03E+08 (6.53E+08)	0.801 (0.229)	0.235 (0.087)	0.190 (0.092)	0.231 (0.117)	1.64E-03 (2.03E-03)	2.13E-03 (1.50E-03)	0.113 (0.106)
Post-PCI	26	1.88E+10 (3.01E+10)	1.84E-04 (6.04E-04)	1.97E+09 (3.40E+09)	0.936 (0.134)	0.224 (0.090)	0.201 (0.073)	0.164 (0.133)	1.19E-03 (3.62E-03)	2.49E-03 (2.85E-03)	0.331 (0.305)
	P	**0.02**	0.60	**0.007**	**0.009**	0.62	0.61	**0.036**	0.52	0.51	**<0.001**

Data presented as mean (SD). P values in bold indicate statistical significance at the 5% level. P values refer to the two groups immediately above.

5.2.5 Conclusions

Work in this chapter suggests that the modified three-element 0-D Windkessel model is an accurate and practical design for modelling realistic coronary microvascular physiology. Slightly better results can be predicted by more complex models such as the modified five-element model. However, the slight improvement in accuracy is associated with a significant increase in user-input which makes the method impractical for use in the current context. Instantaneous accuracy is improved in cases where there is greatest pressure drop across a lesion, which is to be expected, considering that the method for deriving transient flow relies upon the pressure gradient to drive flow; thus small values of dP generate larger errors in Q_{3-D}. Similar to the results of Chapter 4, the accuracy of the computed mean (non-transient) flow remain accurate regardless of lesion severity and this has implications for the calculation of vFFR which considers pressure data averaged over the duration of the entire cardiac cycle. The modified three-element model is an appropriate design for modelling CMV physiology in the context of vFFR and in terms of reproducing realistic coronary flow waveforms.

5.3 The impact of 0-D tuning at the distal boundary

Because the distal boundary condition is unknown without in the absence of invasive intracoronary measurement, estimating it remains a major challenge for the vFFR modelling community.

5.3.1 Generic tuning

In VIRTU-1 generic conditions were used (Chapter 3) (Morris et al., 2013). This gave good diagnostic accuracy (97%) of physiological lesion significance based on data dichotomised according to the ≤0.80 FFR threshold. However, a modest cohort of patients was studied and, on closer inspection of **Figure 3.11**, it can be observed that quantitative accuracy, on an individual case basis, was less impressive. vFFR values deviated from mFFR with a mean error of ±0.06. Therefore, based upon this cohort, with generic boundary conditions, we can only be confident that the mFFR is above or below the threshold for significance if the vFFR is ≥0.86 or ≤0.74. Although useful in many patients, applicability is limited in more marginal lesions. The vFAI model described by Papafaklis et al (Chapter 2 and 4) is based purely upon vessel geometry and ignores the influence of the distal CMV completely (Papafaklis et al., 2014). This is similar to applying a generic boundary condition. The vFFR model by Tu et al does not implement a distal boundary condition. Instead, mean coronary flow velocity derived from TIMI frame counting during induced

hyperaemia is used to tune the 3-D domain (Tu et al., 2014). Consequently, patient-specific data have been used to tune the model. Although this is methodologically advantageous, the induction of hyperaemia is a factor which has limited use of invasive FFR. Thus far, no group has described a precise method for tuning the distal boundary condition on an individual case basis without the induction of hyperaemia. Although relatively crude, and based on multiple levels of assumptions, the vFFR$_{CT}$ model of HeartFlow Inc. perhaps comes closest to achieving this. vFFR$_{CT}$ estimates myocardial mass from cardiac CT and uses this value to estimate total resting blood flow (Taylor et al., 2013). BP is measured non-invasively at the brachial artery. Because pressure drop (coronary venous pressure assumed zero) and total myocardial flow are 'known', coronary outlet resistance (based on a Windkessel) is distributed according to vessel diameter, a relationship based on Murrays law which states that $R \propto D^{-3}$ (see Chapter 2). A generic response to adenosine is then applied to simulate hyperaemia. This model does not account for any intra- or inter-individual heterogeneity in CMVR, nor does it reflect variability in response to adenosine from baseline.

Table 5.8 summarises the accuracy of the different models of vFFR. There is a consistency between these models, in terms of diagnostic and quantitative accuracy perhaps reflecting the maximum ceiling associated with generic distal boundary tuning. This is demonstrated graphically in **Figure 5.7**.

Table 5.8. Accuracy of vFFR models with generic tuning of the distal boundary condition

	Diagnostic accuracy*	**AUROC[#]**	**Agreeability**	**Correlation coefficient**	**Bias ± SD**	**Limits of agreement[$]**
VIRTU-1	97%	0.97	±0.06	0.84	0.02 ± 0.080	± 0.16
vFFR$_{CT}$	86%	0.93	Not reported	0.82	0.02 ± 0.074	± 0.15
vFAI	87.8%	0.92	NA	0.78	0.00 ± 0.085	± 0.17
TIMI method	88.3%	0.93	Not reported	0.81	0.00 ± 0.06	± 0.12

for predicting FFR < or > 0.80. [#]Area under receiver operating curve. [$]Limits of agreement = ±2× SD; NA, not applicable because vFAI is not a measure of FFR. References cited in text. Adapted from Morris et al (Morris et al., 2013) with permission of Elsevier.
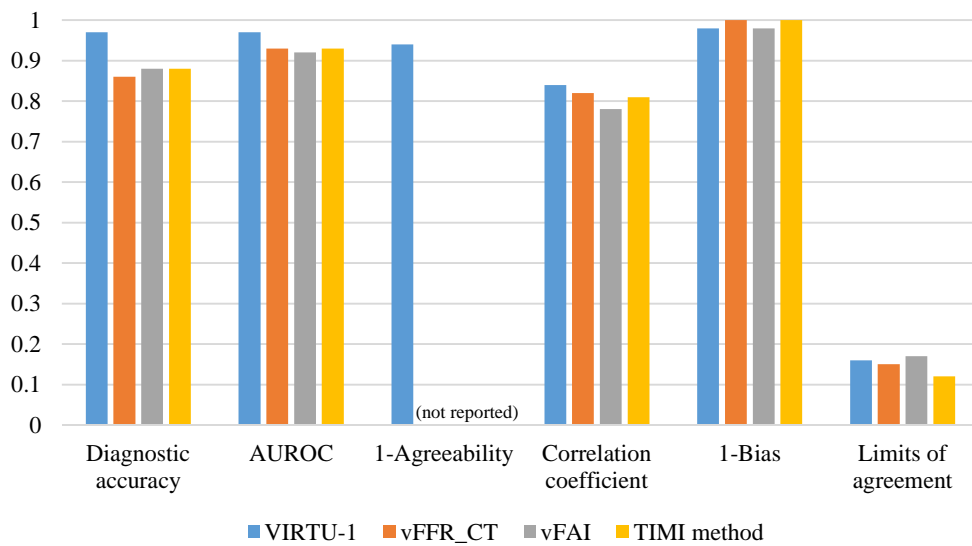
Figure 5.7. Consistency of results of accuracy for models of vFFR using generic (or near-generic) distal boundary condition tuning.
*VIRTU-1 was the only study to publish agreeability data numerically. Abbreviations and explanations same as **Table 5.8**.*

In Chapter 4, the accelerated models of vFFR were applied with generic boundary conditions. A similar and consistent level of accuracy was observed: diagnostic accuracy = 80%, bias = 0.05, and limits of agreement of ± 0.20. However, in Chapters 3 and 4, patient-specific boundary conditions were applied to the VIRTUheart™ model using invasive measurements during ICA. This was associated with significant improvement in the accuracy of vFFR, the mean quantitative error reducing to <1% (cf. 8%).

These data suggest that the use of generic boundary conditions is associated with a relatively consistent error margin. The challenge is in developing a scheme for tuning the model on an individual case basis in the absence of invasive intracoronary measurements.

5.3.2 Parameter sensitivity analysis

The outputs of any model are influenced by variance in input parameters which may occur due to natural biological variability (in health and disease), or due to error in measurement. In the context of vFFR, these include a variety of geometric and physiological parameters. Promising vFFR results have been produced despite limitations in coronary segmentation and reconstruction, and in how physiological parameters are applied in model tuning (Morris et al., 2013, Papafaklis et al., 2014). It is important and useful to understand the relative sensitivity of computed vFFR to individual model input parameters. This way, time and effort can be focused on dominant

parameters whereas parameters with negligible effect on vFFR result can often be assumed or based on averaged data. Sensitivity analysis is a formal mathematical process which allows the influence and interdependencies of individual model inputs to be decomposed and quantified in terms of their effects on model outputs; in this case, the vFFR result.

Sensitivity analysis was performed in order to formally quantify the principal, accuracy-defining model features and parameters.

5.3.2.1.1 Method

Rotational coronary angiograms were segmented and reconstructed according to the methods described in Chapter 3. Data from 20 patients with stable CAD were analysed. The same clinical dataset used in section 5.2.3 was analysed. The analysis was performed using the Sobol decomposition method (Sobol, 2001, Saltelli, 2002) which was applied to the accelerated $vFFR_{steady}$ method described in Chapter 4. The input parameters examined were CMV resistance (R_{CMV}), geometry parameters (K_1 and K_2), and proximal pressure (P_a). This variance-based method can be used to determine the magnitude of effect of individual input parameters on the output of a model, in this case vFFR. The main sensitivity indices provide information about the reduction in model output variance if an input factor would be accurately applied. Therefore, the main sensitivity indices are able to provide a ranking of the individual input parameters responsible for proportions of the model output variance, i.e. the inputs are ranked in order of the level of influence on the vFFR result that they have. Additionally, the total sensitivity indices can be used to identify parameters that have little or even negligible effect on model output and can therefore be fixed to population averages. For the current study, the main and total sensitivity indices have been determined over parameter ranges derived from the patient cohort. This work was carried out in collaboration: the mathematical model was developed and executed by JF, model development, clinical data collection, processing and results analysis were performed by PM.

5.3.2.1.2 Results

Figure 5.8 provides a ranking of the main sensitivity indices and demonstrates that the principal influence on the variation of vFFR values was the total distal CMVR, accounting for 59% of the variance.

K₁ *K₂* *CMVR* *Pa* *Interaction terms*
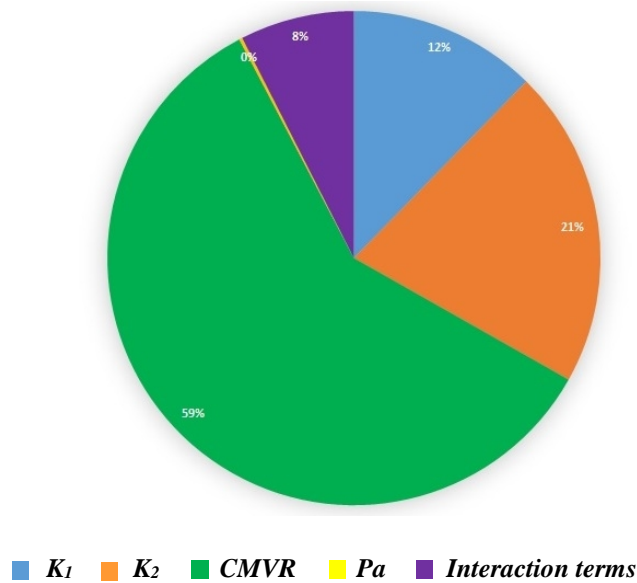
Figure 5.8. Pie-chart demonstrating the relative effect of individual model input parameters on model output (vFFR) variance.

Coronary anatomy and stenosis geometry (characterised by K_1 and K_2) were of secondary importance in the study population, accounting for 33% of vFFR variance. As a summary, a heat-map of the FFR sensitivity indices is displayed in **Figure 5.9**. Only 8% of the model output variance was caused by higher order interaction effects. Interaction (indirect) effects are defined as the difference between the total effect and the direct (main) effect of an input parameter. The magnitude of the interaction effects is demonstrated in **Figure 5.10** which displays the total sensitivity indices divided into the main effects (S_i) and the remainder accounting for higher order interaction effects. A relatively small proportion of the total effect of the individual input parameters can be attributed to interaction effects. The total variance in vFFR caused by proximal pressure (Pa) was less than 1%, as demonstrated by the total sensitivity index value of 0.0038. Therefore, average proximal pressure had negligible (%) effect on vFFR result.

5.3.2.1.3   Discussion

The sensitivity analysis described here demonstrates the relative importance of each input parameter in the precision of vFFR computation. For many years, angiographic assessment of CAD focused solely upon lesion anatomy. More recently it has been demonstrated that physiological assessment (FFR) correlates more closely with clinical outcome than lesion anatomy alone. A number of groups have tried, unsuccessfully to infer physiological lesion significance purely from lesion anatomy, using 2-D and 3-D QCA (Koo et al., 2011, Ben-Dor et al., 2012, Gonzalo et al., 2012). The sensitivity analysis presented in this study explains this collective failure

because the aforementioned studies did not incorporate any measure of CMV resistance in their processing. This study of a population of patients with stable CAD demonstrates that variability in the CMV resistance had a greater influence on the vFFR result than variability in epicardial coronary and lesion anatomy. This highlights how critical it is to include an accurate estimate of CMVR into any virtual FFR model. This also explains the strength and success of FFR over standard and quantitative CAG, because invasive FFR
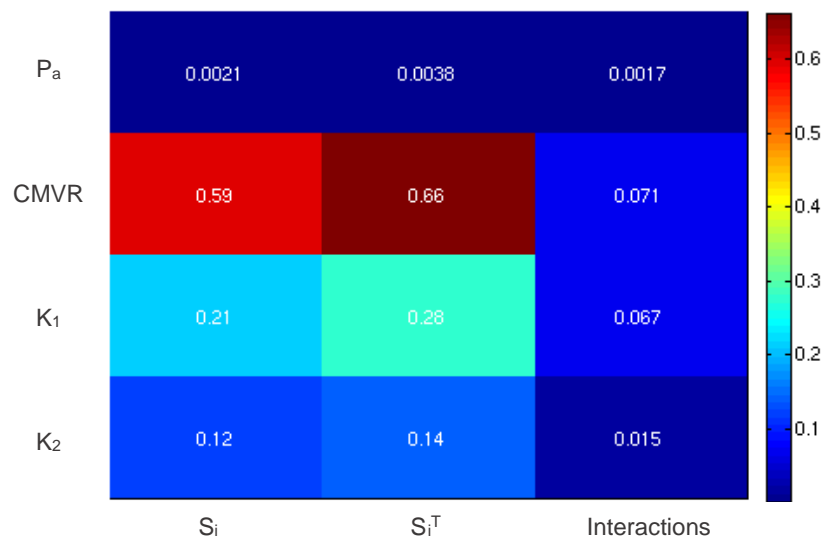
Figure 5.9. The main (S_i) and total (S_i^T) sensitivity indices, and interaction effects.
Data are displayed for the four input parameters: mean Pa, mean CMVR, and geometry parameters K_1 and K_2. The axis on the right indicates the magnitude of the influence on output (vFFR) result with higher values having a stronger influence on result. CMVR is the dominant influence on vFFR result. The colour legend indicates the relative strength of the effect (0-1).

measurement automatically incorporates the magnitude of CMV resistance (Pijls et al., 1993). Similarly, it explains why other published work in this area has been able to report reasonable vFFR accuracy, despite employing relatively imprecise imaging and segmentation protocols (Morris et al., 2013, Norgaard et al., 2014, Papafaklis et al., 2014). The construction of computational workflows which accurately compute FFR, without wire insertion, and without the induction of hyperaemia, require careful tuning of the distal boundary condition parameters (CMVR in particular) on an individual case basis.
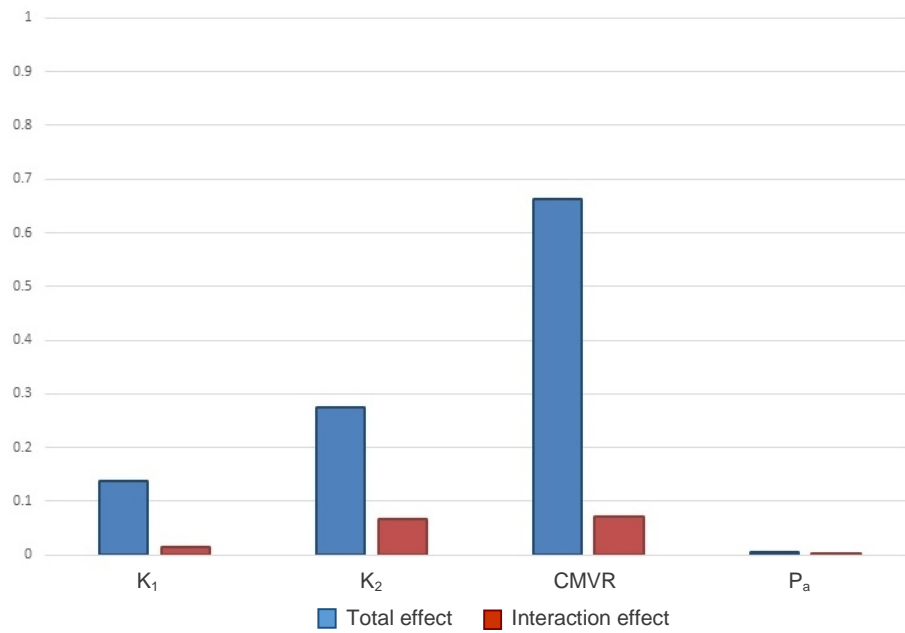
Figure 5.10. Bar-chart demonstrating the magnitude of the total (direct and interactions) effects on vFFR caused by the input parameters CMVR, geometry parameters (K_1 and K_2) and average proximal pressure (P_a).

5.4 A strategy for tuning the 0-D model parameters

Section 5.2 describes the validation of the modified three-element Windkessel for simulating the physiological behaviour of the CMVR. Section 5.3 demonstrates that tuning of the 0-D model parameters is the dominant factor in determining the accuracy of the simulated pressure and flow result on an individual case basis. The aim of this section is to develop, execute and evaluate a novel method for achieving this.

Despite significant interest, funding and financial investment (HeartFlow Inc Funding, CrunchBase, 2015), at the current time, there are no examples of non-invasive strategies for personalised boundary condition tuning in a model of vFFR in use or in the literature; this highlights the magnitude of the challenge. In fact, patient- and case-specific tuning of boundary conditions using non-invasive data represents a wider challenge facing the *in silico* modelling community. Thus far, all published models of vFFR apply generic tuning (Morris et al., 2013, Tu et al., 2014, Papafaklis et al., 2014, Norgaard et al., 2014). Section 5.2.3.1 describes a method for accurately deriving the 0-D parameters within an acceptable level of error and Chapter 4 describes how these can be applied to compute vFFR with <1% error compared to measured data. However,

the optimisation method relies upon invasively acquired pressure data. The major challenge therefore lies in developing a strategy which can infer the 0-D parameters from non-invasive data. More specifically, these data should not rely on intracoronary measurement. Some level of invasive data are acceptable in a model of vFFR$_{ICA}$ if they are acquired during routine diagnostic catheterisation. For example, the tuning of the ventricular back-pressure amplitude uses data from the aortic pressure signal which is measured routinely via the catheter tip. Moreover, the same dataset provides the proximal boundary condition. Whereas vFFR$_{CT}$ has the advantage of being able to compute myocardial mass which is used to generate assumptions regarding distal parameters, vFFR$_{ICA}$ has the advantage of providing a level of routinely available invasive data which potentially can be used to help tune the distal boundary condition.

It is not anticipated that perfect case-specific tuning is required to generate significant improvement in vFFR accuracy. Chapter four demonstrates how even relatively crude approximations can improve vFFR accuracy significantly. A scheme which enables even a gross adjustment of the parameters on a case-specific basis without intracoronary measurement would represent a major advance within the field of intracoronary modelling and within *in silico* medicine more widely.

5.4.1.1   How many parameters need to be tuned?

Both steady-state-based acceleration methods described in Chapter 4 predict vFFR with <1% error, provided that case-specific 0-D parameters were applied. Ideally, the FFR$_{ps\text{-}trns}$ method would be used because this method generates pseudo-transient data regarding the flow and pressure dynamics over time. However, as demonstrated in **Figure 4.12** this method relies upon the tuning of seven parameters: impedance (Z_c), capacitance (C), resistance (R), along with four parameters describing the ventricular back-pressure (P_b) namely the amplitude which is informed by the aortic pressure trace (P_a) and the durations of the pressure ramp-up, flat, and ramp-down phases defined as a fraction of the cardiac cycle. Alternatively, the FFR$_{steady}$ methodology (see **Figure 4.13**) relies upon just a single parameter, total resistance (R_{total}). Because this method incorporates mean values (averaged over the period of the cardiac cycle) of flow, pressure and resistance, the entire distal model reduces down to a single value of resistance which is equal to the sum of Z_c and R in the other model. Although this model cannot produce dynamic data, it was able to accurately predict vFFR with only a single 0-D parameter variable. The long term aim should be to tune the seven parameter model on an individual case basis in order to generate dynamic data. However, at this early developmental stage the pragmatic approach is to attempt to predict only R$_{total}$ because this is simpler, still allows accurate vFFR prediction and is more likely to succeed on a smaller cohort in a pilot proof of concept study.

5.4.1.2 Coronary microvascular resistance

An understanding of the factors influencing coronary microvascular resistance (CMVR) and hyperaemic microvascular resistance (HMR) is important when deciding how to develop a method for predicting 0-D model parameters. The value of the HMR is critical to FFR which is similarly measured under hyperaemic flow conditions. CMVR demonstrates heterogeneity both between individuals and within different regions of the same heart. Studies of HMR demonstrate up to fourfold variability between different hearts in animal (Vergroesen et al., 1987) and human studies (Meuwissen et al., 2001). During diagnostic assessment for CAD, increased HMR is a marker for FFR-CFVR discordance and increased MACE (Meuwissen et al., 2001, van de Hoef et al., 2014). HMR also demonstrates intra-individual variability. A detailed microsphere experiment investigated 384 separate regions of the left ventricular free wall of two canine hearts. There was no correlation between baseline and hyperaemic flow at the local level and a twelvefold variability in CFVR was observed in some regions (Austin et al., 1990). In a study of 169 adults with CAD, PET imaging detected a threefold variation in regional myocardial blood flow highest in the anterior and lateral regions and lowest inferiorly. A gender discrepancy was observed, with baseline myocardial blood flow higher in females than males (Chareonthaitawee et al., 2001). HMR is also influenced by CMV perfusion pressure (P_d), and therefore lesion severity. The mechanism is thought to involve the effect of hydrostatic pressure on the compliant CMV vessels (Kajiya et al., 1986). Studies demonstrate increased HMR in the presence of a stenosis, an affect which reverses with restoration of P_d after PCI (Chamuleau et al., 2003, Spaan, 1985). A further study by the same group demonstrated that after PCI, HMR reduced to a lower level lower than expected (relative to a reference vessel) suggesting chronic remodelling in response to chronic low perfusion pressure. The reduction in CMVR accounted for 34% of the total reduction in coronary resistance after PCI (Verhoeff et al., 2005). CMVR is higher during systole than diastole. Consequently, heart rate is an important influence on flow because relatively time is spent in diastole at higher heart rates.

Increased CMVR and HMR are associated with coronary microvascular dysfunction (CMVD). The clinical and pathological basis for this are summarised in **Table 5.9** and **Table 5.9** respectively.

Table 5.9. Clinical classification of coronary microvascular dysfunction

Type of CMVD	Description	Examples
Without CAD and /or myocardial disease	Reflects established coronary risk factors. Identified by non-invasive imaging. Partly reversible.	*Smoking* - 21% CFVR reduction in asymptomatic smokers (Kaufmann et al., 2000a) *Diabetes mellitus* (Pitkanen et al., 1998) *Hyperlipidaemia* – inverse correlation between CFVR and lipids (Dayanikli et al., 1994, Kaufmann et al., 2000b)
In the presence of CAD	Accompanies stable CAD and unstable acute coronary syndromes. More difficult to identify. Diagnosis often requires combined clinical, invasive and non-invasive approach.	In those with single vessel disease it can occur in myocardial territories subtended by normal arteries (Uren et al., 1993b, Pupita et al., 1990)
In the presence of myocardial disease	Sustained by adverse remodelling of intramural arterioles. Diagnosis is via invasive and non-invasive techniques. Reversibility is variable. Occurs with inherited and secondary cardiomyopathies.	*Hypertrophic cardiomyopathy* – affects macroscopically non-hypertrophied areas also (Knaapen et al., 2008, Maron et al., 1986) *Dilated cardiomyopathy* – independent marker of prognosis (Canetti et al., 2003) *Systemic arterial hypertension* – even in absence of LVH (Vogt et al., 1992) *Aortic stenosis* – multifactorial (see **Table 5.10**)(Choudhury et al., 1997) *Infiltrative cardiac disease -*
Iatrogenic	Post-revascularisation secondary to vasoconstriction and distal embolisation.	May continue for 7 days post PCI (Uren et al., 1993a). Occurs due to α-adrenergic constriction and distal embolization (el-Tamimi et al., 1991, Prati et al., 2003).

CMVD, coronary microvascular dysfunction; CAD, coronary artery disease; LVH, left ventricular hypertrophy.

Table 5.10. Pathogenic mechanisms of coronary microvascular dysfunction

Pathological alteration	Examples
Structural	
Luminal	Post-PCI microembolisation
Infiltrative	Fabry's cardiomyopathy
Vascular remodelling	Hypertrophic cardiomyopathy and systemic arterial hypertension
Vascular rarefaction	Aortic stenosis and systemic arterial hypertension
Perivascular fibrosis	Aortic stenosis and systemic arterial hypertension
Functional	
Endothelial dysfunction	Smoking, diabetes mellitus and hyperlipidaemia
Smooth muscle cell dysfunction	Hypertrophic cardiomyopathy and systemic arterial hypertension
Autonomic dysfunction	Post-PCI
Extravascular	
Decreased diastolic time	Aortic stenosis and tachycardia
Extravascular compression	Aortic stenosis, systemic arterial hypertension and hypertrophic cardiomyopathy

Individual factors frequently coexist. PCI, percutaneous coronary intervention. Based on Camici et al (Camici and Crea, 2007)

5.4.2 Method rationale

Many of the factors which influence HMR can be identified non-invasively from the clinical history, examination and basic bedside tests such as 12-lead electrocardiography (ECG) and echocardiography. It was therefore decided to collect routinely-available clinical data from a larger population of patients with CAD undergoing ICA and FFR estimation. In that way the relationships between known input parameters (clinical data) and the desired output parameters (R_{total}, Z_c, C, R and the parameters of P_b which are derived from measured values as previously described) could be modelled mathematically. For this phase of work, funding was secured from the Wellcome Trust and Department of Health, Health Innovation Challenge Fund (HICF, 2015) (HICF-R6-365).

The hypothesis of the experiment was to investigate whether the distal 0-D parameters could be tuned using routinely available patient-and case-specific data. Data collection was performed under the auspices of the HICF grant. Aspects of the clinical protocol differed from the VIRTU-1 study as detailed here.

5.4.2.1   Project design and ethical approval

This was an analytical observational study. Clinical work was carried out at the South Yorkshire Cardiothoracic Centre at the Northern General Hospital, Sheffield, UK. *In silico* development was performed within the Medical Physics Group, Department of Cardiovascular Science, University of Sheffield, UK. The study was approved by the NHS Research Ethics Committee (NREC 13/YH/0070) and by STH Research and governance (STH16467) and conformed to the Declaration of Helsinki guidelines (http://www.wma.net/) on research involving human subjects.

5.4.2.2   Patients

Patients with stable CAD of any pattern/severity, potentially suitable for PCI, were recruited. Potential participants were identified by a clinical member of the care team from pre-admission clinic lists or from referrals from other Cardiologists. Patients were sent a patient information sheet with their invitation to attend for left heart catheterisation and were consented and recruited to participate in the study by research nurse or doctor (PM, JG) either in the pre-assessment clinic or on the ward. During the PCI a member of the research team (PM) recorded procedure details relevant to the computational modelling on an anonymised data collection form and latterly, directly into the ArQ database (see section 5.4.2.6 below).

5.4.2.3   Inclusion and exclusion criteria

Inclusion criteria included stable symptoms of coronary ischemia, coronary angiographic findings of significant or borderline coronary lesions of any morphology which were potentially suitable for PCI. Exclusion criteria included critical ischemia, severe valvular heart disease, bleeding diathesis precluding ICA, terminal cancer, pregnancy, lack of informed consent, chronic total occlusion of target vessel, acute presentation in the previous 60 days, intolerance of adenosine, nitrate, iodine based contrast media, inability to take dual antiplatelet therapy, target vein graft. Patients with previous history of MI or PCI and those with LMS disease were included.

5.4.2.4   Data collection

Apart from the data collected in the catheter laboratory, similar to those collected in VIRTU-1, new data collection focused upon aspects of clinical history, examination and bedside tests which may help to identify CMV-determining features. A rich dataset was collected from each patient. This is summarised in **Table 5.11**.

5.4.2.5   Transthoracic echocardiography

Transthoracic echocardiography was performed using a Philips CX50 CompactXtreme Ultrasound System (Philips Healthcare, Best, NL). All data were acquired by PM under resting conditions

with concurrent ECG recording, at the bedside, immediately prior to left heart catheterisation. A list of parameters is included in **Figure 5.14** below. Because coronary blood flow is influenced by ventricular myocardial systolic contraction and diastolic relaxation, echocardiography focused upon objective, quantitative measures of systolic and diastolic ventricular function. In addition to the protocol outlined in **Table 5.11**, each valve was assessed using colour Doppler flow mapping. Any additional pathology, including cardiac valve disease, was further assessed according to the operator's normal practice, consistent with British Society of Echocardiography (BSE) guidelines UK (Wharton, 2012). In order to eliminate any bias in reporting, echocardiograms were jointly reported by PM and a BSE accredited echocardiographer physician (PG) who was blinded to the patient details. All echocardiograms were reported according to the minimum dataset detailed in **Table 5.11**.

Table 5.11. Summary of clinical data collected from each patient

Patient record /history	Examination	Cardiac catheter laboratory	ECG	Bedside transthoracic Echocardiography *
Age, gender, ethnicity	Resting pulse rate	2-D QCA	Rate	LV dimensions
Smoker (Y/N/ex) plus pack year history	Resting BP	3-D QCA	Rhythm	Aortic dimensions
MI (+ details of artery, territory and when)	Height, weight and BMI	SYNTAX score	Axis	Ejection fraction
Valve disease (+ details)	FBC	NY risk score	P-R interval	RV systolic function
Lung disease (+ details)	U&E	Dominance	QRS duration	LV systolic function
History of DM, PVD	Random glucose	Bifurcation disease	QT and QT_c interval	LV diastolic function
Other comorbidities	Total cholesterol	Collateral vessels visible	QRS axis	LV wall motion scoring
History of rhythm disturbance (+ details)		Tandem lesions	Q wave territory	MV and AV Doppler
History of hyperlipidaemia		IVUS	T wave territory and axis	LV TDI
History of hypertension		Rotablation	LV voltage criteria	Simpson's biplane ejection fraction
CCS angina score		OCT	ECG scanned	
NYHA class		Complications (+ details)		
Frailty score				
Medications				

QCA, quantitative coronary angiography; LV, left ventricle; RV, right ventricle, MI, myocardial infarction; BMI, body mass index; SYNTAX, SYNergy between PCI with TAXus and cardiac surgery; FBC, full blood count; UE, urea and electrolytes; QTc, corrected QT interval; MV, mitral valve; AV, aortic valve; TDI, tissue Doppler imaging; IVUS, intravascular ultrasound; OCT, optical coherence tomography; CCS, Canadian Cardiovascular Society grading of angina pectoris 1 (Rockwood et al., 2005); NYHA, New York Heart Association Classification of Heart Failure.

5.4.2.6   Data management

A bespoke project database was used instead of the disparate, manual system employed in the RISC study (Chapter 3). Using funds from the Virtual Physiological Human Share (VPH-Share) project (FP7-ICT-2009-6) (E.C. CORDIS, 2015) a bespoke project database was developed with Scientific Computing at STH (MB and SW) within the ArQ software. The database was created in Structured Query Language (SQL) format, a programming language purpose designed for storing and managing data within in a relational database management system. ArQ storage is backed up every 24 hours and historical storage can be retrieved at a variety of time intervals. All patient data was entered into the ArQ database (see **Table 5.11** and **Table 5.12**). The VIRTUheart™ ArQ database provided a structured file upload and storage system. Therefore, all raw digital files were uploaded to ArQ on the University of Sheffield servers behind the University firewall. Raw digital data comprised pressure files, Xcelera imaging, RoCA imaging, along with ECG, datasheet, echo reports, processed data (e.g. mesh, pressure trace and definition files) and results (including the generated files as uploads) in a structured manner. Within ArQ, each patient had a unique entry. All data specific to the patient were stored in a categorised manner. Each patient generated several arterial datasets. Therefore, all data specific to a unique dataset (e.g. artery, QCA, FFR) were stored as child tables at the lesion level. **Figures 5.11** - **5.12** demonstrate the VIRTUheart™ ArQ database GUI and the detail and structure of the data. The ArQ database provided an interrogation and export facility (*.csv). ArQ also allowed selected data to be exported to the VPH-Share web portal (vph-share.eu, 2015) for secure transfer with collaborators and project partners across Europe.
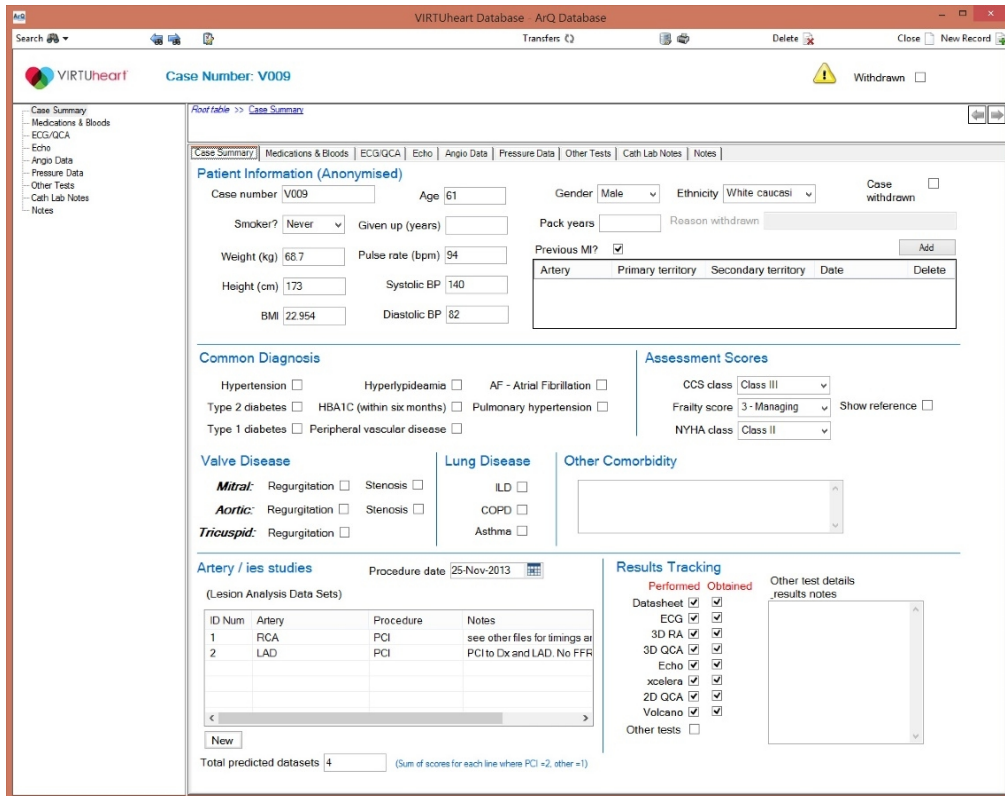
Figure 5.11. VIRTUheart™ ArQ database: main dash demonstrating general patient demographic details and lesions studied for case #9. Data are categorised according to the tabs across the top.
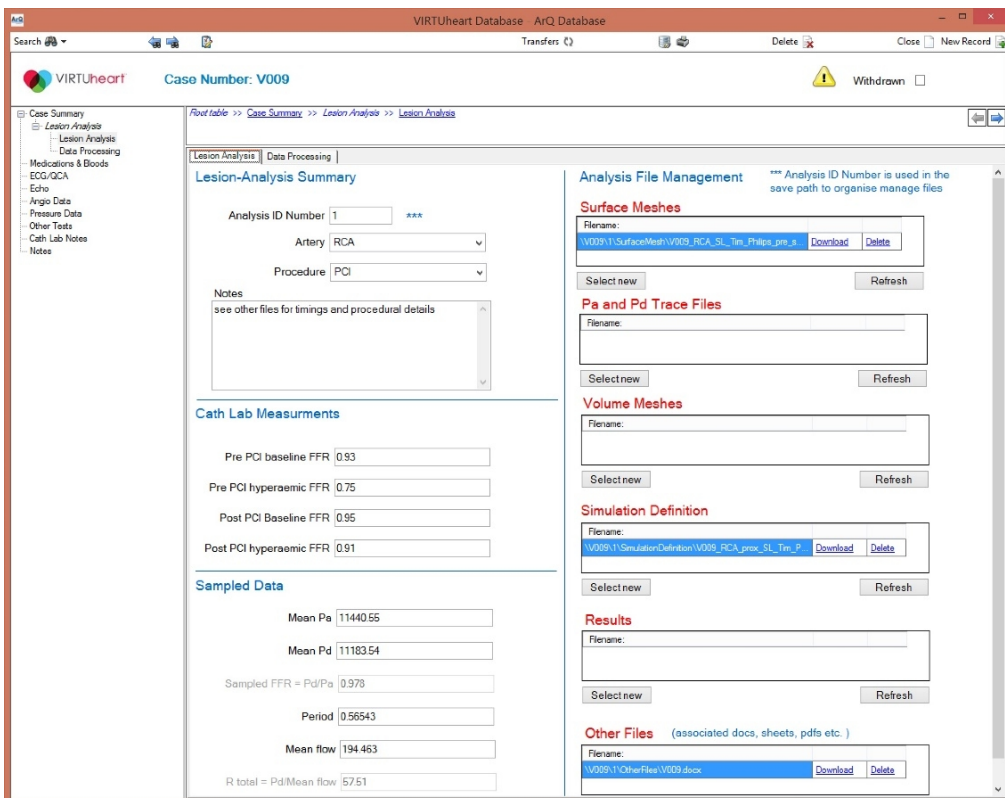
Figure 5.12. VIRTUheart™ ArQ databse: lesion analysis details and file upload.
Each lesion studied has its own lesion analysis page (child table)
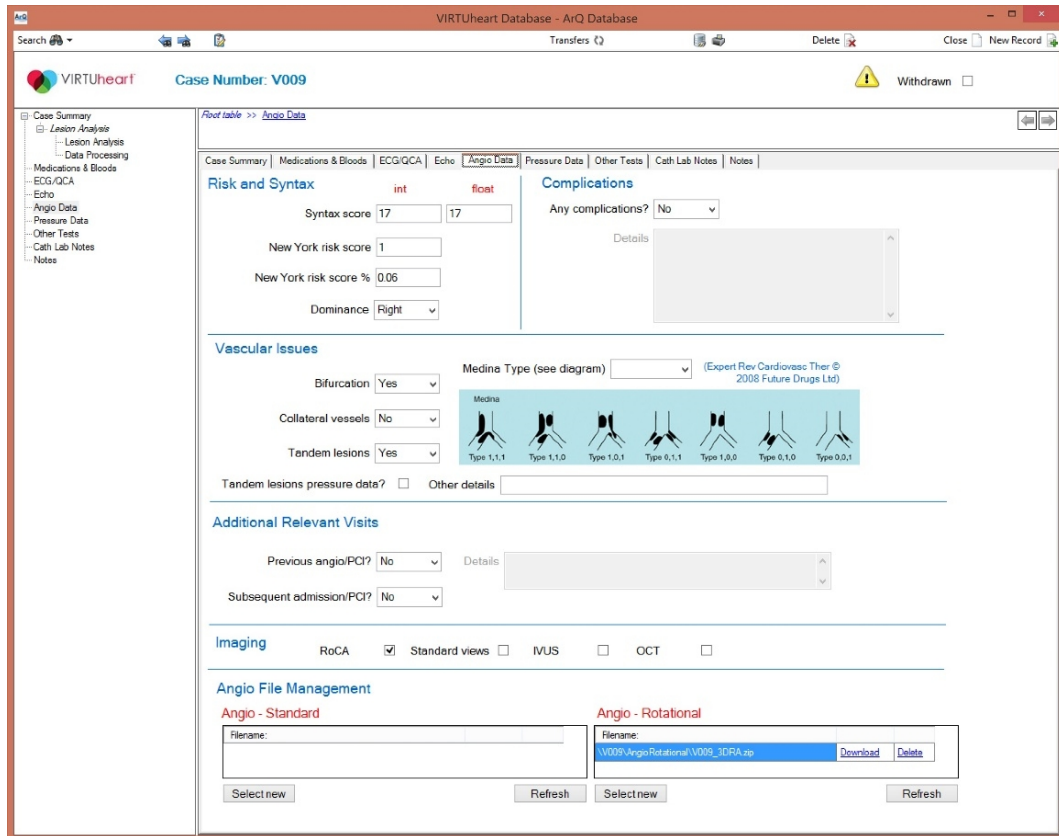
Figure 5.13.VIRTUheart™ ArQ database: angiographic data and file upload
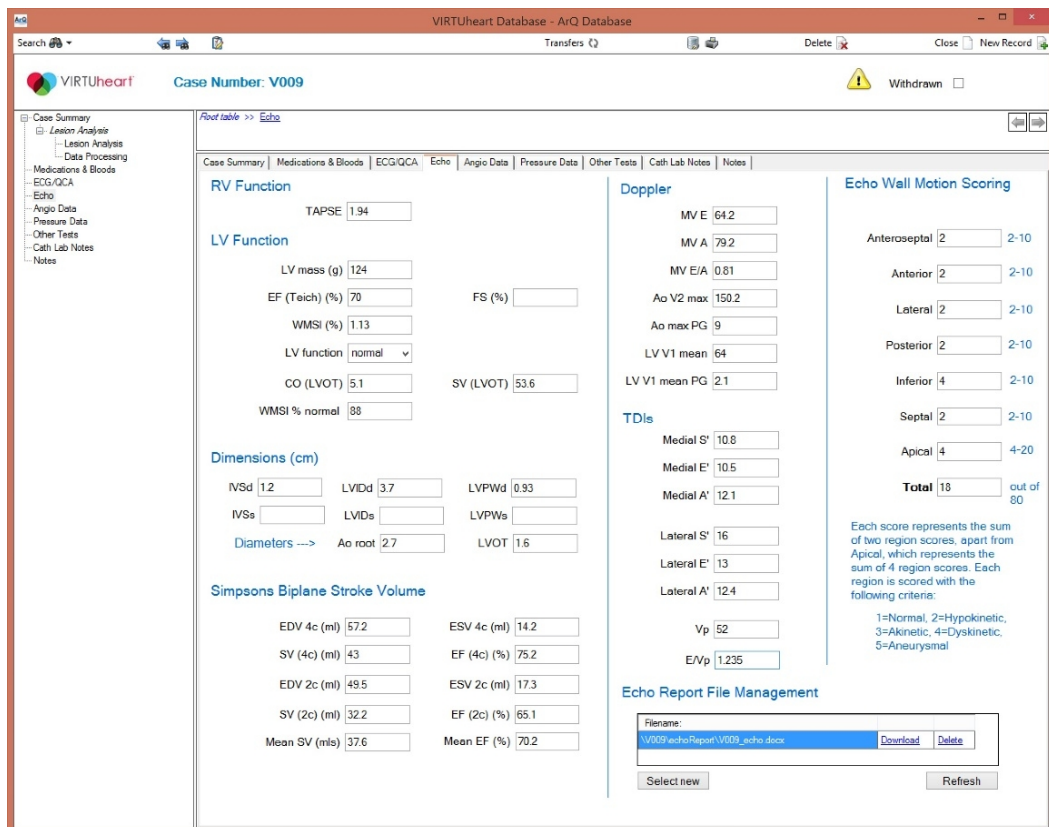
Figure 5.14. VIRTUheart™ ArQ database: echocardiogram data collection and file upload

5.4.2.7   Angiography

The protocol for rotational coronary angiography was identical to that described in Chapter three but, in addition, non-rotational, standard angiographic acquisitions (multiple single plane) were also stored for future use.

5.4.2.8   Segmentation and reconstruction

In silico arterial models were processed as described in Chapter three using the Philips system.

5.4.2.9   Processing

Instability in the GIMIAS based workflow (Chapter 3) necessitated development of the VIRTUheart™ workflow. The workflow was re-coded by DS outside the GIMIAS framework. Development was based upon open source libraries used extensively in the current context using the Visualisation Toolkit (VTK). The new workflow was coded in C# within Microsoft Visual Studio to run on any 64-bit OS. Functionality of the new system was similar to the workflow described in Chapter 3 but stability and user-experience were improved based upon user feedback and the demands of the project. Examples of the workflow environment are included in **Figure 5.15**. As in the previous workflow, ANSYS ICEM and ANSYS CFX routines were called for spatial discretisation and definition file setup. Mesh design and parameters were consistent with the sensitivity analysis in Chapter 4.
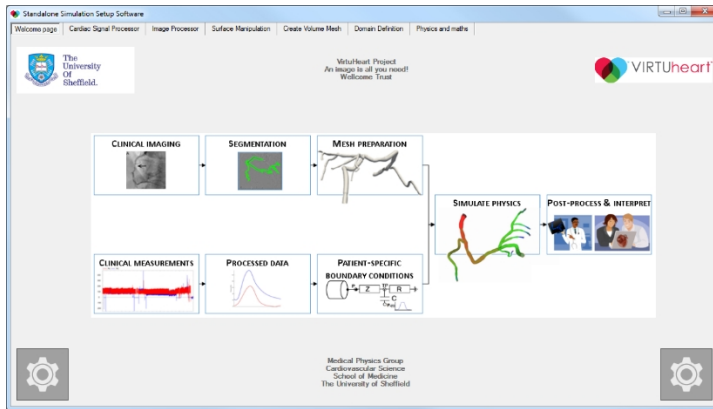
(i) The overview screen demonstrating all functions.
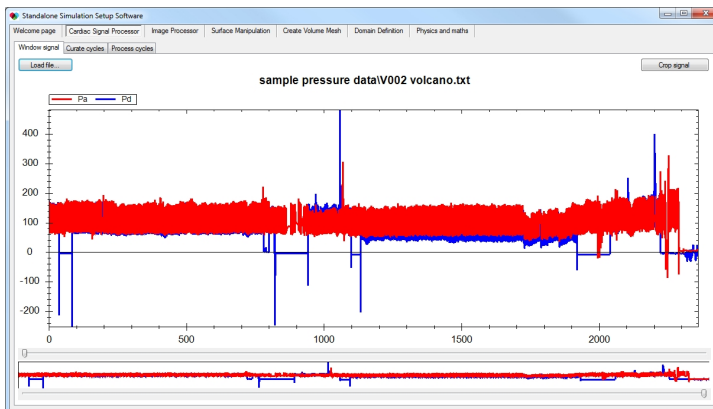
(ii) Pressure data (y axis) are loaded in and the period corresponding to clinical measurement is selected. Red is P_a and blue is P_d. The x axis is procedure time.
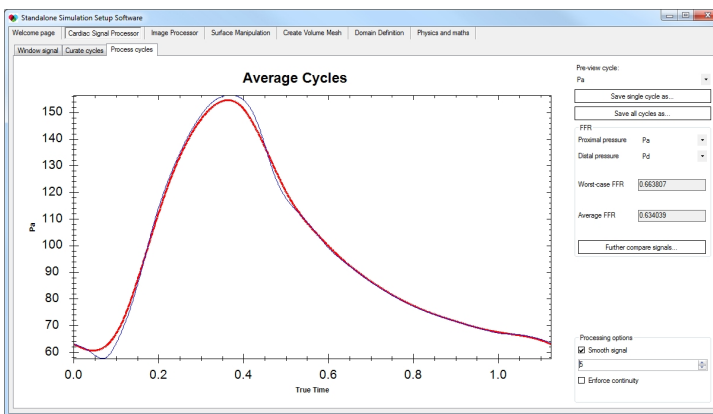
(iii) The cycle data are processed and ensemble averaged into a single representative cycle. These data are used to simulate flow (Q_{CFD}).
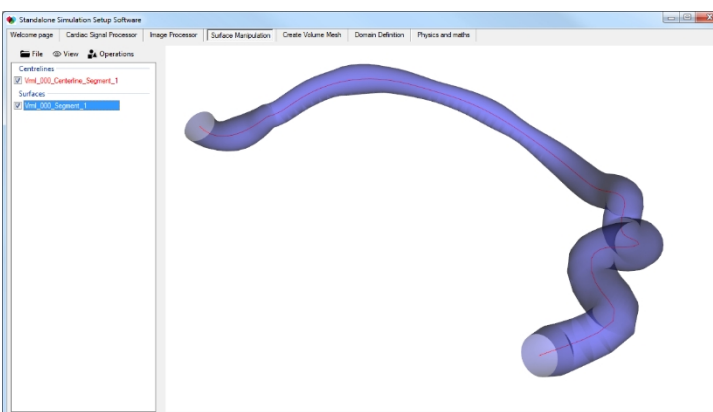
(iv) The *.vrml file (Philips segmentation output) defining the vessel lumen and the centreline is imported
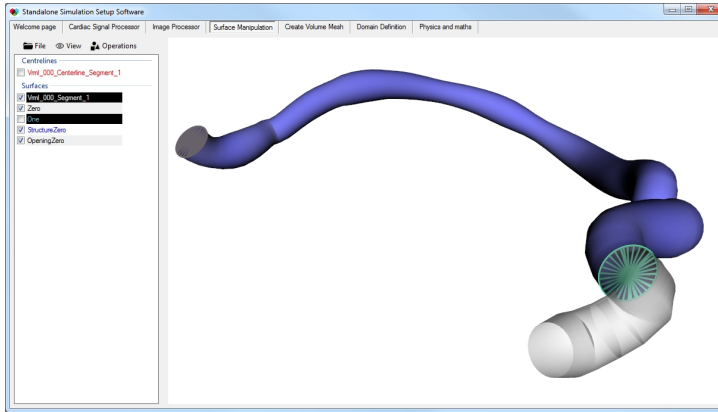
(v) The surface and centreline are manipulated. The region of interest (purple) is extracted and capped (green circle) from the original data (white translucent)
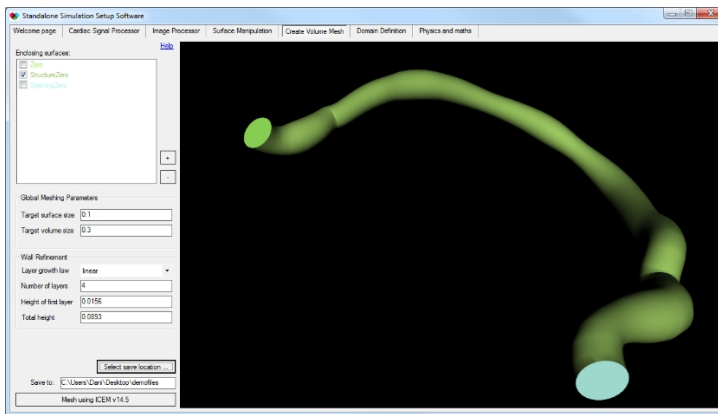
(vi) Meshing of the extracted surface is performed within a separate tab. The mesh parameters (tetrahedra and prism) are defined.
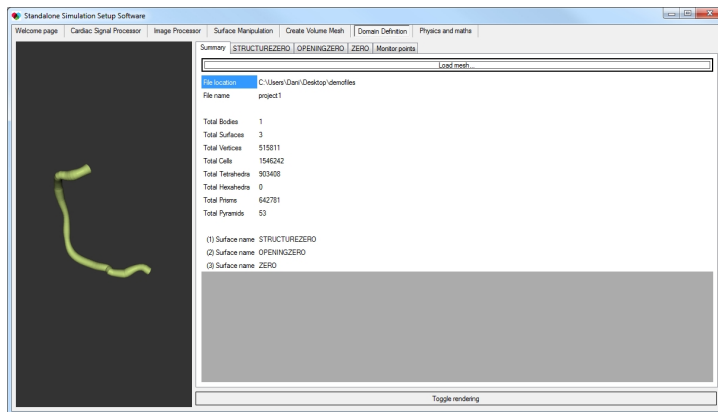
(vii) Mesh characteristics and metrics are viewed.
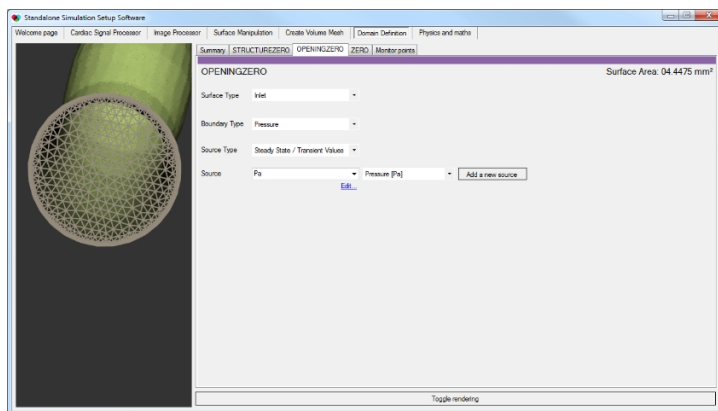
(viii) The boundary conditions are defined for each boundary. Options include transient /static, pressure /flow, value /from file.

Figure 5.15 (this page and previous). The stand-alone VIRTUheart™ workflow environment developed.

5.4.2.10 Simulation

As described in Chapter three, simulation was performed in ANSYS CFX v14.5. Boundary conditions were: wall, rigid wall; proximal, P_a; distal, P_d where Pa and Pd were case-specific, derived from clinical data using the workflow software. Time-step was defined as period /350 which was altered to increase stability of the solution. Residual error target was set 10E-06 with minimum and maximum iterations of 2 and 60 respectively. Other parameters remained similar to those previously described.

5.4.2.11 Statistical methods

Statistical calculations were performed in IBM SPSS Statistics for Windows (IBM Corps, USA).

5.4.2.11.1 Sample size

The required sample size was calculated based upon the primary objective; namely to identify statistically significant relationships between the dependent variable (R_{total}) and the independent variables (non-invasive clinical data) using analysis of variance (ANOVA) and multiple regression analysis. For an anticipated 'medium' effect size (f^2) of 0.15 (F=0.38), at a statistical power level of 0.80, and a probability level of 0.05, Cohen's f^2 effect size for an F-test was used to calculate that 67 datasets were required to identify one significant input variable. 91 samples would be required to identify up to five variables. In order to detect a 'small' effect size (F=0.14), 478 samples would be needed to identify just a single variable. VIRTU-1, which included post-PCI cases, yielded approximately 2 unique datasets per patient. Although the current study did not include post-PCI cases, it did have wider inclusion criteria. The aim was therefore to recruit 50 patients, in order to yield 100 datasets. These patients were from the Wellcome Trust funded project (see section 5.4.2)

5.4.2.11.2 Statistical processing

The outlying labelling rule was applied to exclude any spurious outliers according to the resistance results (Hoaglin and Iglewicz, 1987, Hoaglin et al., 1986). Continuous data were screened for normality of distribution by calculating skewness and kurtosis. Normality was accepted when the skewness statistic value was <1.0 and /or the z-value (statistic/SE) was between -1.96 and +1.96). In addition the corresponding histograms, normal Q-Q and box plots were inspected (Doane and Seward, 2011) and a Shapiro Wilk normality test (p>0.05) was performed (Shapiro and Wilk, 1965). Non-normally distributed data were logarithm (log_{10}) transformed for analysis. One way analysis of variance (ANOVA) with *post hoc* analysis (Fischer's least significant difference) was used to quantify the statistical significance between means. Levine's test was used to ensure homogeneity of variance (p>0.05). Resistance data are presented in non-SI units of Pa min ml^{-1}

because it maintains a practical number for making comparisons. Data can be converted into the SI units of Pa s m^{-3} by multiplying by 60 000 000. Previous analyses demonstrated that 0-D parameter estimation was inferior in cases with FFR>0.95 (see section 4.8) and for that reason, these cases were excluded in the current analysis.

5.4.2.11.3 Linear regression modelling

Linear regression analysis was used to identify candidate predictive variables, i.e. those demonstrating statistically significant relationships with the dependent variable (R_{total}). Candidate variables were screened individually. Statistical significance was accepted at the 5% level ($P \leq 0.05$). Because each regression analysis constitutes a statistical 'model', as opposed to a statistical 'test', no *post hoc* correction for multiple analyses was required. All candidate variables were entered directly into a regression model. A step-wise, backward elimination of the least significant candidate variable was performed manually until five predictive variables remained. The size of the study population precluded division of the dataset into 2/3 training and 1/3 validation sets. Therefore a 1000 fold bootstrap validation was performed for model validation.

5.4.2.11.4 Statistical constraints

The quantitative relationship between R_{total} and diverse non-invasive clinical data are unknown. The aims of the current study were therefore to demonstrate (i) whether a statistical mathematical approach may be useful in identifying relationships between dependent and independent variables and (ii) to determine which categories of non-invasive data appear most influential. This was intended to be hypothesis generating. It was not anticipated to definitively resolve the issue of 0-D tuning. The modest population size precluded any more than five predictive variables to be identified.

5.4.3 Results

5.4.3.1 Patient recruitment and inclusion

69 patients were recruited (Wellcome Trust funded study). Between recruitment and the date of the procedure, four cases were subsequently found to meet the exclusion criteria (two CTOs, one case had no significant CAD and one had recent MI) and were therefore excluded. One patient was withdrawn from the study due to anxiety attack during the pre-operative period. The operator was unable to advance the pressure wire across the target lesion in one case, which was therefore not included in the final analysis. One case was cancelled due infection. One case was cancelled by the patient, and one case was deferred because the patient required elective implantable cardioverter defibrillator implantation. A further case was deferred due to a technical problem with

the X-ray C arm. The quality of the data was inadequate in four patients (e.g. no rotational angiogram or incorrect physiological system employed) which were therefore not included.

5.4.3.2 Segmentation and reconstruction

Seven arterial datasets could not be segmented and reconstructed using the Philips system. This was due to parallel alignment of the epipolar lines, a direct consequence of the constraining nature of RoCA (see discussion). Overall, 52 patients and 104 unique arterial datasets were included in the final analysis. Consistent with Chapter 3, significant limitations were noted regarding the segmentation method. Confidence scoring demonstrated the mutual exclusivity of satisfying multiple important priorities (e.g. ECG gating, minimising overlap, lesion definition, opacification, epipolar line alignment and projection angle separation) while selecting images for segmentation.

Table 5.12 describes the clinical and demographic data collected from each patient and the completeness of collection in the current cohort for each data field. These data are important when interpreting the size and magnitude of effect in the following regression analyses.

Table 5.12. Data description and completeness

Data field	Notes	Data completeness (%) (per-case)
General demographic and physiological data		
Artery	Name of artery	100.0
Arterial code	Artery coded by number	100.0
Lesion code	Lesion-specific unique identifier	100.0
Excluded	Patient /case excluded from the final analysis?	100.0
Reason	Why the patient /case was excluded?	100.0
Age	Age in years	100.0
Sex	Male /female	100.0
Ethnicity	Ethnicity, coded by number	90.4
Smoking status	Current, ex- or never	100.0
Given up	If ex-smoker, for how long?	82.7
Pack-years	Total pack-year smoking history (1 pack year = 20 day^{-1} for one year	88.8
Height	Height in metres	100.0
Weight	Weight in Kg	100.0
BMI	Body mass index in Kg/m^2	100.0
Resting pulse	Palpated in PAC	98.1
Resting SBP	Resting systolic BP measured in PAC	96.2
Resting DBP	Resting diastolic BP measured in PAC	96.2
Comorbidities (Y/N)		
MI history	History of MI (Y/N)	100.0

MI culprit artery	Culprit artery if previous MI	78.8
MI territory 1	Affected region if previous MI	78.8
MI territory 2	Secondary affected region if previous MI	78.8
MI affecting territory of culprit artery?	Y/N	78.8
MI date	Year of previous MI	100.0
Type 2 diabetes mellitus		100.0
Type 1 diabetes mellitus		100.0
Hyperlipidaemia	Defined as on active treatment	100.0
Peripheral vascular disease		100.0
Atrial fibrillation		100.0
Pulmonary arterial hypertension		100.0
Hypertension		100.0
Frailty	As defined by the Canadian Study of Health and Aging Study criteria$^\$$	84.6
NYHA	New York Heart Association class of breathlessness	86.5
CCS	Canadian Cardiovascular Society Class of angina	87.5
Mitral stenosis		100.0
Mitral regurgitation		100.0
Tricuspid regurgitation		100.0
Aortic stenosis		100.0
Aortic regurgitation		100.0
Interstitial lung disease	Diagnosis requires confirmation from specialist clinic with PFTs	100.0
Asthma	Diagnosis requires confirmation from specialist clinic with PFTs	100.0
Chronic obstructive pulmonary disease	Diagnosis requires confirmation from specialist clinic with PFTs	100.0
Procedure details	What procedure did the case undergo? (PCI, diagnostic imaging and pressure wire only or rotablation)	100.0
Measured /processed data		
Baseline FFR		100.0
Hyperaemic FFR		100.0
Mean Pa		100.0
Mean Pd		100.0
Sampled FFR		100.0
Sampled period		100.0
Computed mean flow		100.0
Computed R_{total}	Dependent variable in statistical analysis	100.0
Current active drug treatments (Y/N)		
Beta blocker		100.0
Statin		100.0
Aspirin		100.0
Clopidogrel		100.0
Prasugrel		100.0

Ticagrelor		100.0
ACE inhibition		100.0
Angiotensin receptor blocker		100.0
Spironolactone		100.0
Bendroflumethiazide		100.0
Furosemide		100.0
Nicorandil		100.0
Ranolizine		100.0
Indapamide		100.0
Amlodipine		100.0
Proton pump inhibitor		100.0
Warfarin		100.0
Diltiazem		100.0
Novel oral anticoagulant		100.0

Blood analysis (blood acquired at pre-assessment clinic)

Sodium		99.0
Potassium		99.0
White cell count		99.0
Creatinine		99.0
Estimated glomerular filtration rate		99.0
Glucose		99.0
Total cholesterol		99.0
Haemoglobin		99.0
Urea		99.0
Platelets		99.0
Haemoatocrit		99.0
Mean cell volume		99.0

Electrocardiographic (acquired during pre-assessment clinic)

Rate		95.2
Rhythm	coded by number	95.2
PR interval	ms	95.2
QRS interval	ms	95.2
QT interval	ms	95.2
QRS axis	degrees	92.3
T wave axis	degrees	88.5
Corrected QT interval	ms	95.2
Q waves?	Coded by number according to territory	95.2
LV voltage criteria	in mV as the sum of the deepest S wave in V1/2 and the tallest R wave in V5/6	95.2

Echocardiographic data

TAPSE	Tricuspid annular plane systolic excursion	65.0
LV mass	Left ventricular mass: auto-calculated by Philips CX-50 from IVSDd, LVIDd and LVPWDd	75.0

LVEF Teicholz	Left ventricular ejection fraction based on the Teicholz formula (Vol=(7D^3)/(2.4+D)*	72.0
LV fractional shortening	Left ventricular fractional shortening	65.4
LV cardiac output (LVOT)	Left ventricular cardiac output base don LVOT diameter measurement Doppler time integral and heart rate	60.6
LV stroke volume	Based on the above	77.0
IVSDd	Interventricular septal diameter in diastole	75.0
LVIDd	Left ventricular internal diameter in diastole	75.0
LVPWDd	Left ventricular posterior wall diameter in diastole	75.0
IVSDs	Interventricular septal diameter in systole	67.3
LVIDs	Left ventricular internal diameter in systole	67.3
LVPWDs	Left ventricular posterior wall diameter in systole	67.3
Aortic root diameter		8.7
LVOT diameter		76.9
Ejection fraction	Simpson's biplane measurement from 4 and 2 chamber views	70.0
Stroke volume	Based on the above	70.0
E wave velocity	Doppler PW at mitral valve inlet	73.0
A wave velocity	Doppler PW at mitral valve inlet	73.0
E:A ratio		73.0
Medial and lateral e` and a`	Tissue Doppler imaging	75.0
Medial and lateral E/e`	Ratio of PW at MV and TDI	75.0
Flow propagation velocity (Vp)	Colour M mode at MV inflow (cm/s). A surrogate marker of LVEDP#	59.0
E/Vp ratio	As a marker of diastolic dysfunction	58.0
LV RWMA score for anteriorseptal region	Left ventricular regional wall motion scoring	77.9
LV RWMA score for anteriorseptal region	Left ventricular regional wall motion scoring	77.9
LV RWMA score for lateral region	Left ventricular regional wall motion scoring	77.9
LV RWMA score for posterior region	Left ventricular regional wall motion scoring	77.9
LV RWMA score for inferior region	Left ventricular regional wall motion scoring	77.9
LV RWMA score for septal region	Left ventricular regional wall motion scoring	77.9
LV RWMA score for apex region	Left ventricular regional wall motion scoring	77.9
LV RWMA score total	According to standard BSE 17 segment model (total score /80)	77.9
LV RWMA index	Score total /17	77.9
Angiographic data		
SYNTAX score		90.4
New York PCI risk score		83.7
Arterial dominance		100.0
2-D quantitative coronary angiography data		

Lesion length	mm	53.8
Percentage lesion severity		53.8
Percentage area stenosis		53.8
Calculated normal flow	From Poiseuille equation and QCA data	53.8

Red shading indicates values based on measured data which could not be considered independent variables in the current model. PAC, pre-assessment clinic; MI, myocardial infarction; PFT, pulmonary function tests; ACE, angiotensin converting enzyme; LV, left ventricle; MV, mitral valve; PW, pulse wave Doppler; SYNTAX, Synergy between PCI with Taxus and Cardiac Surgery. $^{\$}$(Rockwood et al., 2005), *(Teichholz et al., 1976), $^{\#}$(Garcia et al., 1997, Garcia et al., 2000).

5.4.3.3   Baseline characteristics

Baseline characteristics of all 53 patients are demonstrated in **Table 5.13**. The angiographic and physiological characteristics of the 104 individual cases are presented **Table 5.14** and **Table 5.15**. Data for R_{total} were normally distributed (skewness = 0.71, kurtosis = -0.11). Two outlying samples were excluded according to the outlier labelling rule on the basis R_{total}.

Table 5.13. Patient characteristics

General demographics	Mean (SD)	Range
Mean age, years	65.5 (10.2)	47 -89
Male	76.9%	
Mean body-mass index, Kg m^{-2}	29.3 (4.6)	21.6 – 44.8
Ethnicity		
White Caucasian	93.8%	
Asian	4.2%	
Black Afro Caribbean	2.1%	
Smoking history		
Current	5.8%	
Ex	65.4%	
Never	28.8%	
CCS class	2.22 (0.74)	1 - 3
NYHA class	2.07 (0.70)	1 - 3
Frailty*	2.81 (0.91)	2 - 6
Comorbidities		
Hypertension	50%	
Hyperlipidaemia	40	
Type 2 diabetes mellitus	15.4%	
Prior myocardial infarction	40.4%	
Peripheral vascular disease	8%	
Atrial fibrillation	4%	
Lung disease*	9.6%	
Valve disease*	2.9%	
Angiographic details		
Dominance		
Right	85%	
Left	6%	
Co-dominant	5%	
SYNTAX	12.0	1.0 - 29.5
New York Risk Score	4.2 (2.8)	0 - 11

Values are mean (SD), range unless stated as %.

Table 5.14. Angiographic and procedural characteristics

Target artery	% or mean (SD)	Range
Left anterior descending artery	47.1%	N/A
Right coronary artery	21.2%	N/A
Circumflex	15.4%	N/A
Left main stem	9.6%	N/A
Diagonal	6.7%	N/A
Procedure performed (case mix)		
No PCI	49.0%	N/A
PCI	50.0%	N/A
PCI and rotablation	1.0%	N/A
Mean QCA details		
Lesion length (mm)	18.51 (11.6)	6.1 – 60.9
Diameter stenosis (%)	54.9% (13.3)	21.0 – 82.5
Area stenosis (%)	77.3% (12.5)	33.5 – 97.0

Table 5.15. Overall physiological case details

Physiological details	Mean	Range
Period of cardiac cycle (s)	0.79 (0.16)	0.49 – 1.70
Myocardial resistance value (Pa min ml^{-1})	106.3 (56.40)	20.67 – 254.90
Arterial blood flow (ml/min)	106.3 (52.70)	35.74- 276.78
Mean Pa (mmHg)	86.3 (13.70)	54.7 – 120.4
Mean Pd (mmHg)	66.84 (16.57)	30.10 – 100.35
FFR (catheter laboratory)	0.754 (0.152)	0.32 – 0.98
FFR (from sampled data)	0.776 (0.150)	0.32 – 0.95

5.4.3.4 Regression modelling

Data regarding regression modelling are presented in the same broad categories as presented in **Table 5.12**.

5.4.3.4.1 Patient demographics and baseline physiology

Of the demographic and baseline clinical data, gender, ethnicity, smoking status, pack-year smoking history and resting systolic blood pressure all had a significant effect on the response variable (R_{total}). These data are presented in Table 5.16. Females had significantly increased R_{total} compared with males (132.5 vs 98.9 Pa min ml^{-1}, P=0.013). White Caucasians had a significantly lower mean R_{total} than Black Afro Caribbeans (103.5 vs 189.90 Pa min ml^{-1}, P=0.03). Current smokers had significantly increased R_{total} (158.0 Pa min ml^{-1}) compared with both ex- (95.4 Pa min ml^{-1}, p=0.03) and never-smokers (113.6 Pa min ml^{-1}, P=0.002).

5.4.3.4.2   Comorbidities

Overall, none of the recorded comorbidities (including history of myocardial infarction) were associated with any differences in R_{total}. However, when data from cases where there was history of MI in the territory of supply of the target artery (group a, n=14) were compared with those with history of AMI outside of the territory of the target artery (group b, n=10) and with those with no history of myocardial infarction (group c, n=62), there was a large and statistically significant difference in R_{total} (154.13 vs 111.8 and 115.0 Pa min ml^{-1} respectively, P=0.02) suggesting that MI affecting the territory of supply of the target artery was a significant predictor of R_{total} for that artery (see **Table 5.16**).

5.4.3.4.3   Sampled and invasively measured data

None of the sampled and invasively measured data demonstrated any significant relationships with R_{total}.

5.4.3.4.4   Current drug therapies

Taking ACE inhibiting medication was associated with a lower mean R_{total} compared with those not actively taking this medication (91.5 vs 118.6 Pa min ml^{-1}, P=0.008). This was also true of furosemide (47.0 vs 111.4 Pa min ml^{-1}, P=0.04) and nicorandil (69.7 vs 115.7 Pa min ml^{-1}, P=0.008). Regression data for these relationships are presented in **Table 5.16**.

5.4.3.4.5   Blood tests

Serum creatinine was associated with small but statistically significant variation in R_{total} (see **Table 5.16**). Each unit increase in creatinine was associated with a reduction in R_{total} of 1 Pa min ml^{-1}. No other blood test (including random glucose) demonstrate any significant relationship with R_{total}.

5.4.3.4.6   Electrocardiographic relations

None of the recorded ECG parameters had any significant relationship with R_{total}.

5.4.3.4.7   Echocardiographic relations

Analysis of echocardiographic parameters was limited by missing data; not every patient was suitable for echocardiography and, in those who were scanned, a full dataset was not always possible. Despite this limitation, significant relationships were identified. LV mass, intraventricular septal wall thickness in systole (IVSWs), mitral valve E:A wave velocity ratio (reflective of increased diastolic dysfunction) and E:Vp ratio (another marker of diastolic dysfunction (Garcia et al., 1997, Garcia et al., 2000)) all demonstrated significant relationships with R_{total}. Wall motion scoring index (WMSI) did not. However, when the data were separated

into cases where a WMSI abnormality matched the supply territory of the target artery and when it did not, there was a significant relationship (see **Table 5.16**). Cases where there was overlap of territory had a significantly higher R_{total} than those where there was no overlap (82.04 vs 115.24 Pa min ml^{-1}, P = 0.024).

5.4.3.4.8   Angiographic and 2-dimensional quantitative coronary angiographic data

QCA-Poiseuille derived 'normal flow' was significantly related to R_{total}, whereas lesion length by 2-D QCA was of borderline significance (adjusted R^2 = 0.051, B coefficient =1.14, P = 0.055). Normal flow is calculated as part of QCA assessment and is a marker of normalised flow through the artery, based upon physiological assumptions and the laws of Bernoulli and Poiseuille. It is a marker of the diameter of the normal segment of artery (Schrijver, 2002).

Table 5.16. Linear regression data for all statistically significant candidate predictive variables.

Variable	Adjusted R^2	B coefficient	Std Error	t	P
General demographic and physiological data					
Female gender	0.052	33.6	17.10	3.8	0.01
Afro Caribbean ethnicity	0.042	34.1	17.20	3.9	0.05
Current smoker	0.084	56.8	18.90	3.0	0.003
Pack-year smoking history	0.171	1.15	0.37	3.1	0.003
Weight	0.048	-0.87	0.35	-2.5	0.016
Resting SBP	0.032	1.216	.514	2.4	0.02
Comorbidities					
MI in supply territory of target artery	0.270	61.8	16.05	3.9	0.0004
Current active drug treatments					
ACE inhibitor	0.039	-23.2	11.57	-2.00	0.048
Nicorandil	0.075	-43.1	15.27	-2.82	0.006
Furosemide	0.037	-61.8	28.25	-2.19	0.031
Blood tests					
Creatinine	0.101	-1.0	0.30	-3.32	0.001
Echocardiographic data					
LV mass (g)	0.051	-0.36	0.15	-2.22	0.030
IVSWs	0.405	24.1	7.2	3.35	0.005
MV E:A ratio	0.140	70.0	20.2	3.46	0.001
E:Vp ratio	0.059	-34.62	16.4	-2.11	0.039
WMI abnormality and artery territory match	0.105	39.30	16.9	2.33	0.024
Angiographic and 2-D QCA					
QCA normal flow	0.103	-45.31	17.17	-2.64	0.011

SBP, systolic blood pressure; LV, left ventricle; IVSWs, intraventricular septal width during systole; MV E:A, mitral valve E:A wave velocity ratio; E:Vp ratio, mitral valve E wave velocity to velocity of flow propagation ratio; WMI, wall motion index; QCA, quantitative coronary angiography.

5.4.3.4.9   Final model

All seventeen candidate variables were entered into a stepwise, backward elimination model. The model eliminated twelve variables, leaving 5 in the final model. With the most significant first, the remaining variables were MI affecting the territory of the target artery, E:A ratio, nicorandil therapy, 2-D QCA normal flow and ACE inhibitor therapy. The final model was associated with an R^2 of 0.37 and a significance of <0.001. **Table 5.17** outlines included variables in the final model.

Table 5.17. Details of the final linear regression model.

Variable	B coefficient	Std error	t	P
Constant	92.19	29.34	N/A	N/A
MI in target artery territory	50.655	19.166	2.643	0.001
E:A ratio	68.774	23.161	2.969	0.001
Nicorandil therapy	-31.536	20.315	-1.552	0.013
2-D QCA normal flow	-48.884	18.240	-2.680	0.019
ACE inhibitor therapy	-15.131	15.340	-.986	0.049

R^2 = 0.37, P<0.00001. E:A, mitral valve E:A wave velocity ratio.

Therefore, the final model for R_{total} (Pa min ml^{-1}) is as follows:

$$R_{total} = \mathbf{89.35}(\mathbf{+44.2}^{\#} \, or \, \mathbf{0}) + (\mathbf{64.07} \cdot E{:}A)(\mathbf{-33.70}^{\$} \, or \, \mathbf{0}) + (\mathbf{-38.56} \cdot norm \, flow)(\mathbf{-19.73}^{*} \, or \, \mathbf{0})$$

Eq 5.4

#, if prior MI has affected the target artery territory; $, if on nicorandil therapy; *, if on ACE inhibitor therapy.

5.4.3.4.10   Bootstrap validation

The results of the 1000 fold bootstrap analysis are summarised in **Table 5.18**. After bootstrap analysis, the only variables to retain predictive significance were MI affecting the target artery territory, and nicorandil therapy.

5.4.3.4.11   Target coronary artery

ANOVA identified no significant difference in R_{total} between individual coronary arteries. These data presented in **Table 5.19**. Patients undergoing PCI had significantly lower resistance than those who did not proceed to PCI (89.4 vs 123.6 Pa min ml^{-1}, P=0.007).

Table 5.18. Details of the bootstrap analysis.

Variable	B coefficient	Std error	P
Constant	119.87	37.41	N/A
MI in target artery territory	55.83	16.96	0.003
E:A ratio	29.09	30.61	0.323
Nicorandil therapy	-46.41	14.82	0.006
2-D QCA normal flow	-35.09	22.06	0.101
ACE inhibitor therapy	-26.58	15.62	0.105

1000 sample analysis.

5.4.3.4.12 Resistance and FFR

FFR was positively correlated with R_{total} ($R^2 = 0.20$, B coefficient = 169.9, F = 24.1, P<0.0001). However, these relationships could be used predictively because they involved invasively measured data. Furthermore, it has already been demonstrated that cases with higher FFR which are more likely to proceed to PCI, have less accurate R_{total} derivation. Therefore, this particular relationship may be methodologically confounded.

Table 5.19. Coronary arterial analysis

Artery	N	Mean (Pa min ml^{-1})	SD	SEM	95% CI for Mean		Range	
					Lower	Upper	Min	Max
LAD	50	100.1	54.3	7.8	84.3	115.8	20.7	254.9
RCA	22	103.6	52.5	11.7	79.0	128.1	21.0	211.2
LCX	15	123.3	66.2	17.1	86.6	160.0	20.7	213.3
LMS	10	112.7	56.1	17.7	72.6	152.8	51.4	194.4
Diagonal	7	110.1	67.8	25.6	48.2	173.7	43.5	247.4
All cases	104	106.3	56.4	5.6	95.1	117.5	20.7	254.9

LAD, left anterior descending artery; RCA, right coronary artery; LCX, left circumflex artery; LMS, left main stem; SD, standard deviation, SEM, standard error of the mean; CI, confidence interval. One way ANOVA between groups analysis: F=0.53, P=0.71

5.4.4 Boundary condition tuning discussion

The method of statistical analysis employed in this analysis has identified significant relationships between the dependent and independent variables. Thus it appears feasible to use this approach to characterise, model and predict CMVR for 0-D model tuning. Because no approach for patient-specific tuning of boundary conditions has previously been described, this represents a major advance. It is reassuring that there is cogency in the relationships identified as significant; many of the candidate variables are already considered influential in the context of CMVR (R_{total} in the current model). Other candidate variables which have been identified were previously undescribed. Although the modest sample size does not preclude statistical anomalies from being

detected (type I statistical error), especially in the context of variables with low frequency, the cogency of these relationships suggests they may be important. **Table 5.20** explores possible mechanistic explanations for the identified candidate variables. It is important not to over-interpret the variables with low frequency (e.g. Afro Caribbean ethnicity and furosemide therapy). Bootstrap analysis and further data collection will confirm or reject these candidate variables.

This work is hypothesis-generating and demonstrates the effectiveness of the approach. It was not intended to comprehensively establish the fundamental relationships.

The current study and statistical approach is limited by the relatively modest population. Therefore, although I have demonstrated the potential for this approach, further work is needed better characterise these relationships into a more comprehensive model. Analysis of a larger sample size may be associated with several of these candidate variables dropping statistical significance whereas others may emerge as important. Nonetheless, it is encouraging that cogent associations and relationships have been identified despite a relatively crude and methodologically limited segmentation protocol.

Many of the statistical relationships important in predictive model of CMVR may be obscured in the current analysis due to higher order polynomial and /or non-linear behaviour. Examples include age and haematocrit which in the linear model were non-significant predictors of R_{total}. However, age demonstrated a significant quadratic relationship with R_{total} ($P = 0.004$), as did haematocrit ($P = 0.042$). Higher order relationships may also explain some of the apparently paradoxical negative correlations, which therefore is not necessarily indicative of a negative linear correlation. Furthermore, significant inter-variable interaction and collinearity effects may remain undetected to this linear regression modelling approach. This may be circumvented by the use of a more sophisticated statistical model (see chapter 7, further work).

The ArQ database proved invaluable in managing the large volume of clinical data. Furthermore, the ArQ query builder software was essential in the structured output of >150 variables. The VIRTUheart™ ArQ database can be updated by any authorised user from anywhere in the world. Thus it is now possible to collect structured and detailed clinical data from a larger study in order to better model 0-D parameters. This has already been tested by an international collaborator.

Table 5.20. Possible mechanistic explanations for candidate variables

Candidate variable	Possible explanation
Female sex	Unknown, but female sex is associated with a preponderance of coronary microvascular dysfunction (CMVD) possibly related to increased plaque microembolisation, autonomic imbalance, and vasodilator (NO) – vasoconstrictor (endothelin-1) imbalance (Kuruvilla and Kramer, 2013).
Afro Caribbean ethnicity	Afro Caribbean ethnicity is associated with increased prevalence of hypertrophy and left ventricular hypertrophy. Both conditions are associated with increased CMVR.
Current smoker	Recognised risk factor for increased CMVD (Crea et al., 2014).
Pack-year smoking history	Recognised risk factor for increased CMVD (Crea et al., 2014).
Weight	Small effect, low adjusted R^2 and hard to explain the negative B coefficient, possibly a statistical anomaly?
Resting SBP	Chronically elevated B is a recognised risk factor for increased CMVD (Crea et al., 2014).
MI in supply territory of target artery	MI is an acknowledged cause of increased CMVR.
ACE inhibitor therapy	Previously undescribed. ACE inhibitors are potent vasodilators which would explain effect.
Nicorandil therapy	Previously undescribed. Nicorandil is a positive lusitrope which enhances myocardial relaxation. This would explain the direction of the relationship.
Furosemide therapy	Previously undescribed. Difficult to explain mechanism.
Serum creatinine	Previously undescribed. Difficult to explain direction of the correlation.
LV mass (g)	Acknowledged that this may theoretically influence CMVR and used (indirectly) in the calculation of vFFR$_{CT}$ (Taylor et al., 2013).
IVSWs	Ventricular hypertrophy is a recognised cause of increased CMVR (Crea et al., 2014).
MV E:A ratio	Previously undescribed but diastolic function is mechanistically important in terms of CMVR and coronary blood flow.
E:Vp ratio	Previously undescribed but diastolic function is mechanistically important in terms of CMVR and coronary blood flow.
WMI abnormality and artery territory match	Previously undescribed but reduced systolic dysfunction may reflect underlying myocardial fibrosis or scarring and thus increased CMVR.
QCA normal flow	Increased flow accompanies reduced resistance.

CMVD, coronary microvascular dysfunction; NO, nitric oxide; SBP, systolic blood pressure; LV, left ventricle; IVSWs, intraventricular septal width during systole; MV E:A, mitral valve E:A wave velocity ratio; E:Vp ratio, mitral valve E wave velocity to velocity of flow propagation ratio; WMI, wall motion index; QCA, quantitative coronary angiography.

Finally, it remains to be decided whether or not the addition of data from non-invasive testing may improve the predictive power of such statistical modelling. Investigations such as such as CMRI, PET, SPECT or perfusion echocardiography have been used to estimate CMVR (Knaapen et al., 2009). Mean blood flow derived from CTCA perfusion may be particularly apposite for this purpose because it yields both anatomical and mean blood flow data which can be used to tune the boundary conditions directly. Although it may not be desirable to build a model reliant additional investigations, this should be considered if the predictive power of the model is improved significantly.

5.5 Overall conclusions

In this chapter, I have demonstrated that realistic coronary flow waveforms can be characterised by coupling the 3-D model to 0-D models in order to represent the influence of the CMVR at the distal outlets. By applying a novel optimisation algorithm, the optimal design (balancing scientific accuracy and practical constraints) was selected for use in the VIRTUheart™ model. The sensitivity analysis demonstrated that the tuning of the 0-D parameters is the dominant influence on the accuracy of vFFR calculations, even more influential than those representing the lesion severity /geometry. Finally, a novel approach to patient-specific tuning of the distal boundary condition was presented. Because error in the tuning of the distal boundary condition is the greatest contributor to vFFR error, this is likely to represent the most significant discovery in this chapter and in this thesis. This work will continue to characterise the relationships between candidate variables and the CMVR more comprehensively.

Chapter Six:

Computing Coronary Flow

6.1 Introduction

Chapters 1-5 focus on the prediction of coronary pressure, in an attempt to predict vFFR. FFR has inspired a revolution in interventional practice by demonstrating the superiority of physiological over anatomical assessment in CAD. FFR is associated with improved clinical and economic end points. However, it is also associated with a number of limitations. Consequently, it may not be the optimal physiological index when assessing the significance of coronary disease. It is proposed that many of these assumptions and limitations may be circumvented by the additional measurement of intracoronary flow rate.

The first consideration is that the derivation of the equation which calculates fractional *flow* reserve from *pressure* data (see section 1.4.1) is based upon the assumption that hyperaemic CMVR (and therefore hyperaemic flow) remains constant pre- and post-PCI; this fundamental premise has been challenged (Chamuleau et al., 2003, Verhoeff et al., 2005):

$$FFR = \frac{Q_{stenosis}}{Q_{norm}} = \frac{P_d}{P_a}$$

Eq 6.1

Second, the independence of vFFR from other dynamic physiological factors such as arterial and venous pressure has also been challenged (Siebes et al., 2002). Third, FFR relies on the assumption of consistent attainment of maximal hyperaemia with a standardised dose of adenosine, yet variability of dose, dosing strategy, and most importantly, response to treatment are reported (Chareonthaitawee et al., 2001, De Luca et al., 2011, Rioufol et al., 2005) (section)1.4.1.4). Fourth, although FFR is influenced by the CMV, it cannot provide information regarding the state of the CMV (see section 1.4.1.10). In theory, this means that lesion significance may be masked by coronary microvascular disease (CMVD). Until recently, the alternative to FFR was to measure CFVR but this is limited by variability in baseline physiology and requires intracoronary Doppler estimation of flow velocity which is notoriously challenging.

There are therefore limitations associated with assessing pressure and flow *independently*. The implications of independent pressure or flow results are outlined in **Table 6.1** and **Figure 6.1**.

Table 6.1. The implication of normal and abnormal flow and pressure indices

Test	Result	Implication
CFVR	Normal (≥2.0)	Healthy epicardial and microvascular compartments (but influenced also by variability in baseline measurement)
	Abnormal (<2.0)	Unhealthy microvascular, or significant epicardial stenosis
FFR	Normal (>0.80)	No significant benefit from revascularisation of epicardial disease
	Abnormal (≤0.80)	Likely benefit from revascularisation of epicardial disease

In theory, concurrent measurement of pressure *and* flow (Q) may be a superior approach because, according to the hydraulic equivalent of Ohms law, rather than yielding a single physiological parameter the calculation of resistance (R) also becomes possible:

$$\Delta P = Q \cdot R \qquad à \qquad R = \frac{\Delta P}{R}$$

Eq 6.2

If P_d is known, and coronary venous pressure is assumed to be negligible, then calculation of both epicardial and CMV resistance can be made (see below). Therefore, combined assessment allows

a more comprehensive understanding of the physiological state of both compartments. Thus the physiological state of the CMV and its relative influence on FFR can be inferred. **Figure 6.1** demonstrates schematically the pathological spectrum of epicardial and CMV physiology relative to the commonly used indices of intracoronary pressure (FFR) and flow (CFVR).
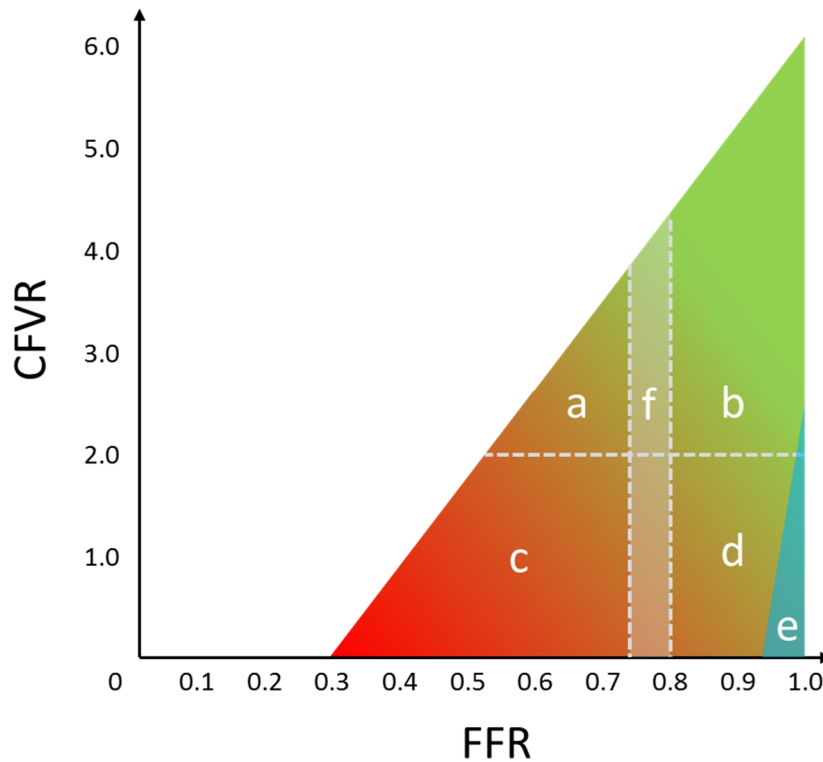

Figure 6.1. The importance of combined pressure-flow measurement during ICA with green and red colouration reflecting good and poor prognosis respectively
Zone a indicates epicardial disease with healthy CMV. Zone b indicates healthy epicardial and CMV physiology. Zone c indicates concordance between FFR and CFVR results. Zone d indicates normal FFR with reduced flow reserve associated with predominately microvascular disease. Zone e indicates those patients with microvascular angina with pure CMV involvement. Only with combined physiological assessment can these individual zones be distinguished. Zone f indicates the grey-zone in FFR threshold between 0.75 and 0.80. Adapted from van de Hoef et al (van de Hoef et al., 2014).

Hyperaemic stenosis resistance (HSR) is an index of intracoronary physiology which incorporates both pressure and flow. It is the ratio of the temporal mean trans-lesional pressure gradient ($\overline{\Delta P}$) and average peak flow velocity (APV) measured by a combined flow (Doppler) and pressure sensitive angioplasty wire, distal to the target coronary lesion:

$$HSR = \frac{\overline{\Delta P}}{APV}$$

Eq 6.3

Assuming a coronary venous pressure (P_v) of zero, the same measurements also allow estimation of CMVR by calculating the velocity-based index of microvascular resistance (IMR):

$$IMR = \frac{P_d - P_v}{APV} = \frac{P_d}{APV}$$

Eq 6.4

Where P_d is the pressure measured distal to the target lesion. In the absence of epicardial disease, P_a can be substituted. HSR provides a more refined physiological assessment which quantifies the degree of coronary resistance attributable exclusively to the stenosis (Kern et al., 2006). A HSR of >0.80 mmHg·cm^{-1}·s is the threshold for ischaemia (Meuwissen et al., 2002). HSR is independent of variations in the hemodynamic conditions and is highly reproducible (Meuwissen et al., 2002, Siebes et al., 2004). An advantage over FFR is that the calculation of HSR is considered robust with variations in maximal hyperaemia because of the inclusion of the ΔP/Q ratio (Meuwissen et al., 2002). In a three-way comparison HSR was superior to both FFR and CFVR in identifying physiological lesion significance and its performance was particularly impressive in cases demonstrating physiologically discordant results between FFR and CFVR (Meuwissen et al., 2002). The importance of physiological discordance was further highlighted by Meuwissen and van de Hoef et al. Meuwissen *et al* studied 181 intermediate coronary lesions. Discordance in physiological lesion assessment (between FFR and CFVR) was observed in 28% of patients (Meuwissen et al., 2001). Patients with a normal FFR (>0.75) but abnormal CFVR (<2.0), had a significantly increased CMVR, suggesting a prominent role of CMVR in the relationship between CFR and FFR, and supporting the notion that increased CMVR may mask the apparent significance of an epicardial lesion. Thus, combined physiological measurements enabled the relative influence of epicardial and CMV disease to be distinguished. The same group performed a similar study of 186 intermediate lesions but followed patients over a twelve month period. Increased MACE was observed in those with concordant abnormal *and* physiologically discordant results, compared to the group with concordant normal values (33.3% vs. 19.7% vs. 5.4%, P = 0.008). HSR was used successfully to identify the group with discordant FFR and CFVR results, i.e. those with worse prognosis (Meuwissen et al., 2008). HSR was a better predictor of MACE than both FFR and CFVR. Perhaps the most compelling evidence in support of combined pressure and flow measurement was published in 2014 by van de Hoef et al who studied 157 intermediate coronary lesions over 11.7 years. 37% of these cases demonstrated discordance between FFR (at the 0.80 threshold value) and CFVR. Compared with concordant normal results, those with normal FFR but abnormal CFVR had a significantly increased MACE rate (28% vs 80%, p<0.001). Conversely, those with normal CFVR and abnormal FFR had a MACE rate equivalent to those with concordant normal results (van de Hoef et al., 2014).

If FFR represents the first major step towards routine physiological lesion assessment, perhaps combined pressure and flow measurement should represent the logical and most rational next step. For over a decade an increasing body of literature has supported combined physiological assessment in the context of interventional coronary artery disease assessment. However, despite the aforementioned benefits, the measurement of coronary flow has become largely ignored in clinical practice and currently is mostly restricted to a limited number of coronary physiological experts and researchers. This is because Doppler signal artefact is commonly encountered (Kern, 2000). Even in expert hands inadequate signal acquisition occurs in up to 15% of cases (Kern et al., 2006). An 'adequate' Doppler signal may not reflect a truly representative result. Although calibration testing widely demonstrates the accuracy of the method, *in vivo* use is limited when there are secondary flow patterns, disturbed, turbulent or rapidly fluctuating flow or where there is a large velocity gradient in the sample volume. Such effects may be observed near bifurcations, stenoses, or immediately downstream of catheters. Furthermore, velocity gradients are large at the vessel walls. High amplitude, low frequency wall artefact is often problematic when the sample volume is close to the vessel wall (Hartley, 1989). When physiological assessment is performed, operators have come to depend almost exclusively on FFR alone due to the relative simplicity of pressure measurement compared with flow. The challenges of measuring coronary flow are well documented and acknowledged, even amongst those who support its use most (Kern, 2000, Siebes et al., 2004, van de Hoef et al., 2012).

There is therefore a need for a simpler and more reliable method for measuring coronary arterial blood flow in routine clinical practice.

Throughout this thesis I have demonstrated the ability to compute coronary flow from angiographic imaging and pressure data using CFD modelling. This method has proven successful in developing and tuning the model of vFFR. In principle, the same method can be used to compute flow in the cardiac catheter laboratory, provided invasively acquired pressure data is available. Although the requirement for pressure measurement is a disadvantage (a limiting factor in FFR uptake and the basis for much of the work in this thesis), these data provide the CFD boundary conditions (mean or transient pressure) and so, unlike vFFR modelling, no gross assumptions are needed in the computation. This is a major advantage. There may therefore be merit in this method in cases where a pressure wire is used. Although the primary aim of this thesis was to develop wireless physiological assessment, it is unlikely to be applicable in every case and it is likely that a subset of cases will continue to warrant further investigation or data collection. Furthermore, if vFFR does not become a commercial success on a wide scale, this method may add value to the standard FFR measurement.

213

The hypothesis for this chapter is that coronary flow can be computed using CFD from angiogram images and the measured translesional pressure gradient data. The aims were twofold. First, the computational model was used to compute the ΔP-Q relationship. Second, the results were validated. As there is no *in vivo* gold-standard test for measuring coronary flow a novel experimental system based on patient-specific 3-D printed coronary arteries was developed for validation purposes.

6.2 Methods

The work in this section was supported initially by a grant from the University of Sheffield Faculty Innovation Fund (X/00598-13-29) and latterly by a Medical Research Council Confidence in Concepts grant (R/140047-11-1). PM was the principal investigator on both grants and IZ and, AN were co-applicants. All three investigators contributed to the work in this chapter.

6.2.1.1   Computational methods

Five patient-specific 3-D arterial geometries were meshed using the optimised meshing parameters described in Chapter 3 and deployed in Chapters 4 and 5. The computation of coronary flow from measured pressure boundary conditions has already been described and applied in Chapter 3 and 5. Computation of translesional pressure gradient ($\mathit{\Delta P}$) was performed applying coronary flow at the inlet boundary and a zero-pressure condition as the outlet condition. The aim of this validation experiment was to demonstrate that the $\mathit{\Delta P}$-Q relationship can be computed accurately. If successful, this method may be apposite for use in the cardiac catheter laboratory. Both transient and steady flows were examined experimentally. However, a steady-state solution based on $\overline{\mathit{\Delta P}}$ was simulated to produce mean flow results (see individual experimental protocols below). In each case, the fluid model was matched to the experimental blood analogue (viscosity and density – see below) and were consistent with the methods described in Chapter 3. In order to extract pressure and flow data from different points within the lumen, a *.vtk centreline was inserted using the skeletonisation function within GIMIAS. The centreline coordinates were used to define a polyline in ANSYS CFX Post and pressure and flow results were extracted at incremental points along this line.

6.2.1.2   Experimental circuit development

To validate the computed ΔP-Q results, a gold-standard reference was required. In the absence of an *in vivo* gold-standard method for measuring coronary flow, a novel experimental flow circuit was developed. The circuit comprised six key elements (see **Figure 6.2**):

- A steady-flow gear pump (a): to generate flow within the human coronary physiological range.

- A pulsatile manifold (b): to convert steady flow into pulsatile flow

- Compliance chamber (d): to eradicate noise relating to vibration artefacts from the flow in the steady-flow condition

- Patient-specific 3-D coronary arterial phantom models (e) to represent realistic coronary anatomy

- Ports built into the circuit to enable instrumentation for physiological monitoring (f and g).

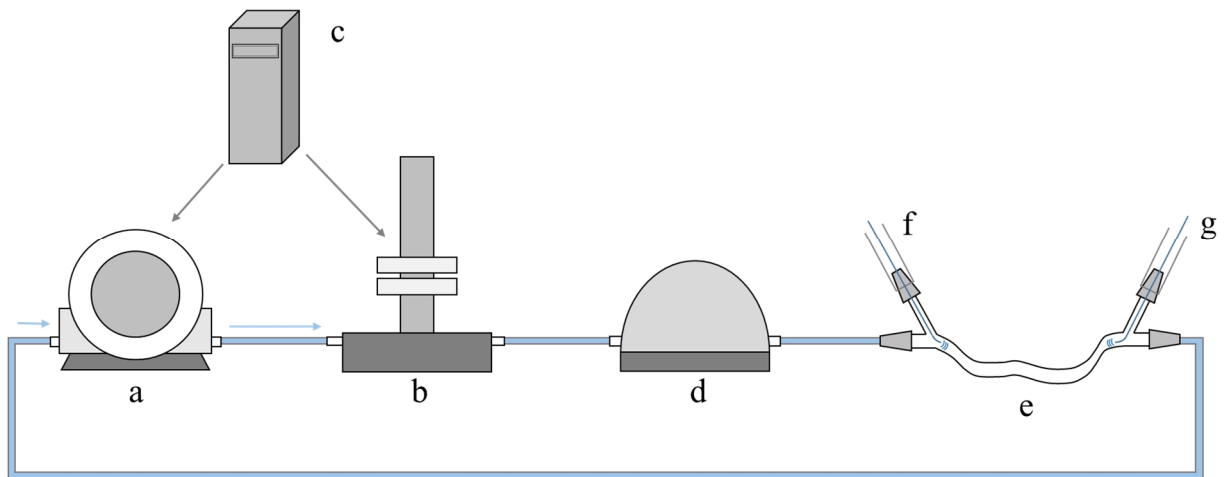- A control system to control the flow and pulsatility (c).

Figure 6.2. Schematic diagram of the experimental flow circuit.
The steady flow gear pump (a) delivers steady flow to the pulsatile manifold which converts steady flow into pulsatile. Both devices are controlled by the programmable command module (c). Fluid passes through the compliance chamber (d) before the 3-D printed artery (e). Ports (f) and (g) are used to pass instruments into the system to monitor pressure and flow.

6.2.1.3   Micropump, pulsatile manifold and command module

The steady-flow gear pump, pulsatile manifold and command module were supplied by the ElectroForce Systems Group (formerly of Bose Corporation MA, USA and now part of TA instruments, MN, USA). The gear pump (Pump Head, Cavity Style, 1760 ml/min) delivered a steady flow in the range 50 - 180 ml min^{-1}. This flow range was selected because it reflects typical physiological coronary flows from baseline up to hyperaemic. Calibration was performed in two stages according to a standard operating procedure. First, the flow produced by the pump was compared with the flow setting selected to calculate the error and this was used to calculate an offset value. Second, the flow rate was calibrated further, prior to each individual experiment and within each unique geometry, and re-checked afterwards. Calibration was performed by measuring

the volume of fluid draining from the system in one minute and repeating this at 10 ml min^{-1} increments across the full range of experimental flows (50 – 180 ml/min). Pump control level (input) and measured flow (output) data were then plotted and the regression coefficient was extracted from the line of best fit (MS Excel). The regression line was used to select the pump setting required to deliver the desired flow rates.

The pulsatile manifold (BioDynamic Test Instruments, Bose Corp, ElectroForce Systems Group) uses a bellows displacement controlled system which modulates the manifold volume in order to deliver a prescribed flow waveform. Both systems were controlled by WinTest® Controls software (version 4.1, Bose, Corp, ElectroForce Systems Group) which allows the mean flow rate and pulsatile waveform to be controlled. Flow (Q) pulsatility was programmed by prescribing the variation in volume (*V*) of the pulsatile manifold as a function of time (*t*) thus flow is equal to:

$$Q = \frac{dV}{dt} = \frac{V_t - V_{t-1}}{dt}$$

$$\text{Eq 6.5}$$

which rearranges to:

$$V_t = (Q_t - \bar{Q}) \cdot dt + V_{t-1}$$

$$\text{Eq 6.6}$$

For each vessel geometry both patient-specific and idealised pulsatile flow waveforms were defined. Patient-specific flow waveforms were computed using the VIRTUheart™ model. The measured pressure boundary conditions were used in the simulation to characterise transient flow and the period of the cardiac cycle (*T*) on an individual patient basis (as described in Chapters 3 and 5). For the idealised waveforms a sinusoidal function was applied thus:

$$Q_t = \bar{Q} + A \cdot sin(2\pi) \cdot \frac{t}{T}$$

$$\text{Eq 6.7}$$

Where the amplitude of oscillation about the mean, A, was set constant. The mean flow rate, Q, and period, T, were controlled via the WinTest® Controls software and adjusted to match the variation of the waveform observed in the patient-specific data. An example of patient-specific and idealised waveforms is demonstrated in **Figure 6.3**.
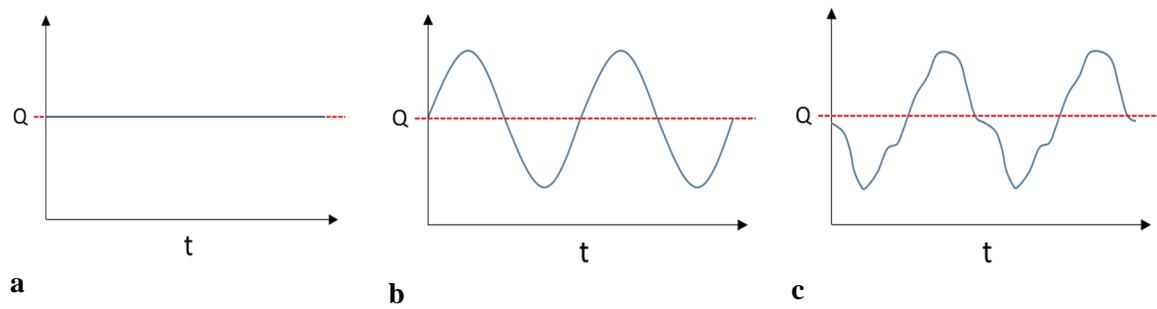
Figure 6.3. Schematic demonstrating the three methods of experimental flow.
(a) demonstrates steady flow, (b) the sinusoidal 'idealised' flow and (c) an example of patient-specific flow derived from measured data. The dotted red line indicates mean flow (Q).

6.2.1.4   Blood mimicking fluid

A glycerol/water solution was used as a blood analogue within the circuit. To obtain a viscosity equivalent to that of blood (0.0035 Pa s), 40% pure glycerol was mixed with 60% water by weight measurement. This gave a density of 1082 kg m^{-3} at a laboratory temperature of 22°. This is consistent with other experimental models of human blood flow (Segur and Oberstar, 1951). Fluid density (ρ) was obtained by weighing five eppendorfs, each containing 14 mls of solution:

$$\rho = \frac{m}{v}$$ Eq 6.8

where *m* is mass and *v* is volume. The density was 1082 kg/m^3 at a viscosity of 3.5 Pa.s in all experiments. An ultrafine polyamide nylon powder (Orgasol® Powders, Arkema Group, Paris, FR) was added to mimic the ultrasonic back-scatter properties of erythrocytes and facilitate Doppler analysis. The unground microspheres have a very narrow particle size distribution approximating that of erythrocytes (10μm). Use of Orgasol powder has been validated within *in vitro* Doppler flow phantoms to produce backscatter properties approximating real blood (Samavat and Evans, 2006, Raine-Fenning et al., 2008). Oragsol™ powder (2001 UD Nat1 Polyamide N12, Arkema) was suspended in the glycerol solution consistent with the methods described in these studies. According to fluid weight, Orgasol particles (1.82% weight) and surfactant (Decon Neutracon, Decon Laboratories LTD, Sussex, UK) (0.9% weight) were mixed thoroughly with the water-glycerol solution (see above), followed by agitation for at least 4 hours.

6.2.1.5   3-D coronary arterial printing
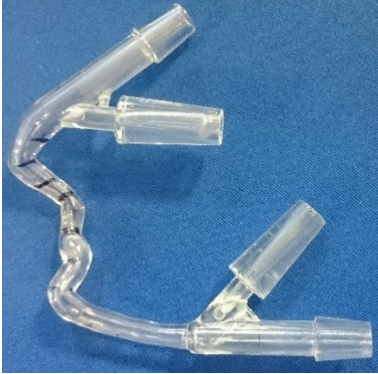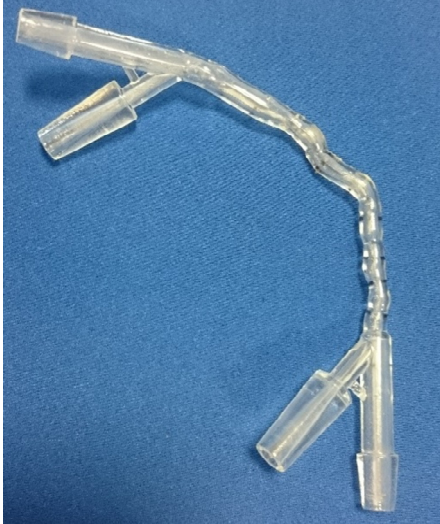
Five patient-specific coronary arterial geometries were selected for 3-D printing. The geometries were selected in order to represent a range of different arteries and lesion severities. Specifically, cases represented physiologically severe (FFR=0.64), borderline (FFR=0.79 and 0.82) and non-significant (FFR=0.86). Cases were segmented and reconstructed *in silico* from coronary

angiography using the VIRTUheart™ workflow using the methods described previously. **Table 6.2** summarises the key features of the printed arterial cases. The luminal surface meshes were converted from *.vtk into surface triangular language (*.stl) format. STL files were transferred to Materialise NV (Leuven, BE) where computer aided design was used to add wall thickness and connection and physiological transducer ports (see **Table 6.2** and **Figure 6.4**). The models were printed using a stereolithography method where the model is printed in a container of epoxy that hardens when struck by the laser printing beam. The printing material was TuskXC2700T. Printing tolerance was ±0.2mm with layer thickness of 0.1mm and minimal wall thickness of 0.8mm. Connector ports were designed for external interference fit with connecting conduits and for internal interference fit with standard clinical Luer fittings. To the best of our knowledge, this is the first example of the use of patient-specific 3-D printed arteries in the context of experimental modelling.

6.2.1.6   Connections and conduits

Experimental components were connected by 5 mm non-compliant transparent tubing by interference fit. Physiological wires were introduced into the circuit using a PCI introducer needle via a haemostatic PCI valve (AccessPLUS Haemostatic Valve, Merit Medical Systems Inc. CA, USA) consistent with standard PCI practice at STH. Prior to experimentation, all air was carefully aspirated from the circuit via the haemostatic valves.

Photograph	Specification
	Case: V001 Artery: LAD FFR: 0.64 Inlet diameter: 4.78mm Min diameter: 1.356 mm Outlet diameter: 2.24mm Stenosis: 72%
	Case: V004 Artery: RCA FFR: 0.79 Inlet diameter: 4.44 Min diameter: 1.282 mm Outlet diameter: 1.74 Stenosis: 71%
	Case: V012 Artery: LAD FFR: 0.72 Inlet diameter: 3.54 mm Min diameter: 1.177 mm Outlet diameter: 2.06 Stenosis: 67%
	Case: V012 Artery: RCA FFR: 0.86 Inlet diameter: 3.16 Min diameter: 1.700 mm Outlet diameter: 2.5 Stenosis: 46%

Case:	V014
Artery:	LCX
FFR:	0.82
Inlet diameter:	3.13
Min diameter:	1.656 mm
Outlet diameter:	1.99
Stenosis:	46.2%

Table 6.2 (and on previous page). Summary of the five 3-D printed coronary geometries
Images are roughly in anatomical position. $^\$$Catheter laboratory measurement under hyperaemic flow conditions. *Diameter. LAD, left anterior descending artery; RCA, right coronary artery; LCX, left circumflex artery. Discolouration of model V012 RCA is secondary to contrast dye.
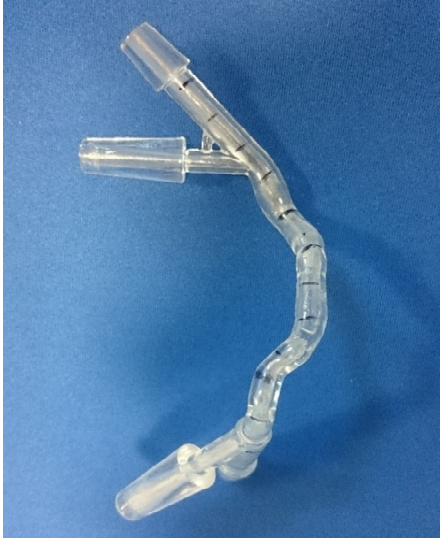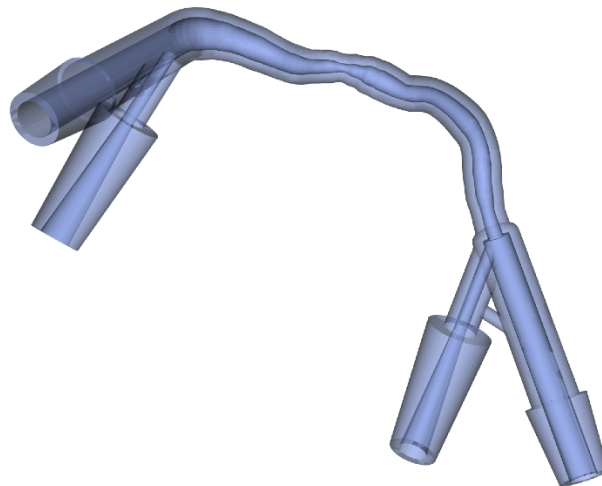
Figure 6.4. Semi-translucent rendering of model V001_LAD roughly in anatomical position, showing the vessel and connector walls and lumens.

6.2.1.7   Pressure measurements

Two systems were used to record pressure within the flow phantom. First, two 70 cm, 5 Fr Mikro-Tip® MPC-500 pressure catheters (Millar Instruments Inc. Houston, TX, US) were used to measure pressure at the proximal and distal pressure ports simultaneously. Due to the diameter of the Millar catheters, this system was restricted to the inlet and outlet pressure ports. Millar readings were

made using the Bose Electroforce WinTest® software and exported by USB memory stick. Second, the Volcano Primewire was used. The Volcano Primewire has a 0.34 mm diameter with a pressure transducer positioned behind the 3 cm radiopaque tip. This allowed the pressure to be recorded at any luminal position consistent with standard clinical practice. The proximal pressure was recorded at the proximal pressure port using the ComboMap Model 6800 system (Volcano, Rancho Cordova, CA, USA) via the P_a pressure port using a clinical pressure transducer (TruWave Disposable Pressure Transducer, Edwards Lifesceinces Corp, CA, US) employed within STH. Readings were taken with the Volcano ComboMap® System Model 6800 (Volcano, Rancho Cordova, CA, USA) and, where appropriate, were exported on CD. To maintain a clinical focus, all equipment and methodology used for the second method (Volcano) were identical to that used in standard STH clinical angioplasty practice.

6.2.1.8 Flow measurement

In the following experiments, flow rate and pulsatility were prescribed precisely by the operator, controlled by the WinTest® Controls software and produced by the gear pump and pulsatile manifold. The accuracy of the flow rate was repeatedly calibrated and checked according to the method detailed above. The prescribed experimental flow was compared with the current clinical flow measurement method, Doppler flow wire, in a head-to-head comparison. The Volcano FloWire® Doppler Guide Wire via the ComboMap® system that was used, was identical to the system used in the catheter laboratory at STH. Similar to the pressure wire, the FloWire has a flexible 3 cm radiopaque tip. The piezoelectric crystals and transducer are located at the very tip. The FloWire® detects flow velocity by pulse wave (PW) Doppler (frequency 12 MHz) with a gate with a range gate location of 5-7mm from the tip in a 30º arc. Trigonometry reveals that the diameter of the range gate spans 3.6 mm. Pulse repetition frequency (PRF) is 12-100 KHz and pulse duration is 1.3 µsec. All velocity signals within the range-gate envelope are reported by the ComboMap. However, only the instantaneous peak velocity (IPV) is used for measurement. This component of the signal corresponds to the fastest moving erythrocytes /particles. The FloWire® software tracks the IPV, averaging it over a specified number of beats (between 1 and 5) and reporting the average peak velocity (APV). ComboMap calculates APV thus:

$$APV_{(cm/s)} \quad = \frac{\sum_{n=R_{-1}}^{R_{x-1}} IPV(n)}{R_x - R_1} \qquad \text{Eq 6.9}$$
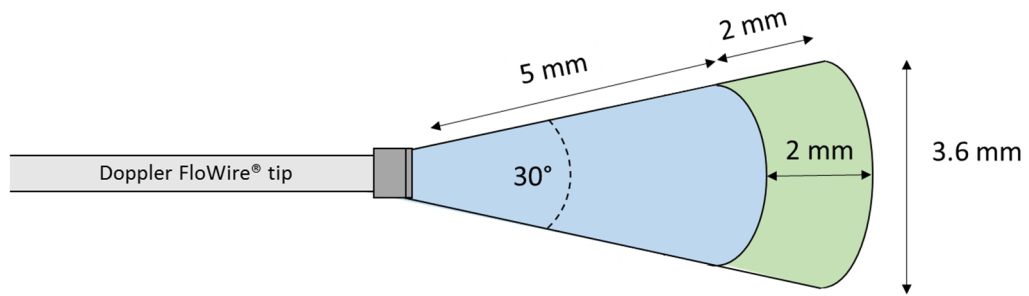
Figure 6.5. Schematic of the dimensions of the Doppler 'window' or 'range gate'.

Figure 6.5 demonstrates the dimensions of the Doppler window, which is adequate to span the entire diameter of most coronary arteries. If the tip is against the vessel wall, but lies in a coaxial position, the range gate may not span the entire diameter but in most cases will still survey the centre of the lumen. For fully developed flow the velocity profile is parabolic, peak velocity occurs in the centre of the lumen and is equal to twice the mean. As described previously (section 2.2.1), for several reasons, coronary arterial flow is often not fully developed, nor parabolic. Furthermore, ensuring alignment of the wire with the axis of the vessel is challenging. The Volcano ComboMap Operators Manual advises users to: "*Locate the tip of the guidewire at the location of interest and adjust guidewire orientation to measure peak velocities*". Standard clinical practice is to position the wire under fluoroscopy screening into the desired location and then to manipulate the wire until the 'optimal' (most dense) Doppler signal is returned.

6.2.2 Experimental protocols

6.2.2.1 Preliminary experiments

The numerical model was simulated using four combinations of two different viscosities (0.0035 Pa.s) and densities (1082 and 1100 kg/m^3) in order to understand the impact of small experimental errors on the results. Vessel geometry data were used to calculate the maximum Reynolds numbers associated with each model at each flow. Photographs of the test rig are demonstrated in **Figure 6.6** to **Figure 6.8**.
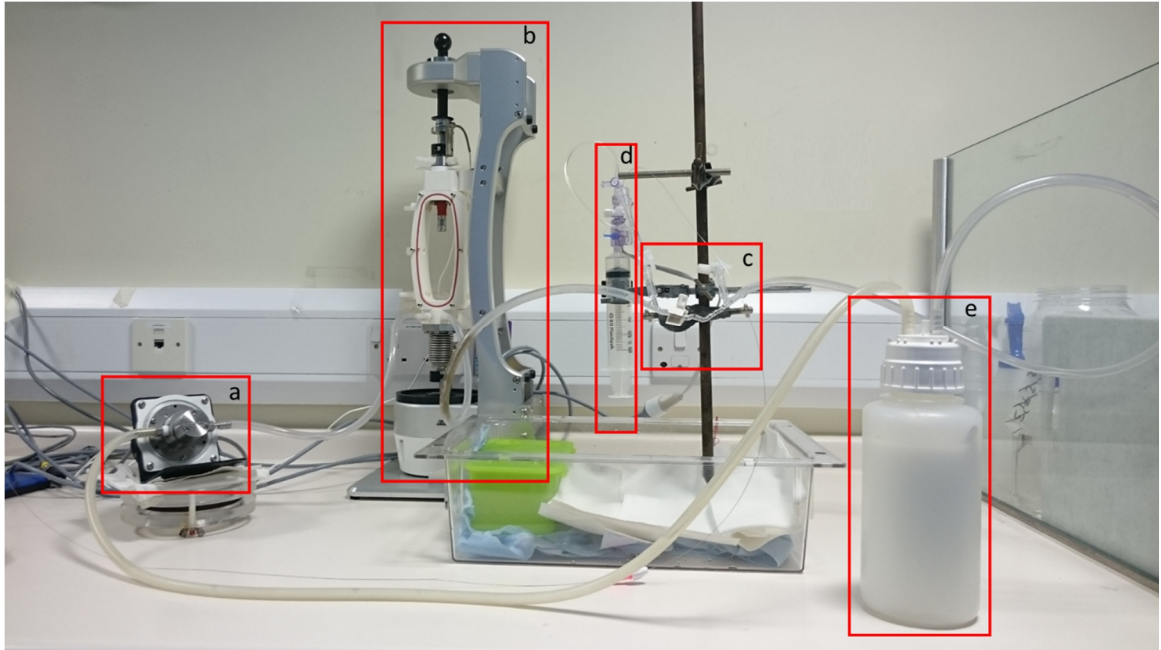
Figure 6.6. The test rig.
The gear pump (a) pump fluid through the pulsatile manifold (b) and then onto the 3-D printed arterial model (c) before returning fluid to the reservoir (e). The syringe and transducer (d) are connected to the proximal pressure port, the position of which is analogous to the catheter tip within the coronary ostium.
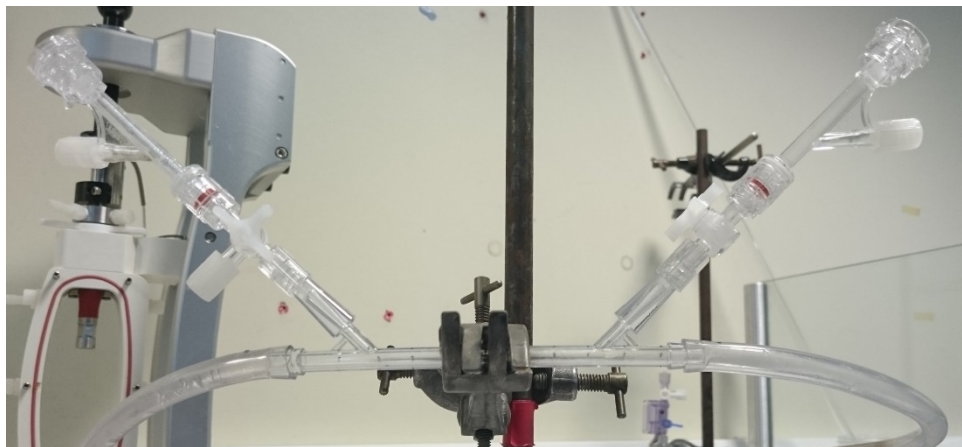
Figure 6.7. A printed model (idealised model) in the circuit with haemostatic valves attached ready for instrumentation.

223
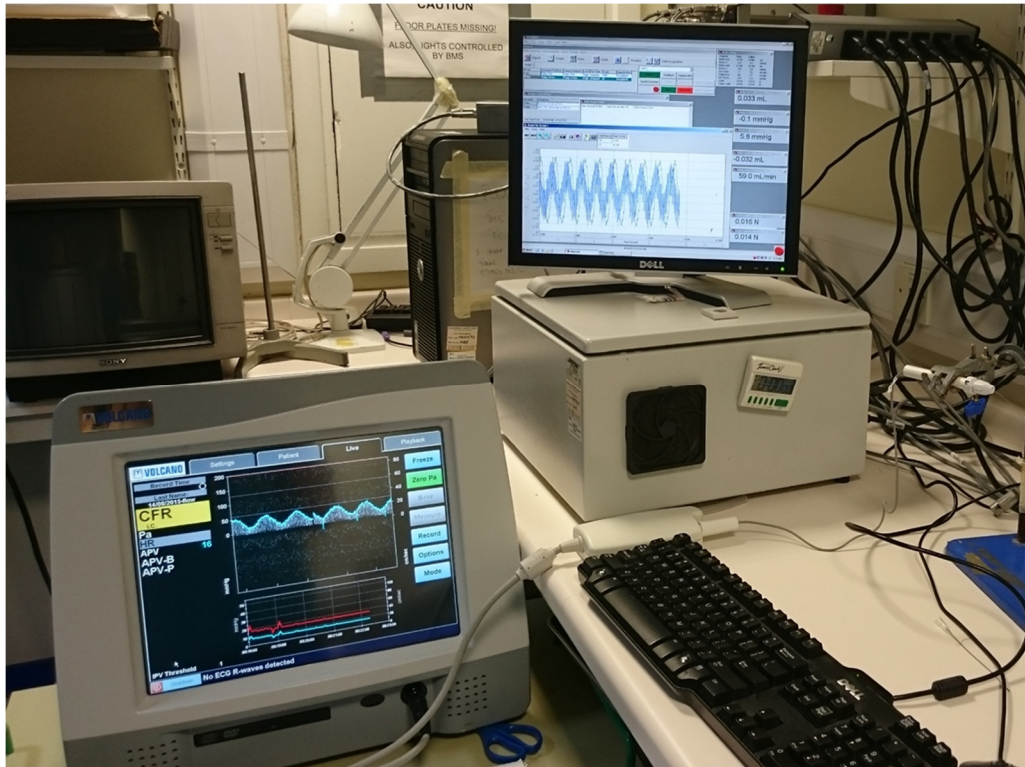
Figure 6.8. The command module (top right) and ComboMap (Volcano) analysis machine (bottom left).

6.2.2.2 Pressure-flow analysis

The principal aim of the current study was to use CFD modelling to predict the pressure gradient-flow (ΔP-Q) relationship. Therefore the experimental circuit was run with all the models, at all flow rates, with steady and pulsatile (idealised sinusoidal and patient-specific) flow. Full calibration was performed before and after each experiment.

The pressure gradient was measured in two ways. In each case the *proximal* pressure was measured from the inlet pressure port using either the volcano (via the Edward's TruWave® transducer) or the Millar system. This is analogous to measuring the Pa pressure at the catheter tip from the coronary ostium /inlet. Distal pressure was first measured from the distal pressure tapping port. However, because this is inconsistent with clinical measurement distal pressure was also measured at the outlet from inside the vessel lumen with the pressure wire. The pressure wire was inserted into the distal lumen via a retrograde approach through the distal port. This was to avoid augmentation of the pressure gradient as a result of the wire within the stenosis. The effect of the wire is not (yet) represented by the CFD model and it was deemed important to perform a like-for-like comparison. In parallel, the equivalent experiments were performed *in silico.* In each case, the computed results were plotted alongside measured values in a plot of pressure gradient versus flow.

If the computed results agreed with experimental values, this would validate the computational method for computing flow from measured pressure conditions.

6.2.2.3   Doppler analysis

The rationale for this experiment was to compare flow measured with the currently employed clinical method, Doppler ultrasound, with the prescribed experimental flow. Because Doppler ultrasound returns a velocity (V) signal and not a volumetric flow rate (Q) a direct comparison could not be made. However, because the dimensions and cross sectional area (A) of the 3-D printed models were known precisely, the relation between the two could be calculated at any location ($Q = V \cdot A$) which enables a comparison of results. As far as appropriate, clinical methodology was used to ensure results were clinically relevant and applicable.

The wire was manoeuvred via a standard clinical haemostatic valve, into the optimal longitudinal position. During initial testing the Doppler-tipped guidewire was manoeuvred, under direct visual guidance in order to ensure the optimal co-axial position within the lumen. It was considered that this approach might offer the best results. However, the Doppler signals returned were suboptimal. Furthermore, this approach is clinically unrealistic; only the location of the wire tip is seen by fluoroscopy and this cannot be used to discern the precise direction of the tip relative to the coronary lumen or if the tip is away from the vessel wall. This method was replaced with the more clinically realistic approach where the guidewire was positioned at the appropriate longitudinal location along the phantom lumen and then manipulated (with an angioplasty guidewire torquer) until the optimal Doppler signal was acquired. Hence, this returned optimal Doppler signals and is consistent with the clinical method (see section 6.2.1.8).

APV was measured at the inlet and outlet under steady-state, sinusoidal and patient specific flows. ANSYS-CFX Pre was used to measure precisely the cross-sectional area at these regions from the computational model of the vessel geometry and these areas were used to convert the prescribed volumetric flow rate into a mean flow velocity. Assuming a parabolic velocity profile the expected APV was double this value. Each measurement was repeated twice (a total of three times) at each location. The velocity scale and the instantaneous peak velocity (IPV) threshold were adjusted for optimal display and tracking of the velocity signal. As in the previous experiment, each artery was evaluated at flow rates in the range 50 -180 ml/min in 10 ml/min increments.

6.2.2.4   Statistical analysis

The level of agreement (precision) between prescribed and measured APV were assessed with Bland-Altmann plots and by calculating the mean, standard deviation and error range from delta

values between measured and prescribed APV. In addition, the coefficient of variation between repeated measurements was calculated. Pearson's correlation coefficient was used to assess the strength of correlation between measured and prescribed values in order to assess the accuracy of linearity in the Doppler signal.

6.3 Results

3-D printing and experimental flow and pressure measurement was carried out successful in all five models. The maximum Reynolds numbers were calculated for each model, at each flow rate, based on the minimal luminal diameter. These data are presented in **Table 6.3**.

6.3.1.1.1 Millar and Volcano systems

The pressure data acquired from the Millar and Volcano systems were compared within the pressure ports to ensure similarity. Both systems returned pressure recordings every 0.005 s. Differences between the systems were found to be consistent at <1%. For both systems under steady state conditions up to the maximum flow rate of 180 ml/min, the maximum observed variability (range) was <1 mmHg.

6.3.1.1.2 CFD and fluid model variability

CFD results are inherently reproducible given identical setup parameters. Ensuring such behaviour in the experimental simulation is more challenging. To evaluate these effects *in silico*, CFD simulations were run at four combinations of viscosity and density to account for variability in the experimental blood analogue fluid. Varying fluid density from 1082 to 1100 Kg/m^2 caused a pressure gradient increase of 0.95%. Increasing viscosity from 0.0035 to 0.004 Pa.s caused an increase in pressure gradient of 6.4%. Increasing both values caused a maximum increase in pressure gradient of 7.2%. These data are reported in **Figure 6.9**.

Table 6.3. Maximum fluid velocities (V) and Reynolds numbers (Re) for each model, at each flow rate.

Flow rate (ml/min)	V001 LAD		V004 RCA		V012 LAD		V012 RCA		V014 LCX		Idealised 50%		Idealised 75%	
	V	Re	V	Re	V	Re	V	Re	V	Re	V	Re	V	Re
60	0.69	257.31	0.77	272.17	0.92	338.94	0.44	205.25	0.46	240.80	0.32	199.38	1.27	398.76
70	0.81	300.20	0.90	317.53	1.07	395.43	0.51	239.45	0.54	280.93	0.37	232.61	1.48	465.22
80	0.92	343.08	1.03	362.89	1.22	451.92	0.59	273.66	0.62	321.06	0.42	265.84	1.69	531.68
90	1.04	385.97	1.16	408.25	1.37	508.41	0.66	307.87	0.69	361.20	0.48	299.07	1.90	598.14
100	1.15	428.86	1.29	453.61	1.53	564.90	0.73	342.08	0.77	401.33	0.53	332.30	2.11	664.60
110	1.27	471.74	1.42	498.97	1.68	621.39	0.80	376.28	0.85	441.46	0.58	365.53	2.33	731.06
120	1.38	514.63	1.54	544.33	1.83	677.88	0.88	410.49	0.93	481.60	0.63	398.76	2.54	797.53
130	1.50	557.51	1.67	589.69	1.99	734.37	0.95	444.70	1.00	521.73	0.69	431.99	2.75	863.99
140	1.61	600.40	1.80	635.05	2.14	790.86	1.02	478.91	1.08	561.86	0.74	465.22	2.96	930.45
150	1.73	643.28	1.93	680.42	2.29	847.35	1.10	513.11	1.16	602.00	0.79	498.45	3.17	996.91
160	1.84	686.17	2.06	725.78	2.44	903.84	1.17	547.32	1.23	642.13	0.85	531.68	3.38	1063.37
170	1.96	729.06	2.19	771.14	2.60	960.33	1.24	581.53	1.31	682.26	0.90	564.91	3.59	1129.83
180	2.07	771.94	2.32	816.50	2.75	1016.82	1.32	615.74	1.39	722.40	0.95	598.14	3.81	1196.29

Based upon minimum cross sectional area.

6.3.1.1.3   Pulsatile, patient-specific and steady-flow data

The pressure gradient was measured under steady- and idealised pulsatile flow conditions for each flow rate. **Figure 6.10** demonstrates paired pressure gradient results under pulsatile and steady flow conditions for each of the patient-specific models. Overall, the difference between measurements at the two flow conditions was negligible (bias, -0.2 mmHg, SD, 0.9 mmHg). The same was true when using patient-specific flow waveforms. Thus in the current experiment, for a given mean flow rate, mean pressure gradient was independent of the pulsatility of the flow.
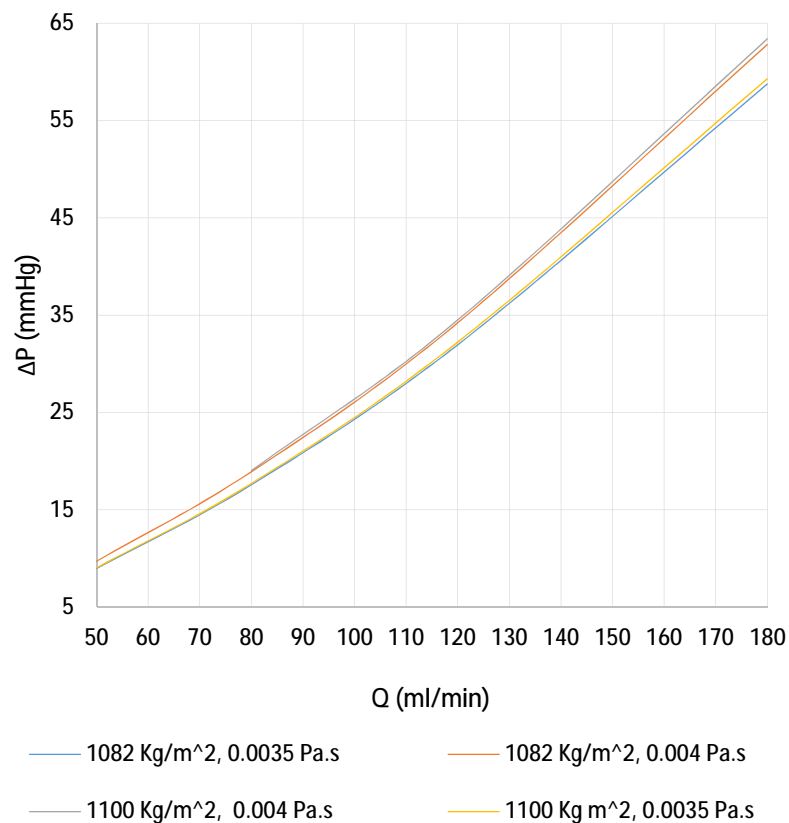
Figure 6.9. Effect of varying density and viscosity parameters in the CFD model.
Case V004 RCA (severe stenosis case). Small variations in viscosity have a greater impact than density.

6.3.1.1.4   Simulation of the pressure gradient-flow relationship

The translesional pressure gradient was computed for each model, at each flow rate, and compared to values measured within the experimental flow circuit. As described in the methods section, pressure gradient was evaluated at the outlet via the pressure port (Millar) and from within the lumen using the pressure wire (Volcano). These data are demonstrated in **Table 6.4** to **Table 6.8**

and in the corresponding **Figure 6.11** to **Figure 6.15**. The figures demonstrate good agreement between *in silico* and *in vitro* results when the transducer was placed within the lumen of the artery but, in some cases, poor agreement when the distal pressure was measured from the outlet pressure port (see explanation in discussion).

The accuracy of the CFD derived ΔP-Q predictions for models at all flow rates is summarised in **Table 6.9** and a Bland-Altman plot is demonstrated in **Figure 6.16**. Overall, accuracy is good with limits of agreement (±1.96×SD) between 3.37 and -4.83 mmHg. As demonstrated in **Figure 6.16**, there is a trend towards underestimating values at higher pressure gradients.

In the context of the coronary circulation, Reynolds numbers are thought not to exceed 500 *in vivo* (Kousera et al., 2014). Due to the nature of the experimental methods (where flow rate is prescribed) this does occur in some models at higher flow rates (see **Table 6.3**). Thus supra-physiological Reynolds numbers may be reached depending on the degree of stenosis. For this reason, precision was re-analysed after excluding cases where Reynolds number >500. After exclusion of these cases, the trend towards a negative bias was eliminated and precision of the model increased with narrower limits of agreement between 1.3 and -2.5 mmHg. These more representative data are presented in **Table 6.10** and **Figure 6.17**.

Assuming a mean P_a of 95 mmHg for all cases, the pressure gradient can be used to calculate the equivalent to FFR in each case. It is clinically relevant to plot error against FFR measurement and these data are presented in **Figure 6.18**. These data are important because they demonstrate excellent agreement across all cases where FFR ≥ 0.70. Clinically, this is the most interesting and important group because it includes those cases closest to the critical 0.80 threshold for FFR. In these cases, bias was negligible (-0.0002 mmHg; SD, 0.53 mmHg). Agreement was poorer in cases where FFR <0.70. However, these cases are likely to include those at higher Reynolds numbers which do not truly reflect coronary pathophysiology. Second, these cases fall into a range whereby management decisions are likely to be non-controversial regardless of what assessment method is used.
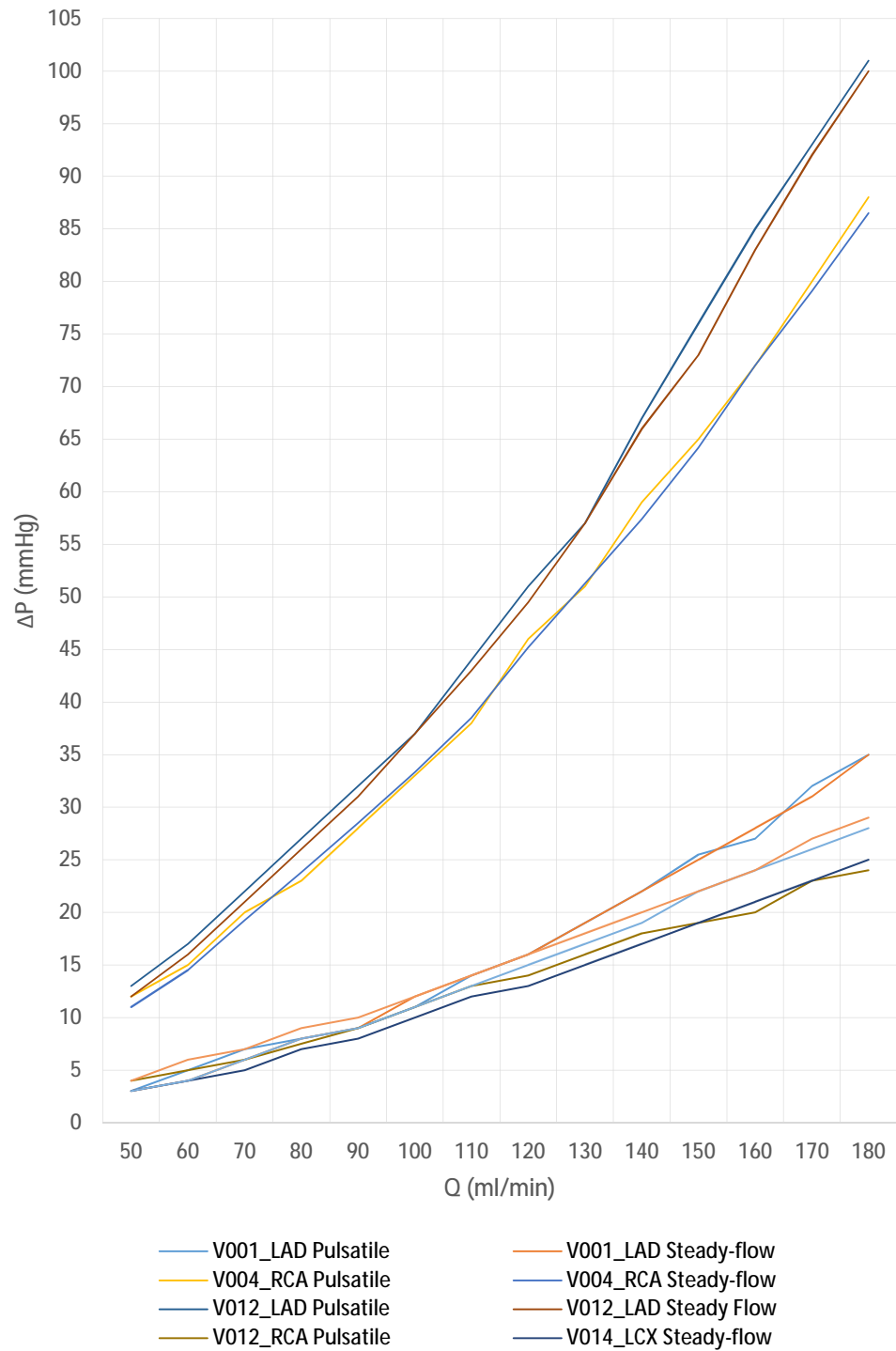
Figure 6.10. Equivalence of pressure gradient measurements under pulsatile and steady flow conditions for each of the five patient specific models.

Table 6.4. Pressure gradient data for V001 LAD.

Flow rate (ml/min)	Pressure gradient (mmHg)			Error (mmHg)*	Error* (%)
	CFD	Lumen	Pressure port		
50	3.6	3	3	-0.6	16.7
60	5.0	5	5	0.0	0.8
70	6.4	7	7	0.6	-9.5
80	7.9	8	10	0.1	-1.4
90	9.5	9	12	-0.5	5.4
100	11.3	11	15	-0.3	2.4
110	13.1	14	17	0.9	-6.5
120	15.1	16	21	0.9	-5.6
130	17.3	19	23	1.7	-10.0
140	19.5	22	27	2.5	-12.6
150	21.9	25.5	30	3.6	-16.4
160	24.4	27	35	2.6	-10.6
170	27.0	32	38	5.0	-18.3
180	29.8	35	42	5.2	-17.4

*between CFD and lumen result.

Figure 6.11. CFD-derived versus measured ΔP-Q relationship for V001 LAD.

Table 6.5. Pressure gradient data for V004 RCA.

Flow rate (ml/min)	Pressure gradient (mmHg)			Error* (mmHg)	Error* (%)
	CFD	Lumen	Pressure port		
50	9.1	9	11	-0.1	1.1
60	12.6	12	14.5	-0.6	4.9
70	15.7	15	19.26	-0.7	4.5
80	19.0	19	23.81	0.0	0.2
90	23.0	22	28.5	-1.0	4.3
100	26.3	27	33.34	0.7	-2.5
110	30.3	29	38.5	-1.3	4.3
120	34.5	37	45.2	2.5	-7.3
130	38.9	42	51.3	3.1	-8.1
140	43.4	47	57.4	3.6	-8.3
150	48.1	52	64.2	3.9	-8.0
160	53.1	60	72.03	6.9	-13.1
170	58.1	66	79.1	7.9	-13.5
180	63.3	75	86.5	11.7	-18.4

between CFD and lumen result.

Figure 6.12. CFD-derived versus measured ΔP-Q relationship for V004 RCA.

Table 6.6. Pressure gradient data for V012 LAD.

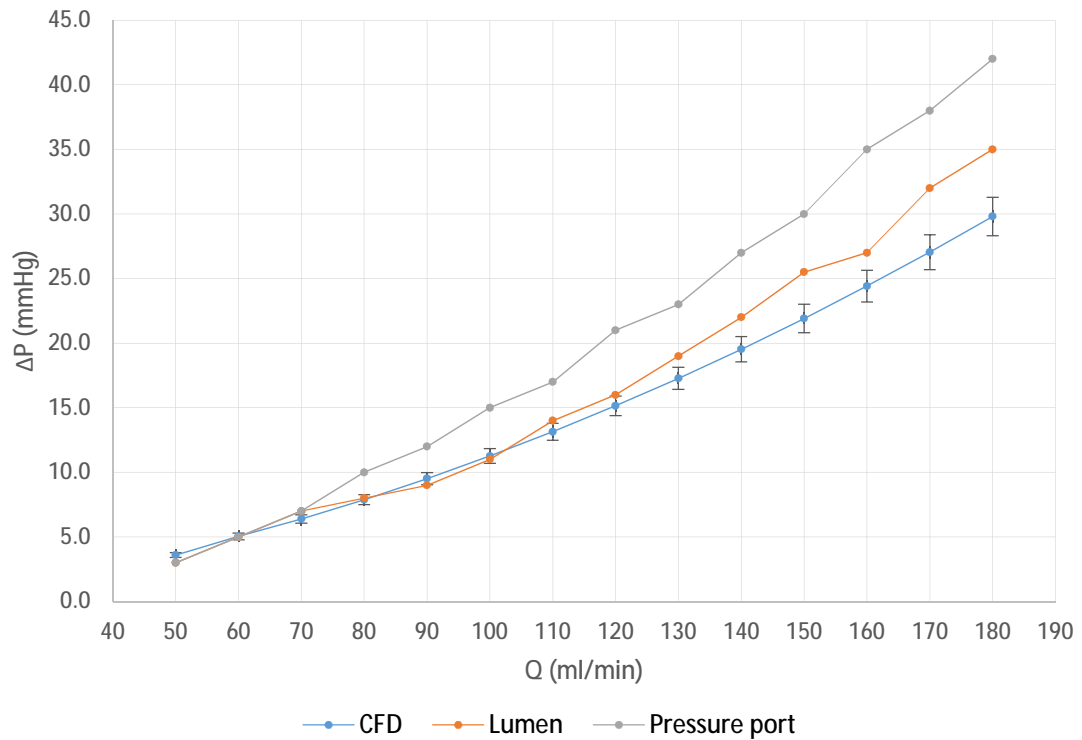| Flow rate (ml/min)	Pressure gradient (mmHg)			Error* (mmHg)	Error* (%)
	CFD	Lumen	Pressure port		
50	8.5	9	11.8	0.5	-6.1
60	11.0	11	15.6	0.0	0.2
70	13.8	13	19.53	-0.8	5.8
80	16.8	16	26.65	-0.8	4.9
90	20.1	20	30.3	-0.1	0.4
100	23.6	24	36.6	0.4	-1.7
110	27.3	28	43	0.7	-2.5
120	31.3	31	49.3	-0.3	1.0
130	35.5	36	56.03	0.5	-1.4
140	40.0	43	64.3	3.0	-7.6
150	44.6	48	72.3	3.4	-7.5
160	49.5	53	80.2	3.5	-7.0
170	54.7	59	90	4.3	-7.9
180	60.1	61	100.2	0.9	-1.5

*between CFD and lumen result.

Figure 6.13. CFD-derived versus measured ΔP-Q relationship for V012 LAD.

Table 6.7. Pressure gradient data for V012 RCA.

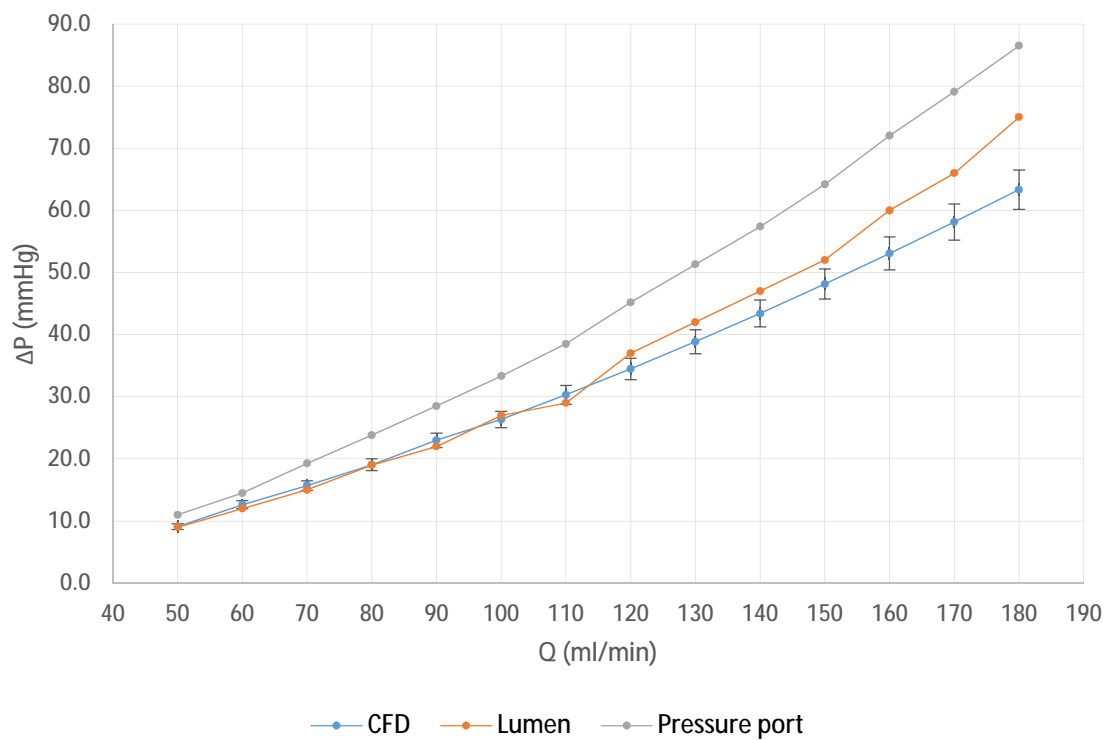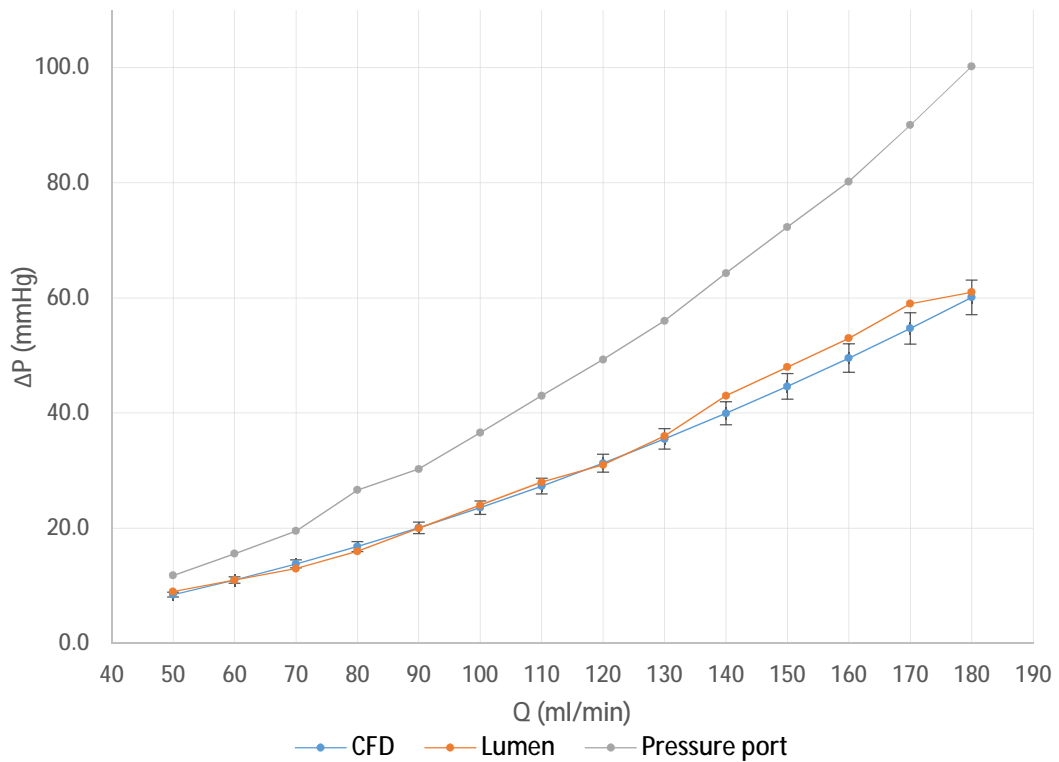| Flow rate (ml/min)	Pressure gradient (mmHg)			Error* (mmHg)	Error* (%)
	CFD	Lumen	Pressure port		
50	3.7	3	3.75	-0.7	19.0
60	4.8	4	4.88	-0.8	16.9
70	6.0	5	6.3	-1.0	17.0
80	7.3	7	7.53	-0.3	4.2
90	8.7	8	9.16	-0.7	8.1
100	10.2	10	10.9	-0.2	1.7
110	11.7	12	12.7	0.3	-2.4
120	13.3	13	14.7	-0.3	2.5
130	15.0	15	16.38	0.0	0.1
140	16.8	17	18.52	0.2	-1.4
150	18.6	19	20.7	0.4	-2.2
160	20.5	21	23.08	0.5	-2.6
170	22.4	23	25	0.6	-2.7
180	24.4	25	27.25	0.6	-2.5

*between CFD and lumen result.
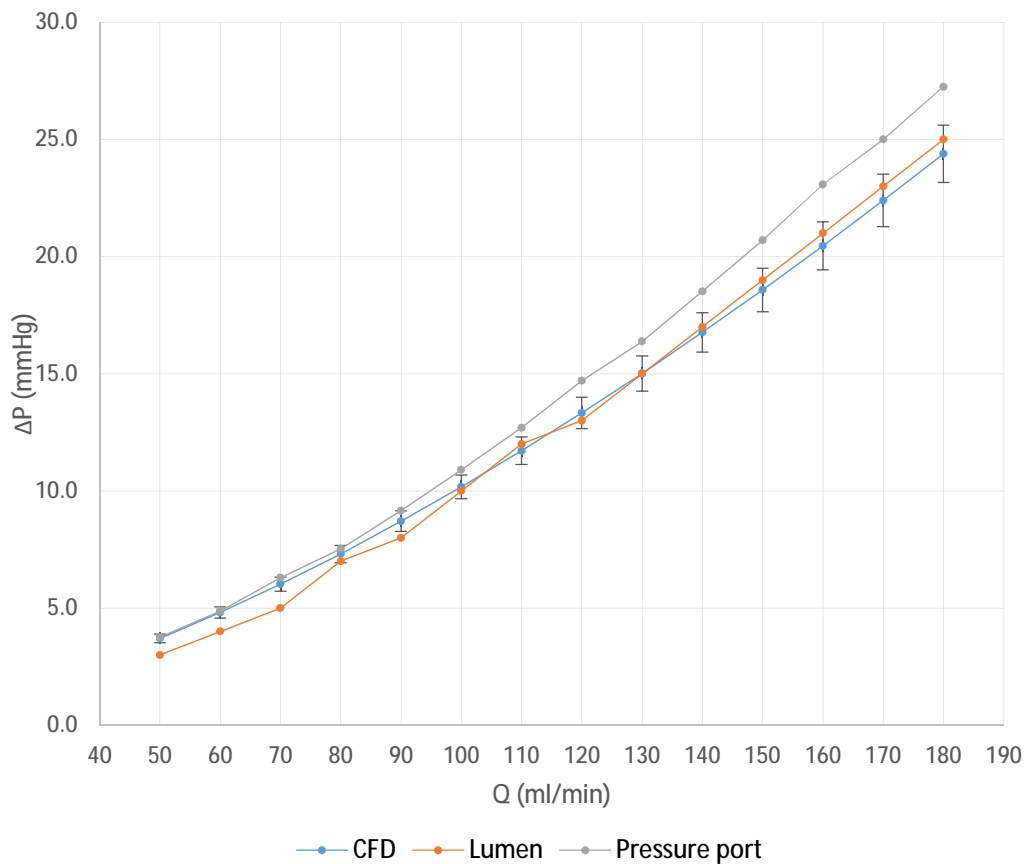
Figure 6.14. CFD-derived versus measured ΔP-Q relationship for V012 RCA.

Table 6.8. Pressure gradient data for V014 LCX.

Flow rate (ml/min)	Pressure gradient (mmHg)			Error* (mmHg)	Error* (%)
	CFD	Lumen	Pressure port		
50	4.5	4	4.78	-0.5	11.7
60	5.8	6	5.88	0.2	-2.9
70	7.2	7	7.24	-0.2	3.1
80	8.7	9	8.76	0.3	-3.5
90	10.3	10	10.45	-0.3	2.5
100	11.9	12	12.2	0.1	-0.8
110	13.6	14	14.01	0.4	-2.7
120	15.5	16	15.98	0.5	-3.6
130	17.4	18	17.64	0.6	-3.7
140	19.3	20	19.76	0.7	-3.4
150	21.4	22	21.95	0.6	-2.7
160	23.6	24	24.2	0.4	-1.8
170	25.8	27	26.57	1.2	-4.6
180	28.1	29	28.95	0.9	-3.1

between CFD and lumen result.
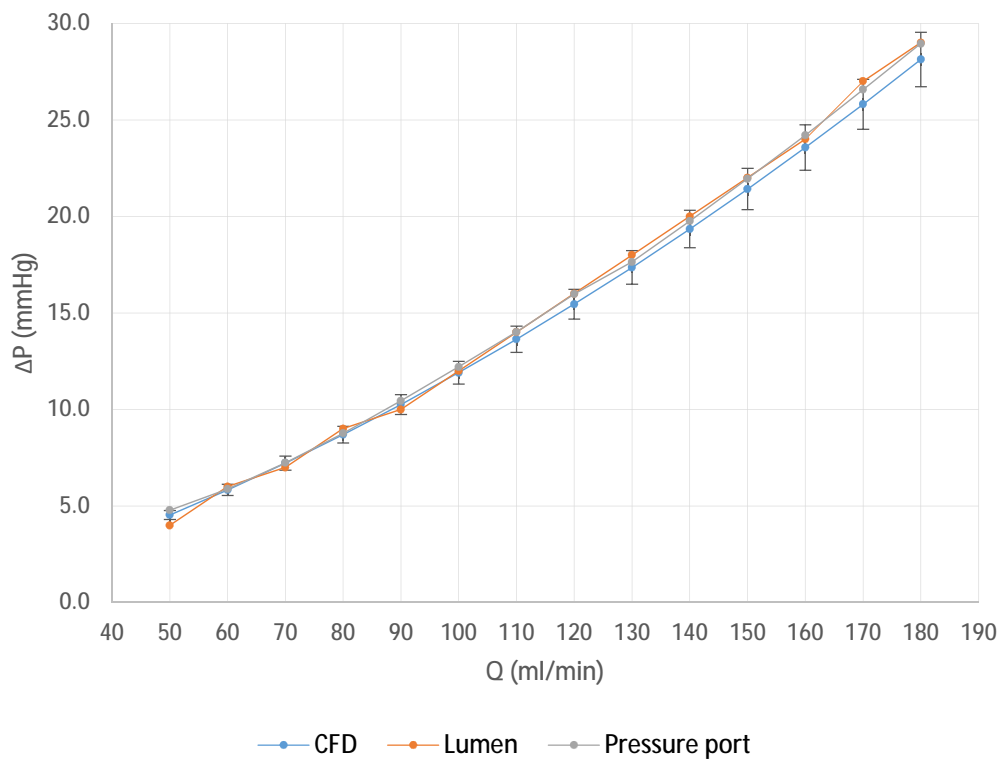
Figure 6.15. CFD-derived versus measured ΔP-Q relationship for V014 LCX.

235

Table 6.9. Accuracy of ΔP-Q predictions in all models at all flow rates

Model	Bias (mmHg)	Std deviation (mmHg)	Min error (mmHg)	Max error (mmHg)
V001 LAD	+0.1	0.55	-0.6	+1
V004 RCA	-2.61	3.92	-11.7	+1.3
V012 LAD	-1.09	1.71	-4.3	+0.8
V012 RCA	+0.1	0.55	-0.6	+1
V014 LCX	-0.35	0.47	-1.20	+0.5
Total	*-0.73*	*2.10*	*-11.7*	*+1.3*

Figure 6.16. Bland-Altman plot of the differences between the ΔP results computed by the CFD method and measured values.

The mean (bias - dark line) is -0.73 and the limits of agreement (dashed lines) are between 3.37 and -4.83. There is a trend of underestimation (negative bias) at higher pressure gradients.

Table 6.10. Accuracy of ΔP-Q predictions in all models at all non-transitional[*] flow rates

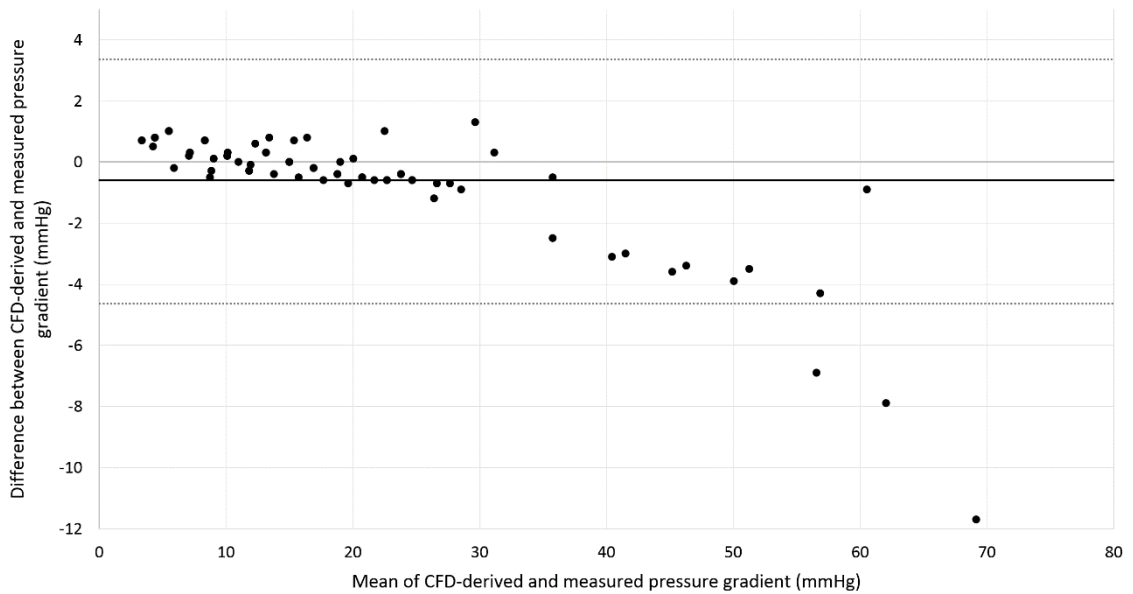| Model	Bias (mmHg)	Std deviation (mmHg)	Min error (mmHg)	Max error (mmHg)
V001 LAD	0.49	0.45	-0.30	+1.0
V004 RCA	0.43	0.68	-0.70	+1.3
V012 LAD	0.13	0.56	-0.50	+0.80
V012 RCA	0.35	0.44	-0.30	+1.0
V014 LCX	-0.18	0.40	-0.70	0.50
Total	*0.20*	*0.64*	*-2.5*	*+1.3*

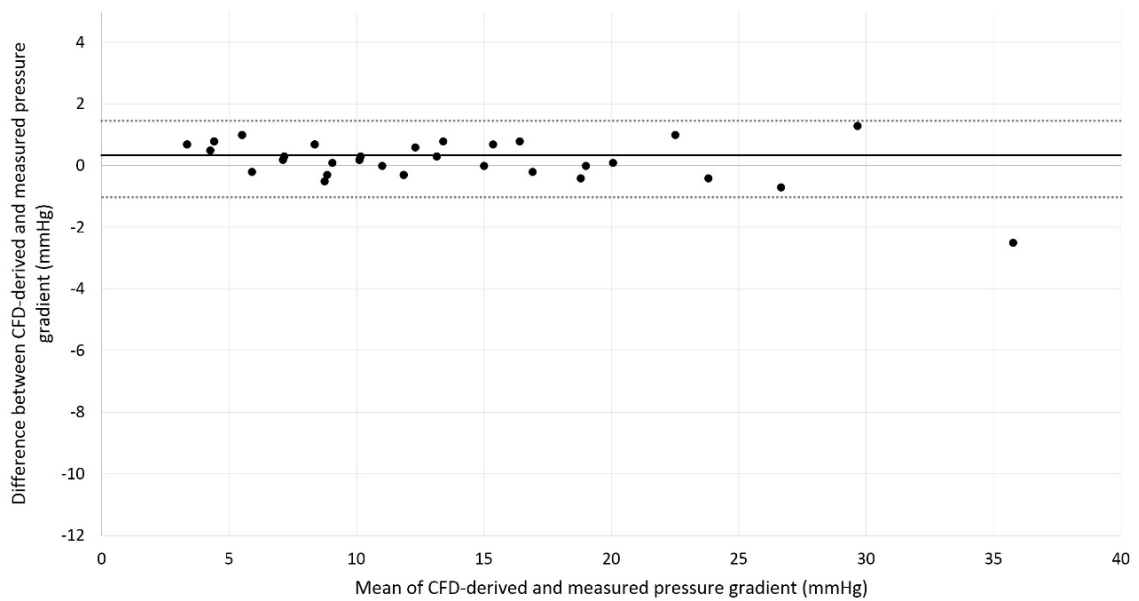[*]*Cases where Re>500 excluded (see Table 6.3).*

Figure 6.17. Bland-Altman plot of the differences between the ΔP results computed by the CFD method and measured values for non-transitional cases.

*The mean (bias - dark line) is 0.20 and the limits of agreement (dashed lines) are between 1.3 and -2.5. The scale of the y axis has been preserved in order to facilitate direct comparison with **Figure 6.16**.*
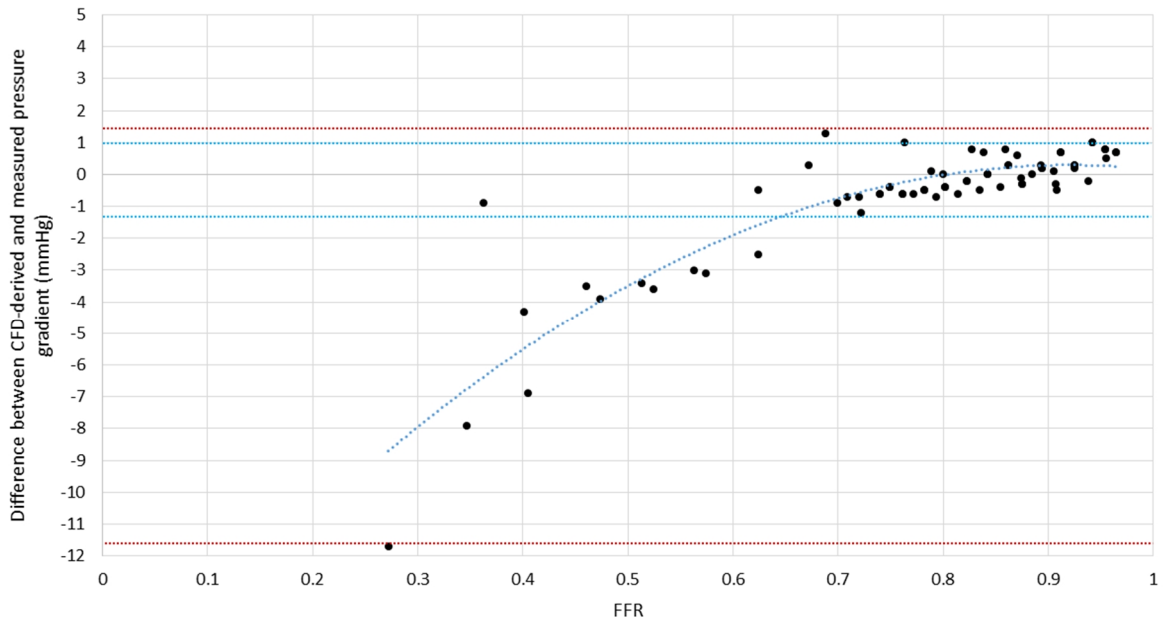
Figure 6.18. Difference between CFD-derived and measured pressure gradient plotted against FFR* in all experimental cases.

The bias (curved blue dotted line) and error increase in cases with FFR < 0.70. The red dotted lines indicate the wide limits of agreement across all cases (-11.7 to 1.3 mmHg) and the much narrower blue dotted lines indicates the limits of agreement in cases where FFR ≥ 0.70 (-1.2 to 1.0 mmHg). *FFR calculated based on the assumption that mean P_a was 95 mmHg in all cases.

6.3.1.1.5   Doppler results

Good quality, dense Doppler traces were obtained in each case (see **Figure 6.19** a,b and c). A good quality signal failed to be obtained for only certain cases at the highest flow rates at the outlet (see **Figure 6.24d** and **Figure 6.25d**). However, even under controlled experimental conditions, several issues were evident. First, it took time to achieve the 'optimum' Doppler signal and this was easily lost. Second, both the quality and magnitude of the signal were extremely sensitive to very small movements of the wire. Third, it was difficult, even with a range of tip bends and under direct visual guidance, to position the tip of the wire away from the vessel wall in coaxial alignment with the lumen. Regardless of the degree of bend applied to the wire tip, the FlowWire® naturally adhered to the vessel phantom wall and it was difficult to twist the wire into a free position. These issues are consistent with *in vivo* experience and published comments (Kern, 2000, Siebes et al., 2004, van de Hoef et al., 2012).
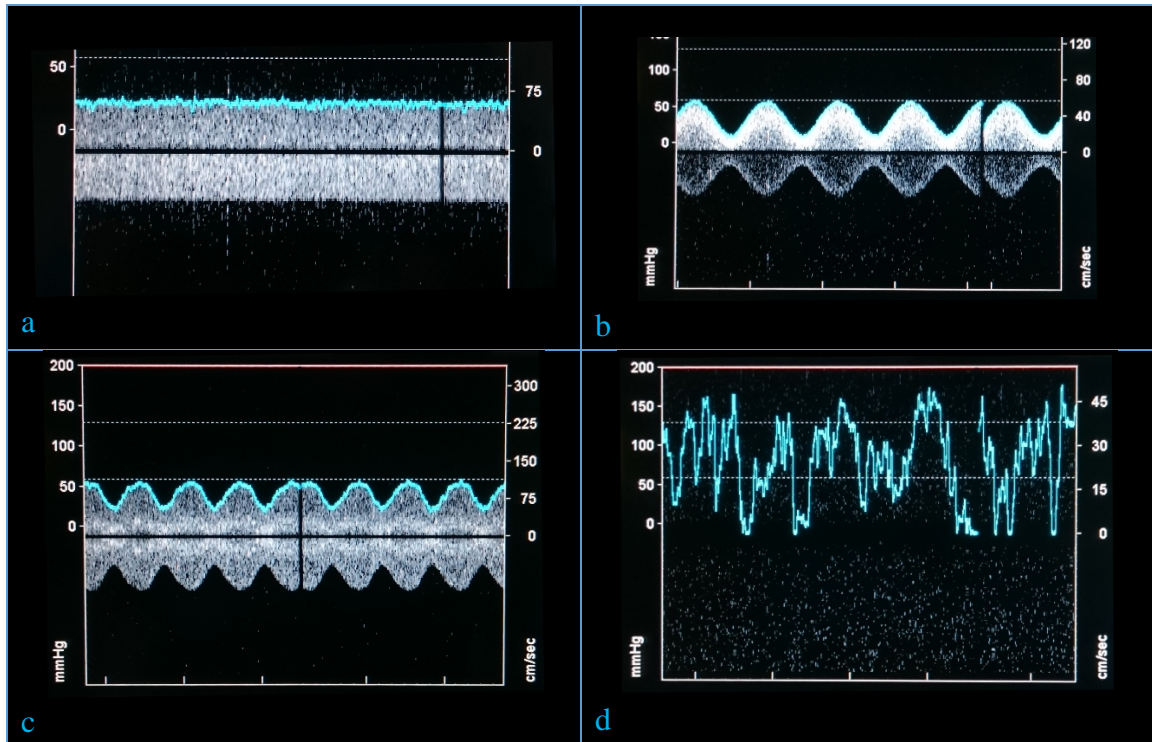
Figure 6.19. Examples of steady (a), pulsatile (b), patient-specific (c) and 'turbulent' Doppler signals. Good quality signals were identified in each case. Only in certain outlet cases at high flow rates was the signal lost as in example (d).

There was an excellent correlation between both the individual and mean Doppler flow velocity results (after excluding poor quality turbulent results – see **Figure 6.24d** and **Figure 6.25d**) and the expected flow velocity result. Pearson's correlation coefficient was >0.98 for all cases. Correlation does not indicate agreement.

Figures 6.20 – 6. 27 demonstrate the Doppler measurements plotted against the expected values. Model V001_LAD is demonstrated in detail (**Figures 6.20-6.23**) whereas data for the other models (**Figures 6.24-6.27**) is summarised. In each case (experimental details in the legends), the three individual measurements (grey lines) and the corresponding mean values (red lines) are plotted against the known flow velocity value.

Figures 6.20 – 6. 27 demonstrate that, in many cases, there is significant variability between the three individual measurements of Doppler flow velocity. Data regarding the coefficient of variability between the three measurements is outlined in
Table 6.11.
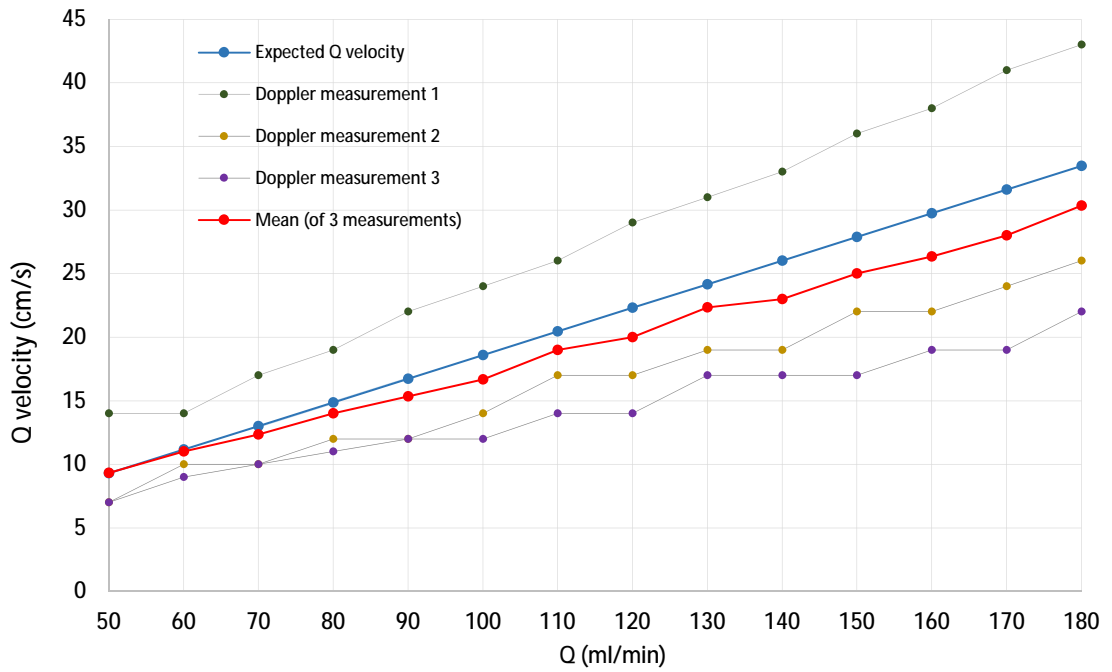
Figure 6.20. Doppler flow velocity measurements at the inlet of model V001_LAD under steady flow conditions.
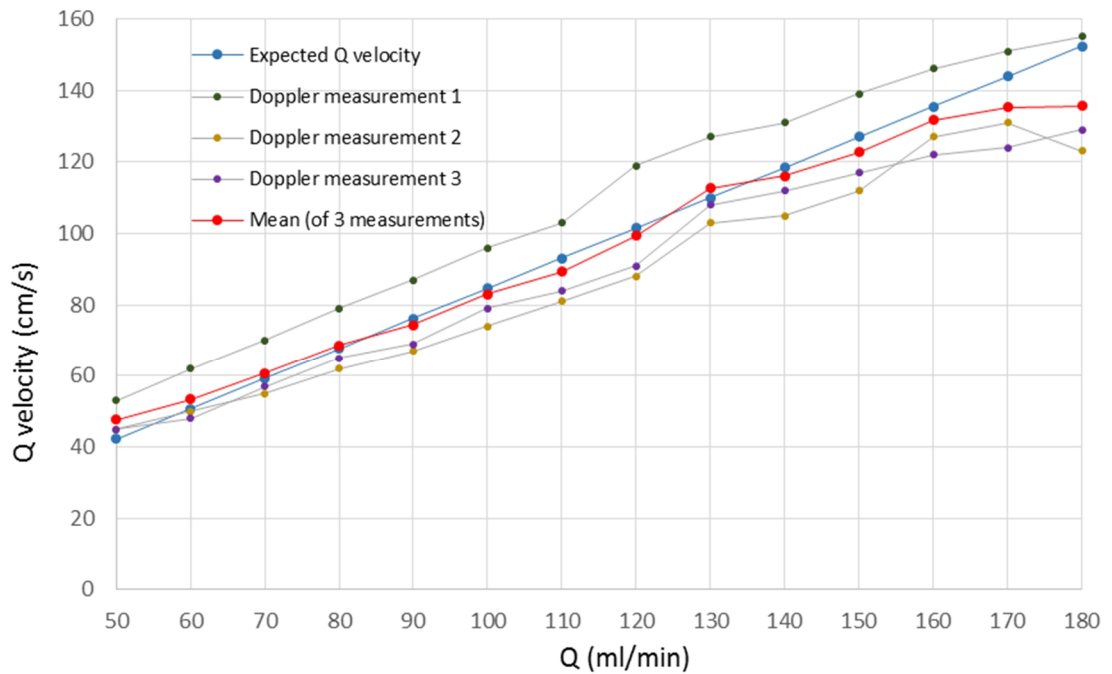
Figure 6.21. Doppler flow velocity measurements at the outlet of model V001_LAD under steady flow conditions.
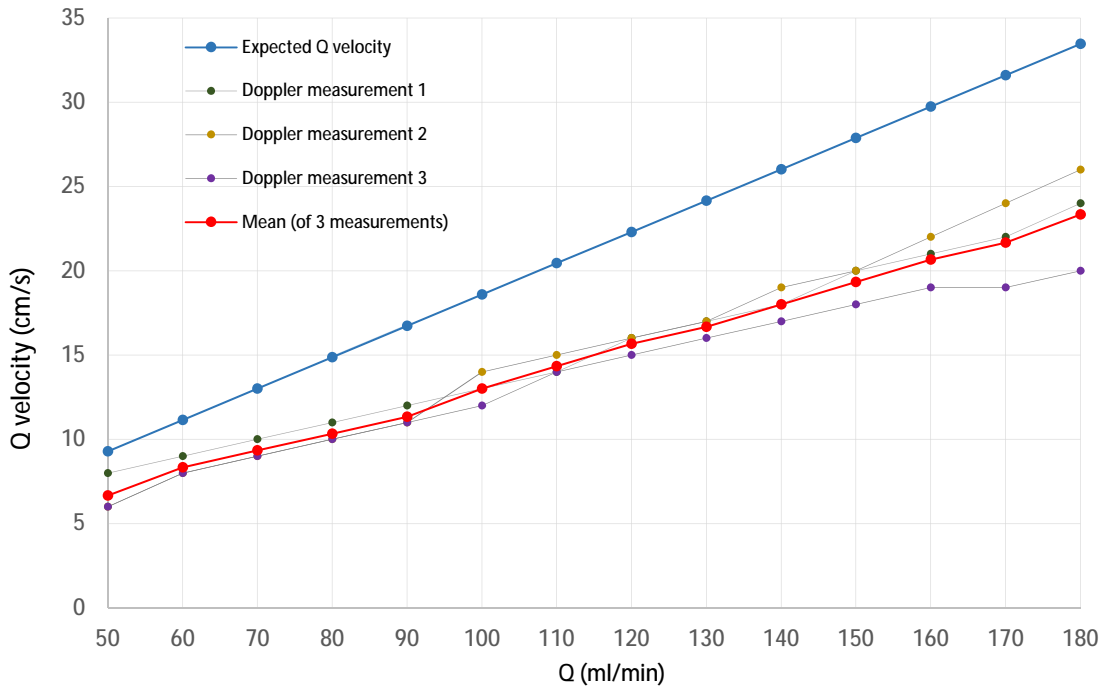
Figure 6.22. Doppler flow velocity measurements at the inlet of model V001_LAD under pulsatile flow conditions.
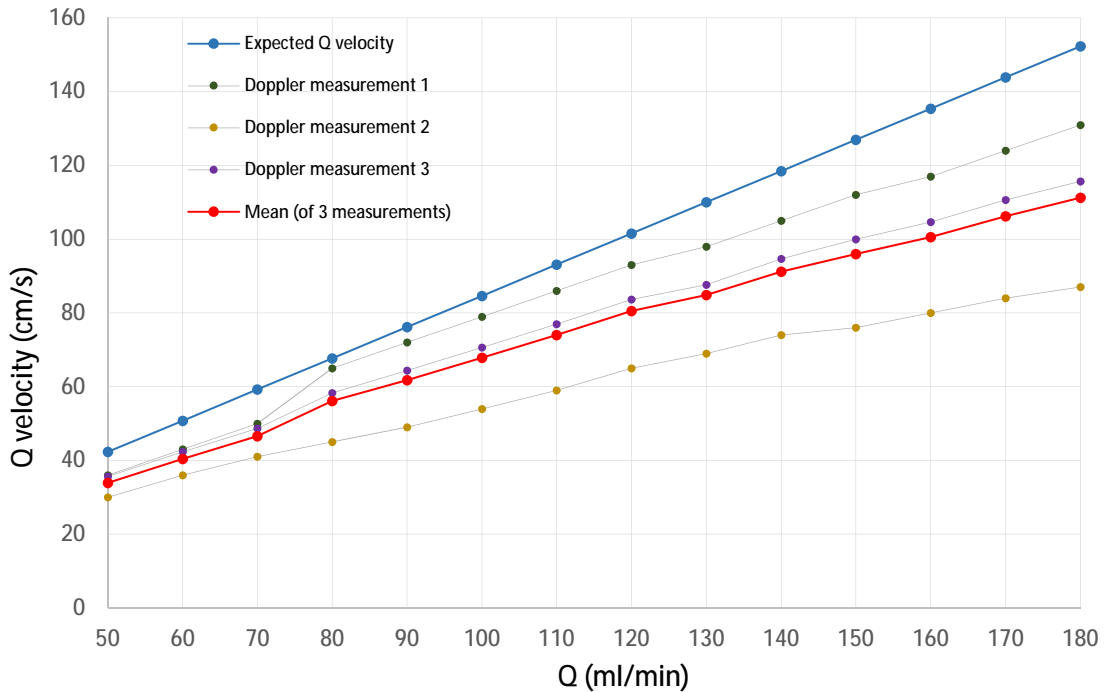
Figure 6.23. Doppler flow velocity measurements at the outlet of model V001_LAD under pulsatile flow conditions.
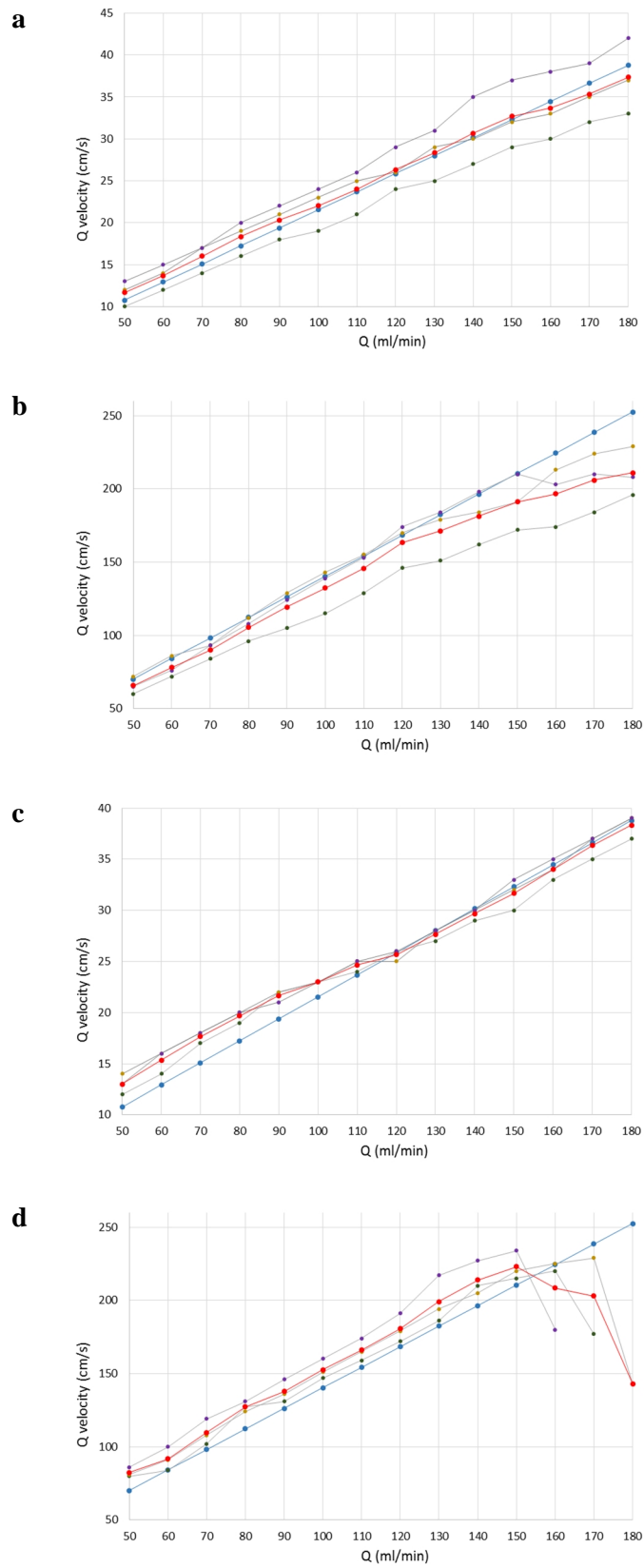
Figure 6.24. Doppler flow measurements for V004_RCA
*Under steady flow conditions at inlet (a) and outlet (b), and under pulsatile
flow conditions at inlet (c) and outlet (d). Legend as in Fig 6.20 - 6.23.*
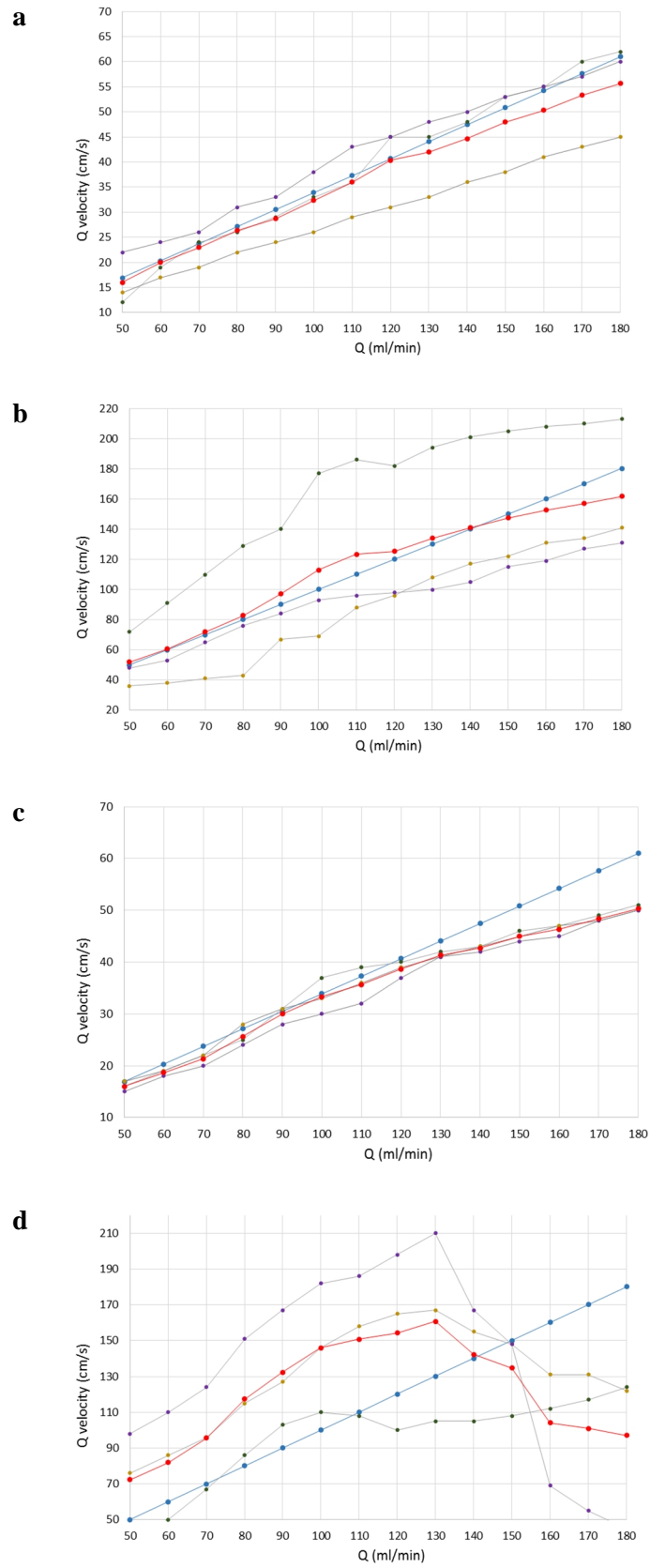
Figure 6.25. Doppler flow measurements for V012_LAD
Under steady flow conditions at inlet (a) and outlet (b), and under pulsatile flow conditions at inlet (c) and outlet (d). Legend as in Fig 6.20 - 6.23.

a

b

c

d
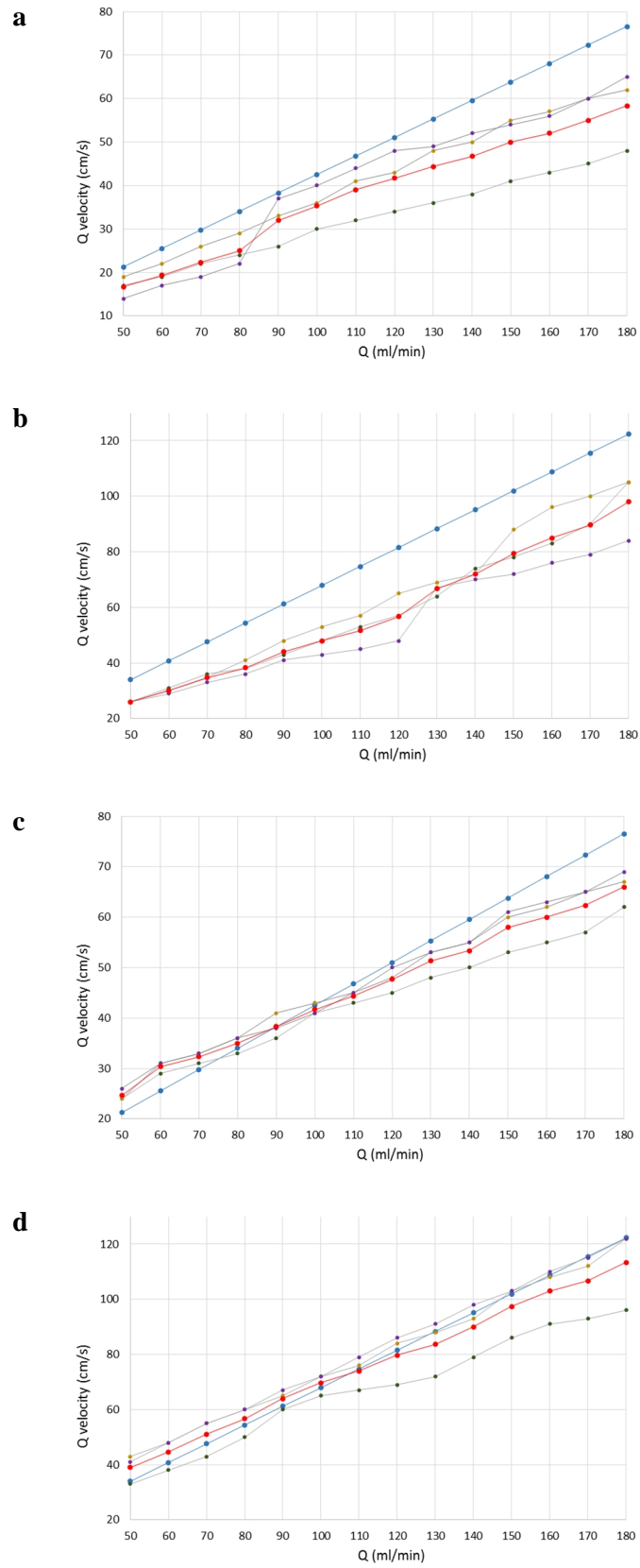
Figure 6.26. Doppler flow measurements for V012_RCA
Under steady flow conditions at inlet (a) and outlet (b), and under pulsatile
flow conditions at inlet (c) and outlet (d). Legend as in Fig 6.20 - 6.23.
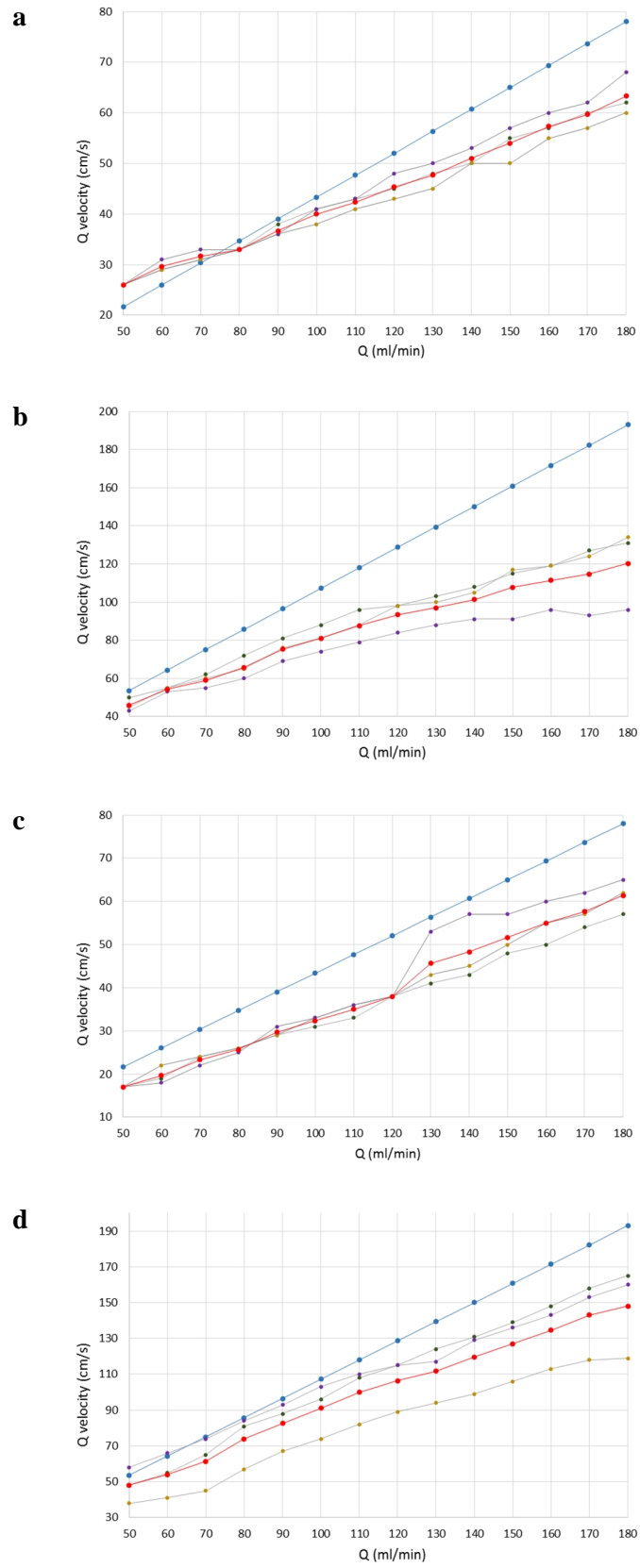
Figure 6.27. Doppler flow measurements for V014_LCX

Under steady flow conditions at inlet (a) and outlet (b), and under pulsatile flow conditions at inlet (c) and outlet (d). Legend as in Fig 6.20 - 6.23.

245

Table 6.11. Summary of the variability in Doppler measurements.

Case	Coefficient of variability at the inlet, all flows	Coefficient of variability at the outlet, all flows	Coefficient of variability at the inlet with exclusions[*]
V001_LAD	7.4%	19.0%	7.1%
V004_RCA	11.6%	9.4%	11.5
V012_LAD	4.5%	30.7%	5.0%
V012_RCA	5.2%	10.7%	4.4%
V014_LCX	3.4%	17.2%	2.7%
mean	*6.42*	*17.4*	*6.14*

[*]*Excluding cases involving transitional Reynolds numbers*

The precision of Doppler in predicting the actual flow velocity is outlined in **Table 6.12** and in the corresponding Bland-Altman plots in

Figure 6.28. These data demonstrate that precision is improved when: the mean Doppler value is used rather than a single measurement (something that is rarely performed *in vivo*), the measurement is taken from the inlet rather than at the outlet and, when the cases with supra-physiological Reynolds numbers (>500) are excluded. As was the case in the previous section, pulsatile waveforms (sinusoidal and patient-specific) generated results equivalent to steady-state.

Table 6.12. Summary of Doppler wire precision overall, at inlet, with exclusions and mean results

	All individual samples	Mean of three individual samples	Individual inlet samples, only	Mean of three inlet samples only	Individual inlet samples, Re <500	Mean of three inlet samples, Re <500
Mean error (bias)	-5.27	-9.05	-4.69	-7.03	-4.69	-4.72
Standard deviation	20.35	10.25	5.52	6.03	5.52	5.59
Minimum error	-109.45	-39.29	-21.02	-16.68	-21.02	-14.01
Maximum error	81.94	5.03	5.49	4.82	5.49	4.82
Limits of agreement	34.6 to -45.2	11.0 to -29.2	6.1 to -15.5	4.8 to -18.9	6.1 to -15.5	6.2 to -15-7
Figure 6.28	*(a)*	*(d)*	*(b)*	*(e)*	*(c)*	*(f)*

All measurements are in cm s^{-1}.

Figure 6.28 (following two pages). Bland-Altman plots demonstrating the difference between individual (a,b,c) and mean (d,e,f) Doppler measurements and expected flow velocity.
(a) all three measurements over all cases, (b) all three measurements, just inlets, (c) all three measurements, just inlets, transitional Reynolds numbers excluded, (d) mean results, all cases, (e) mean results, just inlets, (f) mean results, just inlets with transitional Reynolds numbers excluded. The dark continuous line is the mean (bias) and the interrupted lines represent the limits of agreement. The limits of agreement are narrower (indicating increased precision) for mean results (a,b,c vs d,e,f), and when flow is measured at the inlet (a vs b and d vs e).
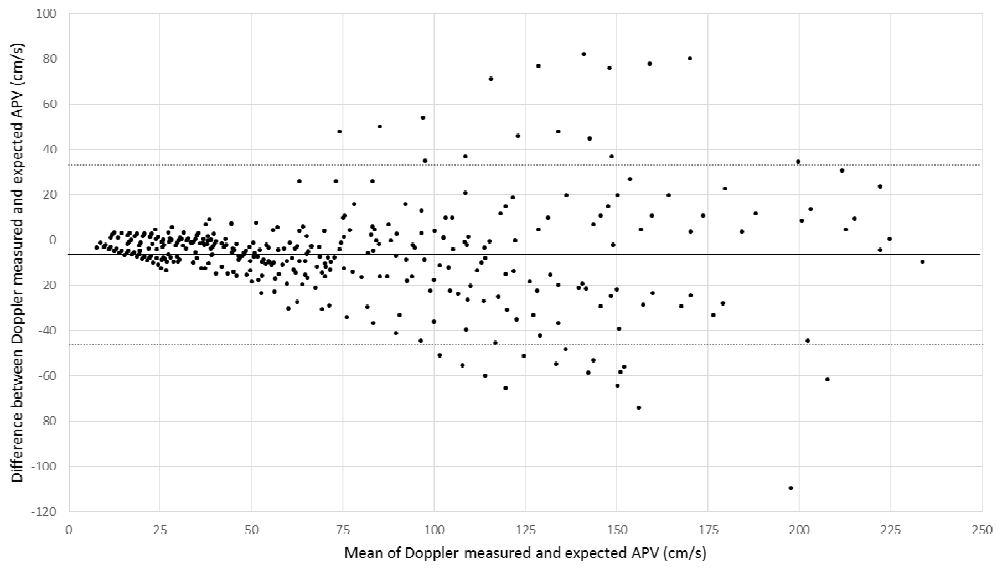
a
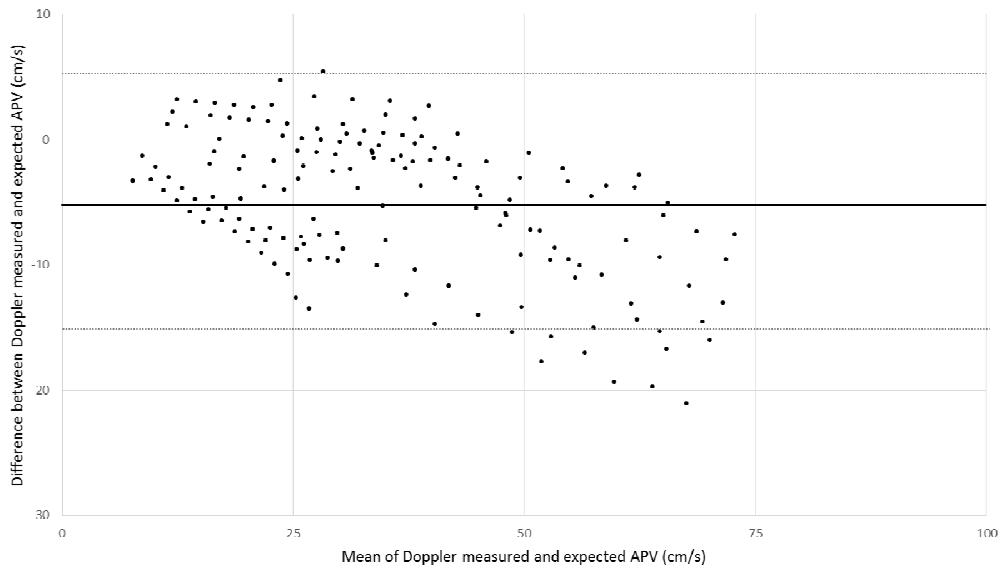
b
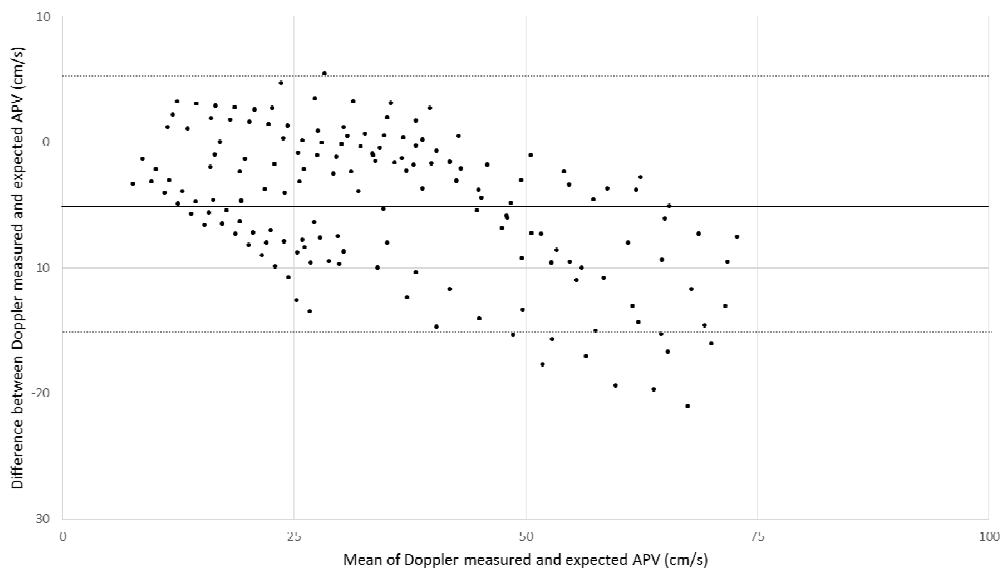
c
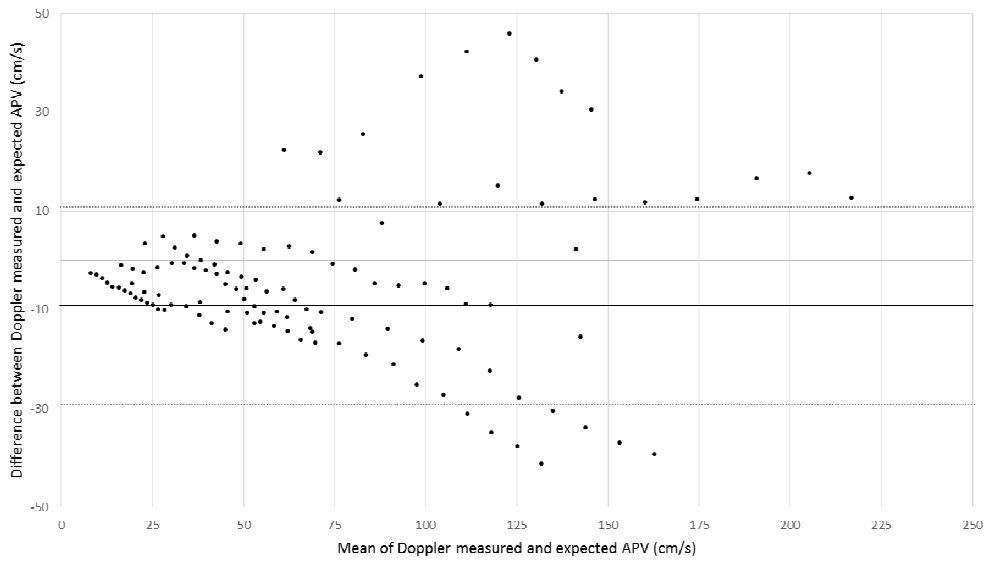
d
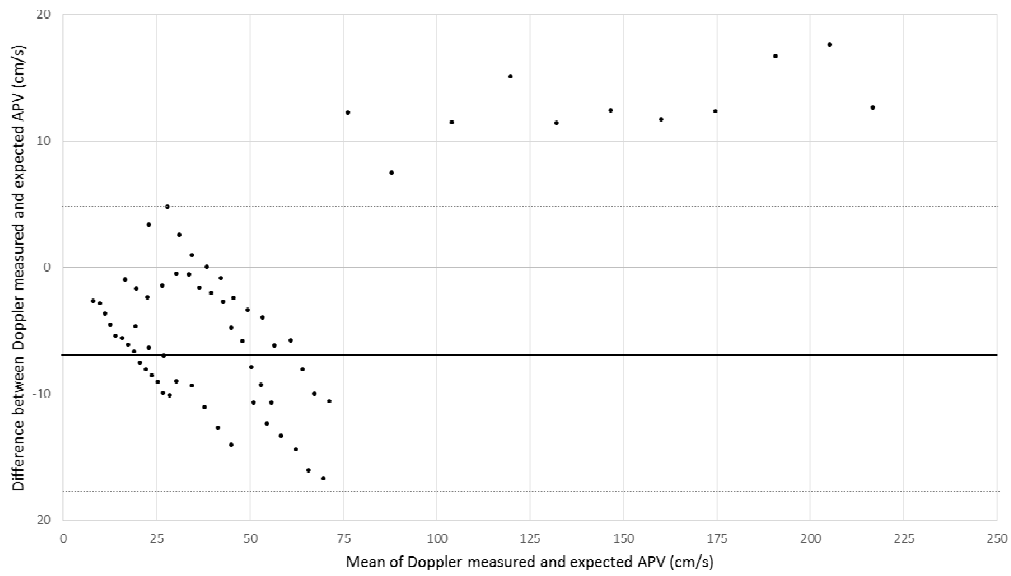
e
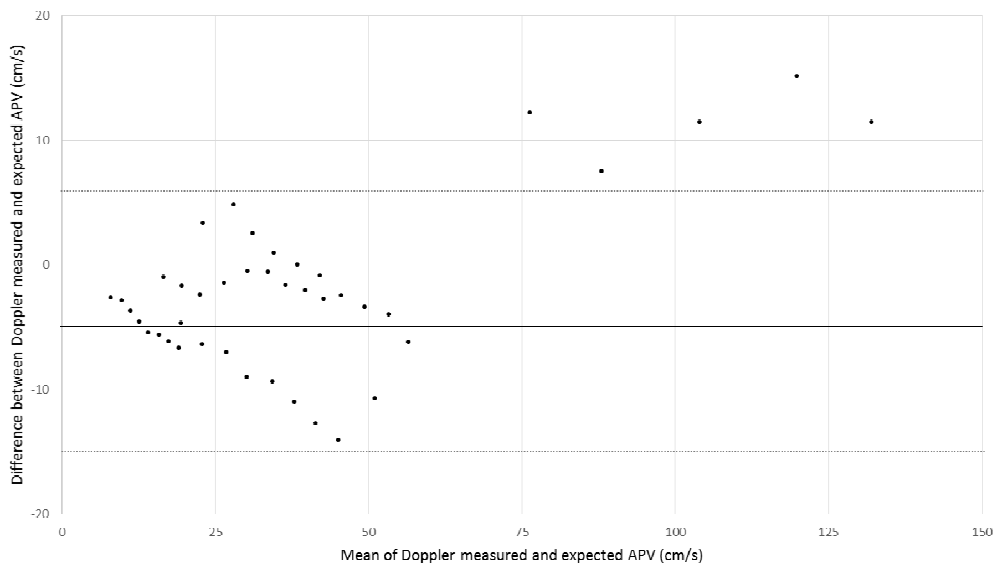
f

6.4 Discussion

In these experiments I have demonstrated that it is feasible to compute the ∆P-Q relationship using a CFD approach. Computed results are in close agreement with the values measured in the flow circuit. In this pilot study of five patient-specific arteries, the computation of ∆P-Q for a patient-specific geometry appears more accurate and stable than the direct measurement of flow using the current clinical standard: Doppler flow velocity. To the author's knowledge, this is the first example of 3-D printing patient-specific coronary arteries.

6.4.1.1   Precision of the novel method

The precision of the novel method was impressive. Limits of agreement were found to be far narrower than those for Doppler analysis (see **Table 6.9** and **Table 6.12**). In many ways, the computation of the ∆P-Q relationship within a known 3-D geometry represents a relatively elementary CFD task. Furthermore, the computation of flow from pressure gradient has already been used in the preceding chapters of this thesis. However, validation and proof of concept is essential prior to taking any further development steps in the direction of clinical translation. Consistent with clinical experience, pressure measurement was more stable and reproducible than Doppler flow velocity. Performance was less impressive at higher Reynolds numbers where a transient solution may better characterise instability or oscillation in the fluid domain. Nevertheless, the method was consistently superior to Doppler over all flow rates and was even more impressive when analysis was restricted to, pathophysiologically, more realistic cases where Reynolds numbers were <500. The discrepancy between the pressure gradient measured at the distal pressure port and that measured intraluminally (see **Figure 6.13**) may be explained by a step expansion of the lumen diameter at the outlet, a consequence of the computer aided design and 3-D printing (see **Figure 6.29**). This concept is well recognised in CFD flow simulation whereby flow separation, vortices and eddy currents develop behind the step which correspond to reduced pressure. This is consistent with the findings that measurement of pressure gradient from the pressure port which is immediately behind the step exaggerates the total pressure drop. Variability in the magnitude of the effect of this phenomenon is reflected by variability in the vessel outlet diameter relative to a fixed connector diameter. There was no step change at the inlet where the computer-aided design matched the diameters of the inlet connection lumen and that of the vessel.
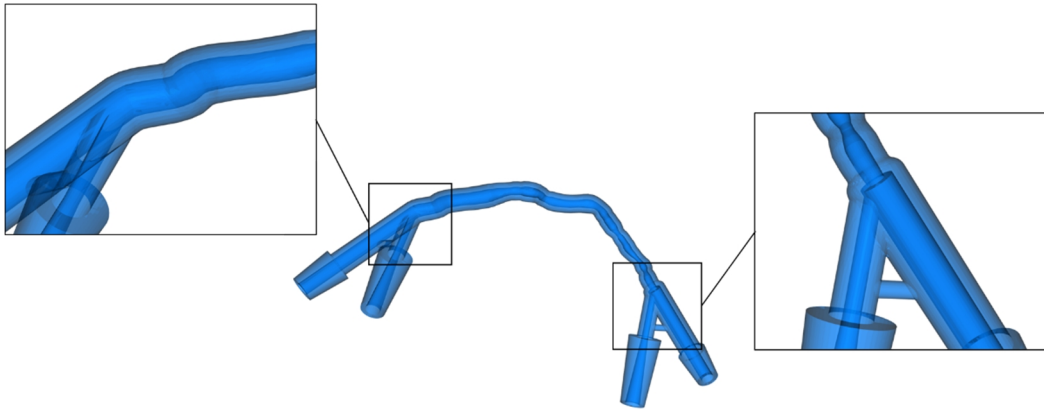
Figure 6.29. Semi-translucent rendering of model V012_LAD demonstrating the smooth inlet transition but backward-facing step at the outlet.

6.4.1.2 Doppler precision

It is interesting, but perhaps not surprising that, even under static conditions the Doppler flow velocity measurement performed sub-optimally. The methodological shortfalls of using Doppler as a surrogate for flow are consistent with the findings of the current study. First, because flow is directional, optimum measurement requires good alignment of the wire tip with flow. Alignment which is less than perfect may capture only a region or vector of the flow thus underestimating true velocity. This is consistent with the results; all Doppler methods tended to underestimate true flow velocity (negative bias) by a significant margin (see **Table 6.12**). Only at the outlet in certain cases did Doppler significantly overestimate expected flow velocity. This may be explained by the presence of high velocity jets emanating from proximal stenoses and may explain why the inlet Doppler measurement was more accurate. As described in Chapter 2, coronary flow is complex and does not follow many of the assumptions upon which laws such as those of Bernoulli and Poiseuille are based. In the context of such a complex 3-D flow field it is perhaps not surprising that a single APV measurement with uncertain coaxial alignment may not reflect the underlying flow rate, is hard to reproduce (coefficient of variability = 6 – 17% in this experiment), hard to interpret, and exhibits significant sensitivity to even small movements of the wire. If these effects are evident within a rigid-walled model under controlled laboratory conditions, they may be further exaggerated *in vivo*. Kousera *et al* simulated the ∆P-Q relationship using clinical data from 19 patients with CAD undergoing ICA, OCT and Doppler flow assessment (Kousera et al., 2014). Their *in silico* model co-registered OCT with ICA data to reconstruct detailed coronary lumen geometries which they simulated using CFD. Measured proximal pressure and Doppler flow velocity data were applied as the proximal and distal boundary conditions. Similar to the Doppler results of the current study, their model consistently underestimated the distal pressure by between

-5 to -12 mmHg, with wide limits of agreement of 12.1 to -14.5 mmHg. The authors state that the '*most likely contributor to error*' in their model was Doppler flow measurement *in vivo*.

6.4.1.2.1 Implications

In all cases, the correlation between actual and Doppler measured flow velocity was excellent. Correlation does not indicate agreement (Bland and Altman, 1995). This is relevant in the computation of CFVR and HSR. In CFVR, the ratio of hyperaemic to baseline flow velocity is calculated. It might be assumed that if the wire tip does not move (which may be difficult to ensure), any scaling effect in the first measurement is present in the second since a similar region of the flow is recorded. However, there is variability in the gradients of the relationships between Doppler flow velocity and actual (see **Figures 6.20 – 6.27**). This may limit the use of Doppler in measuring CFVR. The situation is likely to be worse when calculating HSR, where a single value of hyperaemic flow velocity is used in the calculation, often measured distal to the stenosis via ComboWire® (Volcano). Therefore, there is no allowance for underestimation of true flow velocity and agreeability is vital.

6.4.1.2.2 Virtual stenosis and microvascular resistance'

Based on the outcomes of this thesis, I propose two novel indices of intracoronary physiology, *virtual stenosis resistance* (*vSR*) and virtual *microvascular resistance* (*vMR*):

$$vSR = \frac{\overline{\Delta P}}{\overline{Q}_{CFD}} \qquad\qquad \textbf{\textit{Eq 6.10}}$$

Where $\overline{\Delta P}$ is the mean translesional pressure gradient and $\overline{Q}_{CFD}$ is either mean volumetric flow rate or velocity derived from measured proximal and distal pressures and luminal geometry reconstructed from angiography.

$$vMR = \frac{P_d}{\overline{Q}_{CFD}} \qquad\qquad \textbf{\textit{Eq 6.11}}$$

6.4.1.2.3 Advantages of the novel method /indices

There are several reasons why this novel approach may be advantageous. First, unlike flow, pressure is non-directional which makes *in vivo* measurement more stable and more reproducible. This is why interventional cardiologists have come to rely on pressure measurements in the cardiac catheter laboratory. Second, the developed method computes one physiological parameter from the other. Therefore, only a single measurement needs to be acquired invasively (FFR) and only

one wire needs to be deployed. Third, unlike the vFFR workflow, the boundary conditions of the current model are fully defined and no assumptions are required. The importance of the tuning of the distal boundary condition described in the preceding chapter highlights why this is so advantageous. Fourth, and consistent with the other developments in this thesis, the novel method is software based and requires no hardware additional to that required for a standard FFR measurement. Furthermore, a single steady-state simulation result computes in approximately two minutes. Therefore, in principle, the method can be easily integrated into existing catheter laboratory infrastructure for use during the procedure and the generation of on-table results. Fifth, the novel 3-D method returns a volumetric flow rate which is arguably more robust and objective than a single measure of flow velocity during angiography which is susceptible to under- or over-estimation of the true flow secondary to poor coaxial alignment or positioning of the wire in a high flow jet (more likely with a ComboWire lying distal to the stenosis). Furthermore, the novel method simulates the 3-D flow field which can be post-processed and visualised. Sixth, the current method can be developed so that transient data are computed thus generating a transient flow waveform. Although the analysis was time-consuming, use of the acceleration technique described in Chapter 4 may provide these results in clinically tractable timescales. Finally, the current method replaces the Doppler wire which, even amongst the strongest advocates, is acknowledged to be challenging to use.

6.4.1.2.4   Limitations of the current study /method

Although the results of the current proof-of-concept study are positive, there are several limitations. First, only flow within an unbranched coronary lumen has been investigated. Further work will validate the method in branched 3-D printed arteries. The 3-D files already exist but additional computer aided design will be required prior to printing.

Second, the Reynolds numbers calculated for each model and flow rate were computed assuming steady-flow conditions. Therefore, this may underestimate the maximum Reynolds number during pulsatile flow conditions. Third, because the boundary conditions are known, model accuracy is critically dependent upon the precision of the segmentation and reconstruction. In this experiment, we have applied the same 3-D files for analysis and printing. Although this is appropriate for demonstrating the feasibility of the method, further work will be required to demonstrate the level of error introduced by independent segmentation. However, the printed models provide the perfect means by which to evaluate this since they can be filled with contrast, undergo angiography and thus be re-segmented and compared with the original files. Fourth, unlike the beating heart, the experimental method is static. Although it is possible to print in elastomeric materials, the precision is not yet high enough to allow the effects of cardiac motion to be studied at these length

scales. Furthermore, relative to Doppler analysis, the novel method is likely to be even better *in vivo* where cardiac, ventilator and patient movement make Doppler analysis even more challenging. Fifth, although Materialise NV quote printing tolerance data, it would be ideal to check the quality of the prints via micro-CT analysis. Sixth, in the interests of ensuring a like-for-like analysis, the effect of the wire was not simulated. The effect of the angioplasty wire on the pressure gradient has been simulated numerically and experimentally by other groups (Ashtekar, 2007). Clinically, if this technology is to complement FFR measurement then this effect must be taken into account. Seventh, the range of flow rates used in the current experiments is consistent with normal physiological range but exceeds those expected in physiologically significant CAD. This explains some lack of agreement between computed and measured values at higher Reynolds numbers. However, these effects are controlled for by re-analysing precision after the exclusion of cases where the Reynolds numbers exceeds 500.

6.5 Conclusions

There is a cogent rationale for incorporating coronary flow into the assessment of coronary artery disease but challenges and limitations associated with currently available technology have resulted in clinicians depending almost exclusively upon pressure measurements alone. Therefore, there is a need for a technology which estimates coronary flow which is not associated with similar shortcomings. The work in this chapter has demonstrated the feasibility of using CFD to compute volumetric coronary flow rate from angiography and measured (P_a and P_d) pressure in a fully patient specific model without any assumptions regarding boundary conditions. Thus, under idealised conditions coronary flow can be computed from a standard FFR measurement with no additional invasive work using software that, in principle, can be easily integrated into existing catheter laboratory hardware. These preliminary results suggest that high levels of precision are attainable and, for a variety of reasons, may be superior to the current clinical standard, i.e. flow velocity measured by Doppler wire. This novel method is not associated with the limitations of Doppler assessment which have restricted its use. Further work is required to assess the impact of branches positioned proximal and distal to the stenosis segment. An additional but important scientific output is the development of a novel experimental flow phantom and corresponding experimental protocol. These may now be used for validation of numerical simulation beyond that of coronary physiology (pump and manifold range 50 – 1760 ml/min). The future direction for this work is discussed in Chapter 7.

Chapter Seven:

Conclusions and further work

7.1   Summary of Current Stage of Development

In this thesis I describe a novel computational model capable of predicting intracoronary pressure and /or flow. In Chapter 3 I demonstrated that, even with generic distal boundary conditions, predictions regarding physiological lesion significance using dichotomised data were accurate; vFFR was equivalent to mFFR with 97% accuracy. On an individual case basis, vFFR differed from mFFR by a mean of ±0.08. This is consistent with other studies using a similar approach (Chapter 5). The length of computation exceeded 24 h so in Chapter 4 I described how CFD simulation can be accelerated to 4 minutes. Two methods were developed to achieve this: one

which computes vFFR alone (vFFR$_{steady}$), and one which, in addition, computed pseudo-transient flow and pressure data (vFFR$_{ps-trns}$). Compared with 0-D coupled full transient 3-D analysis, with equivalent tuning, both methods returned a result with <1% error. These methods may be applicable to applications beyond coronary physiology and possibly, even beyond biological modelling. The underpinning methods have received interest from industrial partners and are the subject of a UoS patent application. The achieved timescales and level of precision may justify their inclusion in the final workflow. In Chapter 5 I tackled the most challenging of all the areas of predictive intra-coronary physiological modelling, the distal boundary condition. Three things were demonstrated. First, an apposite 0-D design that reproduces realistic flow as a function of time was identified and validated. Second, the importance of the distal boundary condition tuning was demonstrated in a sensitivity analysis. Third, and most importantly, the feasibility of a novel approach to 0-D tuning was demonstrated. Although further work is required, this represents the most important advance in this thesis. Since publication of the work in Chapter 3, other groups have computed vFFR. However, there is no published work that describes the personalisation of the distal boundary condition. It is likely that the application of NARMAX (see 7.2.1.3) to these data will advance this work. In Chapter 6 I demonstrated how 3-D CFD modelling can accurately compute the coronary ΔP-Q relationship as confirmed by validation of results against experimental data obtained within a novel flow circuit incorporating patient-specific 3-D printed arterial phantom models. This work is important because it validates the methodology used in the preceding three chapters and it represents a novel method which may be practical for use in the cardiac catheter laboratory which enables the accurate computation of flow, stenosis resistance and CMVR. Clinicians have come to depend upon indices derived from intra-coronary pressure measurements because of the challenges of measuring flow. Consequently, research and development in this area has similarly focused on pressure (FFR). Recent work (summarised in Chapter 6.1) demonstrates the added value of combined pressure and flow measurements. Two novel indices of intra-coronary physiology based upon CFD modelling were proposed in Chapter 6; virtual stenosis resistance (vSR) and virtual myocardial resistance (vMR). Both methods compute quickly (2-3minutes) using data generated during routine ICA.

7.2 Further work

Figure 7.1 summarises the vFFR and coronary flow arms of the VIRTUheart™ workflows, broadly indicating the scale of development required at each stage. As reflected in **Figure 7.1**, there are a number of developmental challenges to overcome before the VIRTUheart™ model can be deployed as a clinical tool. Beyond scientific development, a variety of regulatory, commercial, intellectual property, logistic, political and economic related factors must also be considered.
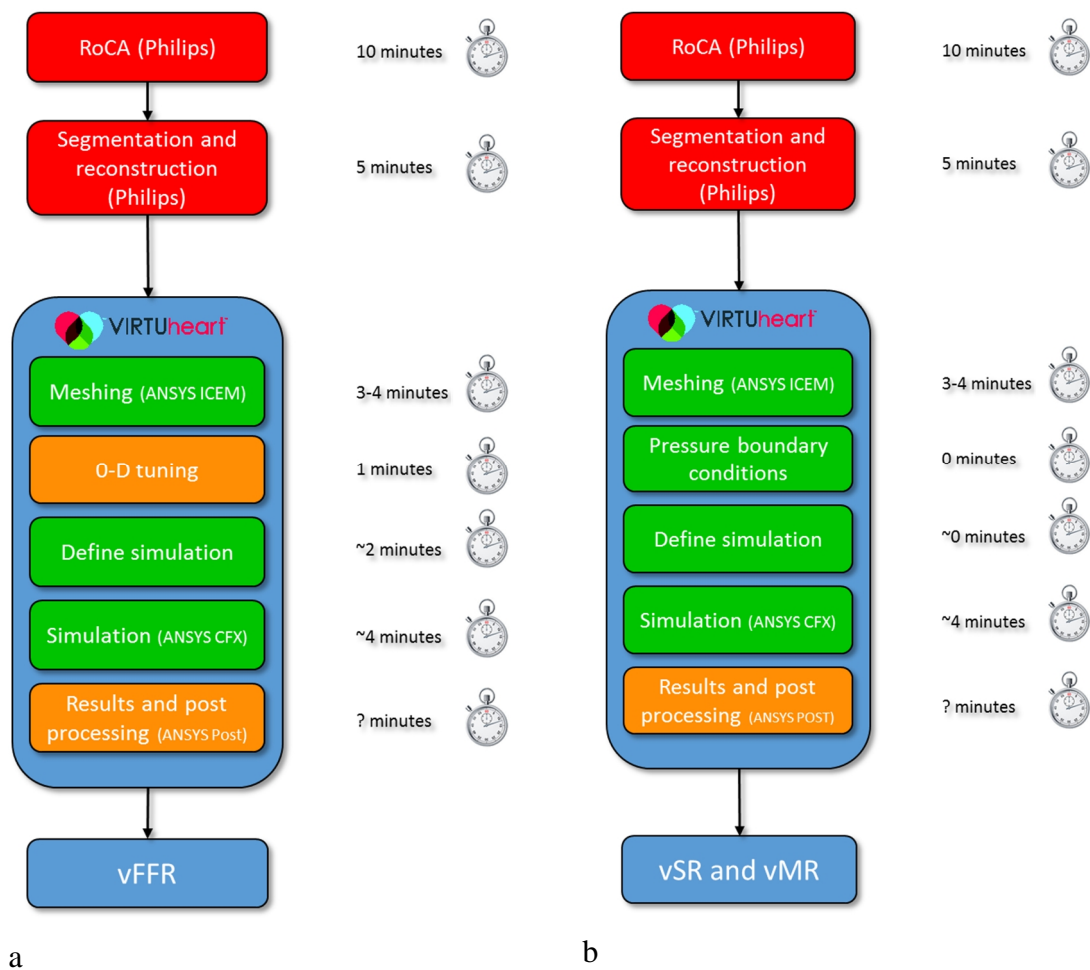
Figure 7.1. A summary of the vFFR and coronary flow workflows.
Red indicates areas of concern at the current time (see below), amber indicates areas where development is required and green indicates areas where development is satisfactory. The stopwatches indicate time associated with the corresponding step.

7.2.1.1   What next for workflow development?

The two highest priorities are first, to implement a segmentation and reconstruction method which can improve segmentation and reconstruction and second, to continue the work demonstrated in Chapter 5.4 in order to derive a mathematical model which allows reliable patient-specific 0-D tuning.

7.2.1.2   Vessel segmentation and reconstruction

Segmentation from medical images, whether they be derived from CTCA or CAG, is crucial to the accuracy of CFD simulation. Throughout this thesis, coronary segmentation and reconstruction

have consistently been problematic. Dependence on the Philips system is associated with a number of limitations summarised in **Table 7.1**.

Table 7.1. A summary of the limitations of the Philips segmentation and reconstruction system

Category Specific factors	Detail/s	Solution (novel system)
Clinical		
Requires RoCA angiogram	Additional set up time. Available in <10% catheter-laboratories. Used in minority of cases. Additional views in PCI cases.	Capability of operating from standard, multiplane angiography
Segmentation method		
Uses only 2 projections	Ignores 119 projections and does not incorporate true 3-D geometry.	Capability of operating from standard, multiplane angiography
Epipolar lines	In RoCA, the epipolar lines always limit segmentation of the proximal and distal arterial segments.	Capability of operating from standard, multiplane angiography or co-registration with CT /IVUS.
Gating	Impossible to select two images which optimally show lesion detail, >30º apart, without overlap, good opacification, minimal foreshortening which are ECG gated.	Capability of operating from standard, multiplane angiography.
Reconstruction		
Axisymmetric	Axisymmetric reconstruction ignores plaque eccentricity	Reconstruction from standard, multiplane angiography which can incorporate ≥2 projections.

RoCA, rotational coronary angiography

Proprietary tools are available for segmenting 'standard' ICA images (QAngio XA 3D RE by Medis Medical Imaging Systems bv, Leiden NL and CAAS QCA 3D by Pie Medical Imaging, Maastricht, NL) but, in common with RoCA, these tools include just two projections meaning that many of the limitations of RoCA are reproduced. Furthermore, the latter does not correct for bed movement between image acquisitions which is an additional limitation. Biplane angiography is an alternative but this is similarly limited by including just two projections and is available in only very few catheter laboratories. Whilst it is possible to co-register angiography with either IVUS or OCT but this is not straightforward and both techniques require the passage of an angioplasty wire which make this impractical in the current context (Kousera et al., 2014). Development of a novel system is required. Within the current group, work has commenced (beyond the bounds of the current thesis) which will allow segmentation from multiple (≥2) views using standard ICA. This approach will circumvent almost all of the problems associated with RoCA but is associated with separate challenges, not least, in correcting for bed and /or patient movements between acquisitions.

7.2.1.3   Distal boundary tuning

As demonstrated in Chapter 3 and Chapter 4.3, the tuning of the coupled 0-D model is the single greatest influence on vFFR accuracy. This thesis and the associated literature consistently demonstrate that the application of distal boundary conditions based upon averaged tuning is associated with an error of ±10%. Universally, therefore this represents a major challenge. It also presents significant opportunity for technological development. In Chapter 5, I describe a novel approach to tuning based upon regression modelling. Multiple linear regression analysis does identify cogent relationships between the dependent and independent variables. Many relationships appear highly significant and withstand 1000 fold bootstrap analysis. Now that proof-of-concept has been demonstrated, it is vital that this work continues. First, a much larger and more representative database is required. Second, a more sophisticated mathematical approach is required which can tease out non-linear, interaction, and higher order polynomial terms. This can be achieved with NARMAX (nonlinear autoregressive moving average modelling with exogenous inputs). NARMAX modelling characterises the terms in the model, ranks them in order of significance to the output variable, determines the model coefficients, builds a predictive model, and validates prediction accuracy. NARMAX is highly appropriate in the context of the CMVR modelling and prediction because, unlike simple linear approaches, it is does not require large datasets and copes well with mixed and diverse variables. Over the last decade NAMRMAX modelling has seen widespread and extremely successful application in a range of applications (Chen S., 1989, Billings, 2013).

At the time of thesis submission, initial NARMAX modelling was being applied to the dataset analysed in Chapter 5.4. NARMAX identified and ranked a number of significant variables, interactions and nonlinear relationships. These are summarised in Table 7.2. Reassuringly, many of the terms identified by NARMAX overlap with those identified by multiple linear regression in Chapter 5 but additional variables and interactions were also identified. Although many of these terms appear previously undescribed, all appear cogent with the current understanding of CMVR and /or the mechanisms described in Chapter 5. The preliminary model predicted CMVR (R_{total}) with an associated R^2 of 0.84 (**Figure 7.2**). This is impressive. This work will continue within the remit of the jointly funded (Wellcome Trust and Department for Health) HICF project and will eventually include and analysis of 100 patients with a wide range of patterns and severities of CAD.

7.2.1.4   Flow Computation

The work in Chapter 6 demonstrates that it appears feasible to compute flow from measured pressure. This work has already received interest from an industrial partner (Volcano Corps). If further development is successful, this may become a more reliable and practical method than

Doppler flow velocity. The key priorities for this work are to develop and validate the method so that the effect of arterial branches is included. The experimental phantom circuit will be ideal for this but will require 3-D printed branched phantoms. The 3-D files for this are prepared. A potential practical issue is that the novel method relies upon pressure measurements and these are not performed routinely, and in some cases, are not possible for all branches. As a solution, a hybrid approach may be feasible whereby measured pressures from the major branches are used to estimate the 0-D parameters of CMVR which can be applied to unmeasured outlet branches.
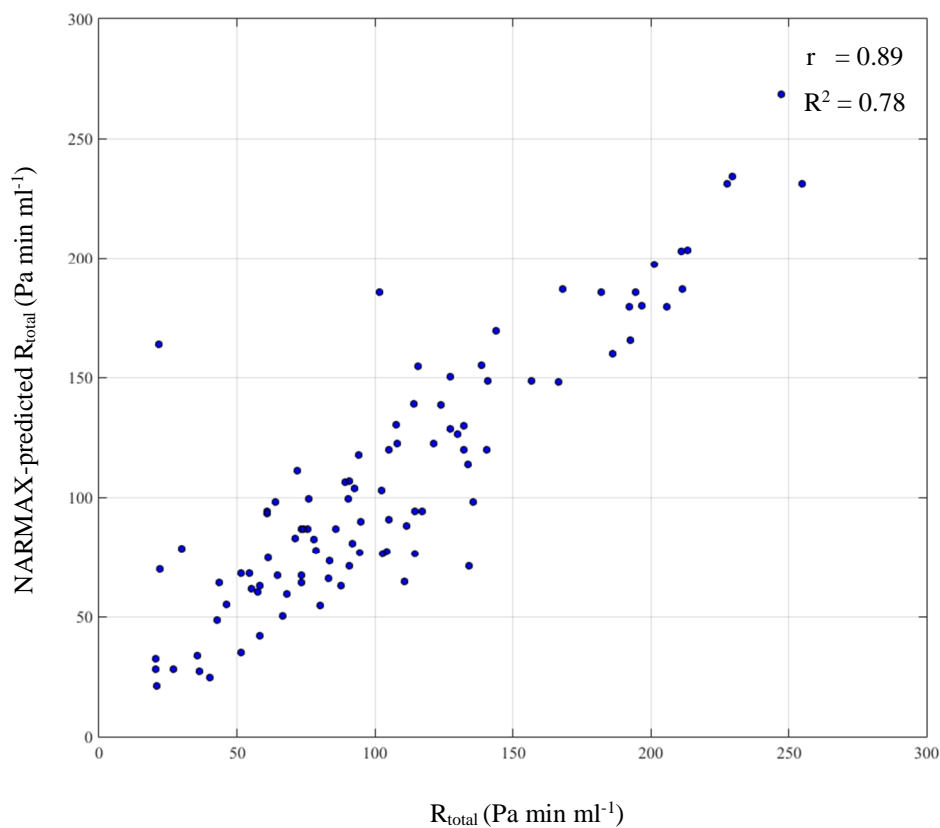
Figure 7.2. Correlation between R_{total} and NARMAX predicted R_{total} based upon the model described in Table 7.1.
Pearson's correlation coefficient (r) = 0.89, R^2 = 0.78.

It is also feasible to use the novel method to compute the transient coronary flow waveform as a function of time, something which could be co-registered with the pressure and ECG signals. This would involve transient CFD analysis, using the time-varying inlet and outlet measured pressures and is something which has already been performed in this thesis. Transient analysis is time-consuming (c. 6-8 hrs) but integrating the accelerated CFD methods described in Chapter 4 would produce results within approximately 4 minutes. Future work should also compare the novel

method with thermodilution which can be used to estimate mean coronary flow. This can simply be tested in the flow circuit. The thermodilution method measures the inverse of the transit time of a bolus of room-temperature saline injected at the catheter tip to the thermos-sensitive guidewire tip. Thermodilution has been validated against Doppler ultrasound in animal and human studies (De Bruyne et al., 2001, Pijls et al., 2002, Fearon et al., 2003b, Barbato et al., 2004) and also allows the index of microcirculatory resistance to be estimated (Fearon et al., 2003a). However, thermodilution cannot generate a flow waveform. Furthermore, the accuracy can be affected by vessel length, number of branches and the volume of injectant.

7.2.1.5   Workflow environment

Clinical vFFR systems should be simple and intuitive in order to maximise adoption and for safe use by physicians who are not CFD experts. During this thesis, the workflow environment was developed from that described in Chapter 3. Development and increased understanding allow components of the workflow to be hard-coded and automated. The current workflow is more streamlined and the graphical user interface is apposite for ongoing development. Future work will see the evolution of two separate versions of the graphical user interface. One will include a range of academic and technical functions and the other will be a more streamlined interface which will be appropriate for use by clinical doctors within a clinical trial.

7.2.1.6   Virtual stenting

Beyond simply replacing invasive FFR, and providing physiological assessment for the many patients not currently afforded it, vFFR offers some additional advantages. Perhaps the most valuable, at least from a clinical perspective is the possibility of 'virtual stenting' whereby the physiological impact of alternative interventional strategies can be trialled *in silico* before treatment is delivered *in vivo*. FFR-guided PCI is already associated with a decrease in the number of stents implanted and it is logical to predict that virtual stenting may increase this effect. A simple, idealised method for virtual stenting has already been implemented in the VIRTUheart™ workflow. Future work will involve developing a library of stent geometries and a comparison of data from before and after *in silico* and *in vivo* stenting. The data for such a comparison is already available from the ArQ database developed as part of this thesis.

7.2.1.7   Repeatability and branches

Additional work will also involve quantification of repeatability and inter-individual variability in the computation of results. However, the results of such an analysis should be interpreted with caution until a definitive segmentation and reconstruction solution is implemented. A simple method for modelling side branches is described in Chapter 3. It would be physiologically more

realistic to tune these individually. The distribution of 0-D outlet resistance values can be determined on the assumption of constant shear-stress. Murray's law states that the energy required for blood flow, and the energy needed to maintain the vasculature is assumed minimal and hence, where k is a constant and r is the radius of the vessel, $Q_i \sim k \cdot r_i^3$. Thus the total resistance of the outlet 0-D model is proportional to $1/r_i^3$. This approach has been demonstrated by several groups (van der Giessen et al., 2011, Taylor et al., 2013, Rossi et al., 2014, Schrauwen et al., 2015). In theory, it is possible to tune the outlet conditions according to knowledge of the distal vessel radii and the NARMAX-informed parameters for the 0-D parameters at the main vessel outlet. Further developmental and implementation work will seek to validate this approach.

Table 7.2. Initial NARMAX analysis.

Product model term	Parameter	Contribution made by model term measured by ERR (%)
eGFR	45.3	75.40
(E:A ratio) × (2-D QCA lesion length)	198.1	4.79
(artery) × (presence of tandem lesions)	148.7	3.82
(sex) × (mean SV)	80.2	3.00
(height) × (PPI)	131.7	1.73
(PPI) × (LVPWs)	-132.5	1.51
(age) ×(Hb)	90.2	1.12
(MI in target artery territory) × (ECG QRS dur)	108.8	0.99
(WCC) × (E:A ratio)	123.9	0.90
(mean SV) × (TDi med E`)	-98.0	0.72
(MI in target artery territory) × (T2DM)	227.8	0.50
(MI Hx) × (T2DM)	-179.1	0.57
(β blocker) × (2-D QCA Poiseuille Res')	179.4	0.33
(smoking: yrs ex) × (ECG PR duration)	84.4	0.33
(BMI) ×(ECG PR duration)	-158.2	0.36
(artery) × (gender)	-217.5	0.32
(sex) × (TDi medial e`)	171.9	0.24
(glucose) × (Doppler V2 max)	773.1	0.25
(sex) × (hypertension)	57.2	0.23
(glucose) × (ECG LV voltage)	-411.9	0.17
(ECG T wave axis) × (2-D QCA norm flow)	87.4	0.17
(aortic stenosis) × (no PCI vs PCI)	-84.3	0.10
		Total = 100%

R^2 for this model = 0.78. Abbreviations as in Chapter 5.

7.2.2 Challenges beyond workflow development

7.2.2.1 Clinical trial evidence

Accuracy is key to the success of vFFR but what constitutes accuracy is yet to be defined. Perhaps most important is whether vFFR correctly assigns a patient to treatment to produce alleviation of symptoms. Currently, this accords with a treatment threshold FFR <0.80. A related measure of accuracy is how close vFFR values approximate measured values over the whole range and if so, how closely is acceptable. Because FFR itself varies between repeat measurements (Petraco *et al.*, 2012), the comparative accuracy of vFFR is also restricted. Furthermore, should accuracy be defined on a per-patient or per-vessel basis? A Bland-Altman plot is the best statistical metric for evaluating vFFR accuracy against FFR but this method does not lend itself to making comparison between different models. Although often quoted, correlation coefficients are misleading and do not reflect agreeability. Ultimately, demonstrating clinical success is vital, regardless of agreement with other methods and prospective, randomised controlled trials will be necessary. Therefore, prior to clinical acceptance, two imperatives must be met. The first is to demonstrate equivalence of vFFR to invasive FFR in clinical practice in situations when FFR is currently used. The second is to compare vFFR tools within traditional decision pathways at the stage of diagnostic angiography (CAG or CTCA) for the many thousands of patients not currently offered physiological assessment. Therefore, beyond the more immediate work of model development, the highest priority is to plan and perform a series of clinical trials.

In the first instance (assuming successful development of the segmentation system), this can be achieved using retrospective data. The Sheffield archive alone contains several thousand angiograms. **Figure 7.3** outlines a potential framework for retrospective validation analysis. This work has commenced with separate analyses being performed in the context of stable CAD, ACS, patients referred for CABG and in those with retrospective FFR data.

A prospective clinical trial will also be required. In the first instance this will be a head-to-head, randomised controlled trial of $vFFR_{ICA}$-guided PCI versus mFFR-guided PCI. The study will be similar in design to the original FAME trial discussed in Chapter 1 and will be powered to demonstrate non-inferiority (Tonino et al., 2010). As the tool develops and improves with additional functions (e.g. virtual stenting) it may become appropriate to compare $vFFR_{ICA}$ and mFFR in order to demonstrate superiority to standard mFFR.

7.2.2.2   Intellectual property (IP)

Two patent applications have been initiated by the UoS (Healthcare Gateway) incorporating the work in Chapter 4.7 and 5.4. Drafting is now underway with a UoS appointed patent attorney. The VIRTUheart™ name, logo and branding are protected by trademark. All of the computer code is protected by copyright. Future work will involve demonstrating the continued value and success of these technologies when the patent comes up for review. This will take place within the Intellectual Property Group Meetings held three times per year under the auspice of the Welcome Trust and Department for Health HICF grant funding.
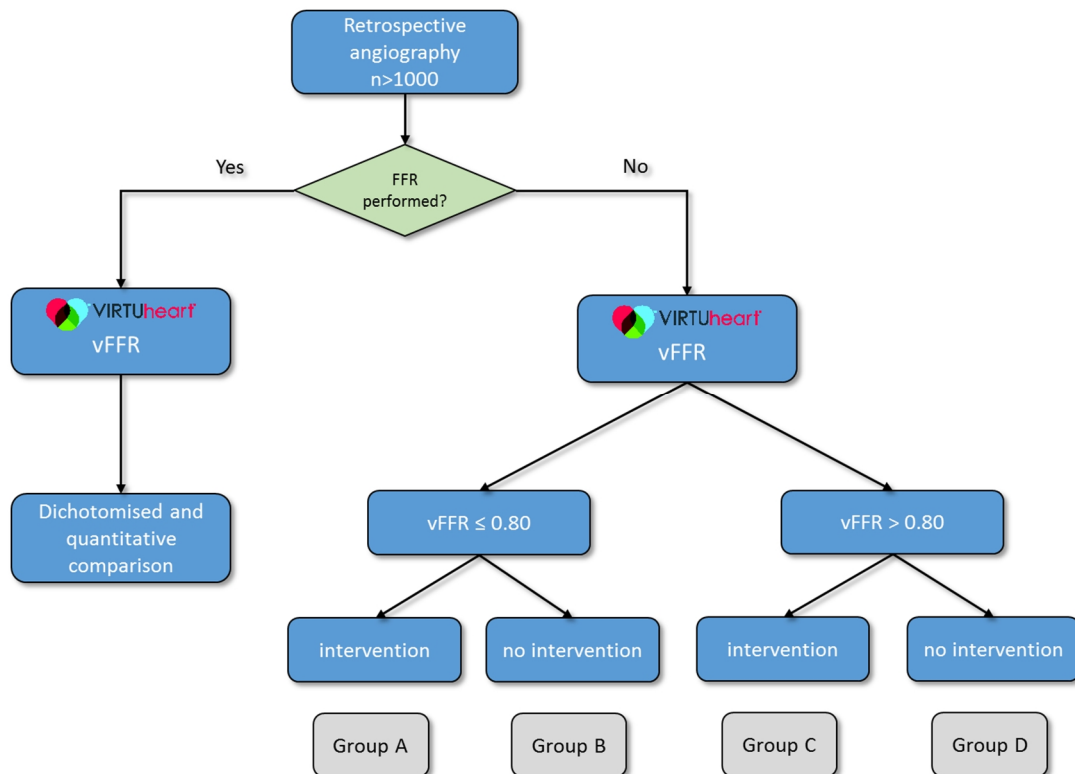
Figure 7.3. Retrospective analysis of the VIRTUheart™ system.
A direct head-to-head comparison can be performed on patients who have undergone FFR measurement previously. In those patients who did not undergo FFR, outcome data can be compared between those in whom vFFR and the clinical decision agreed (groups A and D) and those in whom it did not (groups B and C). Analyses can be made at a per-patient and a per lesion level for those with multi-vessel disease.

7.2.2.3   Regulatory approval

Work will continue to ensure that all the appropriate work is done in preparation for gaining regulatory approval for use of VIRTUheart™ as a Class 2a medical device under the remit of the European Union Medical Devices Directive. Currently, the steps involved are under consultation

with regulatory consultants (NIHR Healthcare Technology Co-operative for Devices for Dignity at Sheffield Teaching Hospitals NHS Foundation). A regulatory landscape for these types of software tools has only recently emerged and the precise level of classification may change subject to ongoing consultation.

7.2.2.4   Commercialisation

Around 1 million PCI procedures are performed annually in the US at a cost of approximately $10 Billion PA; the rewards for successfully modelling vFFR are therefore considerable. There has already been commercial interest from industrial partners in the areas covered by the patents and in the project as a whole. Meetings are scheduled with Volcano Corps and Philips Healthcare to discuss opportunities for developing bringing the tools described in this thesis to market.

7.3 Potential final model

Figure 7.4 outlines a potential framework for the VIRTUheart™ model in routine clinical use for the computation of vFFR and vSR /vMR. The number of patients in which vFFR could replace mFFR will depend upon the error associated with the vFFR result. In computational modelling, error may be influenced by a number of model parameters and is not necessarily constant across all simulations. The sensitivity analysis work described in Chapter 4.3 is continuing (outside of the current thesis). This work will involve many tens of thousands of VIRTUheart™ simulations in order to develop an understanding of the dominant influences upon error. In the near future, this work will enable VIRTUheart™ to generate a case-specific confidence interval with each vFFR (or vSR /vMR) result. Other vFFR models do not provide this facility. Ultimately, overall model precision will determine the number of patients in whom vFFR can confidently replace mFFR and this remains to be determined.

A hybrid approach may be warranted similar to iFR, whereby vFFR can confidently be deployed on the majority of patients (confidence margins do not cross threshold), with mFFR being required in the minority (confidence margins cross threshold). As an extension to this hybrid approach, some patients may warrant additional physiological information and in those, an invasive pressure wire may be used to add flow data to the pressure analysis at minimal additional effort.

It may also be possible to incorporate a system whereby the VIRTUheart™ system continues to 'learn' from routinely performed analyses (**Figure 7.4**, yellow box). This would be an extension to the distal boundary work described in Chapter 5.4 and would involve mFFR data being used to continuously update the ArQ database. This would serve two purposes. First, it would allow

updated boundary condition tuning based on an increasingly large, and more representative population of patients. Second, it would allow continuing validation and quality assurance of the results.
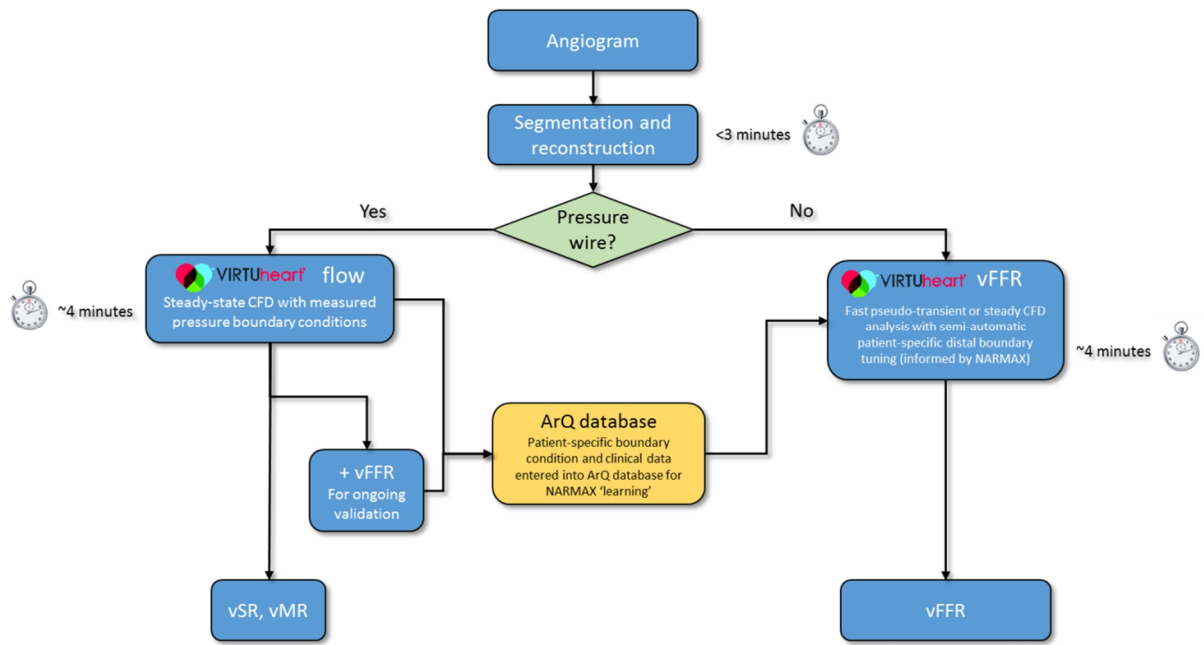
Figure 7.4. Flowchart demonstrating the potential design of VIRTUheart™ in clinical practice. *The stopwatch symbols indicate the time associated with any step which are additional to standard visual angiography.*

Finally, **Figure 7.5** demonstrates the potential place of both vFFR$_{CT}$ and VIRTUheart™ within the general scheme of IHD diagnosis and management compared with current practice. In this figure, chest pain represents the generic start point for the investigation of for IHD.

7.4 Final conclusions

In this thesis, I have developed a computational workflow to estimate 'virtual' FFR from angiographic images. The model is based upon a 3-D CFD domain representing the arterial stenosis with coupled 0-D models at the outlets representing the CMV. It is now termed VIRTUheart™, and is capable of predicting either distal coronary pressure, and hence vFFR, or coronary flow, and thus indices of stenosis and CMV resistance. In addition to angiographic image data, the former model (vFFR) uses readily-available, non-invasive clinical data to tune the distal

boundary condition on an individual case basis. The latter model (coronary flow) requires no additional data or assumptions for computation. Both models operate within clinically tractable timescales and thus can potentially be deployed during ICA. Beyond the scientific validation described in this thesis, clinical trials are needed to demonstrate the efficacy of these models in the clinic.
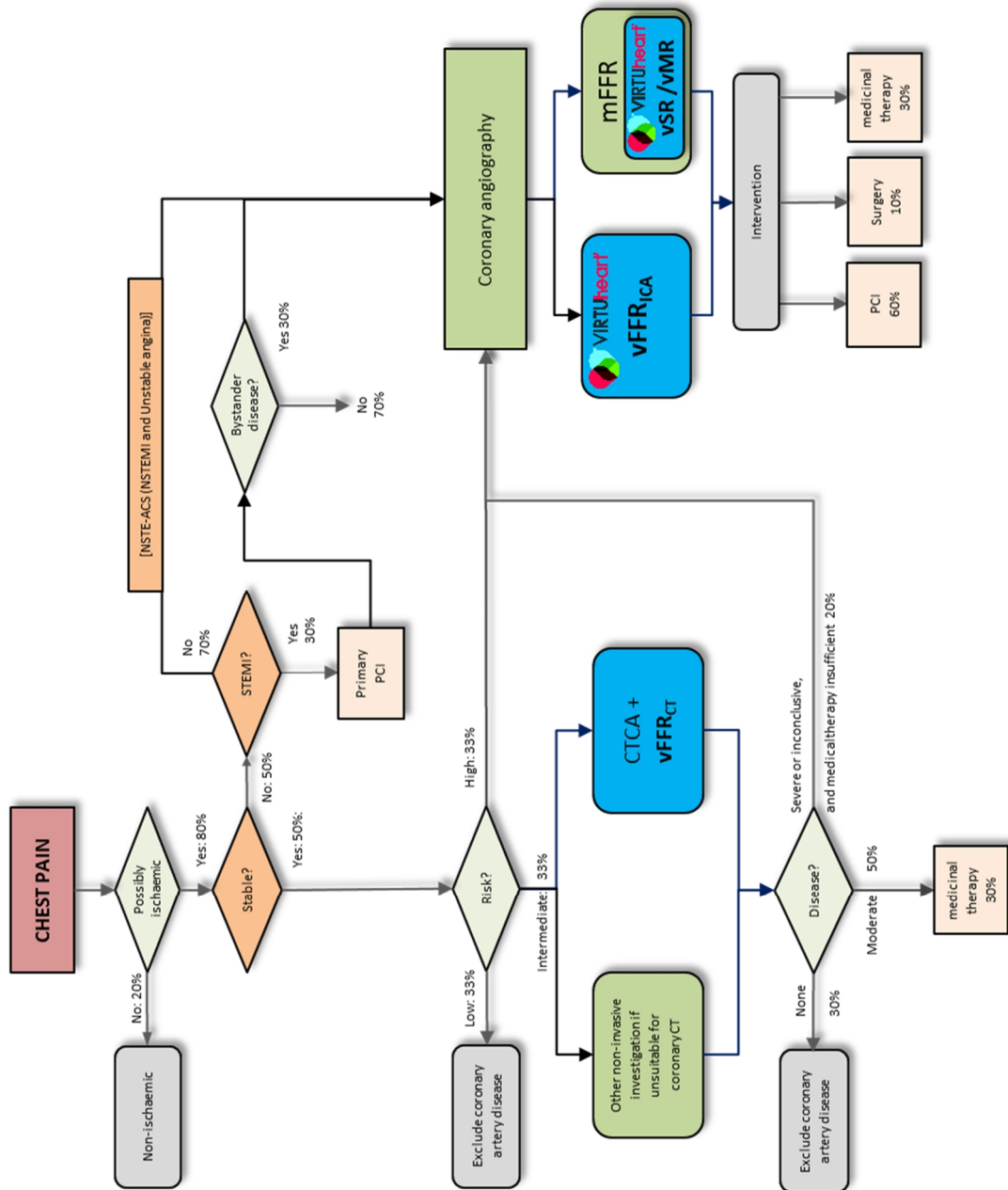
Figure 7.5 Flowchart demonstrating the potential future place of VIRTUheart™ and vFFR_CT in the general scheme for the investigation and management of IHD with approximate proportions of patient flows.
Virtual interventions are in blue.

REFERENCES

ANSYS ICEM CFD 14 – User Manual, 2011. Canonsburg, PA, USA.

ANSYS. 2009. ANSYS CFX-Solver Theory Guide [Online, accessed July 2015].
http://www1.ansys.com/customer/content/documentation/120/cfx/xthry.pdf.

Ashtekar, K. D. B., L.H. Khoury, S.F. Banerjee, R.K. 2007. In Vitro Quantification of Guidewire Flow-Obstruction Effect in Model Coronary Stenoses for Interventional Diagnostic Procedure. Journal of Medical Devices, 1, 185-196.

Austin, R. E., Jr., Aldea, G. S., Coggins, D. L., Flynn, A. E. & Hoffman, J. I. 1990. Profound spatial heterogeneity of coronary reserve. Discordance between patterns of resting and maximal myocardial blood flow. Circ Res, 67, 319-31.

Bamberg, F., Marcus, R. P., Becker, A., Hildebrandt, K., Bauner, K., Schwarz, F., Greif, M., Von Ziegler, F., Bischoff, B., Becker, H. C., Johnson, T. R., Reiser, M. F., Nikolaou, K. & Theisen, D. 2014. Dynamic myocardial CT perfusion imaging for evaluation of myocardial ischemia as determined by MR imaging. JACC Cardiovasc Imaging, 7, 267-77.

Barbato, E., Aarnoudse, W., Aengevaeren, W. R., Werner, G., Klauss, V., Bojara, W., Herzfeld, I., Oldroyd, K. G., Pijls, N. H. & De Bruyne, B. 2004. Validation of coronary flow reserve measurements by thermodilution in clinical practice. Eur Heart J, 25, 219-23.

Barber, D. C. & Hose, D. R. 2005. Automatic segmentation of medical images using image registration: diagnostic and simulation applications. J Med Eng Technol, 29, 53-63.

Bartunek, J., Sys, S. U., Heyndrickx, G. R., Pijls, N. H. & De Bruyne, B. 1995. Quantitative coronary angiography in predicting functional significance of stenoses in an unselected patient cohort. J Am Coll Cardiol, 26, 328-34.

Bech, G. J., De Bruyne, B., Pijls, N. H., De Muinck, E. D., Hoorntje, J. C., Escaned, J., Stella, P. R., Boersma, E., Bartunek, J., Koolen, J. J. & Wijns, W. 2001. Fractional flow reserve to determine the appropriateness of angioplasty in moderate coronary stenosis: a randomized trial. Circulation, 103, 2928-34.

Beller, G. A. & Zaret, B. L. 2000. Contributions of nuclear cardiology to diagnosis and prognosis of patients with coronary artery disease. Circulation, 101, 1465-78.

Ben-Dor, I, Torguson, R., Deksissa, T., Bui, A. B., Xue, Z., Satler, L. F., Pichard, A. D. & Waksman, R. 2012. Intravascular ultrasound lumen area parameters for assessment of physiological ischemia by fractional flow reserve in intermediate coronary artery stenosis. Cardiovasc Revasc Med, 13, 177-82.

Ben-Dor, I, Torguson, R., Gaglia, M. A., Jr., Gonzalez, M. A., Maluenda, G., Bui, A. B., Xue, Z., Satler, L. F., Suddath, W. O., Lindsay, J., Pichard, A. D. & Waksman, R. 2011. Correlation between fractional flow reserve and intravascular ultrasound lumen area in intermediate coronary artery stenosis. EuroIntervention, 7, 225-33.

Berry, C., Van 'T Veer, M., Witt, N., Kala, P., Bocek, O., Pyxaras, S. A., Mcclure, J. D., Fearon, W. F., Barbato, E., Tonino, P. A., De Bruyne, B., Pijls, N. H. & Oldroyd, K. G. 2013. VERIFY (VERification of Instantaneous Wave-Free Ratio and Fractional Flow Reserve for the Assessment of Coronary Artery Stenosis Severity in EverydaY Practice): a multicenter study in consecutive patients. J Am Coll Cardiol, 61, 1421-7.

Berry, J. L., Santamarina, A., Moore, J. E., Jr., Roychowdhury, S. & Routh, W. D. 2000. Experimental and computational flow evaluation of coronary stents. Ann Biomed Eng, 28, 386-98.

Bertoglio, C., Barber, D., Gaddum, N., Valverde, I., Rutten, M., Beerbaum, P., Moireau, P., Hose, R. & Gerbeau, J. F. 2014. Identification of artery wall stiffness: in vitro validation and in vivo results of a data assimilation procedure applied to a 3D fluid-structure interaction model. J Biomech, 47, 1027-34.

Bertrand, M. E., Lablanche, J. M., Bauters, C., Leroy, F. & Mac Fadden, E. 1993. Discordant results of visual and quantitative estimates of stenosis severity before and after coronary angioplasty. Cathet Cardiovasc Diagn, 28, 1-6.

Bessems, D. 2007. On the propagation of pressure and flow waves through the patient-specific arterial system. PhD, Eindhoven University of Technology.

Bessems, D., Rutten, M. C. M. & Rogge, T. R. 2007. A wave propagation model of blood flow in large vessels using an approximate velocity profile function. Journal of Fluid Mechanics, 580, 145-168.

Biglino, G., Giardini, A., Hsia, T. Y., Figliola, R., Taylor, A. M. & Schievano, S. 2013. Modeling single ventricle physiology: review of engineering tools to study first stage palliation of hypoplastic left heart syndrome. Front Pediatr, 1, 31.

Billings, S. A. 2013. Nonlinear System Identification: NARMAX Methods in the Time, Frequency, and Spatio-Temporal Domains, Wiley.

Bland, J. M. & Altman, D. G. 1986. Statistical methods for assessing agreement between two methods of clinical measurement. Lancet, 1, 307-10.

Bland, J. M. & Altman, D. G. 1995. Comparing two methods of clinical measurement: a personal history. Int J Epidemiol, 24 Suppl 1, S7-14.

Boden, W. E., O'rourke, R. A., Teo, K. K., Hartigan, P. M., Maron, D. J., Kostuk, W. J., Knudtson, M., Dada, M., Casperson, P., Harris, C. L., Chaitman, B. R., Shaw, L., Gosselin, G., Nawaz, S., Title, L. M., Gau, G., Blaustein, A. S., Booth, D. C., Bates, E. R., Spertus, J. A., Berman, D. S., Mancini, G. B., Weintraub, W. S. & Group, C. T. R. 2007. Optimal medical therapy with or without PCI for stable coronary disease. N Engl J Med, 356, 1503-16.

Bornschein, B., Arvandi, M., Gothe, R., Rioufol, G., De Bruyne, B., De Pouvourville, G., Desmet, W., Lefevre, T., Fearon, W., Pijls, N. & Siebert, U. 2011. Cost Effectiveness Of Fractional Flow Reserve Measurement In Multivessel Coronary Artery Disease In Belgium And France (PMD40). Value in Health, 14, A233-A510.

Bossers, S. S., Cibis, M., Gijsen, F. J., Schokking, M., Strengers, J. L., Verhaart, R. F., Moelker, A., Wentzel, J. J. & Helbing, W. A. 2014. Computational fluid dynamics in Fontan patients to evaluate power loss during simulated exercise. Heart, 100, 696-701.

Boutsianis, E., Dave, H., Frauenfelder, T., Poulikakos, D., Wildermuth, S., Turina, M., Ventikos, Y. & Zund, G. 2004. Computational simulation of intracoronary flow based on real coronary geometry. Eur J Cardiothorac Surg, 26, 248-56.

Bovendeerd, P. H., Borsje, P., Arts, T. & Van De Vosse, F. N. 2006. Dependence of intramyocardial pressure and coronary flow on ventricular loading and contractility: a model study. Ann Biomed Eng, 34, 1833-45.

Brown, A. G. 2012. Pateint-Specific Local and Systemic Haemodynamics in the Presence of a Left Ventricular Assist Device. PhD, University of Sheffield.

Brown, A. G., Shi, Y., Arndt, A., Muller, J., Lawford, P. & Hose, D. R. 2012a. Importance of realistic LVAD profiles for assisted aortic simulations: evaluation of optimal outflow anastomosis locations. Comput Methods Biomech Biomed Engin, 15, 669-80.

Brown, A. G., Shi, Y., Marzo, A., Staicu, C., Valverde, I., Beerbaum, P., Lawford, P. V. & Hose, D. R. 2012. Accuracy vs. computational time: translating aortic simulations to the clinic. J Biomech, 45, 516-23.

Brown, B. G., Bolson, E., Frimer, M. & Dodge, H. T. 1977. Quantitative coronary arteriography: estimation of dimensions, hemodynamic resistance, and atheroma mass of coronary artery lesions using the arteriogram and digital computation. Circulation, 55, 329-37.

Budoff, M. J., Dowe, D., Jollis, J. G., Gitter, M., Sutherland, J., Halamert, E., Scherer, M., Bellinger, R., Martin, A., Benton, R., Delago, A. & Min, J. K. 2008. Diagnostic performance of 64-multidetector row coronary computed tomographic angiography for evaluation of coronary artery stenosis in individuals without known coronary artery disease: results from the prospective multicenter ACCURACY (Assessment by Coronary Computed Tomographic Angiography of Individuals Undergoing Invasive Coronary Angiography) trial. J Am Coll Cardiol, 52, 1724-32.

Camici, P. G. & Crea, F. 2007. Coronary microvascular dysfunction. N Engl J Med, 356, 830-40.

Canetti, M., Akhter, M. W., Lerman, A., Karaalp, I. S., Zell, J. A., Singh, H., Mehra, A. & Elkayam, U. 2003. Evaluation of myocardial blood flow reserve in patients with chronic congestive heart failure due to idiopathic dilated cardiomyopathy. Am J Cardiol, 92, 1246-9.

Cassar, A., Matsuo, Y., Herrmann, J., Li, J., Lennon, R. J., Gulati, R., Lerman, L. O., Kushwaha, S. S. & Lerman, A. 2013. Coronary atherosclerosis with vulnerable plaque and complicated lesions in transplant recipients: new insight into cardiac allograft vasculopathy by optical coherence tomography. Eur Heart J, 34, 2610-7.

Chamuleau, S. A., Siebes, M., Meuwissen, M., Koch, K. T., Spaan, J. A. & Piek, J. J. 2003. Association between coronary lesion severity and distal microvascular resistance in patients with coronary artery disease. Am J Physiol Heart Circ Physiol, 285, H2194-200.

Chareonthaitawee, P., Kaufmann, P. A., Rimoldi, O. & Camici, P. G. 2001. Heterogeneity of resting and hyperemic myocardial blood flow in healthy humans. Cardiovasc Res, 50, 151-61.

Chen S., B. S. A. 1989. Representations of nonlinear systems-narmax model. Interntional Journal of Control, 49, 1013-1032.

Chien, S. 2007. Mechanotransduction and endothelial cell homeostasis: the wisdom of the cell. Am J Physiol Heart Circ Physiol, 292, H1209-24.

Choudhury, L., Rosen, S. D., Patel, D., Nihoyannopoulos, P. & Camici, P. G. 1997. Coronary vasodilator reserve in primary and secondary left ventricular hypertrophy. A study with positron emission tomography. Eur Heart J, 18, 108-16.

Christou, M. A., Siontis, G. C., Katritsis, D. G. & Ioannidis, J. P. 2007. Meta-analysis of fractional flow reserve versus quantitative coronary angiography and noninvasive imaging for evaluation of myocardial ischemia. Am J Cardiol, 99, 450-6.

Cimen, S., Hoogendoorn, C., Morris, P. D., Gunn, J. & Frangi, A. F. 2014. Reconstruction of coronary trees from 3DRA using a 3D+t statistical cardiac prior. Med Image Comput Comput Assist Interv, 17, 619-26.

Cochrane, T., Kenyon, C. J., Lawford, P. V., Black, M. M., Chambers, J. B. & Sprigings, D. C. 1991. Validation of the orifice formula for estimating effective heart valve opening area. Clin Phys Physiol Meas, 12, 21-37.

Cooper, A., Timmis, A., Skinner, J. & Guideline Development, G. 2010. Assessment of recent onset chest pain or discomfort of suspected cardiac origin: summary of NICE guidance. BMJ, 340, c1118.

Cordis, E. 2015. European Commission: CORDIS : Projects & Results Service : Virtual Physiological Human: Sharing for Healthcare - A Research Environment [Online]. Available: http://cordis.europa.eu/project/rcn/97442_en.html.

Cornelis, G., Bellet, A., Van Eygen, B., Roisin, P. & Libon, E. 1972. Rotational multiple sequence roentgenography of intracranial aneurysms. Acta Radiol Diagn (Stockh), 13, 74-6.

Cox, L. G., Loerakker, S., Rutten, M. C., De Mol, B. A. & Van De Vosse, F. N. 2009. A mathematical model to evaluate control strategies for mechanical circulatory support. Artif Organs, 33, 593-603.

Crea, F., Camici, P. G. & Bairey Merz, C. N. 2014. Coronary microvascular dysfunction: an update. Eur Heart J, 35, 1101-11.

Crunchbase, T. I. G. 2015. HeartFlow Investment [Online]. Available: https://www.crunchbase.com/organization/heartflow [Accessed 23rd July 2015].

Curzen, N., Rana, O., Nicholas, Z., Golledge, P., Zaman, A., Oldroyd, K., Hanratty, C., Banning, A., Wheatcroft, S., Hobson, A., Chitkara, K., Hildick-Smith, D., Mckenzie, D., Calver, A., Dimitrov, B. D. & Corbett, S. 2014. Does routine pressure wire assessment influence management strategy at coronary angiography for diagnosis of chest pain?: the RIPCORD study. Circ Cardiovasc Interv, 7, 248-55.

Curzen, N., Zaman, A., Nolan, J., Norgaard, B. L. & R, R. CT-Derived FFR Alters Angiography-Based Management Plans for Stable Angina - EuroPCR 2015 - TCTMD. EuroPCR 2015, 2015 Paris.

Dattilo, P. B., Prasad, A., Honeycutt, E., Wang, T. Y. & Messenger, J. C. 2012. Contemporary patterns of fractional flow reserve and intravascular ultrasound use among patients undergoing percutaneous coronary intervention in the United States: insights from the National Cardiovascular Data Registry. J Am Coll Cardiol, 60, 2337-9.

Davies, R. F., Goldberg, A. D., Forman, S., Pepine, C. J., Knatterud, G. L., Geller, N., Sopko, G., Pratt, C., Deanfield, J. & Conti, C. R. 1997. Asymptomatic Cardiac Ischemia Pilot (ACIP) study two-year follow-up: outcomes of patients randomized to initial strategies of medical therapy versus revascularization. Circulation, 95, 2037-43.

Dayanikli, F., Grambow, D., Muzik, O., Mosca, L., Rubenfire, M. & Schwaiger, M. 1994. Early detection of abnormal coronary flow reserve in asymptomatic men at high risk for coronary artery disease using positron emission tomography. Circulation, 90, 808-17.

De Bruyne, B., Bartunek, J., Sys, S. U. & Heyndrickx, G. R. 1995. Relation between myocardial fractional flow reserve calculated from coronary pressure measurements and exercise-induced myocardial ischemia. Circulation, 92, 39-46.

De Bruyne, B., Bartunek, J., Sys, S. U., Pijls, N. H., Heyndrickx, G. R. & Wijns, W. 1996. Simultaneous coronary pressure and flow velocity measurements in humans. Feasibility, reproducibility, and hemodynamic dependence of coronary flow velocity reserve, hyperemic flow versus pressure slope index, and fractional flow reserve. Circulation, 94, 1842-9.

De Bruyne, B., Pijls, N. H., Kalesan, B., Barbato, E., Tonino, P. A., Piroth, Z., Jagic, N., Mobius-Winckler, S., Rioufol, G., Witt, N., Kala, P., Maccarthy, P., Engstrom, T., Oldroyd, K. G., Mavromatis, K., Manoharan, G., Verlee, P., Frobert, O., Curzen, N., Johnson, J. B., Juni, P., Fearon, W. F. & Investigators, F. T. 2012. Fractional flow reserve-guided PCI versus medical therapy in stable coronary disease. N Engl J Med, 367, 991-1001.

De Bruyne, B., Pijls, N. H., Smith, L., Wievegg, M. & Heyndrickx, G. R. 2001. Coronary thermodilution to assess flow reserve: experimental validation. Circulation, 104, 2003-6.

De Jong, M. C., Genders, T. S., Van Geuns, R. J., Moelker, A. & Hunink, M. G. 2012. Diagnostic performance of stress myocardial perfusion imaging for coronary artery disease: a systematic review and meta-analysis. Eur Radiol, 22, 1881-95.

De Luca, G., Venegoni, L., Iorio, S., Giuliani, L. & Marino, P. 2011. Effects of increasing doses of intracoronary adenosine on the assessment of fractional flow reserve. JACC Cardiovasc Interv, 4, 1079-84.

De Vecchi, A., Gomez, A., Pushparajah, K., Schaeffter, T., Nordsletten, D. A., Simpson, J. M., Penney, G. P. & Smith, N. P. 2014. Towards a fast and efficient approach for modelling the patient-specific ventricular haemodynamics. Prog Biophys Mol Biol, 116, 3-10.

Dehmer, G. J., Weaver, D., Roe, M. T., Milford-Beland, S., Fitzgerald, S., Hermann, A., Messenger, J., Moussa, I., Garratt, K., Rumsfeld, J. & Brindis, R. G. 2012. A contemporary view of diagnostic cardiac catheterization and percutaneous coronary intervention in the United States: a report from the CathPCI Registry of the National Cardiovascular Data Registry, 2010 through June 2011. J Am Coll Cardiol, 60, 2017-31.

Di Carli, M. F., Dorbala, S., Curillova, Z., Kwong, R. J., Goldhaber, S. Z., Rybicki, F. J. & Hachamovitch, R. 2007a. Relationship between CT coronary angiography and stress perfusion imaging in patients with suspected ischemic heart disease assessed by integrated PET-CT imaging. J Nucl Cardiol, 14, 799-809.

Di Carli, M. F., Dorbala, S., Meserve, J., El Fakhri, G., Sitek, A. & Moore, S. C. 2007b. Clinical myocardial perfusion PET/CT. J Nucl Med, 48, 783-93.

Doane, D. P. & Seward, L. E. 2011. Measuring Skewness. Journal of statistics Education, 19, 1-18.

Douglas, P. S., Taylor, A., Bild, D., Bonow, R., Greenland, P., Lauer, M., Peacock, F. & Udelson, J. 2009. Outcomes research in cardiovascular imaging: report of a workshop sponsored by the National Heart, Lung, and Blood Institute. Circ Cardiovasc Imaging, 2, 339-48.

Eeckhout, E. & Kern, M. J. 2001. The coronary no-reflow phenomenon: a review of mechanisms and therapies. Eur Heart J, 22, 729-39.

El-Tamimi, H., Davies, G. J., Sritara, P., Hackett, D., Crea, F. & Maseri, A. 1991. Inappropriate constriction of small coronary vessels as a possible cause of a positive exercise test early after successful coronary angioplasty. Circulation, 84, 2307-12.

Elveback, L. & Lie, J. T. 1984. Continued high incidence of coronary artery disease at autopsy in Olmsted County, Minnesota, 1950 to 1979. Circulation, 70, 345-9.

Erne, P., Schoenenberger, A. W., Burckhardt, D., Zuber, M., Kiowski, W., Buser, P. T., Dubach, P., Resink, T. J. & Pfisterer, M. 2007. Effects of percutaneous coronary interventions in silent ischemia after myocardial infarction: the SWISSI II randomized controlled trial. JAMA, 297, 1985-91.

Farag, M., Karmonik, C., Rengier, F., Loebe, M., Karck, M., Von Tengg-Koblick, H., Ruhparwar, A. & Partovi, S. 2014. Review of Recent Results Using Computational Fluid Dynamics Simulations in Patients Receiving Mechanical Assist Devices for End-Stage Heart Failure. Houston Methodist DeBakey Cardiovascular Journal, 10, 4.

Fearon, W. F., Balsam, L. B., Farouque, H. M., Caffarelli, A. D., Robbins, R. C., Fitzgerald, P. J., Yock, P. G. & Yeung, A. C. 2003a. Novel index for invasively assessing the coronary microcirculation. Circulation, 107, 3129-32.

Fearon, W. F., Bornschein, B., Tonino, P. A., Gothe, R. M., Bruyne, B. D., Pijls, N. H., Siebert, U. & Fractional Flow Reserve Versus Angiography For Multivessel Evaluation Study, I. 2010. Economic evaluation of fractional flow reserve-guided percutaneous coronary intervention in patients with multivessel disease. Circulation, 122, 2545-50.

Fearon, W. F., Farouque, H. M., Balsam, L. B., Caffarelli, A. D., Cooke, D. T., Robbins, R. C., Fitzgerald, P. J., Yeung, A. C. & Yock, P. G. 2003b. Comparison of coronary thermodilution and Doppler velocity for assessing coronary flow reserve. Circulation, 108, 2198-200.

Feher, J. F. A. 2014. Computational modelling of the sudden expansion pressure drop for the determination of fractional flow reserve. Master of Science, Eindhoven University of Technology.

Feuchtner, G., Goetti, R., Plass, A., Wieser, M., Scheffel, H., Wyss, C., Stolzmann, P., Donati, O., Schnabl, J., Falk, V., Alkadhi, H., Leschka, S. & Cury, R. C. 2011. Adenosine stress high-pitch 128-slice dual-source myocardial computed tomography perfusion for imaging of reversible myocardial ischemia: comparison with magnetic resonance imaging. Circ Cardiovasc Imaging, 4, 540-9.

Fihn, S. D., Gardin, J. M., Abrams, J., Berra, K., Blankenship, J. C., Dallas, A. P., Douglas, P. S., Foody, J. M., Gerber, T. C., Hinderliter, A. L., King, S. B., 3rd, Kligfield, P. D., Krumholz, H. M., Kwong, R. Y., Lim, M. J., Linderbaum, J. A., Mack, M. J., Munger, M. A., Prager, R. L., Sabik, J. F., Shaw, L. J., Sikkema, J. D., Smith, C. R., Jr., Smith, S. C., Jr., Spertus, J. A., Williams, S. V. & American College Of Cardiology, F. 2012. 2012 ACCF/AHA/ACP/AATS/PCNA/SCAI/STS guideline for the diagnosis and management of patients with stable ischemic heart disease: executive summary: a report of the American College of Cardiology Foundation/American Heart Association task force on practice guidelines, and the American College of Physicians, American Association for Thoracic Surgery, Preventive Cardiovascular Nurses Association, Society for Cardiovascular Angiography and Interventions, and Society of Thoracic Surgeons. Circulation, 126, 3097-137.

Fischer, J. J., Samady, H., Mcpherson, J. A., Sarembock, I. J., Powers, E. R., Gimple, L. W. & Ragosta, M. 2002. Comparison between visual assessment and quantitative angiography versus fractional flow reserve for native coronary narrowings of moderate severity. Am J Cardiol, 90, 210-5.

Fleischmann, K. E., Hunink, M. G., Kuntz, K. M. & Douglas, P. S. 1998. Exercise echocardiography or exercise SPECT imaging? A meta-analysis of diagnostic test performance. JAMA, 280, 913-20.

Fleming, R. M., Kirkeeide, R. L., Smalling, R. W. & Gould, K. L. 1991. Patterns in visual interpretation of coronary arteriograms as detected by quantitative coronary arteriography. J Am Coll Cardiol, 18, 945-51.

Food And Drug Administration, U. S. F. A. D. 2014. De Novo Classification Request For Ffrct V. 1.4 (De Novo Summary (DEN130045)) [Online]. Available: http://www.accessdata.fda.gov/cdrh_docs/reviews/DEN130045.pdf [Accessed 24/03/2015 2015].

Frank, O. 1899. Die grundform des arteriellen pulses. . Erste Abhandlung, Mathematische analyse, Z. Biol, 37, 483-526.

Froelicher, V. F., Lehmann, K. G., Thomas, R., Goldman, S., Morrison, D., Edson, R., Lavori, P., Myers, J., Dennis, C., Shabetai, R., Do, D. & Froning, J. 1998. The electrocardiographic exercise test in a population with reduced workup bias: diagnostic performance, computerized interpretation, and multivariable prediction. Veterans Affairs Cooperative Study in Health Services #016 (QUEXTA) Study Group. Quantitative Exercise Testing and Angiography. Ann Intern Med, 128, 965-74.

Frohlich, G. M., Redwood, S., Rakhit, R., Maccarthy, P. A., Lim, P., Crake, T., White, S. K., Knight, C. J., Kustosz, C., Knapp, G., Dalby, M. C., Mali, I. S., Archbold, A., Wragg, A., Timmis, A. D. & Meier, P. 2014. Long-term survival in patients undergoing percutaneous interventions with or without intracoronary pressure wire guidance or intracoronary ultrasonographic imaging: a large cohort study. JAMA Intern Med, 174, 1360-6.

From the British Society of Echocardiography Education Committee. British Society of Echocardiography.

Garcia, M. J., Ares, M. A., Asher, C., Rodriguez, L., Vandervoort, P. & Thomas, J. D. 1997. An index of early left ventricular filling that combined with pulsed Doppler peak E velocity may estimate capillary wedge pressure. J Am Coll Cardiol, 29, 448-54.

Garcia, M. J., Smedira, N. G., Greenberg, N. L., Main, M., Firstenberg, M. S., Odabashian, J. & Thomas, J. D. 2000. Color M-mode Doppler flow propagation velocity is a preload insensitive index of left ventricular relaxation: animal and human validation. J Am Coll Cardiol, 35, 201-8.

Garcia, M. J., Vandervoort, P., Stewart, W. J., Lytle, B. W., Cosgrove, D. M., 3rd, Thomas, J. D. & Griffin, B. P. 1996. Mechanisms of hemolysis with mitral prosthetic regurgitation. Study using transesophageal echocardiography and fluid dynamic simulation. J Am Coll Cardiol, 27, 399-406.

Gasser, T. C., Nchimi, A., Swedenborg, J., Roy, J., Sakalihasan, N., Bockler, D. & Hyhlik-Durr, A. 2014. A novel strategy to translate the biomechanical rupture risk of abdominal aortic aneurysms to their equivalent diameter risk: method and retrospective validation. Eur J Vasc Endovasc Surg, 47, 288-95.

Gaur, S., Achenbach, S., Leipsic, J., Mauri, L., Bezerra, H. G., Jensen, J. M., Botker, H. E., Lassen, J. F. & Norgaard, B. L. 2013. Rationale and design of the HeartFlowNXT (HeartFlow analysis of coronary blood flow using CT angiography: NeXt sTeps) study. J Cardiovasc Comput Tomogr, 7, 279-88.

George, R. T., Arbab-Zadeh, A., Cerci, R. J., Vavere, A. L., Kitagawa, K., Dewey, M., Rochitte, C. E., Arai, A. E., Paul, N., Rybicki, F. J., Lardo, A. C., Clouse, M. E. & Lima, J. A. 2011. Diagnostic performance of combined noninvasive coronary angiography and myocardial perfusion imaging using 320-MDCT: the CT angiography and perfusion methods of the CORE320 multicenter multinational diagnostic study. AJR Am J Roentgenol, 197, 829-37.

George, R. T., Mehra, V. C., Chen, M. Y., Kitagawa, K., Arbab-Zadeh, A., Miller, J. M., Matheson, M. B., Vavere, A. L., Kofoed, K. F., Rochitte, C. E., Dewey, M., Yaw, T. S., Niinuma, H., Brenner, W., Cox, C., Clouse, M. E., Lima, J. A. & Di Carli, M. 2014. Myocardial CT perfusion imaging and SPECT for the diagnosis of coronary artery disease: a head-to-head comparison from the CORE320 multicenter diagnostic performance study. Radiology, 272, 407-16.

Gianrossi, R., Detrano, R., Mulvihill, D., Lehmann, K., Dubach, P., Colombo, A., Mcarthur, D. & Froelicher, V. 1989. Exercise-induced ST depression in the diagnosis of coronary artery disease. A meta-analysis. Circulation, 80, 87-98.

Gibbons, R. J., Abrams, J., Chatterjee, K., Daley, J., Deedwania, P. C., Douglas, J. S., Ferguson, T. B., Jr., Fihn, S. D., Fraker, T. D., Jr., Gardin, J. M., O'rourke, R. A., Pasternak, R. C., Williams, S. V., Alpert, J. S., Antman, E. M., Hiratzka, L. F., Fuster, V., Faxon, D. P., Gregoratos, G., Jacobs, A. K. & Smith, S. C., Jr. 2003. ACC/AHA 2002 guideline update for the management of patients with chronic stable angina--summary article: a report of the American College of Cardiology/American Heart Association Task Force on Practice Guidelines (Committee on the Management of Patients With Chronic Stable Angina). Circulation, 107, 149-58.

Gijsen, F. J., Wentzel, J. J., Thury, A., Mastik, F., Schaar, J. A., Schuurbiers, J. C., Slager, C. J., Van Der Giessen, W. J., De Feyter, P. J., Van Der Steen, A. F. & Serruys, P. W. 2008. Strain distribution over plaques in human coronary arteries relates to shear stress. Am J Physiol Heart Circ Physiol, 295, H1608-14.

GIMIAS. 2015. Graphical Interface for Medical Image Analysis and Simulation [Online]. Available: http://www.gimias.org/.

Go, A. S., Mozaffarian, D., Roger, V. L., Benjamin, E. J., Berry, J. D., Borden, W. B., Bravata, D. M., Dai, S., Ford, E. S., Fox, C. S., Franco, S., Fullerton, H. J., Gillespie, C., Hailpern, S. M., Heit, J. A., Howard, V. J., Huffman, M. D., Kissela, B. M., Kittner, S. J., Lackland, D. T., Lichtman, J. H., Lisabeth, L. D., Magid, D., Marcus, G. M., Marelli, A., Matchar, D. B., Mcguire, D. K., Mohler, E. R., Moy, C. S., Mussolino, M. E., Nichol, G., Paynter, N. P., Schreiner, P. J., Sorlie, P. D., Stein, J., Turan, T. N., Virani, S. S., Wong, N. D., Woo, D., Turner, M. B., American Heart Association Statistics, C. & Stroke Statistics, S. 2013. Heart disease and stroke statistics--2013 update: a report from the American Heart Association. Circulation, 127, e6-e245.

Gonzalo, N., Escaned, J., Alfonso, F., Nolte, C., Rodriguez, V., Jimenez-Quevedo, P., Banuelos, C., Fernandez-Ortiz, A., Garcia, E., Hernandez-Antolin, R. & Macaya, C. 2012. Morphometric assessment of coronary stenosis relevance with optical coherence tomography: a comparison with fractional flow reserve and intravascular ultrasound. J Am Coll Cardiol, 59, 1080-9.

Gorlin, R. & Gorlin, S. G. 1951. Hydraulic formula for calculation of the area of the stenotic mitral valve, other cardiac valves, and central circulatory shunts. I. Am Heart J, 41, 1-29.

Gorlin, R. 1987. Calculations of cardiac valve stenosis: restoring an old concept for advanced applications. J Am Coll Cardiol, 10, 920-2.

Gould, K. L. 1978. Pressure-flow characteristics of coronary stenoses in unsedated dogs at rest and during coronary vasodilation. Circ Res, 43, 242-53.

Gould, K. L. 1985. Quantification of coronary artery stenosis in vivo. Circ Res, 57, 341-53.

Gould, K. L. 2009. Does coronary flow trump coronary anatomy? JACC Cardiovasc Imaging, 2, 1009-23.

Gould, K. L., Lipscomb, K. & Calvert, C. 1975. Compensatory changes of the distal coronary vascular bed during progressive coronary constriction. Circulation, 51, 1085-94.

Gould, K. L., Lipscomb, K. & Hamilton, G. W. 1974. Physiologic basis for assessing critical coronary stenosis. Instantaneous flow response and regional distribution during coronary hyperemia as measures of coronary flow reserve. Am J Cardiol, 33, 87-94.

Grattan, M. T., Hanley, F. L., Stevens, M. B. & Hoffman, J. I. 1986. Transmural coronary flow reserve patterns in dogs. Am J Physiol, 250, H276-83.

Green, N. E., Chen, S. Y., Messenger, J. C., Groves, B. M. & Carroll, J. D. 2004. Three-dimensional vascular angiography. Curr Probl Cardiol, 29, 104-42.

Greenwood, J. P., Maredia, N., Younger, J. F., Brown, J. M., Nixon, J., Everett, C. C., Bijsterveld, P., Ridgway, J. P., Radjenovic, A., Dickinson, C. J., Ball, S. G. & Plein, S. 2012. Cardiovascular magnetic resonance and single-photon emission computed tomography for diagnosis of coronary heart disease (CE-MARC): a prospective trial. Lancet, 379, 453-60.

Hacker, M., Jakobs, T., Matthiesen, F., Vollmar, C., Nikolaou, K., Becker, C., Knez, A., Pfluger, T., Reiser, M., Hahn, K. & Tiling, R. 2005. Comparison of spiral multidetector CT angiography and myocardial perfusion imaging in the noninvasive detection of functionally relevant coronary artery lesions: first clinical experiences. J Nucl Med, 46, 1294-300.

Hamon, M., Fau, G., Nee, G., Ehtisham, J. & Morello, R. 2010. Meta-analysis of the diagnostic performance of stress perfusion cardiovascular magnetic resonance for detection of coronary artery disease. J Cardiovasc Magn Reson, 12, 29.

Hanley, F. L., Messina, L. M., Grattan, M. T. & Hoffman, I. E. 1984. The effect of coronary inflow pressure on coronary vascular resistance in the isolated dog heart. Circ Res, 54, 760-72.

Harper, R. & Reeves, B. 1999. Reporting of precision of estimates for diagnostic accuracy: a review. BMJ, 318, 1322-3.

Hartley, C. J. 1989. Review of intracoronary Doppler catheters. Int J Card Imaging, 4, 159-68.

Hausleiter, J., Meyer, T., Hermann, F., Hadamitzky, M., Krebs, M., Gerber, T. C., Mccollough, C., Martinoff, S., Kastrati, A., Schomig, A. & Achenbach, S. 2009. Estimated radiation dose associated with cardiac CT angiography. JAMA, 301, 500-7.

Health Innovation Challenge Fund | Wellcome Trust [Online, accessed July 2015]. Available: http://www.wellcome.ac.uk/Funding/Innovations/Funded-projects/Health-Innovation-Challenge-Fund/index.htm.

Heijenbrok-Kal, M. H., Fleischmann, K. E. & Hunink, M. G. 2007. Stress echocardiography, stress single-photon-emission computed tomography and electron beam computed tomography for the assessment of coronary artery disease: a meta-analysis of diagnostic performance. Am Heart J, 154, 415-23.

Heusch, G. 2010. Adenosine and maximum coronary vasodilation in humans: myth and misconceptions in the assessment of coronary reserve. Basic Res Cardiol, 105, 1-5.

Higgins, J. P., Williams, G., Nagel, J. S. & Higgins, J. A. 2006. Left bundle-branch block artifact on single photon emission computed tomography with technetium Tc 99m (Tc-99m) agents: mechanisms and a method to decrease false-positive interpretations. Am Heart J, 152, 619-26.

Hoaglin, D. C. & Iglewicz, B. 1987. Fine Tuning Some Resistant Rules for Outlier Labelling. Journal of American Statistical Association, 82, 1147-1149.

Hoaglin, D. C., Iglewicz, B. & Tukey, J. W. 1986. Performance od Some Resitant Rules for Outlier Labelling. Journal of American Statistical Association, 81, 991-999.

Hoffman, J. I. 2000. Problems of coronary flow reserve. Ann Biomed Eng, 28, 884-96.

Horisaki, T. K., O. Imai, S. Inada, T. Suzuki, T. Iinuma, K. Sugiura, H. Bakker, N. Melman, N. 2008b. Feasibility evaluation of dual axis rotational angiography (XperSwing) in the diagnosis of coronary artery disease. MEDICAMUNDI, 52.

Hou, Y., Ma, Y., Fan, W., Wang, Y., Yu, M., Vembar, M. & Guo, Q. 2013. Diagnostic accuracy of low-dose 256-slice multi-detector coronary CT angiography using iterative reconstruction in patients with suspected coronary artery disease. Eur Radiol.

http://vph-portal.eu [Online]. [Accessed July 2015].

Imran, M. B., Palinkas, A. & Picano, E. 2003. Head-to-head comparison of dipyridamole echocardiography and stress perfusion scintigraphy for the detection of coronary artery disease: a meta-analysis. Comparison between stress echo and scintigraphy. Int J Cardiovasc Imaging, 19, 23-8.

Jaarsma, C., Leiner, T., Bekkers, S. C., Crijns, H. J., Wildberger, J. E., Nagel, E., Nelemans, P. J. & Schalla, S. 2012. Diagnostic performance of noninvasive myocardial perfusion imaging using single-photon emission computed tomography, cardiac magnetic resonance, and positron emission tomography imaging for the detection of obstructive coronary artery disease: a meta-analysis. J Am Coll Cardiol, 59, 1719-28.

Janne D'othee, B., Siebert, U., Cury, R., Jadvar, H., Dunn, E. J. & Hoffmann, U. 2008. A systematic review on diagnostic accuracy of CT-based detection of significant coronary artery disease. Eur J Radiol, 65, 449-61.

Jeays, A. D., Lawford, P. V., Gillott, R., Spencer, P., Barber, D. C., Bardhan, K. D. & Hose, D. R. 2007. Characterisation of the haemodynamics of the superior mesenteric artery. J Biomech, 40, 1916-26.

Jeremias, A., Maehara, A., Genereux, P., Asrress, K. N., Berry, C., De Bruyne, B., Davies, J. E., Escaned, J., Fearon, W. F., Gould, K. L., Johnson, N. P., Kirtane, A. J., Koo, B. K., Marques, K. M., Nijjer, S., Oldroyd, K. G., Petraco, R., Piek, J. J., Pijls, N. H., Redwood, S., Siebes, M., Spaan, J. A., Van 'T Veer, M., Mintz, G. S. & Stone, G. W. 2014. Multicenter core laboratory comparison of the instantaneous wave-free ratio and resting Pd/Pa with fractional flow reserve: the RESOLVE study. J Am Coll Cardiol, 63, 1253-61.

Johnson, N. P., Johnson, D. T., Kirkeeide, R. L., Berry, C., De Bruyne, B., Fearon, W. F., Oldroyd, K. G., Pijls, N. H. & Gould, K. L. 2015. Repeatability of Fractional Flow Reserve Despite Variations in Systemic and Coronary Hemodynamics. JACC Cardiovasc Interv, 8, 1018-27.

Johnson, N. P., Kirkeeide, R. L., Asrress, K. N., Fearon, W. F., Lockie, T., Marques, K. M., Pyxaras, S. A., Rolandi, M. C., Van 'T Veer, M., De Bruyne, B., Piek, J. J., Pijls, N. H., Redwood, S., Siebes, M., Spaan, J. A. & Gould, K. L. 2013. Does the instantaneous wave-free ratio approximate the fractional flow reserve? J Am Coll Cardiol, 61, 1428-35.

Joseph, A., Ackerman, D., Talley, J. D., Johnstone, J. & Kupersmith, J. 1993. Manifestations of coronary atherosclerosis in young trauma victims--an autopsy study. J Am Coll Cardiol, 22, 459-67.

Kajiya, F., Tsujioka, K., Goto, M., Wada, Y., Chen, X. L., Nakai, M., Tadaoka, S., Hiramatsu, O., Ogasawara, Y., Mito, K. & Et Al. 1986. Functional characteristics of intramyocardial capacitance vessels during diastole in the dog. Circ Res, 58, 476-85.

Kaufmann, P. A., Gnecchi-Ruscone, T., Di Terlizzi, M., Schafers, K. P., Luscher, T. F. & Camici, P. G. 2000a. Coronary heart disease in smokers: vitamin C restores coronary microcirculatory function. Circulation, 102, 1233-8.

Kaufmann, P. A., Gnecchi-Ruscone, T., Schafers, K. P., Luscher, T. F. & Camici, P. G. 2000b. Low density lipoprotein cholesterol and coronary microvascular dysfunction in hypercholesterolemia. J Am Coll Cardiol, 36, 103-9.

Keijsers, J. M. T. 2012a. Computational modeling of hemodynamics in coronary artery bypass surgery. PhD, Eindhoven University of Technology.

Kern, M. J. 2000. Coronary physiology revisited : practical insights from the cardiac catheterization laboratory. Circulation, 101, 1344-51.

Kern, M. J., Lerman, A., Bech, J. W., De Bruyne, B., Eeckhout, E., Fearon, W. F., Higano, S. T., Lim, M. J., Meuwissen, M., Piek, J. J., Pijls, N. H., Siebes, M. & Spaan, J. A. 2006. Physiological assessment of coronary artery disease in the cardiac catheterization laboratory: a scientific statement from the American Heart Association Committee on Diagnostic and Interventional Cardiac Catheterization, Council on Clinical Cardiology. Circulation, 114, 1321-41.

Kim, H. J., Jansen, K. E. & Taylor, C. A. 2010a. Incorporating autoregulatory mechanisms of the cardiovascular system in three-dimensional finite element models of arterial blood flow. Ann Biomed Eng, 38, 2314-30.

Kim, H. J., Vignon-Clementel, I. E., Coogan, J. S., Figueroa, C. A., Jansen, K. E. & Taylor, C. A. 2010b. Patient-specific modeling of blood flow and pressure in human coronary arteries. Ann Biomed Eng, 38, 3195-209.

Kim, H. J., Vignon-Clementel, I. E., Figueroa, C. A., Ladisa, J. F., Jansen, K. E., Feinstein, J. A. & Taylor, C. A. 2009. On coupling a lumped parameter heart model and a three-dimensional finite element aorta model. Ann Biomed Eng, 37, 2153-69.

Kim, H. Y., Lee, J. W., Hong, Y. J., Lee, H. J., Hur, J., Nam, J. E., Choi, B. W. & Kim, Y. J. 2012. Dual-source coronary CT angiography in patients with high heart rates using a prospectively ECG-triggered axial mode at end-systole. Int J Cardiovasc Imaging, 28 Suppl 2, 101-7.

Kima, H. J., Vignon-Clementelb, I. E., Figueroac, C. A., Jansena, K. E. & Taylor, C. A. 2010. Developing computational methods for three-dimensional finite element simulations of coronary blood flow. 46, 514–525.

Knaapen, P., Camici, P. G., Marques, K. M., Nijveldt, R., Bax, J. J., Westerhof, N., Götte, M. J. W., Jerosch-Herold, M., Schelbert, H. R., Lammertsma, A. A. & Van Rossum, A. C. 2009. Coronary microvascular resistance: methods for its quantification in humans. Basic Res Cardiol, 104, 485-98.

Knaapen, P., Germans, T., Camici, P. G., Rimoldi, O. E., Ten Cate, F. J., Ten Berg, J. M., Dijkmans, P. A., Boellaard, R., Van Dockum, W. G., Gotte, M. J., Twisk, J. W., Van Rossum, A. C., Lammertsma, A. A. & Visser, F. C. 2008. Determinants of coronary microvascular dysfunction in symptomatic hypertrophic cardiomyopathy. Am J Physiol Heart Circ Physiol, 294, H986-93.

Koo, B. K., Erglis, A., Doh, J. H., Daniels, D. V., Jegere, S., Kim, H. S., Dunning, A., Defrance, T., Lansky, A., Leipsic, J. & Min, J. K. 2011a. Diagnosis of ischemia-causing coronary stenoses by noninvasive fractional flow reserve computed from coronary computed tomographic angiograms. Results from the prospective multicenter DISCOVER-FLOW (Diagnosis of Ischemia-Causing Stenoses Obtained Via Noninvasive Fractional Flow Reserve) study. J Am Coll Cardiol, 58, 1989-97.

Koo, B. K., Yang, H. M., Doh, J. H., Choe, H., Lee, S. Y., Yoon, C. H., Cho, Y. K., Nam, C. W., Hur, S. H., Lim, H. S., Yoon, M. H., Park, K. W., Na, S. H., Youn, T. J., Chung, W. Y., Ma, S., Park, S. K., Kim, H. S. & Tahk, S. J. 2011. Optimal intravascular ultrasound criteria and their accuracy for defining the functional significance of intermediate coronary stenoses of different locations. JACC Cardiovasc Interv, 4, 803-11.

Kousera, C. A., Nijjer, S., Torii, R., Petraco, R., Sen, S., Foin, N., Hughes, A. D., Francis, D. P., Xu, X. Y. & Davies, J. E. 2014. Patient-specific coronary stenoses can be modeled using a combination of OCT and flow velocities to accurately predict hyperemic pressure gradients. IEEE Trans Biomed Eng, 61, 1902-13.

Kroon, W., Huberts, W., Bosboom, M. & Van De Vosse, F. 2012. A numerical method of reduced complexity for simulating vascular hemodynamics using coupled 0D lumped and 1D wave propagation models. Comput Math Methods Med, 2012, 156094.

Kuruvilla, S. & Kramer, C. M. 2013. Coronary microvascular dysfunction in women: an overview of diagnostic strategies. Expert Rev Cardiovasc Ther, 11, 1515-25.

Kwok, Y., Kim, C., Grady, D., Segal, M. & Redberg, R. 1999. Meta-analysis of exercise testing to detect coronary artery disease in women. Am J Cardiol, 83, 660-6.

Ladisa, J. F., Jr., Guler, I., Olson, L. E., Hettrick, D. A., Kersten, J. R., Warltier, D. C. & Pagel, P. S. 2003. Three-dimensional computational fluid dynamics modeling of alterations in coronary wall shear stress produced by stent implantation. Ann Biomed Eng, 31, 972-80.

Ladisa, J. F., Jr., Olson, L. E., Molthen, R. C., Hettrick, D. A., Pratt, P. F., Hardel, M. D., Kersten, J. R., Warltier, D. C. & Pagel, P. S. 2005. Alterations in wall shear stress predict sites of neointimal hyperplasia after stent implantation in rabbit iliac arteries. Am J Physiol Heart Circ Physiol, 288, H2465-75.

Lagana, K., Balossino, R., Migliavacca, F., Pennati, G., Bove, E. L., De Leval, M. R. & Dubini, G. 2005. Multiscale modeling of the cardiovascular system: application to the study of pulmonary and coronary perfusions in the univentricular circulation. J Biomech, 38, 1129-41.

Landes, G. 1943. Einige untersuchungen an elektrischen analogieschaltungen zum kreitslaufsystem. Zeitschrift Fur Biologie, 101, 418-429.

Legrand, V., Mancini, G. B., Bates, E. R., Hodgson, J. M., Gross, M. D. & Vogel, R. A. 1986. Comparative study of coronary flow reserve, coronary anatomy and results of radionuclide exercise tests in patients with coronary artery disease. J Am Coll Cardiol, 8, 1022-32.

Li, J., Elrashidi, M. Y., Flammer, A. J., Lennon, R. J., Bell, M. R., Holmes, D. R., Bresnahan, J. F., Rihal, C. S., Lerman, L. O. & Lerman, A. 2013. Long-term outcomes of fractional flow reserve-guided vs. angiography-guided percutaneous coronary intervention in contemporary practice. Eur Heart J, 34, 1375-83.

Liao, R., Luc, D., Sun, Y. & Kirchberg, K. 2010. 3-D reconstruction of the coronary artery tree from multiple views of a rotational X-ray angiography. Int J Cardiovasc Imaging, 26, 733-49.

Libby, P. 2001. Current concepts of the pathogenesis of the acute coronary syndromes. Circulation, 104, 365-72.

Logan, S. E. 1975. On the fluid mechanics of human coronary artery stenosis. IEEE Trans Biomed Eng, 22, 327-34.

Löhner, R. 2008. Applied Computational Fluid Dynamics Techniques: An Introduction Based on Finite Element Methods, Wiley.

Loria, C. M., Liu, K., Lewis, C. E., Hulley, S. B., Sidney, S., Schreiner, P. J., Williams, O. D., Bild, D. E. & Detrano, R. 2007. Early adult risk factor levels and subsequent coronary artery calcification: the CARDIA Study. J Am Coll Cardiol, 49, 2013-20.

Lucas, C. L. 1984. Fluid mechanics of the pulmonary circulation. Crit Rev Biomed Eng, 10, 317-93.

Ludman. P, F. 2014. BCIS Audit Returns Adult Interventional Procedures Janurary 2013 to December 2013. British Cardiovascular Interventional Society.

Lungu, A., Wild, J. M., Capener, D., Kiely, D. G., Swift, A. J. & Hose, D. R. 2014. MRI model-based non-invasive differential diagnosis in pulmonary hypertension. J Biomech, 47, 2941-7.

Maddux, J. T., Wink, O., Messenger, J. C., Groves, B. M., Liao, R., Strzelczyk, J., Chen, S. Y. & Carroll, J. D. 2004. Randomized study of the safety and clinical utility of rotational angiography versus standard angiography in the diagnosis of coronary artery disease. Catheter Cardiovasc Interv, 62, 167-74.

Maier, W., Mini, O., Antoni, J., Wischnewsky, M. B. & Meier, B. 2001. ABC stenosis morphology classification and outcome of coronary angioplasty: reassessment with computing techniques. Circulation, 103, 1225-31.

Marcassa, C., Bax, J. J., Bengel, F., Hesse, B., Petersen, C. L., Reyes, E., Underwood, R., European Council Of Nuclear, C., European Society Of Cardiology Working, G. & European Association Of Nuclear Medicine Cardiovascular, C. 2008. Clinical value, cost-effectiveness, and safety of myocardial perfusion scintigraphy: a position statement. Eur Heart J, 29, 557-63.

Marie, P. Y., Danchin, N., Durand, J. F., Feldmann, L., Grentzinger, A., Olivier, P., Karcher, G., Juilliere, Y., Virion, J. M., Beurrier, D. & Et Al. 1995. Long-term prediction of major ischemic events by exercise thallium-201 single-photon emission computed tomography. Incremental prognostic value compared with clinical, exercise testing, catheterization and radionuclide angiographic data. J Am Coll Cardiol, 26, 879-86.

Maron, B. J., Wolfson, J. K., Epstein, S. E. & Roberts, W. C. 1986. Intramural ("small vessel") coronary artery disease in hypertrophic cardiomyopathy. J Am Coll Cardiol, 8, 545-57.

Martufi, G. & Christian Gasser, T. 2013. Review: the role of biomechanical modeling in the rupture risk assessment for abdominal aortic aneurysms. J Biomech Eng, 135, 021010.

Mc Ardle, B. A., Dowsley, T. F., Dekemp, R. A., Wells, G. A. & Beanlands, R. S. 2012. Does rubidium-82 PET have superior accuracy to SPECT perfusion imaging for the diagnosis of obstructive coronary disease?: A systematic review and meta-analysis. J Am Coll Cardiol, 60, 1828-37.

Mcginn, A. L., White, C. W. & Wilson, R. F. 1990. Interstudy variability of coronary flow reserve. Influence of heart rate, arterial pressure, and ventricular preload. Circulation, 81, 1319-30.

Meijboom, W. B., Meijs, M. F., Schuijf, J. D., Cramer, M. J., Mollet, N. R., Van Mieghem, C. A., Nieman, K., Van Werkhoven, J. M., Pundziute, G., Weustink, A. C., De Vos, A. M., Pugliese, F., Rensing, B., Jukema, J. W., Bax, J. J., Prokop, M., Doevendans, P. A., Hunink, M. G., Krestin, G. P. & De Feyter, P. J. 2008a. Diagnostic accuracy of 64-slice computed tomography coronary angiography: a prospective, multicenter, multivendor study. J Am Coll Cardiol, 52, 2135-44.

Meijboom, W. B., Van Mieghem, C. A., Van Pelt, N., Weustink, A., Pugliese, F., Mollet, N. R., Boersma, E., Regar, E., Van Geuns, R. J., De Jaegere, P. J., Serruys, P. W., Krestin, G. P. & De Feyter, P. J. 2008b. Comprehensive assessment of coronary artery stenoses: computed tomography coronary angiography versus conventional coronary angiography and correlation with fractional flow reserve in patients with stable angina. J Am Coll Cardiol, 52, 636-43.

Meuwissen, M., Chamuleau, S. A., Siebes, M., De Winter, R. J., Koch, K. T., Dijksman, L. M., Van Den Berg, A. J., Tijssen, J. G., Spaan, J. A. & Piek, J. J. 2008. The prognostic value of combined intracoronary pressure and blood flow velocity measurements after deferral of percutaneous coronary intervention. Catheter Cardiovasc Interv, 71, 291-7.

Meuwissen, M., Chamuleau, S. A., Siebes, M., Schotborgh, C. E., Koch, K. T., De Winter, R. J., Bax, M., De Jong, A., Spaan, J. A. & Piek, J. J. 2001. Role of variability in microvascular resistance on fractional flow reserve and coronary blood flow velocity reserve in intermediate coronary lesions. Circulation, 103, 184-7.

Meuwissen, M., Siebes, M., Chamuleau, S. A., Van Eck-Smit, B. L., Koch, K. T., De Winter, R. J., Tijssen, J. G., Spaan, J. A. & Piek, J. J. 2002. Hyperemic stenosis resistance index for evaluation of functional coronary lesion severity. Circulation, 106, 441-6.

Migliavacca, F., Balossino, R., Pennati, G., Dubini, G., Hsia, T. Y., De Leval, M. R. & Bove, E. L. 2006. Multiscale modelling in biofluidynamics: application to reconstructive paediatric cardiac surgery. J Biomech, 39, 1010-20.

Miller, D. D., Donohue, T. J., Younis, L. T., Bach, R. G., Aguirre, F. V., Wittry, M. D., Goodgold, H. M., Chaitman, B. R. & Kern, M. J. 1994. Correlation of pharmacological 99mTc-sestamibi myocardial perfusion imaging with poststenotic coronary flow reserve in patients with angiographically intermediate coronary artery stenoses. Circulation, 89, 2150-60.

Miller, J. M., Rochitte, C. E., Dewey, M., Arbab-Zadeh, A., Niinuma, H., Gottlieb, I., Paul, N., Clouse, M. E., Shapiro, E. P., Hoe, J., Lardo, A. C., Bush, D. E., De Roos, A., Cox, C., Brinker, J. & Lima, J. A. 2008. Diagnostic performance of coronary angiography by 64-row CT. N Engl J Med, 359, 2324-36.

Min, J. K., Berman, D. S., Budoff, M. J., Jaffer, F. A., Leipsic, J., Leon, M. B., Mancini, G. B., Mauri, L., Schwartz, R. S. & Shaw, L. J. 2011. Rationale and design of the DeFACTO (Determination of Fractional Flow Reserve by Anatomic Computed Tomographic AngiOgraphy) study. J Cardiovasc Comput Tomogr, 5, 301-9.

Min, J. K., Berman, D. S., Dunning, A., Achenbach, S., Al-Mallah, M., Budoff, M. J., Cademartiri, F., Callister, T. Q., Chang, H. J., Cheng, V., Chinnaiyan, K., Chow, B. J., Cury, R., Delago, A., Feuchtner, G., Hadamitzky, M., Hausleiter, J., Kaufmann, P., Karlsberg, R. P., Kim, Y. J., Leipsic, J., Lin, F. Y., Maffei, E., Plank, F., Raff, G., Villines, T., Labounty, T. M. & Shaw, L. J. 2012. All-cause mortality benefit of coronary revascularization vs. medical therapy in patients without known coronary artery disease undergoing coronary computed tomographic angiography: results from CONFIRM (COronary CT Angiography EvaluatioN For Clinical Outcomes: An InteRnational Multicenter Registry). Eur Heart J, 33, 3088-97.

Min, J. K., Leipsic, J., Pencina, M. J., Berman, D. S., Koo, B. K., Van Mieghem, C., Erglis, A., Lin, F. Y., Dunning, A. M., Apruzzese, P., Budoff, M. J., Cole, J. H., Jaffer, F. A., Leon, M. B., Malpeso, J., Mancini, G. B., Park, S. J., Schwartz, R. S., Shaw, L. J. & Mauri, L. 2012. Diagnostic accuracy of fractional flow reserve from anatomic CT angiography. JAMA, 308, 1237-45.

Min, J. K., Shaw, L. J. & Berman, D. S. 2010. The present state of coronary computed tomography angiography a process in evolution. J Am Coll Cardiol, 55, 957-65.

Mintz, G. S., Nissen, S. E., Anderson, W. D., Bailey, S. R., Erbel, R., Fitzgerald, P. J., Pinto, F. J., Rosenfield, K., Siegel, R. J., Tuzcu, E. M. & Yock, P. G. 2001. American College of Cardiology Clinical Expert Consensus Document on Standards for Acquisition, Measurement and Reporting of Intravascular Ultrasound Studies (IVUS). A report of the American College of Cardiology Task Force on Clinical Expert Consensus Documents. J Am Coll Cardiol, 37, 1478-92.

Mintz, G. S., Popma, J. J., Pichard, A. D., Kent, K. M., Satler, L. F., Chuang, Y. C., Defalco, R. A. & Leon, M. B. 1996. Limitations of angiography in the assessment of plaque distribution in coronary artery disease: a systematic study of target lesion eccentricity in 1446 lesions. Circulation, 93, 924-31.

Montalescot, G., Sechtem, U., Achenbach, S., Andreotti, F., Arden, C., Budaj, A., Bugiardini, R., Crea, F., Cuisset, T., Di Mario, C., Ferreira, J. R., Gersh, B. J., Gitt, A. K., Hulot, J. S., Marx, N., Opie, L. H., Pfisterer, M., Prescott, E., Ruschitzka, F., Sabate, M., Senior, R., Taggart, D. P., Van Der Wall, E. E., Vrints, C. J., Zamorano, J. L., Baumgartner, H., Bax, J. J., Bueno, H., Dean, V.,

Deaton, C., Erol, C., Fagard, R., Ferrari, R., Hasdai, D., Hoes, A. W., Kirchhof, P., Knuuti, J., Kolh, P., Lancellotti, P., Linhart, A., Nihoyannopoulos, P., Piepoli, M. F., Ponikowski, P., Sirnes, P. A., Tamargo, J. L., Tendera, M., Torbicki, A., Wijns, W., Windecker, S., Valgimigli, M., Claeys, M. J., Donner-Banzhoff, N., Frank, H., Funck-Brentano, C., Gaemperli, O., Gonzalez-Juanatey, J. R., Hamilos, M., Husted, S., James, S. K., Kervinen, K., Kristensen, S. D., Maggioni, A. P., Pries, A. R., Romeo, F., Ryden, L., Simoons, M. L., Steg, P. G., Timmis, A. & Yildirir, A. 2013. 2013 ESC guidelines on the management of stable coronary artery disease: the Task Force on the management of stable coronary artery disease of the European Society of Cardiology. Eur Heart J, 34, 2949-3003.

Morise, A. P. & Diamond, G. A. 1995. Comparison of the sensitivity and specificity of exercise electrocardiography in biased and unbiased populations of men and women. Am Heart J, 130, 741-7.

Morlacchi, S. & Migliavacca, F. 2013. Modeling Stented Coronary Arteries: Where We are, Where to Go. Ann Biomed Eng, 41, 1428-44.

Morris, P. D., Ryan, D., Morton, A. C., Lycett, R., Lawford, P. V., Hose, D. R. & Gunn, J. P. 2013. Virtual Fractional Flow Reserve From Coronary Angiography: Modeling the Significance of Coronary Lesions: Results From the VIRTU-1 (VIRTUal Fractional Flow Reserve From Coronary Angiography) Study. JACC Cardiovasc Interv, 6, 149-57.

Morris, P. D., Taylor, J., Boutong, S., Brett, S., Louis, A., Heppenstall, J., Morton, A. C. & Gunn, J. P. 2015a. When is rotational angiography superior to conventional single-plane angiography for planning coronary angioplasty? Catheter Cardiovasc Interv.

Morris, P. D., Van De Vosse, F. N., Lawford, P. V., Hose, D. R. & Gunn, J. P. 2015. "Virtual" (Computed) Fractional Flow ReserveCurrent Challenges and Limitations. J Am Coll Cardiol Intv.

MORRIS, P., WARRINER, D. & MORTON, A. 2015a. Eureka: Cardiovascular Medicine, London, JP Medical Ltd.

Mosher, P., Ross, J., Jr., Mcfate, P. A. & Shaw, R. F. 1964. Control of Coronary Blood Flow by an Autoregulatory Mechanism. Circ Res, 14, 250-9.

Mowatt, G., Cummins, E., Waugh, N., Walker, S., Cook, J., Jia, X., Hillis, G. S. & Fraser, C. 2008. Systematic review of the clinical effectiveness and cost-effectiveness of 64-slice or higher computed tomography angiography as an alternative to invasive coronary angiography in the investigation of coronary artery disease. Health Technol Assess, 12, iii-iv, ix-143.

Mozaffarian, D., Benjamin, E. J., Go, A. S., Arnett, D. K., Blaha, M. J., Cushman, M., De Ferranti, S., Despres, J. P., Fullerton, H. J., Howard, V. J., Huffman, M. D., Judd, S. E., Kissela, B. M., Lackland, D. T., Lichtman, J. H., Lisabeth, L. D., Liu, S., Mackey, R. H., Matchar, D. B., Mcguire, D. K., Mohler, E. R., 3rd, Moy, C. S., Muntner, P., Mussolino, M. E., Nasir, K., Neumar, R. W., Nichol, G., Palaniappan, L., Pandey, D. K., Reeves, M. J., Rodriguez, C. J., Sorlie, P. D., Stein, J., Towfighi, A., Turan, T. N., Virani, S. S., Willey, J. Z., Woo, D., Yeh, R. W. & Turner, M. B. 2015. Heart disease and stroke statistics--2015 update: a report from the American Heart Association. Circulation, 131, e29-322.

Murray, C. D. 1926. The Physiological Principle of Minimum Work: I. The Vascular System and the Cost of Blood Volume. Proc Natl Acad Sci U S A, 12, 207-14.

Murray, C. J., Vos, T., Lozano, R., Naghavi, M., Flaxman, A. D., Michaud, C., Ezzati, M., Shibuya, K., Salomon, J. A., Abdalla, S., Aboyans, V., Abraham, J., Ackerman, I., Aggarwal, R., Ahn, S. Y., Ali, M. K., Alvarado, M., Anderson, H. R., Anderson, L. M., Andrews, K. G., Atkinson, C., Baddour, L. M., Bahalim, A. N., Barker-Collo, S., Barrero, L. H., Bartels, D. H., Basanez, M. G., Baxter, A., Bell, M. L., Benjamin, E. J., Bennett, D., Bernabe, E., Bhalla, K., Bhandari, B., Bikbov, B., Bin Abdulhak, A., Birbeck, G., Black, J. A., Blencowe, H., Blore, J. D., Blyth, F., Bolliger, I., Bonaventure, A., Boufous, S., Bourne, R., Boussinesq, M., Braithwaite, T., Brayne, C., Bridgett, L., Brooker, S., Brooks, P., Brugha, T. S., Bryan-Hancock, C., Bucello, C., Buchbinder, R., Buckle, G., Budke, C. M., Burch, M., Burney, P., Burstein, R., Calabria, B., Campbell, B., Canter, C. E., Carabin, H., Carapetis, J., Carmona, L., Cella, C., Charlson, F., Chen, H., Cheng, A. T., Chou, D., Chugh, S. S., Coffeng, L. E., Colan, S. D., Colquhoun, S., Colson, K. E., Condon, J., Connor, M. D., Cooper, L. T., Corriere, M., Cortinovis, M., De Vaccaro, K. C., Couser, W., Cowie, B. C., Criqui, M. H., Cross, M., Dabhadkar, K. C., Dahiya, M., Dahodwala, N., Damsere-Derry, J., Danaei, G., Davis, A., De Leo, D., Degenhardt, L., Dellavalle, R., Delossantos, A., Denenberg, J., Derrett, S., Des Jarlais, D. C., Dharmaratne, S. D., et al. 2012. Disability-adjusted life years (DALYs) for 291 diseases and injuries in 21 regions, 1990-2010: a systematic analysis for the Global Burden of Disease Study 2010. Lancet, 380, 2197-223.

Myers, J. G., Moore, J. A., Ojha, M., Johnston, K. W. & Ethier, C. R. 2001. Factors influencing blood flow patterns in the human right coronary artery. Ann Biomed Eng, 29, 109-20.

Mynard, J. P., Davidson, M. R., Penny, D. J. & Smolich, J. J. 2012. A simple, versatile valve model for use in lumped parameter and one-dimensional cardiovascular models. International Journal for Numerical Methods in Biomedical Engineering, 28, 626-641.

Nair, A., Kuban, B. D., Tuzcu, E. M., Schoenhagen, P., Nissen, S. E. & Vince, D. G. 2002. Coronary plaque classification with intravascular ultrasound radiofrequency data analysis. Circulation, 106, 2200-6.

Nakazato, R., Park, H. B., Berman, D. S., Gransar, H., Koo, B. K., Erglis, A., Lin, F. Y., Dunning, A. M., Budoff, M. J., Malpeso, J., Leipsic, J. & Min, J. K. 2013. Noninvasive fractional flow reserve derived from computed tomography angiography for coronary lesions of intermediate stenosis severity: results from the DeFACTO study. Circ Cardiovasc Imaging, 6, 881-9.

Nallamothu, B. K., Spertus, J. A., Lansky, A. J., Cohen, D. J., Jones, P. G., Kureshi, F., Dehmer, G. J., Drozda, J. P., Jr., Walsh, M. N., Brush, J. E., Jr., Koenig, G. C., Waites, T. F., Gantt, D. S., Kichura, G., Chazal, R. A., O'brien, P. K., Valentine, C. M., Rumsfeld, J. S., Reiber, J. H., Elmore, J. G., Krumholz, R. A., Weaver, W. D. & Krumholz, H. M. 2013. Comparison of clinical interpretation

with visual assessment and quantitative coronary angiography in patients undergoing percutaneous coronary intervention in contemporary practice: the Assessing Angiography (A2) project. Circulation, 127, 1793-800.

Nandalur, K. R., Dwamena, B. A., Choudhri, A. F., Nandalur, S. R., Reddy, P. & Carlos, R. C. 2008. Diagnostic performance of positron emission tomography in the detection of coronary artery disease: a meta-analysis. Acad Radiol, 15, 444-51.

National Institute for Clinical Excellence, N. I. F. H. A. C. 2015. The Pressure Wire fractional flow reserve measurement system for coronary artery disease | Advice | NICE. Nice.Nasis, A., Ko, B. S., Leung, M. C., Antonis, P. R., Nandurkar, D., Wong, D. T., Kyi, L., Cameron, J. D., Troupis, J. M., Meredith, I. T. & Seneviratne, S. K. 2013. Diagnostic accuracy of combined coronary angiography and adenosine stress myocardial perfusion imaging using 320-detector computed tomography: pilot study. Eur Radiol, 23, 1812-21.

Nichols, W. W., O'rourke, M. F. & Vlachopoulos, C. 2011. Theoretical, Experimental and Clinical Principles, CRC Press.

Nissen, S. E. & Yock, P. 2001. Intravascular ultrasound: novel pathophysiological insights and current clinical applications. Circulation, 103, 604-16.

Norgaard, B. L., Leipsic, J., Gaur, S., Seneviratne, S., Ko, B. S., Ito, H., Jensen, J. M., Mauri, L., De Bruyne, B., Bezerra, H., Osawa, K., Marwan, M., Naber, C., Erglis, A., Park, S. J., Christiansen, E. H., Kaltoft, A., Lassen, J. F., Botker, H. E., Achenbach, S. & Group, N. X. T. T. S. 2014. Diagnostic performance of noninvasive fractional flow reserve derived from coronary computed tomography angiography in suspected coronary artery disease: the NXT trial (Analysis of Coronary Blood Flow Using CT Angiography: Next Steps). J Am Coll Cardiol, 63, 1145-55.

O'rourke, M. F. 1982. Vascular impedance in studies of arterial and cardiac function. Physiol Rev, 62, 570-623.

Papafaklis, M. I., Muramatsu, T., Ishibashi, Y., Lakkas, L. S., Nakatani, S., Bourantas, C. V., Ligthart, J., Onuma, Y., Echavarria-Pinto, M., Tsirka, G., Kotsia, A., Nikas, D. N., Mogabgab, O., Van Geuns, R. J., Naka, K. K., Fotiadis, D. I., Brilakis, E. S., Garcia-Garcia, H. M., Escaned, J., Zijlstra, F., Michalis, L. K. & Serruys, P. W. 2014. Fast virtual functional assessment of intermediate coronary lesions using routine angiographic data and blood flow simulation in humans: comparison with pressure wire - fractional flow reserve. EuroIntervention, 10, 574-83.

Patel, M. R., Peterson, E. D., Dai, D., Brennan, J. M., Redberg, R. F., Anderson, H. V., Brindis, R. G. & Douglas, P. S. 2010. Low diagnostic yield of elective coronary angiography. N Engl J Med, 362, 886-95.

Pennell, D. J., Sechtem, U. P., Higgins, C. B., Manning, W. J., Pohost, G. M., Rademakers, F. E., Van Rossum, A. C., Shaw, L. J., Yucel, E. K., European Society Of, C. & Soceity For Cardiovascular Magnetic, R. 2004. Clinical indications for cardiovascular magnetic resonance (CMR): Consensus Panel report. J Cardiovasc Magn Reson, 6, 727-65.

Peters, R. J. G., Kok, W. E. M., Mario, C. D., Serruys, P. W., Bär, F. W. H. M., Pasterkamp, G., Borst, C., Kamp, O., Bronzwaer, J. G. F., Visser, C. A., Piek, J. J., Panday, R. N., Jaarsma, W., Savalle, L., Bom, N. & Group, F. T. P. S. 1997. Prediction of Restenosis After Coronary Balloon Angioplasty.

Petraco, R., Escaned, J., Sen, S., Nijjer, S., Asrress, K. N., Echavarria-Pinto, M., Lockie, T., Khawaja, M. Z., Cuevas, C., Foin, N., Broyd, C., Foale, R. A., Hadjiloizou, N., Malik, I. S., Mikhail, G. W., Sethi, A., Kaprielian, R., Baker, C. S., Lefroy, D., Bellamy, M., Al-Bustami, M., Khan, M. A., Hughes, A. D., Francis, D. P., Mayet, J., Di Mario, C., Redwood, S. & Davies, J. E. 2012. Classification performance of instantaneous wave-free ratio (iFR) and fractional flow reserve in a clinical population of intermediate coronary stenoses: results of the ADVISE registry. EuroIntervention.

Petraco, R., Park, J. J., Sen, S., Nijjer, S. S., Malik, I. S., Echavarria-Pinto, M., Asrress, K. N., Nam, C. W., Macias, E., Foale, R. A., Sethi, A., Mikhail, G. W., Kaprielian, R., Baker, C. S., Lefroy, D., Bellamy, M., Al-Bustami, M., Khan, M. A., Gonzalo, N., Hughes, A. D., Francis, D. P., Mayet, J., Di Mario, C., Redwood, S., Escaned, J., Koo, B. K. & Davies, J. E. 2013a. Hybrid iFR-FFR decision-making strategy: implications for enhancing universal adoption of physiology-guided coronary revascularisation. EuroIntervention, 8, 1157-65.

Petraco, R., Sen, S., Nijjer, S., Echavarria-Pinto, M., Escaned, J., Francis, D. P. & Davies, J. E. 2013b. Fractional flow reserve-guided revascularization: practical implications of a diagnostic gray zone and measurement variability on clinical decisions. JACC Cardiovasc Interv, 6, 222-5.

Picano, E., Molinaro, S. & Pasanisi, E. 2008. The diagnostic accuracy of pharmacological stress echocardiography for the assessment of coronary artery disease: a meta-analysis. Cardiovasc Ultrasound, 6, 30.

Pijls, N. H., De Bruyne, B., Peels, K., Van Der Voort, P. H., Bonnier, H. J., Bartunek, J. K. J. J. & Koolen, J. J. 1996. Measurement of fractional flow reserve to assess the functional severity of coronary-artery stenoses. N Engl J Med, 334, 1703-8.

Pijls, N. H., De Bruyne, B., Smith, L., Aarnoudse, W., Barbato, E., Bartunek, J., Bech, G. J. & Van De Vosse, F. 2002. Coronary thermodilution to assess flow reserve: validation in humans. Circulation, 105, 2482-6.

Pijls, N. H., Fearon, W. F., Tonino, P. A., Siebert, U., Ikeno, F., Bornschein, B., Van't Veer, M., Klauss, V., Manoharan, G., Engstrom, T., Oldroyd, K. G., Ver Lee, P. N., Maccarthy, P. A. & De Bruyne, B. 2010. Fractional flow reserve versus angiography for guiding percutaneous coronary intervention in patients with multivessel coronary artery disease: 2-year follow-up of the FAME (Fractional Flow Reserve Versus Angiography for Multivessel Evaluation) study. J Am Coll Cardiol, 56, 177-84.

Pijls, N. H., Kern, M. J., Yock, P. G. & De Bruyne, B. 2000. Practice and potential pitfalls of coronary pressure measurement. Catheter Cardiovasc Interv, 49, 1-16.

Pijls, N. H., Van Gelder, B., Van Der Voort, P., Peels, K., Bracke, F. A., Bonnier, H. J. & El Gamal, M. I. 1995. Fractional flow reserve. A useful index to evaluate the influence of an epicardial coronary stenosis on myocardial blood flow. Circulation, 92, 3183-93.

Pijls, N. H., Van Schaardenburgh, P., Manoharan, G., Boersma, E., Bech, J. W., Van't Veer, M., Bar, F., Hoorntje, J., Koolen, J., Wijns, W. & De Bruyne, B. 2007. Percutaneous coronary intervention of functionally nonsignificant stenosis: 5-year follow-up of the DEFER Study. J Am Coll Cardiol, 49, 2105-11.

Pijls, N. H., Van Son, J. A., Kirkeeide, R. L., De Bruyne, B. & Gould, K. L. 1993. Experimental basis of determining maximum coronary, myocardial, and collateral blood flow by pressure measurements for assessing functional stenosis severity before and after percutaneous transluminal coronary angioplasty. Circulation, 87, 1354-67.

Pitkanen, O. P., Nuutila, P., Raitakari, O. T., Ronnemaa, T., Koskinen, P. J., Iida, H., Lehtimaki, T. J., Laine, H. K., Takala, T., Viikari, J. S. & Knuuti, J. 1998. Coronary flow reserve is reduced in young men with IDDM. Diabetes, 47, 248-54.

Prati, F., Pawlowski, T., Gil, R., Labellarte, A., Gziut, A., Caradonna, E., Manzoli, A., Pappalardo, A., Burzotta, F. & Boccanelli, A. 2003. Stenting of culprit lesions in unstable angina leads to a marked reduction in plaque burden: a major role of plaque embolization? A serial intravascular ultrasound study. Circulation, 107, 2320-5.

Pryor, D. B., Shaw, L., Mccants, C. B., Lee, K. L., Mark, D. B., Harrell, F. E., Jr., Muhlbaier, L. H. & Califf, R. M. 1993. Value of the history and physical in identifying patients at increased risk for coronary artery disease. Ann Intern Med, 118, 81-90.

Pupita, G., Maseri, A., Kaski, J. C., Galassi, A. R., Gavrielides, S., Davies, G. & Crea, F. 1990. Myocardial ischemia caused by distal coronary-artery constriction in stable angina pectoris. N Engl J Med, 323, 514-20.

Raine-Fenning, N. J., Nordin, N. M., Ramnarine, K. V., Campbell, B. K., Clewes, J. S., Perkins, A. & Johnson, I. R. 2008. Determining the relationship between three-dimensional power Doppler data and true blood flow characteristics: an in-vitro flow phantom experiment. Ultrasound Obstet Gynecol, 32, 540-50.

Raman, S. V., Morford, R., Neff, M., Attar, T. T., Kukielka, G., Magorien, R. D. & Bush, C. A. 2004. Rotational X-ray coronary angiography. Catheter Cardiovasc Interv, 63, 201-7.

Rengier, F., Geisbusch, P., Schoenhagen, P., Muller-Eschner, M., Vosshenrich, R., Karmonik, C., Von Tengg-Kobligk, H. & Partovi, S. 2014. State-of-the-art aortic imaging: Part II - applications in transcatheter aortic valve replacement and endovascular aortic aneurysm repair. Vasa, 43, 6-26.

Reymond, P., Vardoulis, O. & Stergiopulos, N. 2012. Generic and patient-specific models of the arterial tree. J Clin Monit Comput, 26, 375-82.

Rigattieri, S., Ghini, A. S., Silvestri, P., Tommasino, A., Ferraiuolo, G., Palamara, A. & Loschiavo, P. 2005. A randomized comparison between rotational and standard coronary angiography. Minerva Cardioangiol, 53, 1-6.

Rioufol, G., Caignault, J. R., Finet, G., Staat, P., Bonnefoy, E., De Gevigney, G., Rossi, R. & Andre-Fouet, X. 2005. 150 microgram intracoronary adenosine bolus for accurate fractional flow reserve assessment of angiographically intermediate coronary stenosis. EuroIntervention, 1, 204-7.

Roache, P. J. 1994. Perspective - a Method for Uniform Reporting of Grid Refinement Studies. Journal of Fluids Engineering-Transactions of the Asme, 116, 405-413.

Roache, P. J. 1997. Quantification of uncertainty in computational fluid dynamics. Annual Review of Fluid Mechanics, 29, 123-160.

Rochitte, C. E., George, R. T., Chen, M. Y., Arbab-Zadeh, A., Dewey, M., Miller, J. M., Niinuma, H., Yoshioka, K., Kitagawa, K., Nakamori, S., Laham, R., Vavere, A. L., Cerci, R. J., Mehra, V. C., Nomura, C., Kofoed, K. F., Jinzaki, M., Kuribayashi, S., De Roos, A., Laule, M., Tan, S. Y., Hoe, J., Paul, N., Rybicki, F. J., Brinker, J. A., Arai, A. E., Cox, C., Clouse, M. E., Di Carli, M. F. & Lima, J. A. 2014. Computed tomography angiography and perfusion to assess coronary artery stenosis causing perfusion defects by single photon emission computed tomography: the CORE320 study. Eur Heart J, 35, 1120-30.

Rockwood, K., Song, X., Macknight, C., Bergman, H., Hogan, D. B., Mcdowell, I. & Mitnitski, A. 2005. A global clinical measure of fitness and frailty in elderly people. Cmaj, 173, 489-95.

Rodriguez, L., Anconina, J., Flachskampf, F. A., Weyman, A. E., Levine, R. A. & Thomas, J. D. 1992. Impact of finite orifice size on proximal flow convergence. Implications for Doppler quantification of valvular regurgitation. Circ Res, 70, 923-30.

Rodriguez, L., Thomas, J. D., Monterroso, V., Weyman, A. E., Harrigan, P., Mueller, L. N. & Levine, R. A. 1993. Validation of the proximal flow convergence method. Calculation of orifice area in patients with mitral stenosis. Circulation, 88, 1157-65.

Roger, V. L., Go, A. S., Lloyd-Jones, D. M., Benjamin, E. J., Berry, J. D., Borden, W. B., Bravata, D. M., Dai, S., Ford, E. S., Fox, C. S., Fullerton, H. J., Gillespie, C., Hailpern, S. M., Heit, J. A., Howard, V. J., Kissela, B. M., Kittner, S. J., Lackland, D. T., Lichtman, J. H., Lisabeth, L. D., Makuc, D. M., Marcus, G. M., Marelli, A., Matchar, D. B., Moy, C. S., Mozaffarian, D., Mussolino, M. E., Nichol, G., Paynter, N. P., Soliman, E. Z., Sorlie, P. D., Sotoodehnia, N., Turan, T. N., Virani, S. S., Wong, N. D., Woo, D. & Turner, M. B. 2012. Heart Disease and Stroke Statistics--2012 Update: A Report From the American Heart Association. Circulation, 125, e2-e220.

Rossi, A., Dharampal, A., Wragg, A., Davies, L. C., Van Geuns, R. J., Anagnostopoulos, C., Klotz, E., Kitslaar, P., Broersen, A., Mathur, A., Nieman, K., Hunink, M. G., De Feyter, P. J., Petersen, S. E. & Pugliese, F. 2014. Diagnostic performance of hyperaemic myocardial blood flow index obtained by dynamic computed tomography: does it predict functionally significant coronary lesions? Eur Heart J Cardiovasc Imaging, 15, 85-94.

Rossi, A., Merkus, D., Klotz, E., Mollet, N., De Feyter, P. J. & Krestin, G. P. 2014. Stress myocardial perfusion: imaging with multidetector CT. Radiology, 270, 25-46.

Roy, P., Steinberg, D. H., Sushinsky, S. J., Okabe, T., Pinto Slottow, T. L., Kaneshige, K., Xue, Z., Satler, L. F., Kent, K. M., Suddath, W. O., Pichard, A. D., Weissman, N. J., Lindsay, J. & Waksman, R. 2008. The potential clinical utility of intravascular ultrasound guidance in patients undergoing percutaneous coronary intervention with drug-eluting stents. Eur Heart J, 29, 1851-7.

Saltelli, A. 2002. Making best use of model evaluations to compute sensitivity indices. Physics Communications, 145, 7.

Samavat, H. & Evans, J. A. 2006. An ideal blood mimicking fluid for doppler ultrasound phantoms. J Med Phys, 31, 275-8.

Santamarina, A., Weydahl, E., Siegel, J. M., Jr. & Moore, J. E., Jr. 1998. Computational analysis of flow in a curved tube model of the coronary arteries: effects of time-varying curvature. Ann Biomed Eng, 26, 944-54.

Sant'anna, F. M., Silva, E. E., Batista, L. A., Ventura, F. M., Barrozo, C. A. & Pijls, N. H. 2007. Influence of routine assessment of fractional flow reserve on decision making during coronary interventions. Am J Cardiol, 99, 504-8.

Schrauwen, J. T. C., Coenen, A., Kurata, A., Wentzel, J. J., Van Der Steen, A. F. W., Nieman, K. & Gijsen, F. H. Functional and anatomical measures for outflow boundary conditions in atherosclerotic coronary bifurcations Computational Fluid Dynamics (CFD) in Medicine and Biology II, 2015 Portugal. Enginerring Conference International.

Schrivjer, M. Angiographic Image Analysis to Assess the Severity of Coronary Stenoses. Ph.D. 2002, University of Twente.

Schuijf, J. D., Bax, J. J., Shaw, L. J., De Roos, A., Lamb, H. J., Van Der Wall, E. E. & Wijns, W. 2006a. Meta-analysis of comparative diagnostic performance of magnetic resonance imaging and multislice computed tomography for noninvasive coronary angiography. Am Heart J, 151, 404-11.

Schuijf, J. D., Wijns, W., Jukema, J. W., Atsma, D. E., De Roos, A., Lamb, H. J., Stokkel, M. P., Dibbets-Schneider, P., Decramer, I., De Bondt, P., Van Der Wall, E. E., Vanhoenacker, P. K. & Bax, J. J. 2006b. Relationship between noninvasive coronary angiography with multi-slice computed tomography and myocardial perfusion imaging. J Am Coll Cardiol, 48, 2508-14.

Schwitter, J., Wacker, C. M., Wilke, N., Al-Saadi, N., Sauer, E., Huettle, K., Schonberg, S. O., Luchner, A., Strohm, O., Ahlstrom, H., Dill, T., Hoebel, N. & Simor, T. 2013. MR-IMPACT II: Magnetic Resonance Imaging for Myocardial Perfusion Assessment in Coronary artery disease Trial: perfusion-cardiac magnetic resonance vs. single-photon emission computed tomography for the detection of coronary artery disease: a comparative multicentre, multivendor trial. Eur Heart J, 34, 775-81.

Segur, J. A. & Oberstar, H. E. 1951. Viscosity of Glycerol and Its Aqueous Solutions. Industrial Engineering and Chemistry, 43, 2117-2120.

Sen, S., Asrress, K. N., Nijjer, S., Petraco, R., Malik, I. S., Foale, R. A., Mikhail, G. W., Foin, N., Broyd, C., Hadjiloizou, N., Sethi, A., Al-Bustami, M., Hackett, D., Khan, M. A., Khawaja, M. Z., Baker, C. S., Bellamy, M., Parker, K. H., Hughes, A. D., Francis, D. P., Mayet, J., Di Mario, C., Escaned, J., Redwood, S. & Davies, J. E. 2013. Diagnostic classification of the instantaneous wave-free ratio is equivalent to fractional flow reserve and is not improved with adenosine administration. Results of CLARIFY (Classification Accuracy of Pressure-Only Ratios Against Indices Using Flow Study). J Am Coll Cardiol, 61, 1409-20.

Sen, S., Escaned, J., Malik, I. S., Mikhail, G. W., Foale, R. A., Mila, R., Tarkin, J., Petraco, R., Broyd, C., Jabbour, R., Sethi, A., Baker, C. S., Bellamy, M., Al-Bustami, M., Hackett, D., Khan, M., Lefroy, D., Parker, K. H., Hughes, A. D., Francis, D. P., Di Mario, C., Mayet, J. & Davies, J. E. 2012. Development and validation of a new adenosine-independent index of stenosis severity from coronary wave-intensity analysis: results of the ADVISE (ADenosine Vasodilator Independent Stenosis Evaluation) study. J Am Coll Cardiol, 59, 1392-402.

Serruys, P. W., Onuma, Y., Garg, S., Sarno, G., Van Den Brand, M., Kappetein, A. P., Van Dyck, N., Mack, M., Holmes, D., Feldman, T., Morice, M. C., Colombo, A., Bass, E., Leadley, K., Dawkins, K. D., Van Es, G. A., Morel, M. A. & Mohr, F. W. 2009. Assessment of the SYNTAX score in the Syntax study. EuroIntervention, 5, 50-6.

Shapiro, S. S. & Wilk, M. B. 1965. An Analysis of Variance Test for Normality (Complete Samples). Biometrika, 52, 591-611.

Shaw, L. J. & Iskandrian, A. E. 2004. Prognostic value of gated myocardial perfusion SPECT. J Nucl Cardiol, 11, 171-85.

Shaw, L. J., Berman, D. S., Maron, D. J., Mancini, G. B., Hayes, S. W., Hartigan, P. M., Weintraub, W. S., O'rourke, R. A., Dada, M., Spertus, J. A., Chaitman, B. R., Friedman, J., Slomka, P., Heller, G. V., Germano, G., Gosselin, G., Berger, P., Kostuk, W. J., Schwartz, R. G., Knudtson, M., Veledar, E., Bates, E. R., Mccallister, B., Teo, K. K. & Boden, W. E. 2008. Optimal medical therapy with or without percutaneous coronary intervention to reduce ischemic burden: results from the Clinical Outcomes Utilizing Revascularization and Aggressive Drug Evaluation (COURAGE) trial nuclear substudy. Circulation, 117, 1283-91.

Shaw, L. J., Bugiardini, R. & Merz, C. N. 2009. Women and ischemic heart disease: evolving knowledge. J Am Coll Cardiol, 54, 1561-75.

Shaw, L. J., Hausleiter, J., Achenbach, S., Al-Mallah, M., Berman, D. S., Budoff, M. J., Cademartiri, F., Callister, T. Q., Chang, H. J., Kim, Y. J., Cheng, V. Y., Chow, B. J., Cury, R. C., Delago, A. J., Dunning, A. L., Feuchtner, G. M., Hadamitzky, M., Karlsberg, R. P., Kaufmann, P. A., Leipsic, J., Lin, F. Y., Chinnaiyan, K. M., Maffei, E., Raff, G. L., Villines, T. C., Labounty, T., Gomez, M. J., Min, J. K. & Investigators, C. R. 2012. Coronary computed tomographic angiography as a gatekeeper to invasive diagnostic and surgical procedures: results from the multicenter CONFIRM (Coronary CT Angiography Evaluation for Clinical Outcomes: an International Multicenter) registry. J Am Coll Cardiol, 60, 2103-14.

Shi, Y., Lawford, P. & Hose, R. 2011. Review of zero-D and 1-D models of blood flow in the cardiovascular system. Biomed Eng Online, 10, 33.

Shrestha, L. 2010. CFD Study on the Branch Sizes in Human Coronary Artery. MS, University of Iowa.

Siebert, U., Bornschein, B., Arvandi, M., Gothe, R., Wilke, M., De Bruyne, B., Fearon, W., Pijls, N. & Warnholtz, A. 2011a. Cost-Effectiveness And Public Health And Budget Impact Of Fractional Flow Reserve-Guided Percutaneous Coronary Intervention In Patients With Multivessel Disease In Germany Health Technology Assessment Society (HTAi) 8th Annual Meeting. Rio de Janeiro.

Siebert, U., Bornschein, B., Arvandi, M., Raffaella, M., Gothe, M. & European Clinical Expert Panel Economic Evaluation Fame Study2. Tr2-1. Cost-Effectiveness And Public Health/Budget-Impact Of Ffr-Guided Pci In Multivessel Patients In 6 European Countries - Analysis Along The Fame Trial Data. Society for Medical Decision Making (SDM) 33rd Annual meeting, 2011b Chicago.

Siebes, M., Chamuleau, S. A., Meuwissen, M., Piek, J. J. & Spaan, J. A. 2002. Influence of hemodynamic conditions on fractional flow reserve: parametric analysis of underlying model. Am J Physiol Heart Circ Physiol, 283, H1462-70.

Siebes, M., Verhoeff, B. J., Meuwissen, M., De Winter, R. J., Spaan, J. A. & Piek, J. J. 2004. Single-wire pressure and flow velocity measurement to quantify coronary stenosis hemodynamics and effects of percutaneous interventions. Circulation, 109, 756-62.

Smith, S. C., Jr., Feldman, T. E., Hirshfeld, J. W., Jr., Jacobs, A. K., Kern, M. J., King, S. B., 3rd, Morrison, D. A., O'neil, W. W., Schaff, H. V., Whitlow, P. L., Williams, D. O., Antman, E. M., Adams, C. D., Anderson, J. L., Faxon, D. P., Fuster, V., Halperin, J. L., Hiratzka, L. F., Hunt, S. A., Nishimura, R., Ornato, J. P., Page, R. L. & Riegel, B. 2006. ACC/AHA/SCAI 2005 guideline update for percutaneous coronary intervention: a report of the American College of Cardiology/American Heart Association Task Force on Practice Guidelines (ACC/AHA/SCAI Writing Committee to Update 2001 Guidelines for Percutaneous Coronary Intervention). Circulation, 113, e166-286.

Sobol, I. M. 2001. Global sensitivity indices for nonlinear mathematical models and their Monte Carlo estimates. Mathematics and Computers in Simulation, 55, 271-280.

Spaan, J. A. 1985. Coronary diastolic pressure-flow relation and zero flow pressure explained on the basis of intramyocardial compliance. Circ Res, 56, 293-309.

Spaan, J. A., Piek, J. J., Hoffman, J. I. & Siebes, M. 2006. Physiological basis of clinically used coronary hemodynamic indices. Circulation, 113, 446-55.

Steinman, D. A. 2002. Image-based computational fluid dynamics modeling in realistic arterial geometries. Ann Biomed Eng, 30, 483-97.

Stergiopoulos, K., Boden, W. E., Hartigan, P., Mobius-Winkler, S., Hambrecht, R., Hueb, W., Hardison, R. M., Abbott, J. D. & Brown, D. L. 2014. Percutaneous coronary intervention outcomes in patients with stable obstructive coronary artery disease and myocardial ischemia: a collaborative meta-analysis of contemporary randomized clinical trials. JAMA Intern Med, 174, 232-40.

Stergiopulos, N., Meister, J. J. & Westerhof, N. 1995. Evaluation of methods for estimation of total arterial compliance. Am J Physiol, 268, H1540-8.

Stergiopulos, N., Young, D. F. & Rogge, T. R. 1992. Computer simulation of arterial flow with applications to arterial and aortic stenoses. J Biomech, 25, 1477-88.

Stewart, S., Hariharan, P., Paterson, E., Burgreen, G., Reddy, V., Day, S., Giarra, M., Manning, K., Deutsch, S., Berman, M., Meyers, M. & Malinauskas, R. 2013. Results of FDA's First Interlaboratory Computational Study of a Nozzle with a Sudden Contraction and Conical Diffuser. Cardiovascular Engineering and Technology, 4.

Stone, G. W., Hodgson, J. M., Goar, F. G. S., Frey, A., Mudra, H., Sheehan, H., Linnemeier, T. J. & Investigators, F. T. C. O. W. U. T. C. 1997. Improved Procedural Results of Coronary Angioplasty With Intravascular Ultrasound–Guided Balloon Sizing.

Sun, L. J., Mi, L., Cui, M., Guo, L. J., Zhang, Y. Z., Zhang, F. C., Niu, J., Li, H. Y., Wang, G. S., Han, J. L., Gao, W., Li, D. & Li, C. P. 2012. [Association between fractional flow reserve and quantitative coronary angiography parameters in intermediate coronary artery stenosis]. Zhonghua Xin Xue Guan Bing Za Zhi, 40, 742-6.

Sun, Z. & Ng, K. H. 2012. Prospective versus retrospective ECG-gated multislice CT coronary angiography: a systematic review of radiation dose and diagnostic accuracy. Eur J Radiol, 81, e94-100.

Sun, Z., Lin, C., Davidson, R., Dong, C. & Liao, Y. 2008. Diagnostic value of 64-slice CT angiography in coronary artery disease: a systematic review. Eur J Radiol, 67, 78-84.

Tamarappoo, B. K., Gutstein, A., Cheng, V. Y., Nakazato, R., Gransar, H., Dey, D., Thomson, L. E., Hayes, S. W., Friedman, J. D., Germano, G., Slomka, P. J. & Berman, D. S. 2010. Assessment of the relationship between stenosis severity and distribution of coronary artery stenoses on multislice computed tomographic angiography and myocardial ischemia detected by single photon emission computed tomography. J Nucl Cardiol, 17, 791-802.

Taverna Workbench 2.5.0 [Online, accessed July 2015]. School of Computer Science, University of Manchester, UK. Available: http://www.taverna.org.uk/download/workbench/2-5/.

Taylor, C. A. & Figueroa, C. A. 2009. Patient-specific modeling of cardiovascular mechanics. Annu Rev Biomed Eng, 11, 109-34.

Taylor, C. A. & Steinman, D. A. 2010. Image-based modeling of blood flow and vessel wall dynamics: applications, methods and future directions: Sixth International Bio-Fluid Mechanics Symposium and Workshop, March 28-30, 2008 Pasadena, California. Ann Biomed Eng, 38, 1188-203.

Taylor, C. A., Fonte, T. A. & Min, J. K. 2013. Computational fluid dynamics applied to cardiac computed tomography for noninvasive quantification of fractional flow reserve: scientific basis. J Am Coll Cardiol, 61, 2233-41.

Teichholz, L. E., Kreulen, T., Herman, M. V. & Gorlin, R. 1976. Problems in echocardiographic volume determinations: echocardiographic-angiographic correlations in the presence of absence of asynergy. Am J Cardiol, 37, 7-11.

Thron, A. & Voigt, K. 1983. Rotational cerebral angiography: procedure and value. AJNR Am J Neuroradiol, 4, 289-91.

Tiefenbacher, C. P. & Chilian, W. M. 1998. Heterogeneity of coronary vasomotion. Basic Res Cardiol, 93, 446-54.

Tonino, P. A., De Bruyne, B., Pijls, N. H., Siebert, U., Ikeno, F., Van' T Veer, M., Klauss, V., Manoharan, G., Engstrom, T., Oldroyd, K. G., Ver Lee, P. N., Maccarthy, P. A. & Fearon, W. F. 2009. Fractional flow reserve versus angiography for guiding percutaneous coronary intervention. N Engl J Med, 360, 213-24.

Tonino, P. A., Fearon, W. F., De Bruyne, B., Oldroyd, K. G., Leesar, M. A., Ver Lee, P. N., Maccarthy, P. A., Van't Veer, M. & Pijls, N. H. 2010. Angiographic versus functional severity of coronary artery stenoses in the FAME study fractional flow reserve versus angiography in multivessel evaluation. J Am Coll Cardiol. United States: 2010 American College of Cardiology Foundation. Published by Elsevier Inc.

Topol, E. J. & Nissen, S. E. 1995. Our preoccupation with coronary luminology. The dissociation between clinical and angiographic findings in ischemic heart disease. Circulation, 92, 2333-42.

Townsend, N. W., K. Bhatnager, P. Smolina, K. Nichols, M. Leal, J. Luengo-Fernandez, R. Raynor, M 2012. Coronary Heart Disease Statistics 2012 edition, London.

Tu, R. K., Cohen, W. A., Maravilla, K. R., Bush, W. H., Patel, N. H., Eskridge, J. & Winn, H. R. 1996. Digital subtraction rotational angiography for aneurysms of the intracranial anterior circulation: injection method and optimization. AJNR Am J Neuroradiol, 17, 1127-36.

Tu, S., Barbato, E., Koszegi, Z., Yang, J., Sun, Z., Holm, N. R., Tar, B., Li, Y., Rusinaru, D., Wijns, W. & Reiber, J. H. 2014. Fractional flow reserve calculation from 3-dimensional quantitative coronary angiography and TIMI frame count: a fast computer model to quantify the functional significance of moderately obstructed coronary arteries. JACC Cardiovasc Interv, 7, 768-77.

Tu, S., Echavarria-Pinto, M., Von Birgelen, C., Holm, N. R., Pyxaras, S. A., Kumsars, I., Lam, M. K., Valkenburg, I., Toth, G. G., Li, Y., Escaned, J., Wijns, W. & Reiber, J. H. 2015. Fractional flow reserve and coronary bifurcation anatomy: a novel quantitative model to assess and report the stenosis severity of bifurcation lesions. JACC Cardiovasc Interv, 8, 564-74.

Tu, S., Xu, L., Ligthart, J., Xu, B., Witberg, K., Sun, Z., Koning, G., Reiber, J. H. & Regar, E. 2012. In vivo comparison of arterial lumen dimensions assessed by co-registered three-dimensional (3D) quantitative coronary angiography, intravascular ultrasound and optical coherence tomography. Int J Cardiovasc Imaging, 28, 1315-27.

Uren, N. G., Crake, T., Lefroy, D. C., De Silva, R., Davies, G. J. & Maseri, A. 1993a. Delayed recovery of coronary resistive vessel function after coronary angioplasty. J Am Coll Cardiol, 21, 612-21.

Uren, N. G., Marraccini, P., Gistri, R., De Silva, R. & Camici, P. G. 1993b. Altered coronary vasodilator reserve and metabolism in myocardium subtended by normal arteries in patients with coronary artery disease. J Am Coll Cardiol, 22, 650-8.

Van Belle, E., Rioufol, G., Pouillot, C., Cuisset, T., Bougrini, K., Teiger, E., Champagne, S., Belle, L., Barreau, D., Hanssen, M., Besnard, C., Dauphin, R., Dallongeville, J., El Hahi, Y., Sideris, G., Bretelle, C., Lhoest, N., Barnay, P., Leborgne, L. & Dupouy, P. 2014. Outcome impact of coronary revascularization strategy reclassification with fractional flow reserve at time of diagnostic angiography: insights from a large French multicenter fractional flow reserve registry. Circulation, 129, 173-85.

Van De Hoef, T. P., Meuwissen, M., Escaned, J., Davies, J. E., Siebes, M., Spaan, J. A. & Piek, J. J. 2013. Fractional flow reserve as a surrogate for inducible myocardial ischaemia. Nat Rev Cardiol, 10, 439-52.

Van De Hoef, T. P., Meuwissen, M., Escaned, J., Sen, S., Petraco, R., Van Lavieren, M. A., Echavarria-Pinto, M., Nolte, F., Nijjer, S., Chamuleau, S. A., Voskuil, M., Van Eck-Smit, B. L., Verberne, H. J., Henriques, J. P., Koch, K. T., De Winter, R. J., Spaan, J. A., Siebes, M., Tijssen, J. G., Davies, J. E. & Piek, J. J. 2014a. Head-to-head comparison of basal stenosis resistance index, instantaneous wave-free ratio, and fractional flow reserve: diagnostic accuracy for stenosis-specific myocardial ischaemia. EuroIntervention.

Van De Hoef, T. P., Nolte, F., Damman, P., Delewi, R., Bax, M., Chamuleau, S. A., Voskuil, M., Siebes, M., Tijssen, J. G., Spaan, J. A., Piek, J. J. & Meuwissen, M. 2012. Diagnostic accuracy of combined intracoronary pressure and flow velocity information during baseline conditions: adenosine-free assessment of functional coronary lesion severity. Circ Cardiovasc Interv, 5, 508-14.

Van De Hoef, T. P., Nolte, F., Echavarria-Pinto, M., Van Lavieren, M. A., Damman, P., Chamuleau, S. A., Voskuil, M., Verberne, H. J., Henriques, J. P., Van Eck-Smit, B. L., Koch, K. T., De Winter, R. J., Spaan, J. A., Siebes, M., Tijssen, J. G., Meuwissen, M. & Piek, J. J. 2014b. Impact of hyperaemic microvascular resistance on fractional flow reserve measurements in patients with stable coronary artery disease: insights from combined stenosis and microvascular resistance assessment. Heart, 100, 951-9.

Van De Hoef, T. P., Nolte, F., Rolandi, M. C., Piek, J. J., Van Den Wijngaard, J. P., Spaan, J. A. & Siebes, M. 2012b. Coronary pressure-flow relations as basis for the understanding of coronary physiology. J Mol Cell Cardiol, 52, 786-93.

Van De Hoef, T. P., Van Lavieren, M. A., Damman, P., Delewi, R., Piek, M. A., Chamuleau, S. A., Voskuil, M., Henriques, J. P., Koch, K. T., De Winter, R. J., Spaan, J. A., Siebes, M., Tijssen, J. G., Meuwissen, M. & Piek, J. J. 2014. Physiological basis and long-term clinical outcome of discordance between fractional flow reserve and coronary flow velocity reserve in coronary stenoses of intermediate severity. Circ Cardiovasc Interv, 7, 301-11.

Van De Vosse, F. N. & Stergiopulos, N. 2011. Pulse Wave Propagation in the Arterial Tree. Annu. Rev. Fluid Mech, 43, 467-499.

Van Der Giessen, A. G., Groen, H. C., Doriot, P. A., De Feyter, P. J., Van Der Steen, A. F., Van De Vosse, F. N., Wentzel, J. J. & Gijsen, F. J. 2011. The influence of boundary conditions on wall shear stress distribution in patients specific coronary trees. J Biomech, 44, 1089-95.

Venkatasubramaniam, A. K., Fagan, M. J., Mehta, T., Mylankal, K. J., Ray, B., Kuhan, G., Chetter, I. C. & Mccollum, P. T. 2004. A comparative study of aortic wall stress using finite element analysis for ruptured and non-ruptured abdominal aortic aneurysms. Eur J Vasc Endovasc Surg, 28, 168-76.

Vergroesen, I., Noble, M. I., Wieringa, P. A. & Spaan, J. A. 1987. Quantification of O2 consumption and arterial pressure as independent determinants of coronary flow. Am J Physiol, 252, H545-53.

Verhoeff, B. J., Siebes, M., Meuwissen, M., Atasever, B., Voskuil, M., De Winter, R. J., Koch, K. T., Tijssen, J. G., Spaan, J. A. & Piek, J. J. 2005. Influence of percutaneous coronary intervention on coronary microvascular resistance index. Circulation, 111, 76-82.

Villa-Uriol, M. C., Berti, G., Hose, D. R., Marzo, A., Chiarini, A., Penrose, J., Pozo, J., Schmidt, J. G., Singh, P., Lycett, R., Larrabide, I. & Frangi, A. F. 2011. @neurIST complex information processing toolchain for the integrated management of cerebral aneurysms. Interface Focus, 1, 308-19.

Volcano Corp. 2001. Functional Management: ComboWire® XT Guide Wire [Online]. http://eu.volcanocorp.com/products/combowire-xt.php. [Accessed 07/10/2013 2013].Vogt, M., Motz, W. & Strauer, B. E. 1992. Coronary haemodynamics in hypertensive heart disease. Eur Heart J, 13 Suppl D, 44-9.

VPH-SHARE.EU. 2015. http://vph-share.eu [Online].

Wang, R., Yu, W., Wang, Y., He, Y., Yang, L., Bi, T., Jiao, J., Wang, Q., Chi, L., Yu, Y. & Zhang, Z. 2011. Incremental value of dual-energy CT to coronary CT angiography for the detection of significant coronary stenosis: comparison with quantitative coronary angiography and single photon emission computed tomography. Int J Cardiovasc Imaging, 27, 647-56.

Weese, J., Groth, A., Nickisch, H., Barschdorf, H., Weber, F. M., Velut, J., Castro, M., Toumoulin, C., Coatrieux, J. L., De Craene, M., Piella, G., Tobon-Gomez, C., Frangi, A. F., Barber, D. C., Valverde, I., Shi, Y., Staicu, C., Brown, A., Beerbaum, P. & Hose, D. R. 2013. Generating anatomical models of the heart and the aorta from medical images for personalized physiological simulations. Med Biol Eng Comput, 51, 1209-19.

Westerhof, N. & Elzinga, G. 1991. Normalized input impedance and arterial decay time over heart period are independent of animal size. Am J Physiol, 261, R126-33.

Westerhof, N., Bosman, F., De Vries, C. J. & Noordergraaf, A. 1969. Analog studies of the human systemic arterial tree. J Biomech, 2, 121-43.

Westerhof, N., Elzinga, G. & Sipkema, P. 1971. An artificial arterial system for pumping hearts. J Appl Physiol, 31, 776-81.

Westerhof, N., Lankhaar, J. W. & Westerhof, B. E. 2009. The arterial Windkessel. Med Biol Eng Comput, 47, 131-41.

Westerhof, N., Stergiopulos, N. & Noble, M. I. M. 2010. Snapshots of Hemodynamics: An Aid for Clinical Research and Graduate Education, New York, Springer.

Wetterer, E. 1940. Quantitative Beziehungen zwischen stromstarke und Druck im natu̇rlichen Kreislauf bei zeitlich variabler Elasticitat des Artriellen Windkessels. Zeitschrift für Biologie, 100, 260-317.

Wharton, G. S., R. Allen, A. Brewerton, H. Jones, R. Kanagala, P. Lloyd, G. Masani, N. Mathew, T. Oxborough, D. Rana, B. Sandoval J. Smith, N. Wheeler, R. 2012. A Minimum Dataset for a Standard Transthoracic Echocardiogram

White, C. W., Wright, C. B., Doty, D. B., Hiratza, L. F., Eastham, C. L., Harrison, D. G. & Marcus, M. L. 1984. Does visual interpretation of the coronary arteriogram predict the physiologic importance of a coronary stenosis? N Engl J Med, 310, 819-24.

Wijns, W., Kolh, P., Danchin, N., Di Mario, C., Falk, V., Folliguet, T., Garg, S., Huber, K., James, S., Knuuti, J., Lopez-Sendon, J., Marco, J., Menicanti, L., Ostojic, M., Piepoli, M. F., Pirlet, C., Pomar, J. L., Reifart, N., Ribichini, F. L., Schalij, M. J., Sergeant, P., Serruys, P. W., Silber, S., Sousa Uva, M. & Taggart, D. 2010. Guidelines on myocardial revascularization. Eur Heart J, 31, 2501-55.

Wilson, R. F., Wyche, K., Christensen, B. V., Zimmer, S. & Laxson, D. D. 1990. Effects of adenosine on human coronary arterial circulation. Circulation, 82, 1595-606.

Windecker, S., Kolh, P., Alfonso, F., Collet, J. P., Cremer, J., Falk, V., Filippatos, G., Hamm, C., Head, S. J., Juni, P., Kappetein, A. P., Kastrati, A., Knuuti, J., Landmesser, U., Laufer, G., Neumann, F. J., Richter, D. J., Schauerte, P., Sousa Uva, M., Stefanini, G. G., Taggart, D. P., Torracca, L., Valgimigli, M., Wijns, W. & Witkowski, A. 2014. 2014 ESC/EACTS Guidelines on myocardial revascularization: The Task Force on Myocardial Revascularization of the European Society of Cardiology (ESC) and the European Association for Cardio-Thoracic Surgery (EACTS)Developed with the special contribution of the European Association of Percutaneous Cardiovascular Interventions (EAPCI). Eur Heart J, 35, 2541-619.

Wingard, D. L., Suarez, L. & Barrett-Connor, E. 1983. The sex differential in mortality from all causes and ischemic heart disease. Am J Epidemiol, 117, 165-72.

Witzenbichler, B., Maehara, A., Weisz, G., Neumann, F. J., Rinaldi, M. J., Metzger, D. C., Henry, T. D., Cox, D. A., Duffy, P. L., Brodie, B. R., Stuckey, T. D., Mazzaferri, E. L., Jr., Xu, K., Parise, H., Mehran, R., Mintz, G. S. & Stone, G. W. 2014. Relationship between intravascular ultrasound guidance and clinical outcomes after drug-eluting stents: the assessment of dual antiplatelet therapy with drug-eluting stents (ADAPT-DES) study. Circulation, 129, 463-70.

World Health Organization, 2013. The top 10 causes of death. [Accessed 20/09/2013].

World Health Organization. 2014. World Health Oragnisaton | The top 10 causes of death [Online]. World Health Organization. Available: http://www.who.int/mediacentre/factsheets/fs310/en/.

Xiong, G., Figueroa, C. A., Xiao, N. & Taylor, C. A. 2011. Simulation of blood flow in deformable vessels using subject-specific geometry and spatially varying wall properties. Int J Numer Method Biomed Eng, 27, 1000-1016.

Yoganathan, A. P., Chandran, K. B. & Sotiropoulos, F. 2005. Flow in prosthetic heart valves: state-of-the-art and future directions. Ann Biomed Eng, 33, 1689-94.

Yong, A. S., Ng, A. C., Brieger, D., Lowe, H. C., Ng, M. K. & Kritharides, L. 2011. Three-dimensional and two-dimensional quantitative coronary angiography, and their prediction of reduced fractional flow reserve. Eur Heart J, 32, 345-53.

Young, D. F., Cholvin, N. R., Kirkeeide, R. L. & Roth, A. C. 1977. Hemodynamics of arterial stenoses at elevated flow rates. Circ Res, 41, 99-107.

Zeng, D., Boutsianis, E., Ammann, M., Boomsma, K., Wildermuth, S. & Poulikakos, D. 2008. A study on the compliance of a right coronary artery and its impact on wall shear stress. J Biomech Eng, 130, 041014.

Zeng, D., Ding, Z., Friedman, M. H. & Ethier, C. R. 2003. Effects of cardiac motion on right coronary artery hemodynamics. Ann Biomed Eng, 31, 420-9.

Zervides, C. & Giannoukas, A. D. 2013. Computational phlebology: reviewing computer models of the venous system. Phlebology, 28, 209-18.

Zhang, Y., Farooq, V., Garcia-Garcia, H. M., Bourantas, C. V., Tian, N., Dong, S., Li, M., Yang, S., Serruys, P. W. & Chen, S. L. 2012. Comparison of intravascular ultrasound versus angiography-guided drug-eluting stent implantation: a meta-analysis of one randomised trial and ten observational studies involving 19,619 patients. EuroIntervention, 8, 855-65.

ZHAO. FENG & XIE. XIANGHUA 2013. An Overview of Interactive Medical Image Segmentation. Annals of the BMVA 1-22.